Title
Conditions Influencing Sediment Transport in Coastal Environments

Author
Allen, Rachel M

Publication Date
2018

Peer reviewed|Thesis/dissertation

Conditions Influencing Sediment Transport in Coastal Environments

by

Rachel M. Allen

A dissertation submitted in partial satisfaction of the

requirements for the degree of

Doctor of Philosophy

in

Engineering - Civil and Environmental Engineering

in the

Graduate Division

of the

University of California, Berkeley

Committee in charge:

Professor Evan A. Variano, Chair
Professor Mark T. Stacey
Professor Laurel G. Larsen

Spring 2018

Conditions Influencing Sediment Transport in Coastal Environments

Abstract

Conditions Influencing Sediment Transport in Coastal Environments

by

Rachel M. Allen

Doctor of Philosophy in Engineering - Civil and Environmental Engineering

University of California, Berkeley

Professor Evan A. Variano, Chair

The water column at Point Sal, on the coast of California, is stratified by temperature, and internal bores propagate through the region regularly. We collected velocity, temperature, and turbulence measurements in the bottom boundary layer at a 30−m deep site for 2 months during summer 2015. We estimated the turbulent shear production (P), turbulent dissipation rate (ϵ), and vertical diffusive transport (T), to investigate the near-bed local turbulent kinetic energy (TKE) budget. The local TKE budget showed an approximate balance ($P \approx \epsilon$) during the observational period, and buoyancy generally did not affect the TKE balance. On a finer resolution timescale, we explored the balance between dissipation and models for production, and observed that internal waves did not affect the balance in TKE at this depth. Characterizing the turbulence budget near the bed can lead to understanding and prediction of resuspension and transport of sediments.

Estuary marshes need bay-sourced sediment to keep up with sea level rise, and managing such crucial habitats requires numerical models of sediment transport. Over the course of 20 months in the field, we examined three parameters commonly applied as external inputs in numerical models. Our instrumentation measured tidal currents, water level, turbulent stresses, wave conditions, suspended sediment concentration and (briefly) suspended floc size at up to 4 sites at 1 and 2 m mean lower-low water on the 11-km wide mudflat of San Pablo Bay, California. Through these measurements, we computed bottom roughness, bed erodibility, and settling velocity. Bed roughness decreased by an order of magnitude from 10^{-5} to 10^{-6} at the more storm-influenced site during the stormy season. We attributed this to strong winter storms which last longer and are oriented on-shore. The bed erodibility parameter increased with the spring-neap cycle during periods with low storm activity, and increased up to 6 fold concurrent with winter storms. Suspended particle size (and settling velocity) decreased with greater tidal currents. The reduced settling velocity associated with a smaller particle size contributed to the higher suspended sediment populations observed during spring tides. With many sediment models being developed and implemented around the world, we focus on ground-truthing numerical models through our search for bottom roughness, erodibility, and floc size from field data. This characterization of sediment pa-

rameters will enable numerical models to be more physically grounded and predictive in environments like San Pablo Bay.

Stratification in estuaries is important for tidal exchange, vertical mixing, and sediment transport. In estuarine shallows, a framework of strain-induced periodic stratification (SIPS) is traditionally applied for interpreting the onset of stratification. We explored the mechanisms of SIPS as well as frontal advection for inducing stratification in the estuarine shoals of San Pablo Bay, California. Our instrumentation measured salinity, temperature, water level, and (at a subset of the sites) velocity at 5 sites across the bay over a period of 20 months. At a single site during a handful of the periods, we also measured vertical gradients in salinity. These measurements revealed that both SIPS and frontal advection were responsible for inducing stratification. When SIPS was responsible for creating stratification, it was more likely that mixing would erase it. When frontal advection was responsible, stratification was erased by advection and by mixing. A theoretical investigation of the lateral movement of stratification depth showed that mixing was more important than advection for allowing stratification along estuarine shoals. As the bed slope decreased, the role of mixing became even more dominant in controlling stratification. This spatial view of stratification revealed the possibilities for stratification and destratification along broad estuarine shoals.

Estuary margins are the connection between land and sea. At three different margin regions of San Francisco Bay, we explore flow, turbulence, and sediment transport. Measurements of velocity, Reynolds stress, salinity, temperature, and suspended sediment at these sites over 6 hour periods suggest that some sites are depositing upstream during high water, while other are eroding. Salinity stratification developed at some sites during mid-ebb, and the smaller tidal creeks showed a basin-scale seiche. While this seiche motion had a strong role in driving near bed velocities, its role in suspended sediment flux was minimal. From high-frequency measurements of vertical velocity and suspended sediment concentration, we computed settling velocity, however our investigation suggests that sediment advection remains too important at these sites to rely on this measurement strategy. This study suggests numerous paths for future work, which will further characterize the connection at estuary margins.

The objective of this dissertation is to explore parameters and processes pertaining to sediment transport in estuarine and coastal environments. Chapter 1 offers a brief introduction to the concepts of turbulence, sediment transport, and salinity stratification. Chapter 2 investigates the turbulence budget in the bottom boundary layer of the California inner shelf, in a region influenced by internal waves, as published in Ocean Dynamics (Allen, Simeonov, Calantoni, Stacey, & Variano, 2018). Chapter 3 presents field investigations on a seasonal scale of three parameters necessary for numerical sediment modeling. In chapter 4, we explore the balance between two stratification mechanisms in broad estuarine shallows, and discuss a framework for considering the destratification mechanism. Chapter 5 presents our results from a field study in San Francisco estuary margins, focusing on observed seiching as well as our ability to investigate particle settling. Finally, chapter 6 contains a summary of the findings from this work.

To Sylvi

Contents

List of Figures

List of Tables

Acknowledgments

My research advisors, Evan Variano, Jessie Lacy, and Mark Stacey, have inspired me and supported my study of sediments. Each of you has different strengths, and it has been a wonderful experience learning to balance and utilize your expertise. Evan, you have this ability to make sentences clearer and stronger and an enthusiasm to tackle absolutely any aspect of research, whether it's getting a drill to work or treating error in my data. Jessie's depth of knowledge both challenges and inspires me. Getting to work on the same project that you are tackling has meant that you have insightful thoughts at every turn. Your commitment to carve out a piece of it for me to work on and your willingness to meet often twice in a day has given me the space and support to dive in. Mark, I will always be inspired by your kindness, perceptiveness, honesty, and incredible depth of thought. You can dive in to any question with speed and make my interpretation of it deeper. Not many folks get to work so closely with such a fantastic team of advisors - I feel so lucky to be part of this.

Thank you to the assortment of folks I also consider advisors. Shelley Okimoto, thank you for managing all of the things that I forget to do until last minute, and for making this department work like a team. I'm not sure how you do, but you do. Tina Chow, your vision in our lab and your support on my qualifying exam have been invaluable. Joe Calantoni and Julian Simeonov, thank you for hosting me for a whole summer in Mississippi. It was so valuable to me to have that time to dive in to a project, to get out in the field, and there's no way chapter 2 would look anything like it does without your support. Thank you Rusty Holleman and Lissa MacVean. You are this incredible example of what one can do coming out of Mark's lab, and whenever I get to talk to you I get creative ideas and realistic support. Laurel Larsen, it has been wonderful to get to be part of your group every once in a while. Your classes were great, I loved getting to work on projects with you, and you've been incredibly generous with your lab space and equipment.

There has been a wonderful group of students and post-docs in the Environmental Fluid Mechanics and Hydrology group over the years. From helping me solve Matlab problems, to thinking about how to write, to coming in the field or cleaning up afterwards, to discussions at group meeting, you have been examples and support in getting this done. Thank you, in no particular order, Margaret Byron, Nimish Pujara, Ankur Bordoloi, Ian Tse, Cristina Poindexter, Kim Huynh, Teri Oehmke, Jackie Ma, Rosanna Neuhausler, Olivia Hoang, Michelle Hummel, Jason Simon, Diane Taylor, Alex Anderson-Connolly, Gabrielle Boisramé, and Dave Dralle. In particular, I want to thank Susan Willis and Megan Williams. You were inspiring and supportive when you were at Berkeley, and you figured out how to keep doing that when you moved away.

Thank you to my colleagues and friends at USGS and SFEI. The USGS team of Theresa Fregoso, Joanne Ferreira, Cordell Johnson, Pete Dal Ferro, Tim Elfers, Jenny McKee, Rob Wyland, and Emily Carlson - thank you for your work on the projects that I've been part of and your support in science. I'm so lucky to have worked at SFEI - what a caring place with such a strong mission. Dave Senn, Jen Hunt, Alicia Gilbreath, Jay Davis, and others:

thank you. In particular, Meg Sedlak, your enthusiasm for everything is remarkable. You were a great supervisor and you are an incredible role model.

I've also had wonderful support groups. My peer group morphed from Maddie Foster-Martinez and Will Tarpeh to Jen Lawrence and Joe Charbonnet, but all of you have been generous, supportive, kind, questioning, and inspiring. You help me pursue science, explain it, and set goals. I'm still working on all of it, but the support and friendship in this pursuit has meant that I feel like I'm part of a community I believe in. Thank you also to Rachel Dzombak and my MPOWIR group. This collection of women scientists has, likewise, been grounding and inspiring.

On the personal end, I am so lucky to be part of the Bay Area Mountain Rescue Unit. It has been, and is, my home. I love our trainings, I love our missions, and I love getting to challenge myself and to try to make our unit better. Thank you to just some of the people I've gotten to know through this unit: Blake Gleason, Chris Kantarjiev, Rachel Farrand, John Chang, Matt Jacobs, John Zirinsky, Alice Ng, and Matt Malkowski. You are wonderful friends and fantastic partners. Somehow, I still have friends outside of BAMRU. Thank you Sarah Hanson, Michelle Donnelly, Carynne McIver, James Ritterpusch, Sandy and Tim Larkin, Jen and Steve MacQuiddy, Kyle Barbour, Miriam McQuade, Martha Hasenhuttl, Joey Smith, and Mike Kowalski for your flexiblity, your friendship, and your support in pursuing a dissertation and doing this whole search and rescue thing.

Finally, I don't know how I would have touched this without my family. Lala and Papa - your kindness is inspiring. Viola Birss, you are a role model. Pup Gould, you are too, but in a very different way. In the way of work hard and figure it out, and always have a joke, like the time the doctor said he could just tell that guy was crazy.... Milena Borsdorff, what a wonderful sister you are. Maddie Foster-Martinez, I can't believe I got to spend (nearly) all of grad school with your desk feet from mine. You have been inspiring and kind, time and time and time again. Sylvi Cohn, thank you for everything. I couldn't have found a better place to be. Alex Grishaver, I feel your love and your friendship throughout. Mom and Dad, you are why I thought I could do this. You believe in me every time and you are willing to dig me out of whatever hole, and help me dig myself out. Libby and Hannah, you are funny and believe I'm wonderful and support me no matter what. Of all the things to get through, we will get through them.

To everyone I didn't name here, know that I value you immensely and blame it on the stroke.

Chapter 1

Introduction

As estuary forms where the freshwater running out of a river meets the salty tidal flow of the ocean. Estuaries are often home to rich aquatic ecosystems, and many of the world's cities and ports, including Tokyo, New York City, Sao Paulo, and San Francisco, are built around estuaries. As a tidal system, water and sediments are continuously moved into and out of an estuary, and the shape of the estuary – where mudflats form, where channels allow for ship passage, and where coastal wetlands grow – depends on the transport of sediment. An estuary's ability to transport sediment, in particular how sediment is distributed vertically in the water column, is tied to vertical mixing through turbulence and vertical stratification due to salinity.

Estuarine sediments on the bed and in the water column can have important effects on the ecosystem. Sediment can carry nutrients, such as nitrogen and phosphorous, which can supply the base of the food web or, in excess, drive eutrophication. Sediments also transport contaminants, such as polychlorinated biphenyls and mercury. Marsh growth requires external sediment supply to keep up with sea level rise (Callaway, Borgnis, Turner, & Milan, 2012). When suspended in the water column, fine sediments can provide habitat and protection from predation for pelagic fish, such as delta smelt (Feyrer, Nobriga, & Sommer, 2007). Suspended sediment also limits light penetration into the water column, suppressing phytoplankton growth. In estuaries otherwise susceptible to eutrophication, light limitation can be a strong control against its harmful effects. However, locations with limited primary production may have overall ecosystem suppression due to high turbidity. Sediment dynamics play an important role in estuary past, present, and future. They have been the focus of research at UC Berkeley from the early 20^{th} century through today (Ettema & Mutel, 2014).

Fine sediments are passively transported by fluid flows and actively settle through the water due to their heavier density. Fluid flows cause sediment advection by mean currents, and diffusion through turbulent mixing, as described by the Reynolds averaged advection-diffusion equation:

$$\frac{\partial \overline{C}}{\partial t} = -\frac{\partial}{\partial x_i}\left(\overline{u_i' C'}\right) - \frac{\partial \overline{u_i}\,\overline{C}}{\partial x_i} - w_s \frac{\partial \overline{C}}{\partial x_3} \tag{1.1}$$

Here, suspended sediment concentration is given by C, flow velocities are u_i, and w_s is the size-class averaged settling velocity of the suspended material, negative for falling particles. Reynolds averages are represented by overbars, and primes denote fluctuating quantities. The term on the left describes the accumulation of suspended sediment concentration. The first term on the right hand side reflects transport due to turbulent fluxes, the second term is advective transport by the mean flow, and the third term is transport due to particle settling.

A model of fine sediment transport requires both sediment advection and diffusion (equation 1.1) and fluid momentum (Toorman, 2000). The sediment transport equation requires accurate settling velocities, mass diffusivity (or Schmidt number), as well as erosion and deposition fluxes. The momentum equation requires turbulence closure, suspension density from the sediment transport model, and potentially a rheological model to give suspension viscosity. Models of sediment transport require an understanding of the physical processes as well as a grasp of the physical parameters.

1.1 Turbulence and Sediment Transport

Turbulence and suspended sediment can interact in a number of important ways.

The type of sediment on the bed (e.g. rough and rocky or smooth) can impact how turbulence develops in the water column, with a rockier bed promoting strong turbulence in the wave and current boundary layers.

Fine sediments interact with the bed through deposition and entrainment. Deposition occurs when the downward settling surpasses turbulent mixing. Entrainment is the resuspension of material off the bed. A common model predicts that resuspension occurs when bed shear stress (due to turbulence, waves, and their interaction) surpasses a critical shear stress. The critical bed shear stress can be horizontally patchy due to grain size, bed form, or biogenic variation. It can also vary in time with these same processes, or due to consolidation. For example, the degree of transmission of turbulent and wave energy to the bed affects bed consolidation, the ability of the bed to absorb wave and turbulent energy, and sediment resuspension. The model also describes the rate at which sediment erodes depending on the applied shear stress.

Turbulence affects how particles flocculate in the water column: mixing can allow for smaller particles to collide and produce larger flocs, but even more mixing can induce shear and yield smaller flocs. The size of the flocs drives how fast they settle - larger flocs will settle faster, while small flocs remain suspended and transport much farther during a tidal cycle. Inversely, particle settling can also impact turbulence: enough particle settling can yield a sediment-stratified water column, suppressing turbulent mixing.

How these processes change in space and time, on millimeter to system-wide spatial scales and on turbulent and wave timescales of seconds to process scales at decades and beyond, can drive sediment transport, turbulent development, and their framework for interaction. These ideas are explored in chapters 3 and 5.

1.2 Turbulence and Salinity Stratification

In estuaries, salinity stratification can limit turbulent mixing. Stratification by salinity causes separation of turbulent regimes, vertically or horizontally, which inhibits mixing, and can allow for multiple flow directions in distinct hydrodynamic cells. However, strong enough turbulent mixing can overcome this stratification, unifying flow. Especially when stratification allows for flow in opposite directions or the occurrence of internal waves, turbulence can be created at an internal interface or breaking waves.

Longitudinally, estuaries set up an exchange flow that escorts freshwater out of the system. Estuaries can vary from strongly stratified by salinity (fjords), to time-dependent salt-wedges, to well-mixed systems (Geyer & MacCready, 2014). Parameters such as the mixing number and the horizontal freshwater Froude number distinguish these systems, and characterize the estuarine transport defined by river outflow velocity scaled by the maximum frontal propagation speed and the effectiveness of tidal mixing in a stratified estuary. However, the structure of an estuary can be important: lateral salinity gradients can operate in opposition to and dominate along-channel straining.

The balance between salinity stratification and turbulent mixing on both a lateral and longitudinal basis can impact flow and transport on subtidal to spring-neap, storm-event, season, or annual scales. We explore these ideas in chapters 2 and 4.

1.3 Numerical Models

Numerical models in estuarine systems incorporate as many of these mixing and transport processes as possible and pertinent.

For example, one model exploring sediment transport in San Pablo Bay applied a 3-dimensional unstructured grid to capture water surface elevation, current velocities, advection, mixing, and settling (Bever & MacWilliams, 2013). It incorporates wave energy through a model of the wave action balance equation, which enables sediment resuspension through combined current and wave induced bed shear stress. It models the morphologic evolution of the seabed by computing erosion, deposition, and net sediment flux through the seabed, and includes 4 particle classes which can settle, erode, and deposit, but not aggregate or shear.

Another model exploring sediment transport in the San Francisco Bay Delta invoked a 2-dimensional unstructured grid, with a directly coupled link between the hydrodynamic and sediment transport components (Achete, van der Wegen, Roelvink, & Jaffe, 2015). Its hydrodynamic component yields shear stresses, which are coupled off-line with a water-quality model that solves the advection-diffusion equation. Like the Bever and MacWilliams, 2013 model, it does not simulate flocculation, including only a single particle size.

These models demonstrate careful examples of sediment modeling in San Francisco Bay, but they do not include all of the processes potentially important for sediment transport,

nor do they incorporate the full scale of spatial and temporal variability. The field work presented here will help guide future sediment transport models.

1.4 San Francisco Bay

New understanding of San Francisco Bay will come from detailed understanding of physical, chemical, biological, and geological questions. Cloern and Jassby, 2012 articulated some of the changes in San Francsico Bay induced by humans, and they highlight the imperative of monitoring to observe and understand long-term trends. The system as a whole faces pressures from the human environment, and the context for system response will adjust, perhaps in unanticipated ways, with sea level rise. Our ability to understand and predict such changes depends on continued monitoring and focused studies.

1.5 Dissertation Structure

Turbulence drives sediment resuspension and distribution in the water column. Stratified environments can suppress turbulent mixing, but also allow for internal waves to move through the water column and generate mixing, especially in coastal shelf regions (Arthur & Fringer, 2014; Walter, Squibb, Woodson, Koseff, & Monismith, 2014). In the near-shore, how is turbulence near the bed impacted by the presence of internal waves? As we explore the conditions impacting near-bed turbulence in chapter 2, we reveal the context and environment for sediment suspension and transport.

Numerical models aim to predict sediment concentrations and transport in places like San Francisco Bay. To function accurately, they require a handful of external parameters, which are generally set based on guesses or limited measurements, and are often fixed in time and space (e.g., Bever & MacWilliams, 2013; Achete et al., 2015). In chapter 3, we use field measurements of parameters including bottom roughness, bed erodibility, and settling velocity to investigate their variation on a seasonal scale. With field-based understanding of parameter variation, we can improve predictions from numerical sediment transport models.

Stratification in the water column decouples the surface and near-bed waters, suppressing mixing and transport of scalars such as sediment. Along the estuarine tidal axis, vertical salinity gradients vary with the tidal cycle, producing stronger stratification on ebb (J. H. Simpson, Brown, Matthews, & Allen, 1990). Lateral to tidal channels, advection of salinity gradients can yield stronger stratification on flood tides (Scully & Geyer, 2012). However, studies of stratification induction have been more limited on broad estuarine shallows. In chapter 4, we show that both periodic straining and frontal advection can lead to stratification in such shallows, inducing stratification at differing phases of the tidal cycle. The timing and extent of stratification development impacts the ability of tidal flows to transport sediment and other scalars.

Finally, tidal creeks connect rivers to the body of the estuary, and can gain or lose sediment on timescales ranging from sub-tidal to decadal or longer. In parts of San Francisco Bay, it has been seen that particles settle faster with increasing turbulence (A. Manning & Schoellhamer, 2013); in other parts, turbulence is tied to particles breaking down and settling slower (chapter 3). In chapter 5, I focus on estuarine creeks in an attempt to establish this relationship at the edges of the Bay. While we cannot fully characterize this connection, this work offers insight, data, and additional questions regarding hydrodynamics and transport in tidal creeks.

This dissertation explores the conditions yielding sediment transport in estuarine environments. I focus on bottom boundary layer turbulence, bed resuspension, water column stratification, and hydrodynamics and sediment transport in estuary margins. Each of these addresses some of the parameters necessary for a numerical model of sediment transport, and brings us closer to a physical understanding of the processes driving sediment transport.

Chapter 2

Turbulence in the presence of internal waves in the bottom boundary layer of the California inner shelf

2.1 Introduction

The continental shelf connects the deep ocean with the coastline. Transport and gradients in temperature, nutrients, freshwater, sediment, and pollutants control the quality of the shelf as a habitat for marine life. Complex physical forcings, including tides, coastal upwelling, internal waves, wind shear, and river outflows, drive mixing and transport. The connections between large scale forcing and the generation of local turbulence is key for understanding mixing and energy balances in the coastal system.

In stratified systems like the California inner shelf, internal waves affect the energy dynamics. Internal tides on the inner shelf are generated by tidal currents moving across shelf breaks, and they provide a link between energy injection at large scales and energy dissipation at small scales (Lamb, 2014). A significant portion of tidal wave energy contributes to the generation of nonlinear internal waves, including bores (waves of depression on a multi-hour timescale), internal solitary waves (on a 10-minute timescale), and undular bores comprising both (Helfrich & Melville, 2006). It is hypothesized that turbulence generated by internal wave breaking at boundaries is a significant sink of energy in the ocean (Munk & Wunsch, 1998), which has led to a number of studies on internal wave breaking and interaction with the bottom boundary (Arthur & Fringer, 2014). Turbulence generated by internal wave breaking can re-distribute nearshore temperature, nutrients, larvae, sediment, and oxygen (Pineda, 1994; Leichter, Wing, Miller, & Denny, 1996; Omand et al., 2011; Bourgault, Morsilli, Richards, Neumeier, & Kelley, 2014; Walter et al., 2014). Weakly non-linear internal tides often appear as horizontally propagating modal waves. If most of the vertical density variation is in the upper half of the water column, they appear as waves of depression. Non-linearity and dispersion cause such waves to form a train of shorter, strongly non-linear,

internal solitary waves (Lamb, 2014). For example, the transformation of a nonlinear internal wave across Oregon's continental shelf from a solibore-like state to solitary waves has been tracked and observed (Moum, Farmer, Shroyer, Smyth, & Armi, 2007). Along that path, the wave lost energy at the same rate that energy was lost to turbulent dissipation. However, the questions of how internal waves affect turbulence, and whether turbulence contributes to internal wave energy loss, remain.

Turbulence in the bottom boundary in the coastal ocean has been observed for decades (Gross & Nowell, 1983). The role of internal waves on the production and loss of turbulence in the bottom boundary remains unknown, and relatively few studies have investigated the question to date. We characterize turbulence through the Turbulent Kinetic Energy (TKE) equation,

$$\frac{\partial k}{\partial t} + \overline{u_j}\frac{\partial k}{\partial x_j} = -\frac{\partial}{\partial x_j}\left(\frac{1}{\rho_0}\overline{u_j' p'} + \frac{1}{2}\overline{u_i' u_i' u_j'} - \nu\frac{\partial k}{\partial x_j}\right) - \overline{u_i' u_j'}\frac{\partial \overline{u_i}}{\partial x_j} - \nu\overline{\frac{\partial u_i'}{\partial x_j}\frac{u_j'}{\partial x_i}} - \frac{g}{\rho_0}\overline{\rho' u_3'} \quad (2.1)$$

where Reynolds averages are represented by overbars here, and also by brackets $\langle\ \rangle$ elsewhere in this manuscript, and $k = \frac{1}{2}\left(\overline{u_1'^2} + \overline{u_2'^2} + \overline{u_3'^2}\right)$. The left-hand side of 2.1 describes TKE accumulation and advection by mean currents, together characterizing the time rate of change of turbulence following the mean flow. The right-hand side of 2.1 describes sources and sinks of turbulence. The first three terms are energy flux divergences including transport by pressure fluctuations, transport by turbulence itself, and transport by molecular viscosity. The fourth term on the right-hand side is shear production of turbulence, often represented as P. It reflects the rate at which energy is transferred from the mean flow to the turbulent flow. The fifth term is TKE conversion to heat, represented as ϵ. The last term is TKE conversion to potential energy, B. If the flow is stably stratified, turbulence can mix denser water higher in the water column, yielding an upward flux of density. Thus, a positive buoyancy flux represents a loss of TKE to potential energy. If the flow at a site is homogeneous in space and steady in time, then the accumulation and transport terms have no effect on the TKE budget. Thus, the local TKE budget simply becomes,

$$P = \epsilon + B \quad (2.2)$$

where turbulence generated locally through shear production is lost locally to buoyant mixing and turbulent dissipation. We note that if the water column is unstable, with more dense waters above less dense waters, buoyant mixing will be negative, and will generate turbulence.

Shear production often makes the bottom boundary a source of turbulence in marine systems. Studies of strong tidal flows in well- or partially-mixed coastal environments have shown that near the bed, production and dissipation are in balance locally (Gross & Nowell, 1983; Trowbridge, Geyer, Bowen, & Williams III, 1999; T. B. Sanford & Lien, 1999). Similarly, in a stratified tidal flow it is found that dissipation and production are in balance near the bed, and buoyancy fluxes are negligible (Shaw & Trowbridge, 2001). However, farther from the bed sources and decay of turbulence remain difficult to quantify. Feddersen, Trowbridge, and Williams, 2007; Davis and Monismith, 2011, and Walter et al., 2014 have found

that dissipation exceeds shear production, yet buoyancy fluxes are still negligible, suggesting that other sources of turbulence must be important. Feddersen et al., 2007 observe that production is much less than dissipation in the mid water-column in unstratified near-shore measurements, and conclude that vertical turbulent transport must be large.

Two recent studies investigated bottom boundary layer turbulence budgets in the presence of internal waves in shallow regions. In stratified flows above a coral reef (Davis & Monismith, 2011) and on the California continental shelf (Walter et al., 2014), it was found that dissipation and production were balanced near the bed, while dissipation exceeded production above 1 m. They theorized that horizontal advection transported turbulence into the measurement volumes. Above the coral reef, transport was attributed to irregularities and roughness of the reef (Davis & Monismith, 2011). They found that the presence of internal waves could increase stratification, flow speed, shear, and dissipation in the bottom boundary layer. On the California shelf, breaking nonlinear internal waves generated and transported turbulence (Walter et al., 2014). At this site, including the buoyancy term did not improve the imbalance between production and dissipation above the bed; buoyancy was typically at least one order of magnitude smaller than dissipation, and including it merely increased the magnitude of the right-hand side of 2.2 (Walter et al., 2014). To summarize, while few studies have investigated turbulence in the bottom boundary layer during internal wave activity, there is evidence that internal waves contribute TKE to the near-bottom region.

Considering the contribution to TKE from internal waves near the bed, studies have also investigated patterns of energy loss from internal waves. Following a series of internal waves, dissipation was observed to increase during the trailing edge of each of the first four waves (Moum, Klymak, Nash, Perlin, & Smyth, 2007). After the passage of the internal waves, the bottom boundary was continuously turbulent, with about 100 times more dissipation than prior to the wave train passage. A similar increase in dissipation at the trailing edge of an internal bore passage in the stratified mid-water column was observed, while dissipation at the bottom boundary increases during the leading edge of the bore (Walter, Woodson, Arthur, Fringer, & Monismith, 2012; Walter et al., 2014). A similar pattern was also observed in numerical studies of an internal bore on a sloping shelf, where dissipation at the bottom boundary increased as an internal wave arrived, and dissipation in the mid-water column increased during the trailing edge (Arthur & Fringer, 2014). They saw that dissipation at the bottom boundary accounted for about 2/3 of all dissipation in the domain, while dissipation in the interior was responsible for the remaining 1/3.

We investigated the role of internal waves on turbulent dissipation in the bottom boundary. We performed new observations of turbulence in the bottom boundary layer under internal waves, observing a system where the presence of internal waves affected flow in the bottom boundary, and stratification largely did not extend down to the boundary layer. In Section 2.2, we describe the field site and the observations collected on the California Coast. Section 2.3 covers the data cleaning and processing, which we used to compute the quantities considered in the remainder of the paper. In Section 2.4, we describe the observations, arriving at our focus on turbulence in the bottom boundary layer. Section 2.5 considers the

implications of our findings, focusing on the relationship between production and dissipation and the connection between dissipation and internal waves. Section 2.6 offers a summary and some conclusions. This work was published in an Ocean Dynamics article (Allen et al., 2018).

2.2 Observations

The observations and analysis presented here are part of a larger study on exchange in the inner shelf, funded through an Office of Naval Research (ONR), Departmental Research Initiative (DRI). In the interest of forecasting ocean dynamics and stratification from the deep ocean through to the shoreline, the so-called Inner Shelf DRI is focused on understanding inner shelf processes, and their spatial and temporal variability. The chosen study area is the vicinity of Point Sal, CA, on the California Coast about 45 km south of San Luis Obispo (figure 2.1). These data come from a pilot experiment as part of the DRI, designed to gain familiarity with the study area and test equipment prior to the larger field campaign conducted in late 2017. The pilot study was named the Point Sal Inner Shelf Experiment (PSIEX), and was conducted during the summer of 2015. The internal waves observed in this study were also observed on a broader spatial scale during the same time frame (Colosi, Kumar, Suanda, Freismuth, & MacMahan, 2017). Colosi et al., 2017 see these internal waves propagating on-shore, not reflecting off the coast, and give further details on the larger scale input for these waves.

As part of PSIEX, we deployed two large bottom landers, called quadpods, outfitted with instrumentation to investigate bottom boundary layer turbulence under internal waves. The quadpods were deployed off the R/V Oceanus on 13 June 2015 and recovered on 7 August 2015, yielding 2 months of nearly continuous data. Quadpod 1 was located at 34° 57.263′N by 120° 42.235′W, about 4.3 km from the coast and at about 36 m of water depth. Quadpod 2 was located at 34° 57.230′N by 120° 41.421′W, about 1.25 km from quadpod 1, 3.1 km from the coast, and in about 30 m of water (figure 2.1). In between these two sites, the bottom slope was 0.4 to 0.5 degrees (Colosi et al., 2017). Instrumentation on quadpod 1 was similar in character to quadpod 2, but we focus, with few exceptions, on data from quadpod 2 in this manuscript (table 2.2, figure 2.2). Quadpod 2 included two Nortek HR Aquadopps sampling at 2 Hz for 45 min of every hour, one looking down to the bed located at 0.86 m above bed (mab) and the other looking upwards located at 0.78 mab. Bin spacing in Aquadopp profiles was set at 0.025 m, yielding high resolution velocity and turbulence profiles. Quadpod 2 also included two Sontek Acoustic Doppler Velocimeters (ADVs) sampling at 20 Hz, one located at 0.25 mab and one at 1.25 mab, sampling for 24 min every 3 hours. The instrument separation was set to satisfy, $\Delta z/z \sim 5$, where Δz is the separation between instruments and z is the height above the bed of the lower instrument (following Shaw & Trowbridge, 2001). Conductivity, temperature, and pressure (CTD) were monitored with a Seabird SBE 49 located at 1.84 mab, sampling at 2 Hz and through a chain of 5 Seabird SBE 56 temperature loggers located roughly at 4, 5, 6, 7, and 8 mab,

Figure 2.1: Quadpods 1 and 2 were located off of Point Sal, on the California inner shelf. Quadpod 1 was located at 34° 57.263′N by 120° 42.235′W, and quadpod 2 was located at 34° 57.230′N by 120° 41.421′W. Data from quadpod 2 primarily is discussed in this work. The coast runs at 15 degrees north. This map was created in Caltopo (caltopo.com) using Google satellite imagery.

Instrument	Sampling Scheme	Location	Dates Collected
Aquadopps	2 Hz, 45 min burst every hour	0.78 (uplooking), 0.86 (downlooking) mab	13 Jun - 7 Aug
Sontek ADVs	20 Hz, 24 min burst every 3 hours	0.25, 1.25 mab (horizontal) (quadpod 2)	13 Jun - 7 Aug
Nortek AWACs	One profile collected every 20 min for mean profiles, acoustic surface wave tracking data collected for 20 min every hour	3 mab (uplooking)	13 Jun - 7 Aug
CTD	2 Hz, 45 min burst every hour	1.84 mab	13 Jun - 30 Jun
Temperature loggers (5)	1 Hz, continuous	Spaced every meter from 4-8 mab	13 Jun - 7 Aug

Table 2.1: Instrument positions and specifications on quadpod 2 are shown. Dates collected represent the periods during the summer of 2015 when data of sufficient quality were collected from each instrument. The CTD battery failed on 30 June 2015.

respectively. The temperature loggers collected data at 1 Hz, continuously, while the CTD collected for 45 min bursts every hour. The CTD batteries failed after 30 June 2015. Wave and current data were collected by a Nortek Acoustic Wave and Current Profiler (AWAC), which was positioned at 2.3 mab looking upwards. Acoustic surface tracking (AST) data from the AWAC was collected for 20 min every hour at 4 Hz, and mean current profiles were collected from 1 min bursts every 20 min, with bins spaced at 0.5 m.

2.3 Flow and turbulence quantities

2.3.1 Data Cleaning

Data cleaning and analysis was performed to reduce noise contributions to measured quantities when possible, and remove problematic measurements when necessary. To clean the Sontek ADV data, we identified points where the correlation was below 70%. When fewer than 40 points in a row failed the correlation test (2 seconds), we interpolated across the removed data. If more than 40 points in a row failed the correlation test, the data were replaced with NaNs. After correlation cleaning, any data that had an instantaneous velocity greater than 1 ms^{-1} was replaced with an interpolated value. If more than 5% of the data

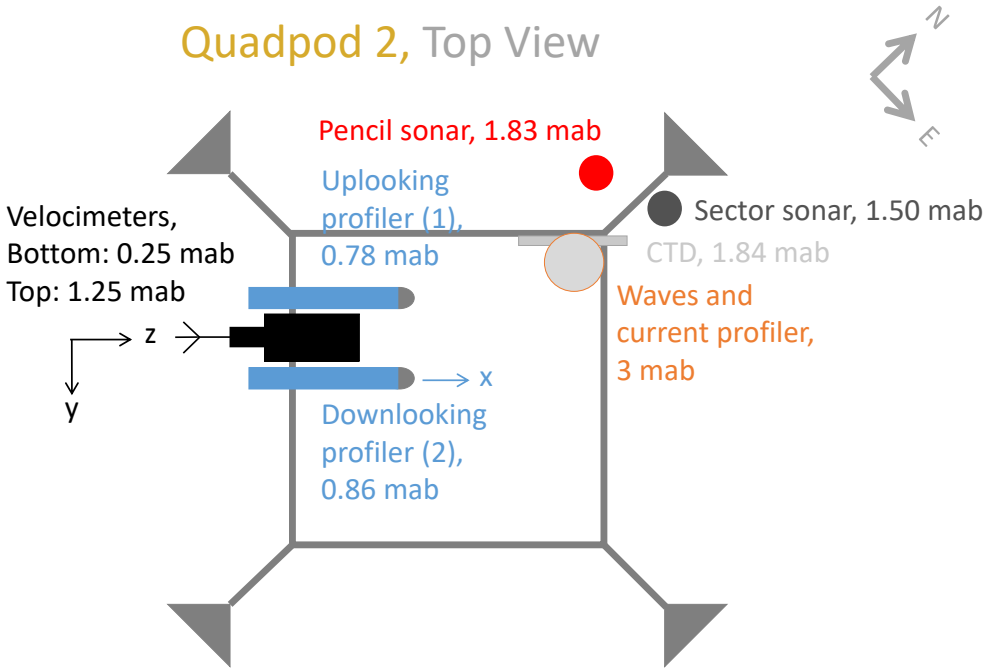

Figure 2.2: The locations of the instruments on Quadpod 2 are sketched here in plan view, with their heights above the bed (in m) listed. The Aquadopps were oriented with their x-direction pointing at 44 degrees N. The cardinal direction depicts the orientation of the frame relative to true N. Bed scanning sonar (pencil beam and sector scan) were also deployed, but the data are not considered in this manuscript.

from a given burst was replaced with NaNs, we excluded that burst from the analysis. Because the Sontek ADVs did not have internal compass or orientation sensors, we rotated the data from instrument coordinates to global coordinates based on the heading, pitch, and roll from the down-looking Aquadopp. Slight errors in the vertical orientation of the ADV were not critical, as the method used to remove waves from turbulence can accommodate small errors in instrument orientation (Shaw & Trowbridge, 2001). Finally, because the two ADVs were not burst synced, there was a slight drift in their clocks over the course of the deployment. We found the rate of drift by cross-correlating the signals from the two instruments, and corrected for the drift so that the timestamps were internally consistent.

Aquadopp data were first cleaned to remove contaminated bins, either from bins representing below the bed, bins contaminated by the quadpod struts, or bins from 0.7 to 0.9 mab where flow was affected by the instruments themselves (figure 2.4). The compass from the down-looking Aquadopp used to reference the Sontek ADVs also acted as a master for the up-looking Aquadopp; we adjusted the velocities in ENU coordinates for the up-looking Aquadopp to the values provided by the down-looking Aquadopp. We computed a local velocity gradient $\left(\frac{\partial \overline{u}}{\partial z}\right)$ at the ADV heights from the nearest 5 Aquadopp bins, corresponding to a 0.125 m range. If the R^2 from this linear fit was less than 0.8, we did not include the velocity gradient in the analysis of turbulence quantities.

Because the ADVs were oriented horizontally, flow past the instrument could be influenced by the instrument wake. Figure 2.3 shows velocities in east and north coordinates during bursts 5 and 14. When the mean flows were directed towards the instrument, as in burst 5, we assume that the instrument did not affect the turbulent statistics. In burst 14 we see that the mean flow was traveling away from the instrument, and therefore the measurement volume was possibly in the turbulent wake created by the instrument itself. We therefore removed data where the mean current was oriented in a 90−degree cone away from the instrument, in order to remove the potential influence of an instrument generated turbulent wake. As the final filter for turbulence quantities, we removed bursts when the mean flow magnitude was less than 0.02 ms^{-1}. From the AWAC, AST data was cleaned using a despiking algorithm to remove noisy data (Goring & Nikora, 2002).

2.3.2 Mean flow

Mean flow characteristics were computed from the cleaned ADV, Aquadopp, and AWAC data. For Aquadopp data, velocity profiles were computed from the burst means at each cell height, rotated to the direction of mean flow, where the direction of mean flow was adjusted during each 45−minute burst, and changed during the full data set. The mean profiles enabled a first computation of the friction velocity, u_*, by applying the log profile,

$$U(z) = \frac{u_*}{\kappa} \ln\left(\frac{z}{z_0}\right) \tag{2.3}$$

Here, z_0 represents the wall thickness, where velocity goes to 0. Values of u_* computed from log profiles when flow was directed around east and west directions (75-140 degrees and

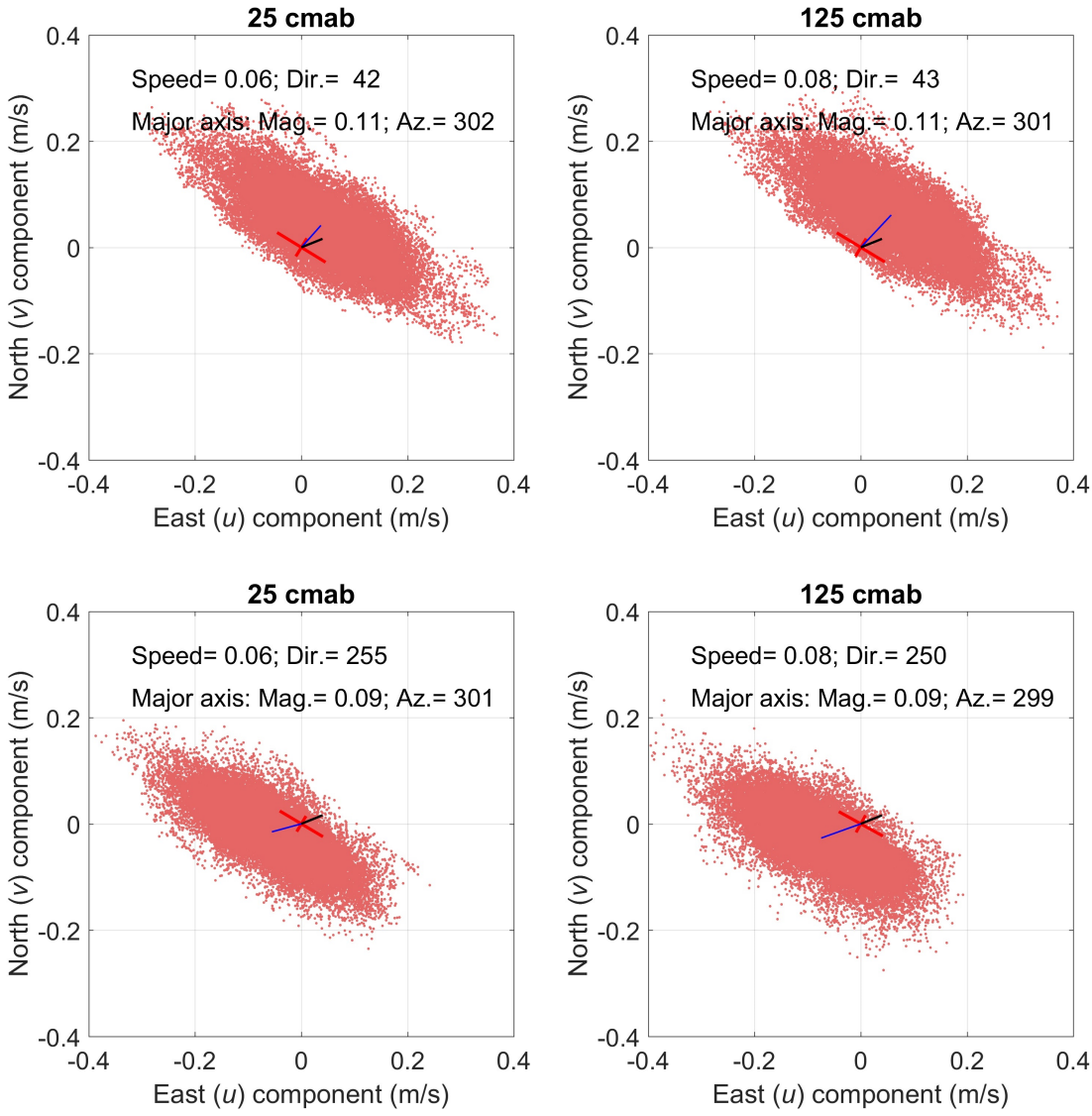

Figure 2.3: All instantaneous velocities measured at 0.25 mab (left) and 1.25 mab (right) are shown with pink dots, after cleaning, during burst 5 (above) and burst 14 (below). The direction of mean flow is indicated with a blue vector, and the position of the ADV is shown in black. The ADV body was oriented at 44 degrees N, relative to the measurement volume. When the mean flow is pointed in the opposite direction as the ADV, as in the lower figures, flow must travel around the instrument before it is measured in the sample volume. Thus, there is potential for the instruments to contaminate the turbulence statistics. These cases were removed from the analysis.

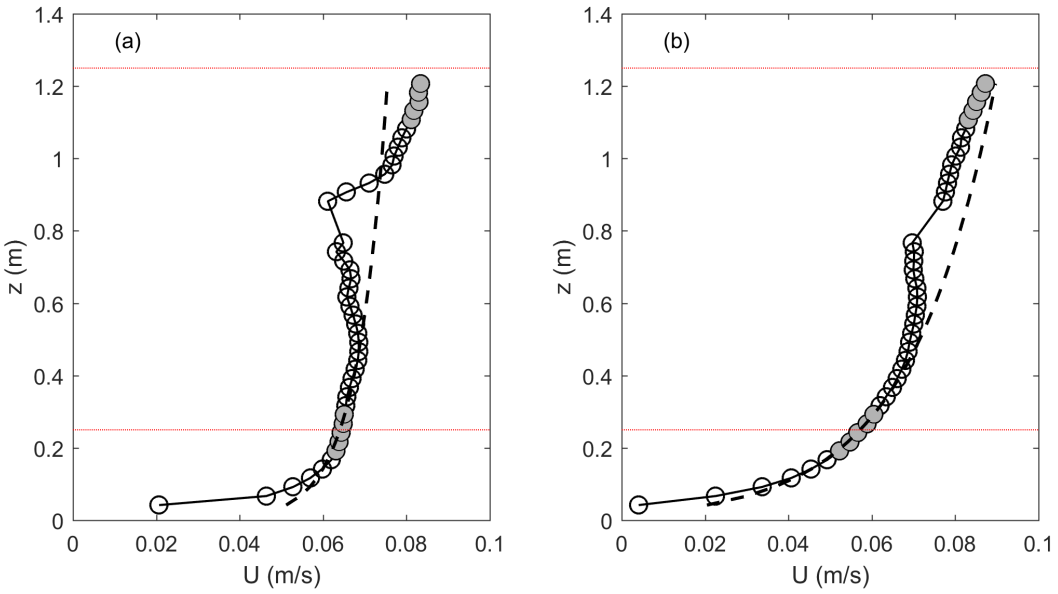

Figure 2.4: Law of the wall fits (equation 2.3) to Aquadopp data from bursts 5 (a) and 14 (b), collected at 13 Jun, 2015 02:00 and 14 Jun, 2015 23:00, respectively. Data from depths 0.11 to 0.39 mab were used in the law of the wall fit, shown as a black dashed line. ADVs were located at heights marked by horizontal dashed lines. Velocity gradients $\left(\frac{\partial \overline{u}}{\partial z}\right)$ at those heights, denoted with grey filled circles, were used in the computation of shear production, P. Influence of the Aquadopps and frame on the mean velocity profile can be seen at $0.7-0.9$ mab, where the mean velocity is reduced.

250-300 degrees) were removed from analysis of turbulence quantities, due to possible frame interference.

2.3.3 Wave characteristics

Spectral wave characteristics were calculated from ADV and Aquadopp measurements. Representative near-bottom wave orbital velocity, u_{br}, was computed using (Wiberg & Sherwood, 2008),

$$u_{br} = \sqrt{2 \sum_i \left(S_{xx} + S_{yy}\right)_i \Delta f_i} \tag{2.4}$$

where the frequency, f, was limited to the range of 0.2 Hz to 0.02 Hz. Consequently, both high frequencies that are dominated by turbulence and frequencies that are below most surface waves were removed. S_{xx} and S_{yy} represent the two horizontal components of velocity power

spectra, respectively. Significant wave period, T_s, was computed (Madsen, 1994) as

$$T_s = \frac{\sqrt{2}\sum_i S_{xxi}\Delta f_i}{\sum_i f_i S_{xxi}\Delta f_i}. \tag{2.5}$$

Significant wave height, H_s, was computed as

$$H_s = 4\sqrt{m_0} \tag{2.6}$$

where m_0 is the variance of the measured wave heights from the AWAC AST.

2.3.4 Density structure

Density was computed from temperature and salinity using the Gibbs Sea Water TEOS toolbox (McDougall & Barker, 2011). First, absolute salinity was computed from measured practical salinity. Then, temperature, salinity, and pressure were used to compute density. Temperature was measured at several depths in the water column, but salinity was measured only by the CTD, at 1.84 mab. We observed that salinity and temperature largely vary together in this system, indicating that temperature is a good proxy for total density. To account for the unmeasured salinity variation higher in the water column, we used our data to estimate a best fit between salinity and temperature,

$$salinity = 6.042 \cdot 10^7 \cdot temperature^{-8.438} + 33.53 \tag{2.7}$$

The fit (figure 2.5) was applied to temperature data from the temperature loggers, Aquadopps, ADVs, and AWAC on both quadpods to yield water column density. While this fit allows salinity to vary somewhat over low temperatures, during high temperatures it changes little. The assumption seems reasonable for the measured data, where salinity varies little when temperature is above 12 degrees, observed near Pt. Sal (Dever & Winant, 2002). At our site, temperatures ranged from 10 to 17 degrees. Thus, even though our simultaneous temperature and salinity measurements only span a temperature range of 10 to 12.5 degrees (figure 2.5), the relationship (equation 2.7) covers most of the required variation. We also report temperature only, since our prediction of density relies most firmly on that quantity. Water column stratification was computed from adjacent temperature loggers using

$$N^2 = -\frac{g}{\rho_0}\frac{\partial \overline{\rho}}{\partial z} \tag{2.8}$$

where N^2 is the buoyancy frequency squared.

2.3.5 Turbulence quantities

Wave and turbulent velocity signals were separated (decoupled) using an established technique (Shaw & Trowbridge, 2001). Wave orbital motions, defined as the signal that is

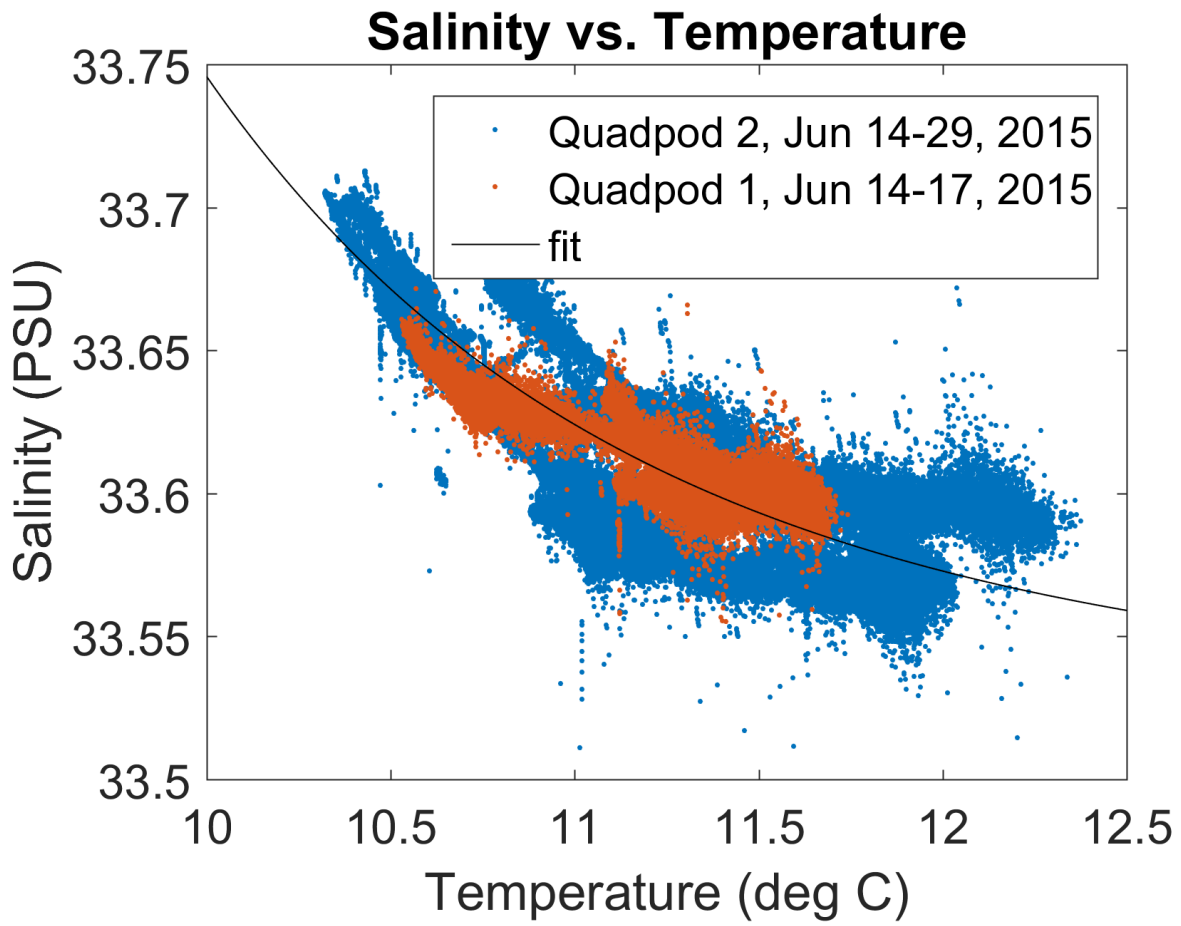

Figure 2.5: Shown is the relationship between salinity and temperature measured at the CTDs at 1.8 mab from both quadpod 1 and quadpod 2. The best fit relationship, shown with a black line, yielded equation 2.7.

coherent between the two sensors, were removed from the time series. We applied an ogive test to the integrated co-spectra to evaluate the effectiveness of the wave removal. The ogive test compares the shape of an ogive curve,

$$Og_{u'w'}(f) = \int_0^f Co_{u'w'}\left(\hat{f}\right) d\hat{f} \tag{2.9}$$

with an expected form based on atmospheric boundary layer behavior (Kaimal, Wyngaard, Izumi, & Coté, 1972). Here, $Co_{u'w'}$ is the $u'w'$ cospectrum. Because the ogive curve from the fluctuating quantities did not show a large shift at surface wave frequencies, we conclude that the decoupling effectively removed the wave orbital velocities. Reynolds stresses were computed once from the fluctuating velocity signals following removal of wave orbital velocities. Stresses were computed in frequency space to remove the effect of instrument

noise,

$$\langle u'w' \rangle = \int_0^{f_{noise}} Co_{u'w'}(f)\, df \tag{2.10}$$

where f_{noise} indicates the frequency above which instrument noise dominates the fluctuating signal. As noted below, we compared this method for computing Reynolds stress with an alternative technique.

We used covariance analysis to remove the remaining noise from the Reynolds stress and TKE estimates. The instruments were deployed in a low sensitivity/ high max velocity (2.5 ms^{-1}) mode, in anticipation of more energetic wave conditions. Therefore, overall instrument noise was high and generally dominated the flow signal at frequencies above 0.5 Hz. TKE was computed from the auto-covariance, $C_{uu}(\tau) = \langle u_i'(t_0) u_i'(t_0 + \tau) \rangle$, where u_i' represents the fluctuating signal from the Shaw-Trowbridge decomposition for each of the u, v, and w directions (Shaw & Trowbridge, 2001). In an auto-covariance analysis, we expect random noise, unrelated to physical processes, to have no correlation between subsequent data points. Thus, after a single time step lag, $\tau(step = 1) = \tau_1$, instrument noise is removed. Note that instrument noise was low in the u-direction, (figure 2.6,a and d) because flow was aligned with the orientation of the instrument during burst 5 (figure 2.3). We used the value of $C_{uu}(\tau_1)$ for the burst $\langle u_i' u_i' \rangle$.

The second method for computing Reynolds stress relied on the cross-covariance (C_{uw} and C_{vw}), where $C_{uw}(\tau) = \langle u'(t_0) w'(t_0 + \tau) \rangle$, and similar for C_{vw} (figure 2.6, b and e). Similar to the auto-covariance, instrument noise should be captured at τ_0. Because we do not have an expected form for the de-correlation of the Reynolds stress, and because during some bursts the cross-covariance increased after a few lag points, we used the average of C_{uw} from τ_1 through τ_5 as the burst estimate of the Reynolds stress (figure 2.6, b and e, black dots). The value was well aligned with the Reynolds stress estimate from the integrated co-spectrum below 0.5 Hz. We selected the cross-covariance method for the remainder of the analysis because it allows for contributions to the Reynolds stress from frequencies above 0.5 Hz, while the frequency-space method did not. Note that lags τ_1 through τ_5 correspond to time differences of 0.05 s through 0.25 s. Because the Kolmogorov timescales (i.e. shortest turbulent timescales) were 0.1 s at the smallest, the variation in the cross-correlation at these lags, $\tau < 10\tau_\eta$, largely should not be from turbulence.

The Reynolds stress estimates from 0.25 and 1.25 mab yielded a second calculation for the friction velocity using $u_*^2 = \sqrt{\langle u'w' \rangle^2 + \langle v'w' \rangle^2}$. The log profile method produces more scattered estimates of the friction velocity than a direct measure through Reynolds stresses, and Reynolds stress estimates provide the most fundamental measure of bed stress (Sherwood, Lacy, & Voulgaris, 2006). Log profile estimates of friction velocity rely on vertically averaged shear estimates and the law of the wall, which assume a constant-stress region.

Turbulent shear production was computed directly from the Reynolds stress and mean shear using

$$P = -\langle u'w' \rangle \frac{\partial \overline{u}}{\partial z} - \langle v'w' \rangle \frac{\partial \overline{v}}{\partial z} \tag{2.11}$$

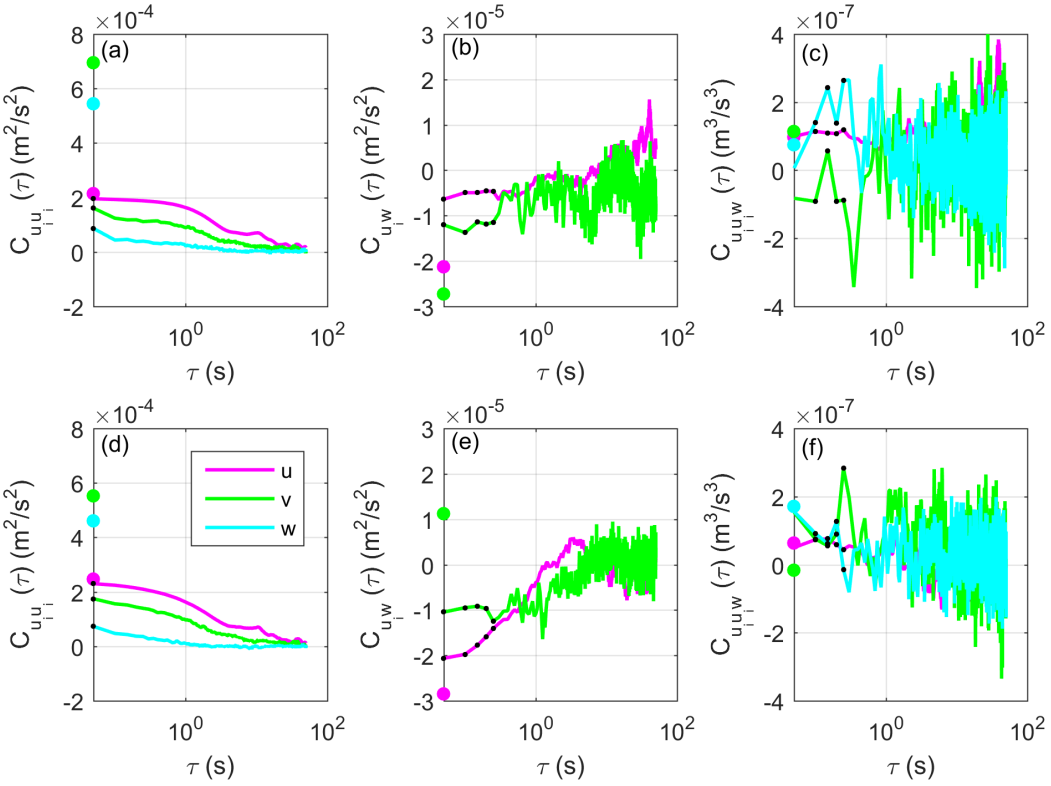

Figure 2.6: Shown are the computations of turbulent kinetic energy (a,d), Reynolds stress (b,e), and turbulent diffusive flux (c,f) at 1.25 mab (a-c) and 0.25 mab (d-f) during burst 5 using covariance methods. (a,d) show the computation of TKE from the auto-covariance C_{uu}. Instrument noise is captured in the auto-covariance at τ_0 (no time lag), marked by colored circles. (b,e) show the cross-correlation of u' and v' with w', used for computing the Reynolds stress. (c,f) show the cross-correlation of u'^2, v'^2, and w'^2 with w', used for computing the triple correlation. Black dots in all figures denote the values used in computing the bulk quantity from each auto-covariance or cross-covariance.

The mean shear was computed from Aquadopp velocity profiles at the elevation of the ADVs. In the case of the upper ADV (1.25 mab), the Aquadopp profile was truncated at 1.2 mab due to reflections off the quadpod, so the velocity gradient at 1.2 mab was used as an approximation. Turbulent eddy viscosity was computed from the same quantities as shear production using,

$$\nu_T = -\frac{\langle u'w' \rangle}{\frac{\partial \overline{u}}{\partial z}} \tag{2.12}$$

Because instrument noise was high and turbulence was low, using the inertial dissipation method to compute turbulent dissipation rate, ϵ, from ADV velocity spectra Bluteau, Jones, and Ivey, 2011 was not successful. Therefore, we used a structure function based method using Aquadopp data (Wiles, Rippeth, Simpson, & Hendricks, 2006). The second order structure function, computed in beam coordinates, is related to the turbulent dissipation rate (Pope, 2000),

$$D_{LL}(z,r) = \langle (v'(z) - v'(z+r))^2 \rangle = C_v^2 \epsilon^{2/3} r^{2/3} \tag{2.13}$$

where C^2 is a constant, generally between 2 and 2.2 from atmospheric studies. From each 45-min burst, we computed separate dissipation estimates from 2, 5, and 15-min sections, yielding multiple estimates of dissipation every hour. As part of the data overview, we have plotted the 15-min estimates (figure 2.10). It is unknown what effect the presence of surface wave orbital velocities may have on the dissipation estimated by this technique (Wiles et al., 2006). Because surface waves are large at this site, we posit it unlikely there was an effect, and the lack of similarity between surface waves and dissipation lends credence to this supposition (figure 2.10). For measurements collected beneath the surface, the method finds dissipation within 16% of measurements of dissipation from the spectral integral method, suggesting that it does reflect dissipation as intended (McMillan & Hay, 2017). The presence of the frame and instruments in the water column caused elevated TKE dissipation rates at 0.3 to 1.2 mab, therefore, we consider ϵ up to 0.3 mab only in further analyses. One unfortunate consequence was that we were unable to compare P and ϵ at 1.25 mab. We capture error in our dissipation estimates at 0.25 mab by computing the 95% confidence intervals on these quantities while mean velocity remains largely stationary for 3 hours (figure 2.7). For a period with no internal waves in the bottom boundary, this yielded $3.14 \cdot 10^{-7}$(2.4 to $4.1 \cdot 10^{-7}$) m^2/s^3; for the period with internal waves, this yielded $0.96 \cdot 10^{-7}$(0.78 to $1.2 \cdot 10^{-7}$) m^2/s^3.

We used two alternate methods to compute higher time resolution estimates of additional turbulent quantities, based on Aquadopp data. The first relies on the law of the wall,

$$\frac{u_*^3}{\kappa z} \tag{2.14}$$

where u_* was defined using equation 2.3. As the quantity (2.14) relied on data from Aquadopps, we were able to compute it for 45-min out of every hour, rather than 24-min every 3 hours (Sontek ADVs).

The second estimate for turbulence quantities requires a further simplification:

$$\frac{C_D^{3/2} \langle u \rangle^3}{\kappa z} \tag{2.15}$$

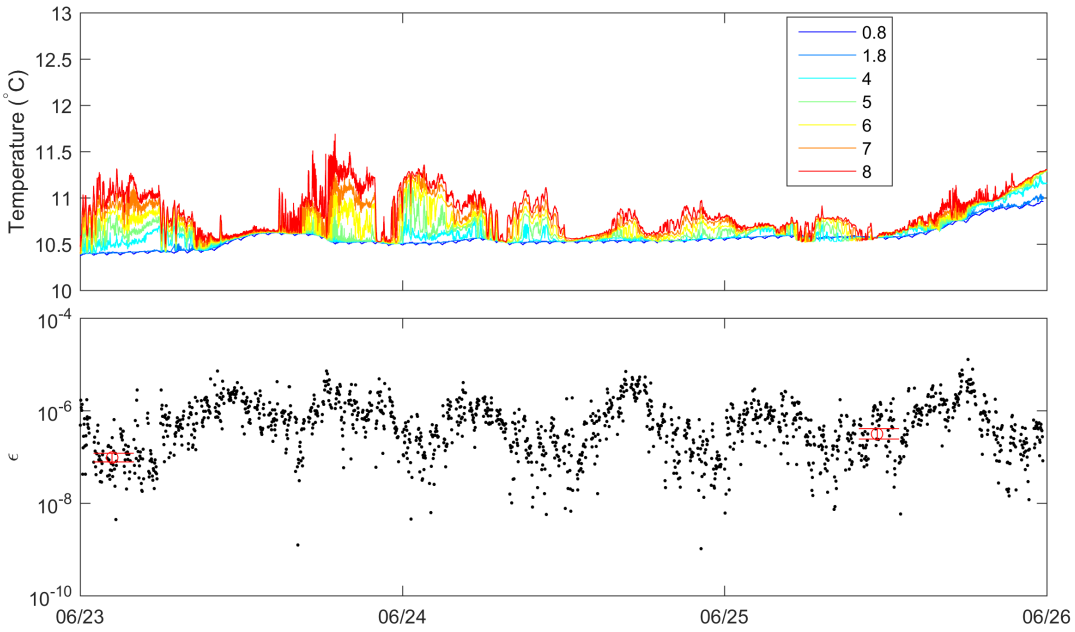

Figure 2.7: Upper: Temperature at 0.8 to 8 m above bed, during the June 23 to June 26, 2015 period. Lower: Dissipation (ϵ) during the same period at 0.25 mab, as measured by the Aquadopp. Red symbols indicate two periods during which we computed error on dissipation (95% confidence intervals). The first (in the morning on June 23) is during a period with strong stratification, and the second (mid-day on June 25) is during a period when the bottom was not stratified.

Here the drag coefficient, C_D, is computed from a best fit between the mean velocity at both 0.25 mab and 1 mab, and u_* (figure 2.8), yielding two different estimates for drag: $C_{D,25}$ and $C_{D,100}$, respectively,

$$u_*^2 = C_D \langle u \rangle^2 \tag{2.16}$$

On a sandy bed like the one at our field site, we would expect a drag coefficient from the mean velocity at 1 mab of about 0.003 (Gross & Nowell, 1983), and we find $C_{D,100} = 0.0038 \pm 0.0003$ (figure 2.8, b). However, the fit between u_* and $\langle u \rangle$ is much tighter based on the mean velocity measured at 0.25 mab (figure 2.8, a). We therefore use the computed drag coefficient at 0.25 mab of $C_{D,25} = 0.022 \pm 0.001$ for the remaining analysis. This choice acknowledges that surface waves should not affect the measured mean velocities, and that the presence of the frame between the 0.25 mab and 1 mab measurement sites may influence the measured fit. While the magnitude of the measured drag coefficient at 0.25 mab is not as meaningful, the patterns inform us about turbulence in the bottom boundary. We also tested allowing $C_{D,25}$ to vary in time, based on the size of surface waves, and we were unable to find a reliable fit. Therefore, in equation 2.15, we rely on the drag coefficient from 0.25 mab and compute $\langle u \rangle$

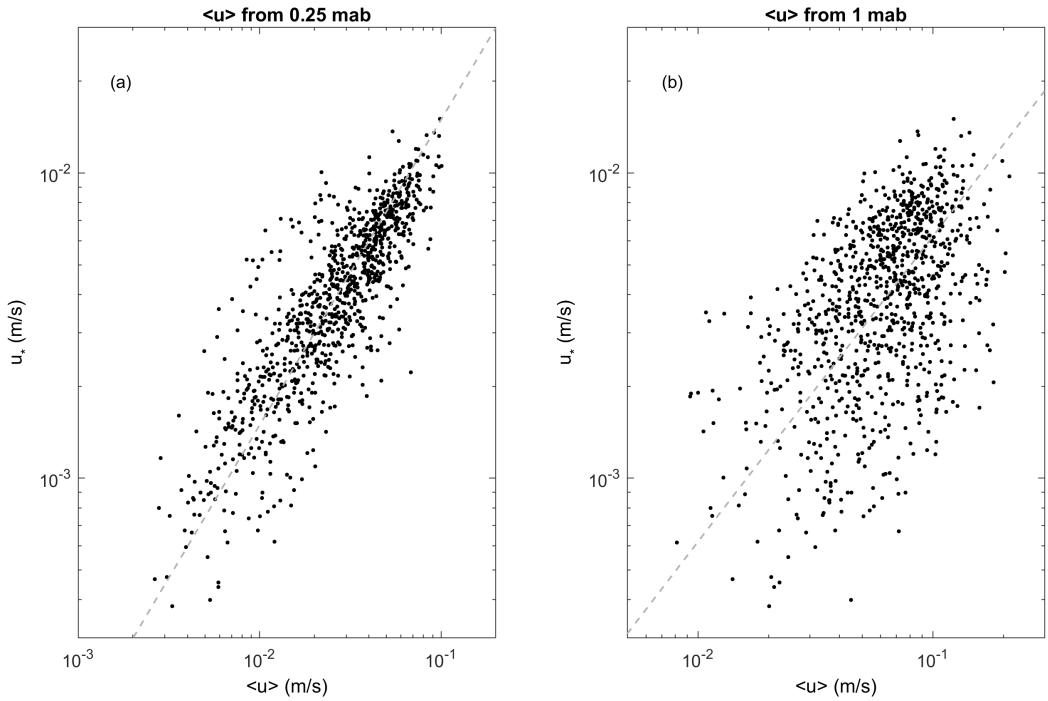

Figure 2.8: Shown is a comparison between u_* and $\langle u \rangle$ given mean velocity at (a) 0.25 mab and (b) 1 mab. The bulk best fit drag coefficient via equation 2.16 was $C_{D,25} = 0.022 \pm 0.001$ and $C_{D,100} = 0.0038 \pm 0.0003$.

from 2, 5, and 15 minute averages of the Aquadopp data, yielding a few different estimates of the energy in the bottom boundary layer.

Commonly, estimates of (2.14) and (2.15) are used to compute dissipation. However, they rely on assumptions that TKE is steady state, the measurements are near a wall, and all energy produced locally through shear production is dissipated locally. Therefore, we refrain from attributing the quantities generated by (2.14) and (2.15) to a specific term from (2.1). We considered them to be more similar to estimates of turbulent production captured by local shear profiles (2.14) and local velocity (2.15), and we compared them to measured turbulent production (figure 2.9). We focused this comparison on turbulence production because $u_*^2 \sim -\langle u'w' \rangle$ and $\frac{u_*}{\kappa z} \sim \frac{\partial u}{\partial z}$. We observed that production computed via Reynolds stresses (equation 2.11) was similar to these quantities (figure 2.9).

To compute turbulent diffusive transport, $T = -\frac{\partial \langle u_i' u_i' w' \rangle}{\partial z}$, we computed the turbulent diffusive flux, $\langle u_i' u_i' w' \rangle$, at 0.25 and 1.25 mab, and then computed T by differencing one estimate from the other, and differencing each estimate against the predicted diffusive flux value of zero at the bed. Turbulent diffusive flux was computed from a modified cross-correlation. Specifically, we computed $C_{uuw}(\tau) = \langle u'(t_0)u'(t_1)w'(t_0+\tau) \rangle$, where the repeated

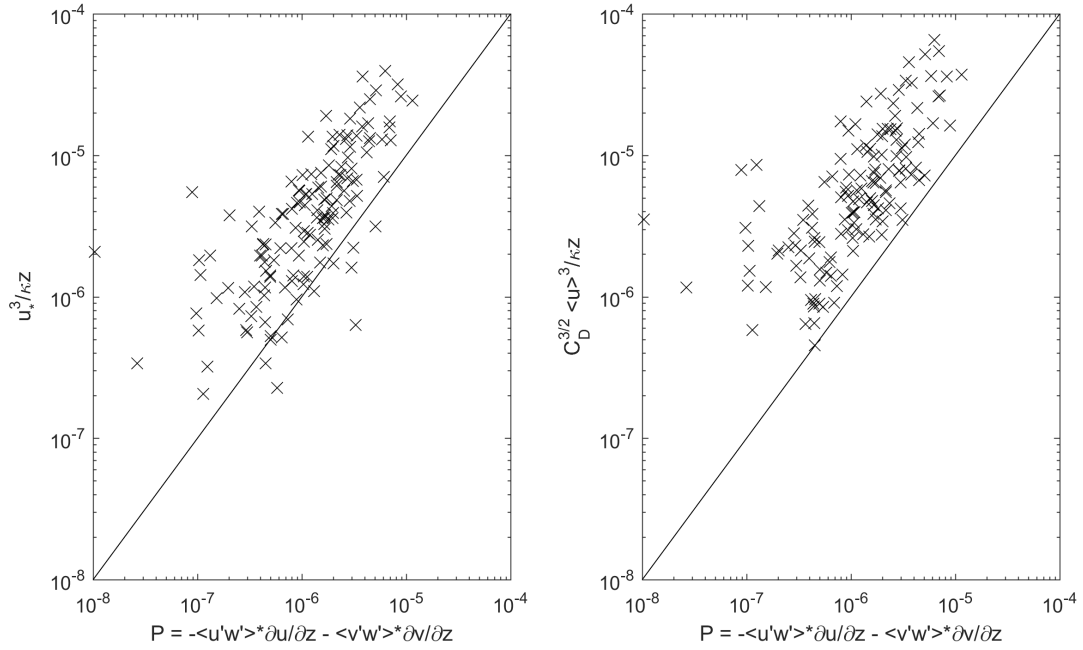

Figure 2.9: Left: Shown is production computed via Reynolds stresses compared with a law of the wall fit, from 0.25 mab. The solid line (in both figures) represents a 1:1 relationship. Right: Shown is production computed via Reynolds stresses compared with energy from wall drag, $\frac{C_{D,25}^{3/2}\overline{u}^3}{\kappa z}$. While $\frac{C_{D,25}^{3/2}\overline{u}^3}{\kappa z}$ is larger in magnitude than production from Reynolds stresses, the trend matches well.

value, u', v', or w' is lagged by one point against itself, which is then cross correlated with w', which allowed us to remove noise from the TKE component, as described above, when computing the triple correlation. In analogy to the Reynolds stress computation, we estimated $\langle u_i' u_i' w' \rangle$ from the average of the values at lags τ_2 through τ_5 (figure 2.6, c and f, black dots). We ignored both τ_0 and τ_1 in this case, since at lag τ_1 there may still be noise from the correlation between $u'(t_1)$ and $w'(t_1)$.

We also estimated buoyant production or destruction of TKE in the bottom boundary layer, by computing $B = \nu_T N^2$. Here, we used ν_T as described (2.12) from 0.25 m above the bed, and N^2 (2.8) from 0.87 to 1.87 m above the bottom, acknowledging that this yielded an overestimate of stratification in the bottom 0.25 m. Finally, we estimated the inertial term, $\frac{\partial k}{\partial t}$, by evaluating the change in TKE from one burst to the next. Estimates of the remaining terms in the TKE equation (2.1) could not be computed since the required observations were not available.

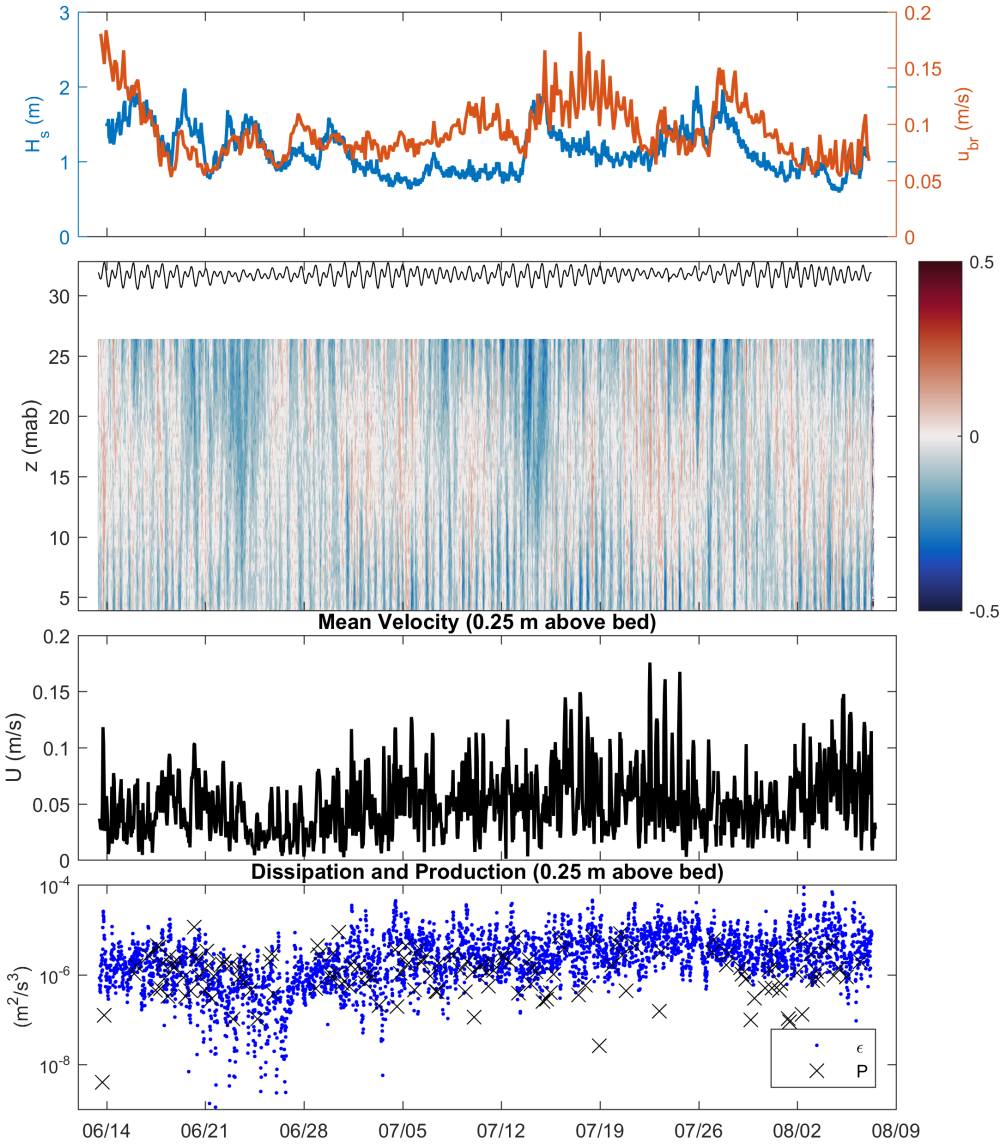

Figure 2.10: Flow and wave observations for the full deployment, 13 June 2015 through 7 August 2015, are shown at quadpod 2. Significant wave height, H_s, and wave orbital velocity, u_{br}, were computed by equeations 2.6 and 2.4, respectively. Mean velocities (in E-W direction) and mean water elevation were measured by the AWAC. The near bed velocity magnitude (U) gives the intensity of the currents during each burst, measured by the Aquadopp. Production and dissipation were computed from equations 2.11 and 2.13, respectively. Production estimates are reported every 3 hours, for 24 min bursts. Dissipation estimates are reported from 15 min sections of 45 min bursts, every hour.

2.4 Results

2.4.1 Site characteristics

During the observational period from 13 June 2015 to 7 August 2015, significant wave heights, H_s (2.6), varied between 0.6 and 2.0 m (figure 2.10). Wave periods (2.5) ranged between 5 and 20 seconds, with peak wave intensity at 12 seconds. Near-bed bottom orbital velocities (2.4) were weak, $u_{br} = 0.1$ ms^{-1}, although they were stronger than typical mean flows, $U_{hor} = 0.05$ ms^{-1}. The observed surface wave conditions correspond to wave lengths of 40 m to 300 m, computed via the full surface water wave dispersion relation, $\omega^2 = gk \tanh(kh)$. Since kh values range from 0.5 to 4.0, these waves are not considered shallow ($kh < \pi/10$). The shortest waves fell in to the deep-water regime, ($kh > \pi$), while the majority of the waves present were in the transitional regime. At peak wave intensity, the wave length was $L = 166$ m, and $kh = 0.95$. The waves may generally be considered small amplitude with $ka < 0.1$ for most observed wave conditions. However, at the highest wave amplitudes ($a = 1$ m), waves 63 m and shorter are not small amplitude waves.

Mean total depth, plotted once every hour, shows the tidal behavior during the deployment (figure 2.10). The primary flow direction shifted between the surface and the bottom (figure 2.10), showing the role of internal waves in separating flow near the surface from flow near the bed.

The height of the current bottom boundary layer, $\delta = \sqrt{\nu_T T_t}$, extended about 3 m above the bed, where the typical eddy viscosity, $\nu_T = 4 \cdot 10^{-4}$ m^{s}s^{-1} (equation 2.12) and $T_t = 12.4$ hours was the M2 tidal period. By the same metric, the wave boundary layer extended only about 0.05 m above the bed. Consequently, the height of the wave boundary layer was well below the ADV located at 0.25 mab; all turbulence analyses were performed above the wave boundary layer, but within the current boundary layer.

Below 2 mab, water was less stratified than higher in the water column, with median (and standard deviation, computed on a log-scale) $N^2 = 4.1$ (1.5 to 11) $\cdot 10^{-5}$ Hz^2 at 1.3 mab. Above the bottom boundary layer, buoyancy frequencies increased with median (and standard deviation) $N^2 = 9.4$ (4.0 to 22) $\cdot 10^{-5}$ Hz^2 at 2.9 mab, and $N^2 = 13$ (6.0 to 26) $\cdot 10^{-5}$ Hz^2 at 7.5 mab (figure 2.11, d). The highest 1-hour N^2 between 4 m and 8 m ab reached $2 \cdot 10^{-3}$ Hz^2. Figure 2.11 illustrates how internal bores displaced the pycnocline, bringing regions of strong stratification lower into the water column. Using 1-hour averaged data, N^2 was lowest near the bed, and increased higher in the water column. The CTD located at 1.84 mab did not log data after 30 June 2015, which limited our ability to estimate stratification in the bottom boundary layer. During the time period from 13 June 2015 through 30 June 2015, the bottom water column was well mixed with $N^2 < 10^{-4}$ 1/s^2 over 87% of the time. Using N^2 data from sensors at 1.84 mab and 0.87 mab, and velocity shear data from the Aquadopp profile, centered at 1.2 mab, we computed a gradient Richardson number, $Ri_g = N^2/S^2$, during the period. We found $Ri_g < 0.25$ over 75% of the time (figure 2.11, e) implying that most of the time bottom boundary layer turbulence was not suppressed by stratification. Because we did not have high precision temperature sensors in the lowest

part of the water column, we could not further bound Ri_g in the bottom boundary where we focused our analysis.

2.4.2 Internal Waves

Internal wave structures, including bores, undular bores, solitons, and reverse undular bores, were all observed during the experimental period (Colosi et al., 2017). Bores appear on a 2 to 3 per day timescale, generated by tide interactions with the shelf break, and last about $6-12$ hours. Often, though not exclusively, bores appeared at the measurement station near high water. Here, a bore is seen as a period of warm water appearing lower in the water column (Colosi et al., 2017). Lateral velocities in the bottom boundary were impacted by internal waves. Figure 2.12 highlights phases of a bore. "Before" the bore arrival, near bed velocities were directed on-shore. During the "bore trough", when warm waters entered the bottom region, near bed velocities were oriented off-shore, consistent with wave orbital velocities during the trough of a progressive wave. "After" the bore passage, near bed velocities were strong and on-shore. The measured dissipation rates are also shown during the bore passage. Gradient Richardson numbers were below critical for most periods.

2.4.3 Turbulence in the bottom boundary

During the observational period from 13 June 2015 to 7 August 2015, the turbulence dissipation rate at 0.25 mab (with log-normal standard deviation) was $2 \cdot 10^{-6}$ ($5.4 \cdot 10^{-7}$ to $7.4 \cdot 10^{-6}$) $\mathrm{m^2 s^{-3}}$. The observed values were similar to values observed at 0.3 mab in Southern Monterey Bay, $\epsilon = 10^{-7} - 10^{-5}$ $\mathrm{m^2 s^{-3}}$ (Walter et al., 2014). The corresponding Kolmogorov timescale, $\tau_\eta = \left(\frac{\nu}{\epsilon}\right)^{1/2}$, was estimated as $\tau_\eta = 0.7$ (0.1 to 1.3) s. The flow Reynolds number was estimated as $Re = 195$(42 to 700). We computed the Reynolds number from $Re = \frac{u_*^4/\epsilon}{\nu}$, which follows the traditional form $Re = \frac{u_* L}{\nu}$, where u_* was estimated from the Reynolds stress, and the turbulent length scale was estimated from $L = \frac{u_*^3}{\epsilon}$.

We measured bulk eddy viscosities (95% confidence bounds) in the bottom boundary layer of $\nu_T = 4.2$ (3.7 to 4.6) $\cdot 10^{-4}$ $\mathrm{m^2 s^{-1}}$ at 0.25 mab, and $\nu_T = 6$ (4.3 to 7.8) $\cdot 10^{-4}$ $\mathrm{m^2 s^{-1}}$ at 1.25 mab (figure 2.13). Eddy viscosity increased farther from the bed, as expected in a bottom shear flow. Reynolds stress in the direction of mean flow, $\langle u'w' \rangle$, was negative, as expected, and unchanging between 0.25 and 1.25 mab, suggesting that our data were collected in the constant stress layer. Turbulent production was positive and larger near the bed, also consistent with a bottom shear layer.

2.4.4 Local TKE budget

When turbulence in the bottom boundary is locally balanced, (2.1) may be simplified to $P = \epsilon(+B)$, which assumes accumulation, advection, and other transport do not contribute to turbulence in the bottom boundary. In general, turbulence in the bottom boundary was

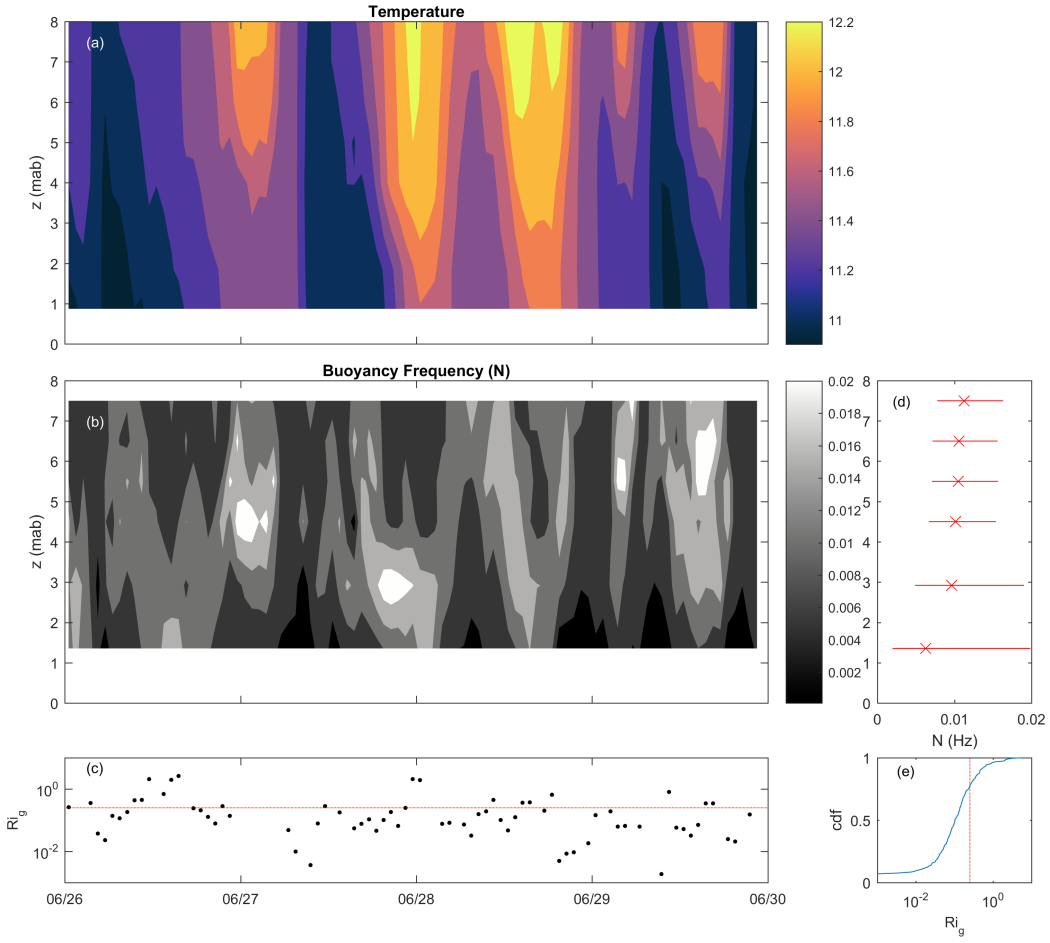

Figure 2.11: Shown is an example of internal wave activity displacing the thermocline, from 26 June 2015 through 30 June 2015. The CTD at 1.84 mab was functioning during this period, and was used to resolve the stratification above and below 1.84 mab. (a) Temperature (degrees C) was measured between 0.8 m and 8 mab. Internal waves are periods when warm water is seen entering lower in the water column; about $4-5$ internal waves are observed here. (b) Buoyancy frequency (N, in Hz) were computed between the temperature sensors using (2.8). (c) Gradient Richardson numbers (plotted on a log scale) were computed centered at 1.25 mab. (d) The median and standard deviation of N at each elevation (computed on a log-scale) and the (e) cumulative distribution function (on a log scale) of Ri_g was computed for the period 13 June 2015 through 30 June 2015. The red lines in (c) and (e) denote the critical Richardson number, $Ri_g = 0.25$.

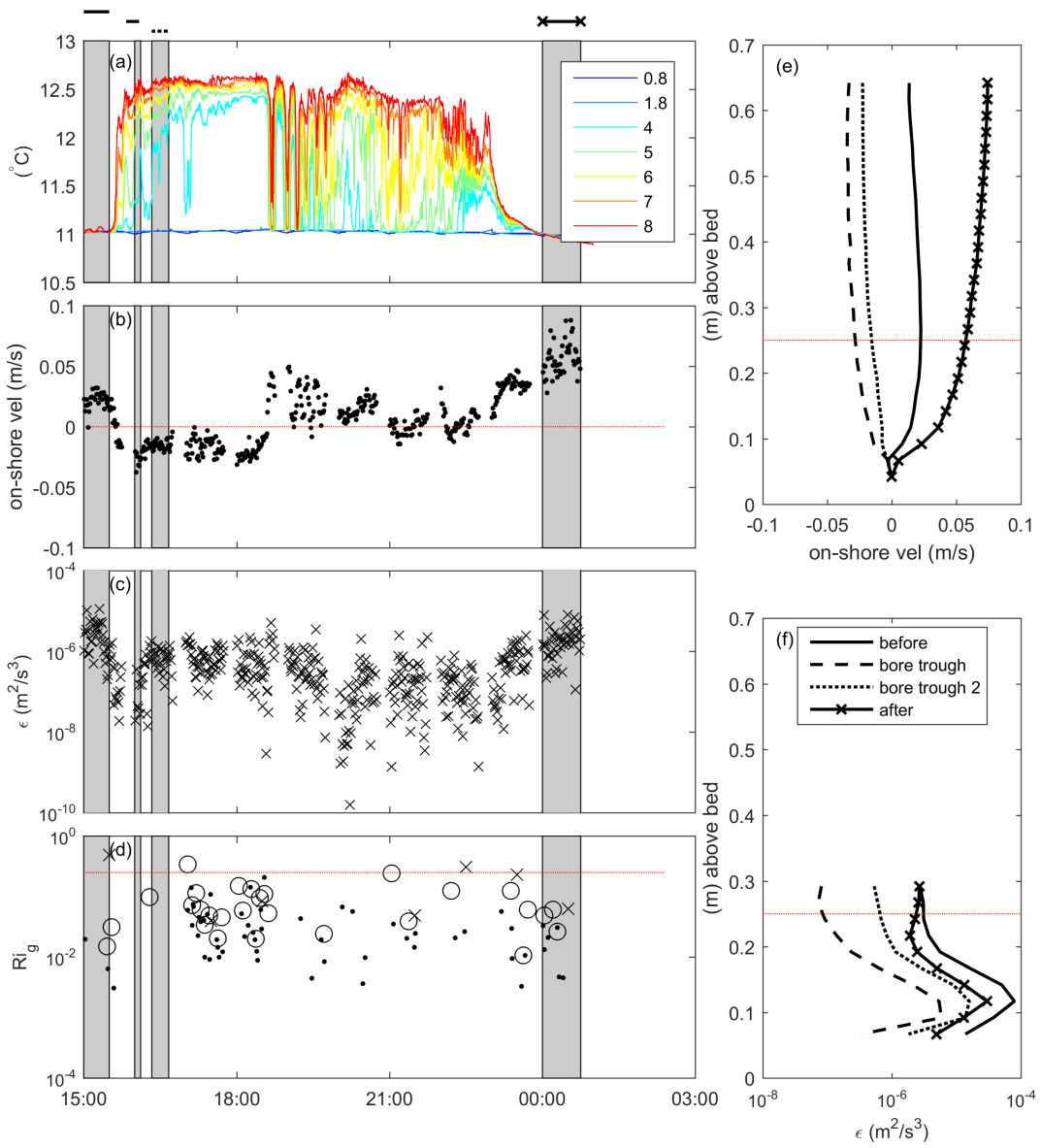

Figure 2.12: Shown is a close view of near-bottom dynamics during an internal bore, from 19 June 2015 at 15:00 to 20 June 2015 at 01:00. (a) Temperature was measured from 0.8 to 8 mab, showing the arrival and departure of a bore (defined as warmer temperatures descending in to the bottom region). Grey boxes highlight phases of the bore dynamics. (b) Velocity is shown in the cross-shore direction at 0.25 mab, positive on-shore. The horizontal line denotes 0 velocity. Profiles of on-shore velocity during the highlighted periods are shown (e). (c) TKE dissipation from 1-min bursts, at 0.25 mab. Profiles of dissipation rate during the highlighted periods are shown (f). (d) Gradient Richardson number was computed from 1-min averages (dots), 5-min averages (circles), and 45-min averages (x), at 1.25 mab. Ri_g is omitted when the mean shear was not calculable due to low shear and high variance, which was common at 1 and 5 min timescales. The horizontal line depicts the critical Ri_g at 0.25. (e) and (f) show profiles of on-shore velocity and dissipation rate from highlighted periods in (b) and (c), respectively. Near-bottom currents responded to the phase of the internal wave.

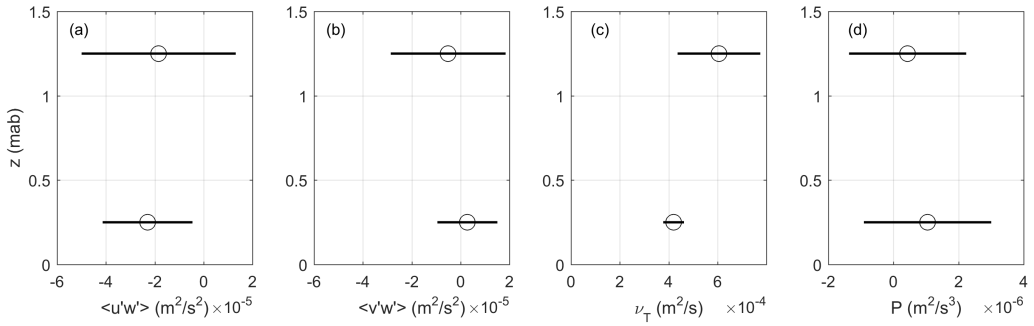

Figure 2.13: Shown are summary statistics for turbulence in the bottom boundary layer. (a) Reynolds stress is shown in the direction of mean flow (u). (b) Reynolds stress in the "cross-stream" direction (v). (c) Eddy viscosity, computed via (2.12). (d) Shear production, computed via (2.11). Black lines show standard deviation (for Reynolds stresses and P) and 95% confidence bounds (for ν_T).

explained by mean flow, with dissipation predicted by (2.15) reasonably well. When buoyancy is small relative to dissipation, which appears true for these data, the local turbulence budget simplifies further to $P = \epsilon$. Figure 2.14,a shows that this further simplification applied at 0.25 mab, albeit in an imperfect fashion. While production and dissipation were generally similar in magnitude and are consistent with the dominant thinking that production and dissipation should be balanced in the bottom boundary, there may be error in our data that we are not fully able to quantify, and other terms in the analysis (2.1) that we cannot measure. We refer to this as the "approximate" balance between production and dissipation. The result was broadly consistent with other observational studies of near bed turbulence in coastal environments where production and dissipation are in balance near the bed, and dissipation exceeds production farther from the bed (Gross & Nowell, 1983; Trowbridge et al., 1999; T. B. Sanford & Lien, 1999; Shaw, Trowbridge, & Williams, 2001; Reidenbach, Monismith, Koseff, Yahel, & Genin, 2006; Walter et al., 2014).

For the observations presented here, dissipation exceeded production. We quantify the energy deficit as the separation from the 1:1 line in figure 2.14,a, or $ED = k(\epsilon - P)$, where $k = \frac{\sqrt{2}}{2}$. When the energy deficit was positive, there may be an unaccounted for net source or input, and when it was negative the missing terms may be net sinks or exports. While the computations presented here represent our best efforts to compute these terms accurately, it remains challenging to quantify the energy deficit precisely. This quantity relies on the difference between two measurements with large errors, and the two techniques to compute these terms may not be consistent. Regardless, we compare them as a first guess towards the energy budget (figure 2.14,b). Thus, we find that the approximate balance between production and dissipation was not good enough to say that no other terms are important for estimating TKE in the bottom boundary layer, and we acknowledge that noise or error in these computations may play a role.

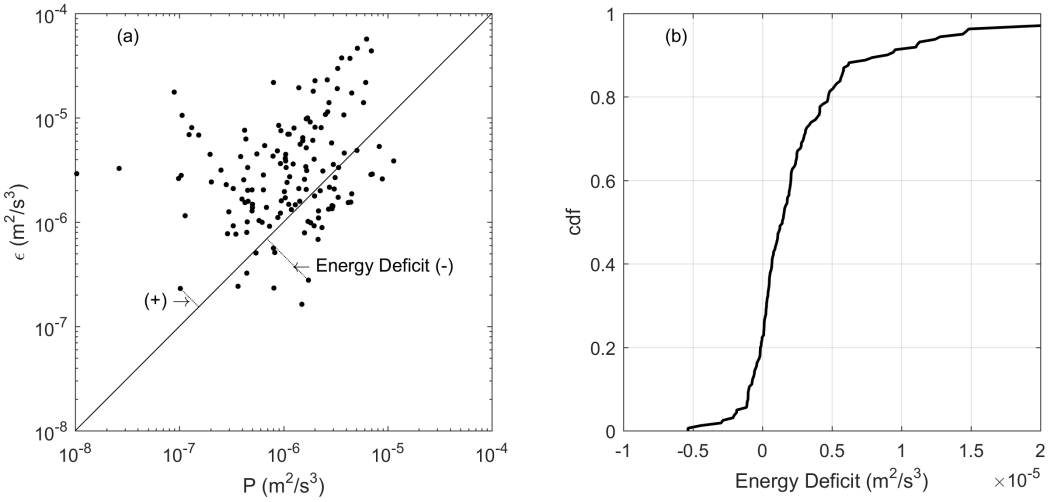

Figure 2.14: (a) Shown is the balance between dissipation (ϵ) and shear production (P) of TKE at 0.25 mab. The 1:1 line denotes when $\epsilon = P$. The energy deficit, computed as the distance to the 1:1 line, is positive when ϵ exceeds P, and negative otherwise. (b) the cumulative distribution function of the energy deficit is presented.

2.5 Discussion

2.5.1 Data Quality

Measuring turbulence in the bottom boundary layer can be quite challenging. While our observations yielded highly temporally resolved data enabling a detailed view of the local TKE budget, extensive filtering was needed to exclude data affected by instrument noise, instrument failure, or frame interference. We were able to compute mean quantities; wave statistics; and turbulent shear production, dissipation, vertical diffusive transport, buoyant mixing, and inertial change at 0.25 mab. However, we do not have the ability to evaluate the potential importance of horizontal advection of TKE. We also do not investigate the potential importance of wave/turbulent stresses (e.g. $\widetilde{u'w'}$), which could play a role in the TKE budget in study regions where strong surface waves are common. In addition, wave motions may have biased the computed values of the turbulent dissipation rate, and the potential magnitude of their impact is unknown.

2.5.2 Production-Dissipation Balance

While production and dissipation have some discrepancies over the entire observational period (figure 2.14), we take a closer look at the overall balance. Three possible explanations for a discrepancy between production and dissipation, aside from error in estimating these

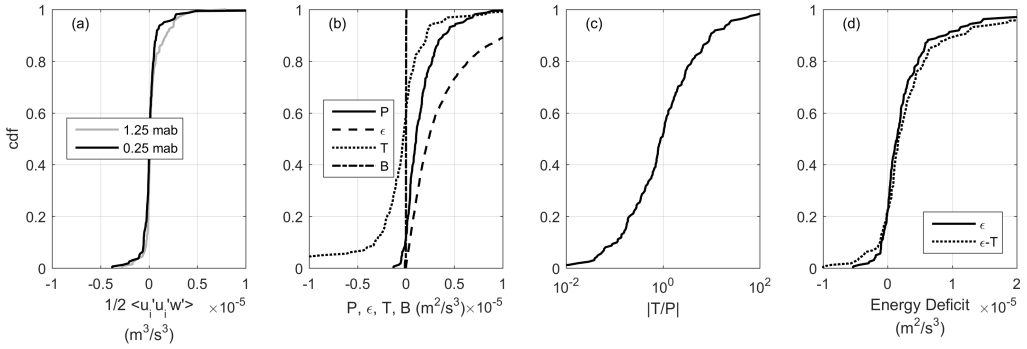

Figure 2.15: Shown are cumulative distributions functions (cdf) of terms that contributed to the TKE budget at 0.25 mab. (a) The vertical turbulent diffusive flux was generally positive at both 0.25 mab and 1.25 mab. (b) Shear production (P), dissipation (ϵ), turbulent diffusive transport (T) at 0.25 mab, were of similar magnitudes. Buoyancy (B) was much smaller than the other terms. (c) The magnitude of (T/P) shows that T was within 10-fold of P over 80% of the time. Thus, T scales approximately with P, by order of magnitude. (d) The energy deficit, as computed in figure 2.14, assuming P balanced by ϵ only, is compared with the deficit assuming P balanced by $\epsilon - T$. Including T in the budget did not make it more balanced.

quantities, include inertial accumulation or loss, buoyant destruction, and turbulent diffusive transport of TKE.

If local turbulence is changing rapidly in time, the inertial term, $\frac{\partial k}{\partial t}$ from (2.1), may contribute to the local budget. We computed the inertial term from noise-removed components (figure 2.6,a,d), and found that the magnitude was below $1.5 \cdot 10^{-7}$ m^{2}s^{-3} at all measured times. While the 3-hour timestep for our data may under-estimate the total contribution, the magnitude of the inertial term was two orders of magnitude smaller than P and ϵ, which suggests that the inertial term did not substantially contribute to the turbulence budget.

In stratified flows, TKE may be converted to potential energy through buoyant mixing, B. While we showed that the gradient Richardson number is less than its critical value over 75% of the time (figure 2.12,d), there may be periods when stratification suppresses turbulence. However, an estimate of buoyant mixing showed that this quantity was much less than P and ϵ over the course of the deployment (figure 2.15,b), which suggests that the buoyant mixing term did not substantially contribute to the local budget.

Turbulent diffusive transport in the vertical direction, $T = -\frac{\partial}{\partial z}\left(\frac{1}{2}\langle u_i' u_i' w' \rangle\right)$, may be a mechanism for import or export of TKE. When more turbulence is diffused downward past the upper sensor than downward past the lower sensor, there is a net import of turbulence through the transport term. Likewise, if more turbulence is diffused upward past the upper sensor than upward past the lower sensor, the transport term acts to export TKE. Figure 2.15,a shows that turbulent diffusive flux, $\langle u_i' u_i' w' \rangle$, was generally positive at both 0.25 mab and 1.25 mab. Turbulent diffusive transport was generally negative, whether it was computed

as the difference between 0.25 mab and the bed, or between 1.25 mab and 0.25 mab (figure 2.15,b) suggesting T acted as a sink for TKE near the bottom boundary. Turbulent diffusive transport was within one order of magnitude of P ($0.1 < |T/P| < 10$) over 80% of the time, and within 2 orders of magnitude of P over 95% of the time, showing that transport scales approximately with production (figure 2.15,c). When included in the overall TKE budget, turbulent diffusive transport did not significantly alter the overall balance. In fact, the energy deficit increased slightly when T was included in the budget as a "loss", $P = \epsilon - T$ (figure 2.15,d). While turbulent diffusive transport may have contributed to the TKE budget, it was likely not an important export mechanism in the bottom boundary.

Turbulent diffusive transport has been investigated in a handful of observational (Ölçmen & Simpson, 2008) and numerical (Yakovenko, 2011; Howard & Serre, 2015) studies. We present data showing that turbulent diffusive transport acted to export TKE from the bottom boundary region, and was often within one order of magnitude of shear production. Our results were consistent with the findings of Yakovenko, 2011, who showed that in a turbulent patch formed during a breaking internal wave, a water-column global TKE budget was balanced between shear production, advection, and dissipation, but locally buoyancy and turbulent diffusive transport were important. Because TKE dissipation rates can vary 100-fold between phases of internal waves and between regions of the water column, turbulent diffusive transport may be important as a source of TKE for regions that are otherwise source limited. However, we did not have high enough resolution data to investigate this possibility.

We have no a priori reason to expect the observed differences between production and dissipation; we conclude that there was either a bias introduced by our data analysis, or another term in the TKE budget was active. As noted above, we may rule out inertial change and buoyancy, as they were significantly smaller than other quantities. However, the remainder of the unquantified terms that may contribute to the TKE (2.1) include TKE advection vertically (or horizontally) towards the instruments from higher (or nearby) in the water column, transport of TKE by pressure fluctuations, and transport of TKE by molecular viscosity. In addition, terms unspecified in (2.1) corresponding to internal wave-turbulence interactions could play a role (Reynolds & Hussain, 1972). Without the necessary observations to quantify these components, we speculate that it is possible that some of them contribute to the TKE budget. Noting the internal wave activity at this site (Colosi et al., 2017), we move on from the long-time scale production-dissipation balance and focus the remainder of our analysis in an effort to understand the role of internal wave motions in turbulence energetics in the bottom boundary layer.

2.5.3 Role of Internal Waves

An attempt to predict turbulent dissipation on the timescale of internal waves was inspired by the large scale internal bores. Here, we denote the phase of internal bores by using the near-bottom temperature sensors. When temperature was constant in the bottom region (up to 8 mab), we call the near-bottom region "unstratified". When temperature at 8 mab

was higher than near the bottom, we say that the region is "stratified". We designated the 2-hour transition from unstratified to stratified as "transitional" (e.g., Colosi et al., 2017), as this period indicates the beginning of internal bores (figure 2.16,a). Based on previous work, we predicted that turbulence may be higher during the onset of internal waves, or our "transitional" period. In particular, Walter et al., 2014 noted that dissipation is higher near the bed as the bore arrives at the sensors. Similarly, Arthur and Fringer, 2014 discuss how near-bed turbulence should spike when a bore passes. However, the magnitude of this increase in dissipation depends on where the bore breaks on the bed, and may not be observable.

When dissipation predicted during "transitional" periods was compared to "stratified" or "unstratified" periods, they were very similar (figure 2.17). Here, TKE is shown on the x-axis as (2.15), which allows us to anticipate the dissipation based on the velocity. Equation 2.15 assumes that all dissipation is due to local shear production produced by drag from a wall. Given a near-bed internal bore that begins to break, we expect that the measured dissipation might be higher than what is predicted under this assumption. However, dissipation during transitional periods did not appear to be higher than dissipation during other periods, suggesting that internal wave onset did not increase local dissipation at the site measured. Internal waves that break more towards the shore generally do not alter turbulence in the bottom boundary (Arthur & Fringer, 2014). Additionally, at a site with energetic internal waves the role of buoyant mixing, B, was only important when internal waves shoaled over a coral reef (Davis & Monismith, 2011). The lack of a relationship between the phase of internal waves and turbulent energetics agrees with our finding that buoyant mixing is negligible.

2.6 Summary and Conclusions

Understanding the turbulence budget at the bottom boundary will enable better predictions of mixing and transport in coastal shelves and contribute to our models of energy transformation by internal waves. Here, we used acoustic measurements of mean and turbulent velocities to characterize the near-bed turbulence at a 30m deep site on the California shelf near Point Sal.

In agreement with previous studies, our results indicated that the near-bed shear production and turbulent dissipation had an approximate balance over a period of eight weeks. The observation site has many drivers of flow dynamics, including vertical stratification, lateral density gradients, tides, surface waves, and internal waves. Our results indicated that the relationship between shear production and dissipation was largely unaffected by the weak stratification produced buoyancy near the bed, and was likewise un-remedied by turbulent diffusive transport. While turbulent diffusive transport was similar in magnitude to dissipation, it generally acted to export TKE from the bottom boundary. However, including turbulent diffusive transport in the local TKE budget did not improve the balance between production and dissipation. Consequently, it was not an important import or export

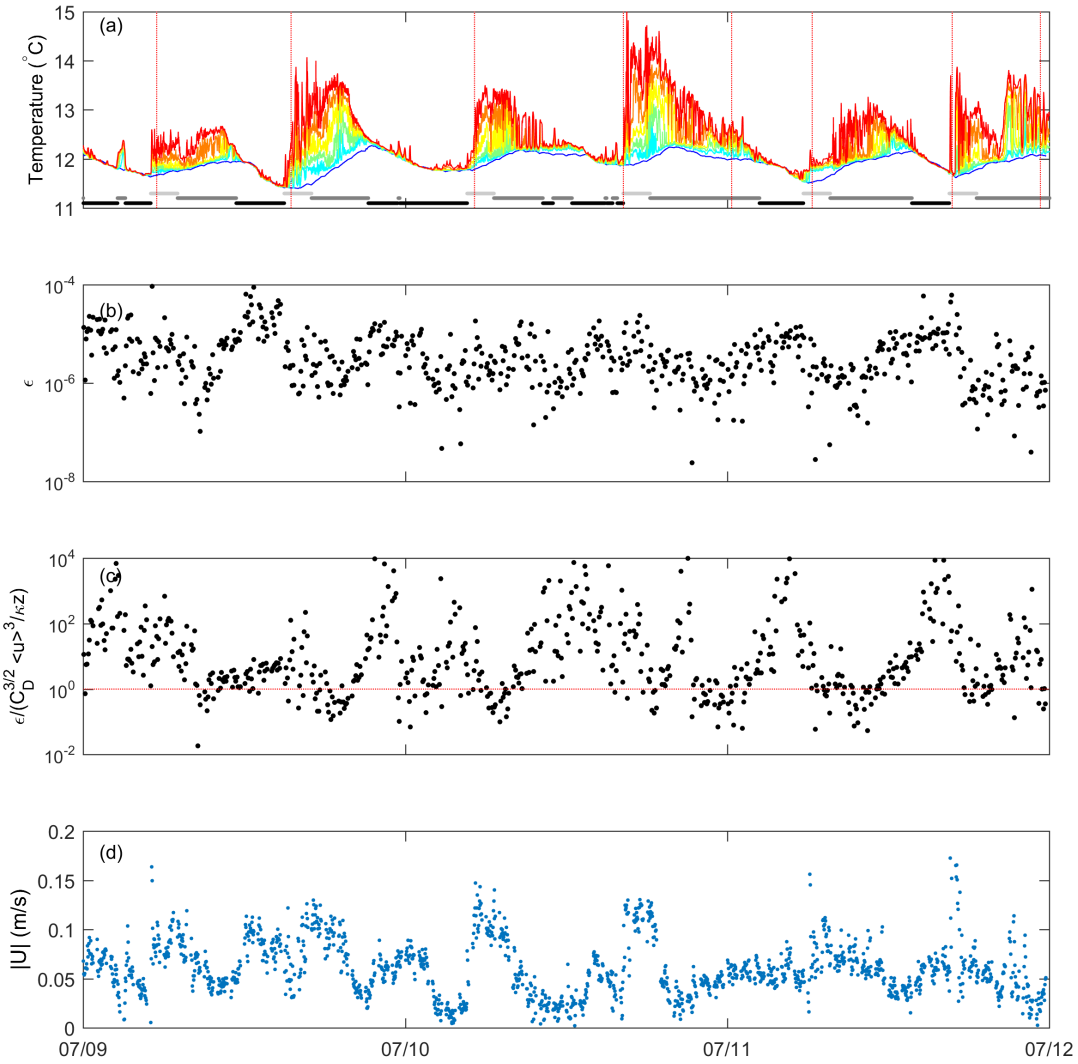

Figure 2.16: (a) Temperatures measured between 0.8 and 8 mab, from 9 July 2015 through 12 July 2015 are shown. The temperature colors are the same as those presented in figure 2.12,a. The horizontal lines on the bottom denote the phase of internal wave, with the lowest black lines showing no stratification, the highest light grey lines showing the beginning of internal waves, and intermediate lines denoting the bulk and end of stratified periods. Vertical lines denote internal waves, as identified by Colosi, Kumar, Suanda, Freismuth, and MacMahan, 2017. (b) The turbulent dissipation rate (ϵ) at 0.25 mab is shown. (c) The turbulent dissipation rate (ϵ) divided by the quantity computed from (2.15, using $C_{D,25}$), both from 0.25 mab is shown. As discussed, this should show excess energy in the bottom boundary layer, not produced by mean currents. (d) Mean current in the bottom boundary layer, again from 0.25 mab.

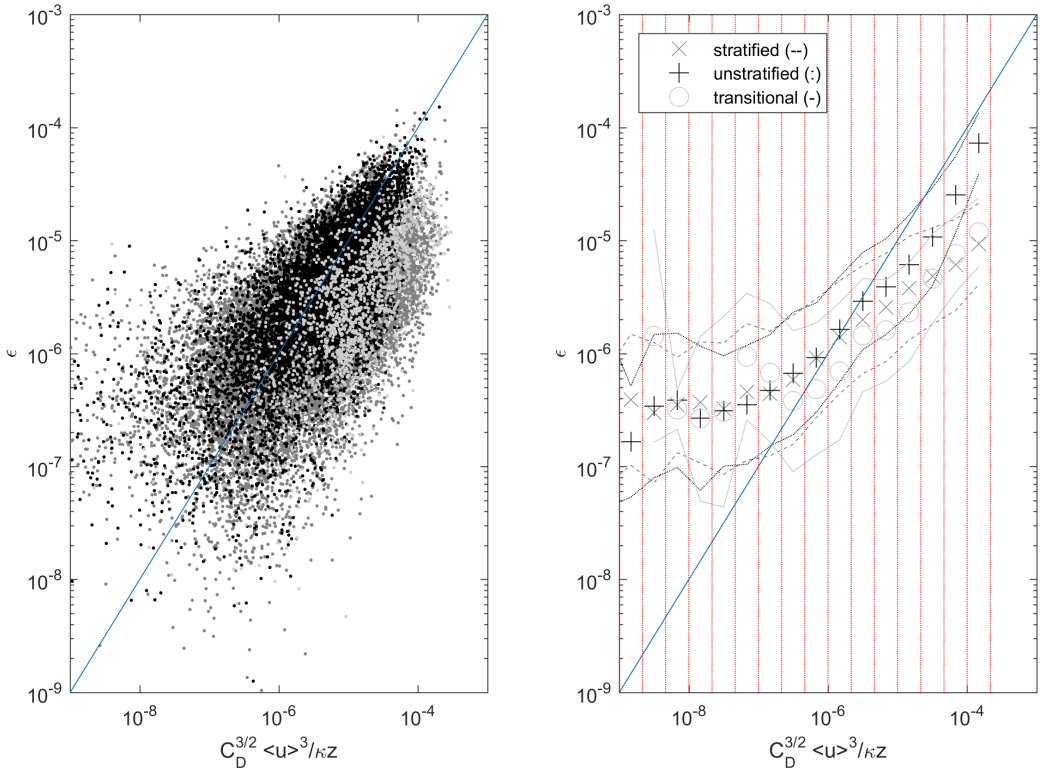

Figure 2.17: We present a comparison between energy in the bottom boundary layer (computed via (2.15) using $C_{D,25}$) and dissipation. In the left panel, the raw data is shown, from 0.25 mab. In the right panel, data was binned, and the mean and error bars (on a log scale) are shown. As in figure 2.16,a, stratified, unstratified, and transitional periods are denoted by grey, black, and light grey, respectively.

mechanism in the bottom boundary.

We also examined the role of internal waves on energy dissipation, and did not observe any effect. Dissipation, scaled by energy produced by mean currents in the bottom boundary region, did not vary with the phase of internal waves. This may indicate that internal waves affect the mean velocity at the same timescale as they drive dissipation, suggesting that the role of internal waves on turbulence cannot be viewed through this lens. We did not observe an increase in (scaled) dissipation in the bottom boundary layer near the onset of internal waves, as we anticipated. We conclude that the impact of internal waves on the near-bottom turbulence was not discernable at this site.

We investigated turbulence in the bottom boundary through the approximate balance between production and dissipation. We did not find any influence of internal bores on the turbulence equilibrium. Our study constitutes a high temporal resolution view into tur-

bulence in the bottom boundary layer in the presence of mid-water column internal bores. While the importance of internal waves in ocean mixing and creating turbulence have been well studied, questions remain regarding the role of the bottom boundary on internal wave energy budgets and the role of internal waves on turbulence in the bottom boundary. Understanding turbulence generation, transport, and dissipation near the bed can help predict and characterize sediment resuspension and motion.

Chapter 3

Seasonal Variation in Sediment Parameters in San Pablo Bay Shoals

3.1 Sediment Dynamics in Tidal Estuaries with Strong Seasonal Variation

Observational and modeling work has been done on sediment transport on shorter timescales in places like San Francisco Bay, (e.g., MacVean & Lacy, 2014; Brand et al., 2010; D. H. Schoellhamer, Ganju, & Shellenbarger, 2008; Bever & MacWilliams, 2013), and modeling has been done on decadal timescales (e.g., van der Wegen & Jaffe, 2014). Such work has focused on the roles of wind, waves, tides, turbulence, and tidal asymmetries in yielding sediment resuspension, sediment distribution through the water column, and sediment transport. Changes on a seasonal scale may affect sediment transport dynamics, but have been less well studied. In the San Francisco Bay region, seasons mean strong daily winds and no rainfall in the summer, and calmer periods punctuated by multi-day storm events bringing winds and rain in the winter. As with other places around the world, seasons also mean more growth and production in the spring, summer, and fall, and shorter periods of sunlight in the winter. With this work, we focus on the role of such seasonal scale factors on sediment dynamics.

Numerical models of sediment transport require site-specific inputs including bottom roughness, erodibility, and particle settling velocity (Lesser, Roelvink, van Kester, & Stelling, 2004). Often, these parameters are tuned within models to yield reasonable-looking suspended sediment concentrations, as field data only rarely produce such parameters. Improvements to processes or parameters in sediment transport models may yield increases in predictive ability. For example, Bever and MacWilliams, 2013 found that the timing of model-predicted sediment peaks in San Pablo Bay differed from the field-observed peaks by up to a few hours, thereby affecting sediment flux. With many sediment models being developed and implemented around the world, we focus on ground-truthing numerical models through our search for bottom roughness, erodibility, and flocculated particle size from field-based data.

Numerical models, such as those from Deltares, 2018, address sediment exchange between the bed and water column (source and sink terms) through deposition and erosion equations:

$$D = w_s c \left(1 - \frac{\tau_b}{\tau_d}\right) \tag{3.1}$$

$$E = M\left(\tau_b - \tau_{crit}\right) \tag{3.2}$$

The deposition equation (3.1) describes how much sediment is lost to the bed due to particle settling in the water column through the deposition flux D (kg/m^2/s). This quanity is set by the particle settling velocity, w_s (m/s), the suspended sediment concentration near the bed, c (kg/m^3), the bed shear stress, τ_b (kg/m/s^2), and the critical shear stress for deposition, τ_d (kg/m/s^2). The erosion equation (3.2), just one of a number of different ways this could be formulated, indicates sediment suspension due to shear stress at the bed, where the erosion flux E (kg/m^2/s) is given by the first-order erosion rate M (s/m), the bed shear stress, and the critical stress for erosion, τ_{crit} (kg/m/s^2). While sediment concentration, c, is solved for in the models, parameters such as settling velocity, w_s, erosion rate, M, and critical stress for deposition and erosion, τ_d and τ_e, must be specified as inputs or tuning parameters.

The sediment bed roughness, z_0, describes the momentum exchange between the bed and the flow. For cohesive sediment beds, this parameter can yield a positive feedback of mud deposition. Mud deposition causes the bed roughness to decrease; when this happens, bed shear stress also decreases and mud consequently continues to deposit. The sediment bed roughness strongly depends on the conditions of the bed, including grain size and wave forms, and is often set external to the model rather than solved for within the system.

Numerical models of sediment transport serve many purposes, from predicting light limitation due to suspended sediment to simulating the long-term response of bed morphology in the face of sea-level rise. As conditions continue to change and as predictions for the future resemble the past in fewer ways, process-based models enable us to anticipate what is to come. To support improvements in processed-based models, our work provides specific parameters for San Francisco Bay on a seasonal scale, as well as our inferences about what affects these parameters more broadly.

3.2 Background of 3 key parameters

We review sediment transport dynamics in shallow estuarine environments as well as the specific parameters explored here that can help improve in numerical models.

3.2.1 Bottom Roughness

Flows near the bottom boundary typically follow a log profile,

$$u(z) = \frac{u_*}{\kappa} \ln\left(\frac{z}{z_0}\right) \tag{3.3}$$

where the mean velocity profile, $u(z)$ is dependent on the friction velocity, u_*, and on the hydrodynamic bed roughness, z_0. A rougher bottom, characterized by a larger z_0, injects more turbulence to the boundary layer.

The hydrodynamic bed roughness can often be predicted from the physical features of the bed, via

$$z_0 = \frac{k_b}{30} = \frac{k_d + k_r + k_m}{30}. \tag{3.4}$$

Here, the effective bed roughness, k_b, comprises grain roughness, k_d; ripple roughness, k_r; and movable bed roughness, k_m (Nielsen, 1992). For example, L. Wright, Kim, and Friedrichs, 1999 found $z_0 = 2.4{\cdot}10^{-4}$ m at a muddy 60 m deep site on the California coast during January and Feb 1996. The corresponding k_b was 0.7 cm, suggesting that the bottom roughness was induced by infaunal feeding voids, burrows, worms, and biologically produced hummocks and depressions, as viewed by a profiling camera.

Predicting z_0 through measurements of grain size or bed forms does not always yield appropriate metrics, especially in muddy estuaries. When computed through hydrodynamic equations (e.g. 3.3), z_0 yields a predictive yet not always physical parameter. Therefore it is worth exploring z_0's variation in time, alongside the studies of how k_b varies in time (e.g., L. Wright et al., 1999; Trembanis, Wright, Friedrichs, Green, & Hume, 2004). Brand et al., 2010 found constant median bottom roughness values of $z_0 = 2 \cdot 10^{-5}$ m and $3.1 \cdot 10^{-5}$ m on the shoals of South San Francisco Bay in Feb-March 2009, roughnesses much larger than would be predicted from the $4-40$ μm bed grain size. Similarly, Brand, Lacy, Gladding, Holleman, and Stacey, 2015 modeled and Jessica R. Lacy and MacVean, 2016 measured a smoother bottom roughness during winter ($z_0 = 2 \cdot 10^{-5}$ m and $1.1 - 1.5 \cdot 10^{-4}$ m, respectively) than summer ($z_0 = 3.4 \cdot 10^{-4}$ m and $2.4 - 5.4 \cdot 10^{-4}$ m) in San Francisco Bay. Brand et al., 2015 suggested that this seasonal change could be due to winnowing of fine material from the bed during summer. However, the bed particle grain size does not change between the seasons, so they postulate (as do Jessica R. Lacy and MacVean, 2016) that it is more likely the shift occurs due to a summer increase in biogenic roughness. Jessica R. Lacy and MacVean, 2016 also note that the roughness computed from hydrodynamic data is $1-2$ orders of magnitude larger than what would be predicted from measuring grain size alone. R. T. Cheng, Ling, Gartner, and Wang, 1999 saw a slight flood-ebb variation in bottom roughness in South San Francisco Bay. They suggested that the smaller z_0 on ebb results from the stronger ebb currents causing bed erosion, resulting in a reduction in form drag. Thus, the transition to smaller z_0 when currents exceeded $0.25 - 0.3$ m/s corresponded to the onset of sediment erosion, where bed shear stress surpasses the critical shear stress.

While the deviation between physical bottom roughness and hydrodynamic bottom roughness is most common in muddy environments, a handful of studies yielded pertinent results from sandy bed locations. In particular, Fong, Monismith, Stacey, and Burau, 2009 saw asymmetrical sand waves yield a higher bottom roughness in flood direction in the San Francisco Bay Delta, during an experiment from Jan-Feb 2003. They saw a smaller bottom roughness when ebb currents approached the steeper face of the sand waves, consistent with the effects of streamlining. J. R. Lacy, Sherwood, Wilson, Chisholm, and Gelfenbaum,

2005 demonstrated the importance of temporal variation in bottom roughness studying sand waves on the inner shelf near grays harbor, Washington, during May-July 2001. They found an apparent bottom roughness (k_b) of $10^{-4} - 10^{-1}$ m. Allowing k_b to vary in numerical models yielded τ_b up to 50% lower and 150% higher than the τ_b found with a constant k_b.

Models commonly use single, constant values for bottom roughness (e.g., Ferre, Sherwood, & Wiberg, 2010; He, Scott, Graham, & Binns, 2014). Given that hydrodynamic bottom roughness can change in time and space as the physical bottom alters, and can vary independently of the bed, this estimate may be insufficient. Ralston, Cowles, Geyer, and Holleman, 2017 allowed bottom roughness to vary in space and with grid resolution in a numerical model of the Connecticut River Estuary. In this environment, linearly varying the bottom roughness captured the depth-limited sand wave height. However, the bottom roughness was also needed to compensate for insufficient grid resolution: to adequately reproduce the timing of mixing events the stratification Richardson (Ri_{st}) number was reduced, requiring an artificially larger bottom roughness, though with finer grid resolution this requirement was diminished.

In muddy environments, there is a sense that bottom roughness is not tied to grain size or other defined physical parameters. However, studies have not yet directly investigated the temporal and spatial variation in bottom roughness in such locations. In addition, the challenge of predicting bottom roughness frequently becomes a source of uncertainty in numerical models (Grant & Madsen, 1986). With this work, we characterize the temporal variation in bottom roughness, and link its change to possible physical parameters.

3.2.2 Bed Erodibility

Fine sediment erosion occurs when shear stresses from currents and waves act on the sediment-water interface. Erosion is often classified into surface erosion, mass erosion, and the entrainment of fluid mud, with surface erosion, when small particles or flocs are detached from the surface due to abrasion from the flow, occurring most often in muddy estuaries like San Pablo Bay (Mehta, 2014). The erodibility rate, E, (kg/m^2/s), can be predicted through many different versions of an erosion formula. One of the more general forms is given by (Grabowski, Droppo, & Wharton, 2011)

$$E = M(\tau_b - \tau_{crit}(z))^n \text{ for } \tau_b > \tau_{crit} \tag{3.5}$$

where erosion occurs when the applied bed shear stress, τ_b, exceeds a critical shear stress for erosion, τ_{crit}. Parameters M and n have flexible units, and can be allowed to vary with depth. A simplification of equation 3.5, known as type II erosion, unlimited erosion, or standard linear erosion, sets this model for the linear case ($n = 1$), and does not allow τ_{crit} or M to vary with depth, equation 3.2 (e.g., L. P. Sanford & Maa, 2001; Mathew & Winterwerp, 2017). This generally applies well when the amount of eroded material is small enough such that no depth effect is observed. In San Pablo Bay, with shallow waters and increases in SSC typically less than 500 mg/L over a tidal cycle, the erosion depth is generally only a few floc diameters, suggesting depth dependence is not important.

Currently, we are unable to predict the erodibility of cohesive sediment (Grabowski et al., 2011). It is linked to hydrodynamic properties, such as bed shear stress, as well as sediment properties, including physical, geochemical, and biological aspects. For example, Joensuu et al., 2018 noted how the role of benthic macrofauna was larger in muddy sediments than sandy sediments. In low energy environments in South San Francisco Bay, fine silts settle out and the cohesive bed is higher strength, while at higher-energy, wavier sites, the bed coarsens with sandier sediment and is more erodible (Jones & Jaffe, 2013). Significant spatial variations of sediment erodibility have been observed in estuarine and coastal environments, however the magnitude and even the sign of these variations remains challenging to predict (Grabowski et al., 2011).

Far fewer studies have investigated temporal variation in erodibility and have generally focused on diurnal/ tidal cycles or seasonal variation. Seasonal variation can be driven by extracellular polymeric substance (EPS) production or growth in benthic communities (Grabowski et al., 2011). However, Brand et al., 2015 attributed seasonal differences in bed erodibility in South San Francisco Bay to changes in sediment supply. During winter and spring, large fresh water flows deposit small sediments on top of the consolidated material, which are easily erodible. This agrees with the R. Krone, 1979 conceptual model for San Francisco Bay, which suggests that more erodible fine sediments are winnowed from the bed during summer yielding a less erodible bed, while the appearance of a more erodible bed in the winter may be due to winter storms depositing easily eroded new material, resuspending, and reworking the existing sediment bed. D. H. Schoellhamer et al., 2008 suggest that higher bed erodibility in the winter could yield the shift they observed in resuspension dynamics in San Pablo Bay. Such a shift could come from a winnowing of the bed from winter to summer, a shift in particle size or biostabilization, or seasonal changes in bed stabilization due to benthic biota, such as clam density.

On a tidal scale, Brennan, Schoellhamer, Burau, and Monismith, 2002 suggest that bed erodibility varies between phases of the tide, due to salinity variations with 8 PSU during flood and 14 PSU during ebb. In a lab experiment, Mariotti, Valentine, and Fagherazzi, 2015 found that after repeated "tidal" cycles, the resuspended material formed larger flocs and decreased the erodibility of the bed. They also found that extended exposure to shear stress increased the pool of eroded sediment over time. These suggest that the dynamics at play in muddy environments can be unsteady and the nature of cohesive sediment erodibility can change on tidal and longer timescales.

Such temporal variation can yield different responses in different locations. Wiberg, Law, Wheatcroft, Milligan, and Hill, 2013 saw no spatial or temporal variation in bed erodibility for the first 12−month period of an experiment on mudflats in a meso-tidal channel-flat region. During the second winter season however, they found an increase in erodibility in the channel. They concluded that seasonal variation in sediment supply and bed consolidation led to this temporal and spatial fluctuation.

Numerical models of sediment transport often include a linear model for sediment erodibility, such as equation 3.2, but rarely allow for temporal variation. Brand et al., 2015's model in South San Francisco Bay set a more erodible bed during winter than summer. Measure-

ments herein show the temporal variation of sediment erodibility in a muddy environment, focusing on the under-explored seasonal and spring-neap scales. An exploration of temporal and spatial variation suggests possible controlling factors. Quantifying this variability can guide the development of numerical models for sediment transport.

3.2.3 Settling Velocity

Settling of non-flocculated materials is rather straightforward: the settling rate generally increases with increasing particle size and density, and adjusts with changing shape (Dietrich, 1982). For flocculated sediment however, settling velocity is more challenging, as particle size, density, and shape can all change on short timescales. In particular, work towards characterizing floc settling velocity focuses on the processes controlling floc aggregation and breakup. Aggregation occurs when particles collide and stick together. Breakup is induced when turbulence shears large particles apart, or when the intensity of collisions surpasses a threshold (K. Dyer & Manning, 1999).

In general, discussions of floc dynamics often characterize them as microflocs (< 160 μm) and macroflocs (> 160 μm) (A. J. Manning, 2001). Generally, macroflocs are less dense than micro flocs or primary particles, as they have large pockets of water surrounded by a small mass of particulate matter. Despite this, large flocs settle faster: the equation for particle settling velocity goes with diameter squared, but density to the first power.

Aggregation and breakup, the controls on floc size, can be affected by physical processes such as concentration, turbulence, salinity, and pH, as well as biological processes. With higher concentration of suspended matter, particles have more of a chance to collide, leading to larger flocs and faster settling. Turbulence can either yield increases or decreases in floc size. Turbulence, as well as Brownian motion and differential settling, can cause small particles to collide, yielding larger flocs if they stick together (Burd & Jackson, 2009; K. R. Dyer, 1989). At high turbulence levels on the other hand, the size of flocculated particles can exceed the size of small turbulence scales like the Kolmogorov lengthscale, leading to shearing and breakup of flocs (Winterwerp, 1998; Verney, Lafite, Claude Brun-Cottan, & Le Hir, 2011), and most work on flocs in estuarine environments has found that this mechanism dominates (Hill, Newgard, Law, & Milligan, 2013; Safak, Allison, & Sheremet, 2013; Yang et al., 2016; Schwarz et al., 2017). For example, smaller flocs were more dominant lower in the water column in the saline Atchafalaya Bay, showing how bottom-shear-driven breakup can be more important than sorting of particles by settling (Sahin, Ari Guner, Ozturk, & Sheremet, 2017). Other work has found that floc size increases with increased salinity (R. B. Krone, 1962), in particular when salinity transitions from 1 to 15 ppt. At these higher salinities, particles are more likely to adhere after a collision. Finally, floc size can decrease with increasing pH (Mietta, Chassagne, & Winterwerp, 2009). The balance between these controls on floc size can be highly site and condition dependent.

While many studies have found that floc size and settling velocity increase with decreasing turbulence, the opposite result was observed in San Francisco Bay (A. Manning & Schoellhamer, 2013). This spatial survey showed that settling velocity increased 39 min after

an increase in tidal velocity. They suggested that slack tides allowed faster-settling flocs to deposit, while such flocs were kept suspended in the water column by current induced turbulence during high flows. Given that floc characteristics largely do not change throughout the Bay (Ganju, Schoellhamer, Murrell, Gartner, & Wright, 2007), this suggests that floc dynamics in San Francisco Bay may differ from those in other water bodies.

The controls on floc size can change with time. Verney et al., 2011 and Markussen and Andersen, 2014 found hysteresis during a tidal cycle in lab and field experiments, respectively. Markussen and Andersen, 2014 showed that large flocs formed during decelerating tides when shear decreased below 1 s^{-1}, but they persisted during accelerating tides until a threshold of 4 s^{-1}, suggesting that time allowed flocs to bond more and become more resistant to breakup. On a spring-neap cycle, Hill et al., 2013 found an order of magnitude lower suspended particle concentrations during neap tides, along with less resuspension and less floc transport from the channel to adjacent flats. A summertime increase in transparent extracellular polymers and decrease in water column mixing allowed the formation of larger flocs and a stronger vertical gradient of flocs in the water column (Fettweis & Baeye, 2015).

Measuring floc size or settling velocity for real systems remains challenging, as flocs cannot be removed from their environment and accurately measured. The Laser In Situ Scattering and Transmissometry (LISST) uses a "multi-angle optics" technique to characterize particle size in the water column by emitting a single-frequency laser, and detecting the scattering of the beam by suspended particles (Agrawal & Pottsmith, 2000). An acoustic doppler velocimeter (ADV) measures implicitly the acoustic backscatter in the water column, allowing a characterization of the total suspended sediment concentration. With high-frequency measurements of acoustic backscatter and vertical velocity, the instrument yields the vertical turbulent flux of suspended sediment, $\overline{w'C'}$. If horizontal advection and temporal change of sediment are negligible, a single ADV can yield a measure of particle settling velocity, w_s, as (Fugate & Friedrichs, 2002; Cartwright, Friedrichs, & Smith, 2013)

$$w_s = \frac{\overline{w'C'}}{C - C_{wash}} \tag{3.6}$$

where a background "washload" concentration, C_{wash} is removed from the total concentration, C, following the modification from Cartwright et al., 2013. This washload is assumed to be composed of small, non-settling particles that do not contribute to a vertical gradient in suspended material. As noted above, this technique requires sediment to be both steady in time and constant laterally, relative to particle settling. In a location with slow settling velocities and large possible gradients, this assumption may not always be true.

Floc size remains poorly understood and characterized, and important for numerical studies. When settling velocity was halved in a numerical model, events with high SSC lasted days longer (Jordi, Basterretxea, Casas, Angles, & Garces, 2008). With this work, we investigate the balance between resuspension, flocculation, de-flocculation, settling, and deposition on tidal timescales, identifying a shift in floc dynamics between spring and neap frames. This detail of floc dynamics can help guide and refine numerical models of suspended sediment transport.

3.2.4 Site Description

San Pablo Bay is a sub-embayment of San Francisco Bay, located downstream of the Sacramento and San Joaquin Rivers. These rivers traverse the bay through a single main channel, which ranges from $11 - 24$ m deep with a mostly sandy bed. The main channel flows out to Central San Francisco Bay at the southern end of the Bay. Two smaller rivers, the Petaluma River and Sonoma Creek, flow in to San Pablo Bay along its northern edge. The remainder of the Bay consists of a large shoal of 190 km^2 to the north, which is less than 4 m deep and mud-dominated, and a similar southern shoal of 43 km^2. During low tide, mudflats are exposed along the margins of the Bay. Tides are mixed semi-diurnal; the tidal range in San Pablo Bay is as large as 2.5 m during spring tides, and only 1 m during neap tides. Lower-low water often follows higher-high water, resulting in an ebb-dominated system (R. Cheng & Gartner, 1984). Tidal currents can reach up to 1.5 m/s within the channel; they diminish on the mudflats (D. H. Schoellhamer et al., 2008). Tidal resonance within San Francisco Bay yields a net north-south circulation between San Pablo Bay and South Bay (R. Krone, 1979).

The Mediterranean climate of Northern California yields a generally dry summer and wet winter. Salt from the Pacific Ocean encroaches up to Suisun Bay during the summer months, but is often limited to San Pablo Bay during wetter winters (Conomos, for the Advancement of Science, & of Limnology and Oceanography, 1979). During these winter periods, water levels are elevated and sediment transport is larger (Monismith, Kimmerer, Burau, & Stacey, 2002).

Waves in San Pablo Bay are generally locally-generated and wind-driven with limited fetch, and significant wave heights have been measured as high as 0.6m with a 4−second period at a depth of $5 - 6$ m MLLW (D. H. Schoellhamer et al., 2008), and up to 0.5 m with a 3.5−second period at 1 m MLLW (MacVean & Lacy, 2014). Because wave periods are so small, wave orbital velocities interact with the bottom only at the shallowest parts of the Bay; for a 2 second wave period, the wave orbital velocity impacts the bed at water depths of 3 m or less. Summer winds in San Francisco Bay are commonly north-westerly, coming in to San Pablo Bay from the south, and diurnal, strongest in the afternoon, as described by Hayes, Kinney, and Wheeler, 1984. These daily onshore breezes during the spring and summer generate waves in the shallow shoals, and create an environment for sediment transport (R. Krone, 1979). Winter winds are more varied, and can include southerly cold fronts that last for multiple days (Hayes et al., 1984).

Over the last 150 years, sediment loads have changed dramatically in the San Francisco Bay-Delta, including San Pablo Bay. Hydraulic mining in the Sierra Nevada mountains released large amounts of sediment; a quarter billion cubic meters of gold mining debris accumulated in San Pablo Bay in the mid-late 1800's, reducing the depth by 0.85 m (van der Wegen & Jaffe, 2014). Towards the end of the 19th century, hydraulic mining stopped and dam construction began, and sediment supply to the Bay decreased dramatically (S. A. Wright & Schoellhamer, 2004). By the late 1900's, intertidal flats attached to Bay edges narrowed and shoals and channels deepened. More sediment was lost out to sea than entered

the Bay thanks to the rivers (van der Wegen & Jaffe, 2014). Marsh areas once open are now closed off, and they no longer accumulate fine sediments or reduce its loss to the ocean (R. Krone, 1979).

Currently, the largest sediment supply to San Pablo Bay comes from the Carquinez Strait (0.76 Mt/year), with other supplies from local tributary streams (0.28 Mt/year), net erosion off the bottom of San Pablo Bay (0.45 Mt/year), and net import of dredged material (0.04 Mt/year). Sediment is lost to deposition on tidal marshes (0.08 Mt/year) and seaward into Central Bay (1.45 Mt/year) (D. H. Schoellhamer et al., 2008). Thus, the sediment shoals are increasing, thanks to resuspension and deposition by locally generated wind waves (van der Wegen & Jaffe, 2014). However, sediment concentration in San Francisco Bay as a whole appears to have recently transitioned from a transport-controlled process to supply-controlled, as evidenced through a rapid clearing of waters in 1999 (DavidH. Schoellhamer, 2011). Thus, if sediment supply to San Pablo Bay continues to decline, the bay may eventually succumb to margin erosion (van der Wegen & Jaffe, 2014).

Sediment is carried in to San Pablo Bay during the winter wet season, and R. Krone, 1979 suggests that it is winnowed and redistributed by tides during the summer dry season. The summer sediment bed is coarser and less erodible, indicating that it has been reworked and redistributed since winter storms deposited the fresh material (R. Krone, 1979). The idea of a more erodible sediment bed in winter may support the observation of higher SSC during winter winds than during equivalent summer conditions (D. H. Schoellhamer et al., 2008). Alternatively, D. H. Schoellhamer et al., 2008 suggest that a difference in wind direction, which affects the fetch, could yield the observed SSC difference between winter and summer, and the question remains currently unresolved.

On a tidal and wind-event timescale, sediment movement in San Pablo Bay occurs due to tides, winds, water level, and their interaction. MacVean and Lacy, 2014 found that tides are not a primary factor in controlling sediment resuspension from the bed in the shoals. Rather, waves are the principle factor controlling resuspension, while current-generated turbulence plays an important role in vertical mixing. Shallower waters see higher concentrations of sediment, since resuspension at the range of depths is similar but the shallower water column means that sediment is less diluted. At a deeper part of San Pablo Bay where waves were too small to resuspend sediment locally, advection played a role in yielding high local SSC (D. H. Schoellhamer et al., 2008). Here, increased river outflow from the Delta did not appear to affect local SSC. Throughout San Pablo Bay, the magnitude and direction of sediment fluxes onto and off of the shoals depend on the interactions of wind waves, tides, sediment supply, and water level, as well as the spring/neap cycle and the timing of wave events relative to water level and current direction.

The current conceptual model of sediment transport indicates that sediment enters the Bay during large winter and spring flows, and is redistributed throughout the bay by tidal and wave-driven processes (D. H. Schoellhamer et al., 2008).

3.2.5 In this paper

This work focuses on tidal, spring-neap, and seasonal scale measurements of bottom roughness (section 3.4.2), bed erodibility (section 3.4.3), and settling velocity (section 3.4.4) in San Pablo Bay. We suggest possible indicators for change in the observed parameters, and provide values for use in numerical models of San Francisco Bay as well as similar high-energy, muddy, estuarine environments.

3.3 Methods

3.3.1 Data Collection

From November 2013 through April 2015, and again in May and June of 2016, we deployed oceanographic instrumentation in San Pablo Bay (table 3.1, figure 3.1). The sites were located at 1 and 2 m MLLW, as noted by the second character in the site names, eg. M1T was located at 1 m MLLW, while M2T was at 2 m MLLW. When instruments functioned fully, we collected velocity, salinity, temperature, depth, and suspended sediment concentration (via optical and acoustic backscatter) information. On occasion, an ADV was not deployed or it malfunctioned. In those cases we report CTD data only.

The deployed ADVs sampled at 10 Hz, collecting 2100 points in 3.5 min every 15 or 20 minutes, gathering turbulence, waves, and mean flow information. We used both ocean and field Sontek ADV probes, which have samples volumes at 0.18 and 0.1 m from the probe head, respectively. In all cases, we oriented the sample volume near 0.3 mab.

Each ADV was deployed with an external OBS sensor, collecting optical information on suspended sediment concentration at 0.3 mab. In many cases, growth accumulated on the instruments during the deployment, artificially elevating the optical backscatter. We therefore deleted optical data after about 1 month into each deployment. We used a calibration between grab samples for suspended sediment concentration, optical backscatter, and acoustic backscatter to give continuous measurements of suspended sediment concentration, as described in section 3.3.2. The ADVs were also deployed with an external pressure sensor, which was used, along with the high frequency velocity data, to calculate wave statistics.

The deployed CTDs collected information every 5 minutes, on salinity, temperature, depth, and occasionally optical backscatter.

Because some of the deployed ADVs did not perform during the CHC16 deployment, we predicted tides and tidal currents from harmonic components of the observed tides at previous periods using T-Tide (Pawlowicz, Beardsley, & Lentz, 2002). This yielded velocity and pressure data at site M2T during CHC16, which we applied for the particle size analysis, section 3.4.4. Comparing measured depth with T-Tide generated depth, we find that the reproduction approximated actual results in a reasonable fashion (figure A.1).

We use these predictions to yield approximate estimates of tidally derived quantities. In particular, we generated u_* during CHC16, using the fit $u_* = 0.0598|U|$ based on CHC13 and CHC14 data at M2T. This allowed an estimate of $\tau(z)$ (3.8) and τ_{bcw} (3.9). For equation

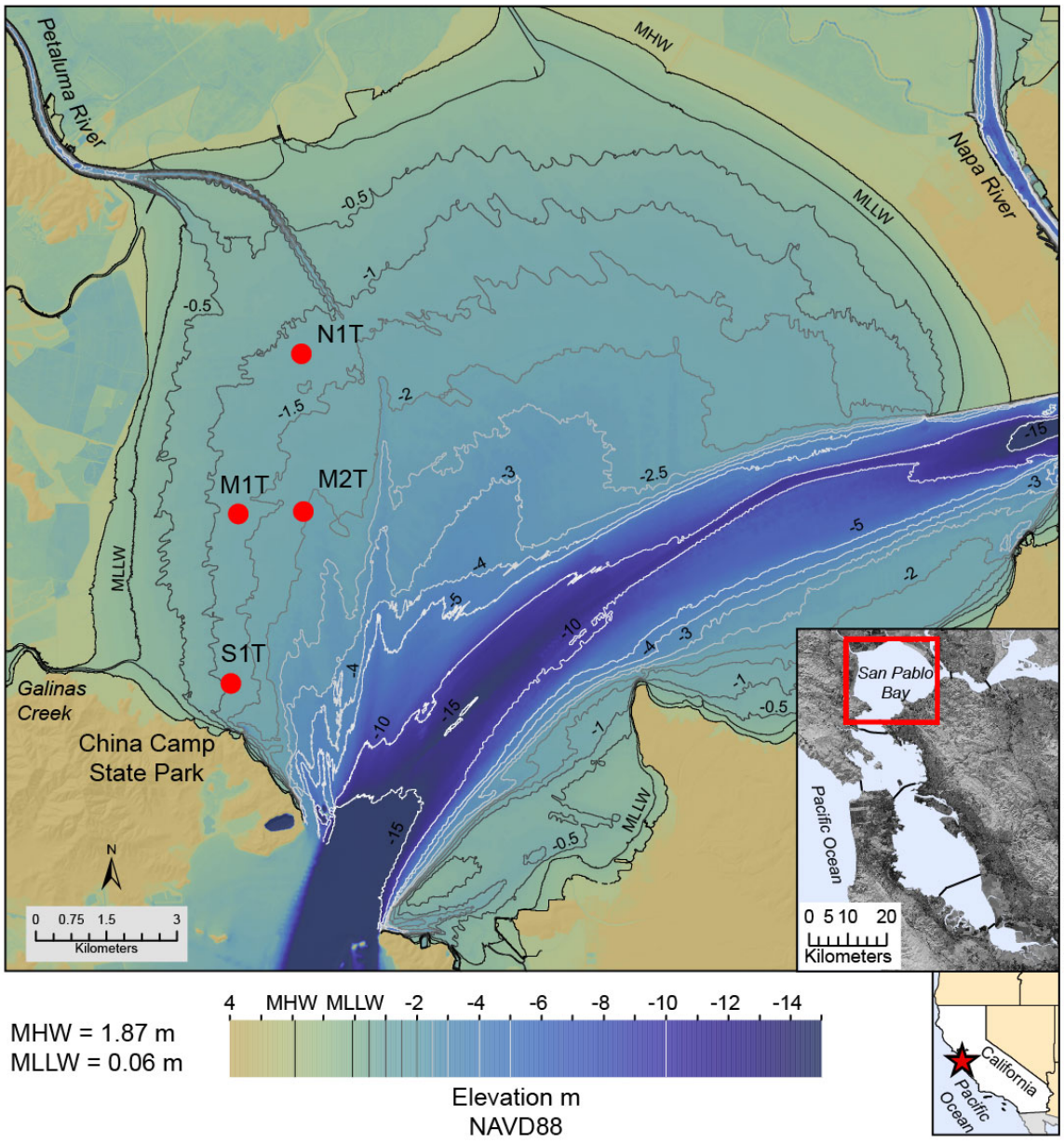

Figure 3.1: Bathymetry of San Pablo Bay relative to NAVD88 with the stations from this experiment. The insets in the lower right show San Pablo Bay within the San Francisco Bay system and the location of San Francisco Bay (star) in California.

3.9, we allowed the angle between currents and waves, ϕ, to be both 0° (aligned) and 90° (cross), producing the extremes of τ_{bcw}. The cross-current generated τ_{bcw} was between 70 and 100% of the aligned-current generated τ_{bcw}.

We also use T-Tide to compute the spring-neap cycle for each site: from the T-Tide yielded water level, the tidal range was obtained by the difference between high water and the following low water. In this strongly semi-diurnal environment, a strong ebb (large tidal range) was immediately followed by a weak ebb. Spring and neap tides were defined by the strongest tidal range in a 24−hour period. Using T-Tide for this metric allowed us to control for slight variations in instrument placement.

3.3.2 ADV calibration to SSC

Suspended sediment concentration (SSC) can be determined from an ADV by calibrating acoustic backscatter against conventional SSC samples (Fugate & Friedrichs, 2002; George Voulgaris & Meyers, 2004; Brand et al., 2010). We used a two-step process to yield high time resolution SSC data. First, we calibrated optical backscatter from the OBS to conventional grab measurements of SSC (figure 3.2). Second, for each ADV and deployment, we calibrated the acoustic backscatter from ADV (amp) to the optical-backscatter-derived SSC (SSC_o), by computing a least-squares fit to $\log_{10}(SSC_o) = m * amp + b$. The calibrated acoustic backscatter was then used to give continuous measures of SSC for this study.

Occasionally, the acoustic backscatter quality declined but the optical backscatter remained high. In these cases we stopped after step (1), and used the optical-backscatter-derived SSC.

3.3.3 Wave-Turbulence Decomposition and Bed Shear Stress

The Reynolds stress, $\rho\overline{u'w'}$, reflects the shear stress exerted in the water column by the fluctuating component of turbulent velocities. From the Reynolds stress, the friction velocity, u_*, is defined as

$$u_*^2 = \sqrt{\overline{u'w'}^2 + \overline{v'w'}^2} \tag{3.7}$$

Computing the Reynolds stress requires removing the mean velocity and the oscillating wave velocity from the high-frequency measurements collected by the ADV.

We tested two primary methods for removing the wave stress from the Reynolds stress, one that involves removing the wave signal based on the frequency of wave motions (Bricker & Monismith, 2007), and one that captures and removes the wave signal based on pressure measurements using the correlation between pressure and velocity, from Shaw and Trowbridge, 2001 and Feddersen and Williams, 2007. Wave motions contaminated the measured stresses between approximately 0.2 and 0.8 Hz, corresponding to wave periods of 1.25 to 5 s. Pressure measurements during this deployment were imperfect, leading to artificially low H_{rms} when measured by the pressure sensor for a number of deployments (figure A.2). However, even though at times the scale of pressure measurements was wrong, the Feddersen and

Site	instrument	CHC13 Nov '13 - Feb '14	SPA Feb '14 - Jun '14	SPB Jun '14 - Sep '14	SPC Sep '14 - Dec '14	CHC14 Dec '14 - Feb '15	SPD Feb '15 - Apr '15	CHC16 May '16 - Jun '16
N1T 38.076°, −121.447°	Sontek ADV	0.305	0.30	0.30	0.33	0.295	0.335	–
	OBS	0.305	0.29	0.30	0.30	0.3	0.33	–
	RBR CTD	0.88	0.89	0.87	0.925	0.79	0.59	0.60
	Paroscientific Pressure	0.32	0.30	0.35	0.34	0.38	0.50	–
	RBR Bursting Pressure	–	–	–	–	1.31	–	–
M1T 38.046°, −122.463°	Sontek ADV	0.315	–	–	–	–	–	–
	OBS	0.3	–	–	–	–	–	–
	Seapoint SS	0.71	–	–	–	1.01	–	–
	RBR CTD	0.86	–	–	–	1.11	–	–
	Paroscientific Pressure	0.375	–	–	–	–	–	–
M2T 38.046°, −122.447°	Sontek ADV	0.31	–	–	–	0.30	–	–
	OBS	0.305	–	–	–	0.3	–	–
	Seapoint SS	–	–	–	–	–	–	0.49
	RBR CTD	–	–	–	–	–	–	0.30
	RBR CTD	0.95	–	–	–	0.56	–	1.40
	Seabird CTD	0.66(bs)	–	–	–	–	–	0.84(bs)
	Paroscientific Pressure	1.09	–	–	–	0.97	–	0.97
	LISST	–	–	–	–	–	–	0.50
S1T 38.013°, −122.465°	Sontek ADV	0.29	0.30	0.30	–	0.315	0.285	0.32
	OBS	0.295	0.29	0.30	–	0.30	0.29	0.33
	RBR CTD	0.91	0.87	0.90	0.97	0.91	0.90	0.50
	Paroscientific Pressure	0.36	0.35	0.35	–	0.36	0.375	0.32

Table 3.1: Summary of instrumentation. Site locations are listed under the site name, as shown in figure 3.1. Instrument type and brand are listed, and numbers indicate the elevation of the sampling volume above bed (m) when they were deployed. Instruments that were moored at some distance below the surface are listed as (bs). Deployments were run sequentially with the exception of CHC16, which occurred about 1 year after the completion of SPD. All data is released under Jessica R. Lacy, Allen, Foster-Martinez, Ferreira, and O'Neill, 2017

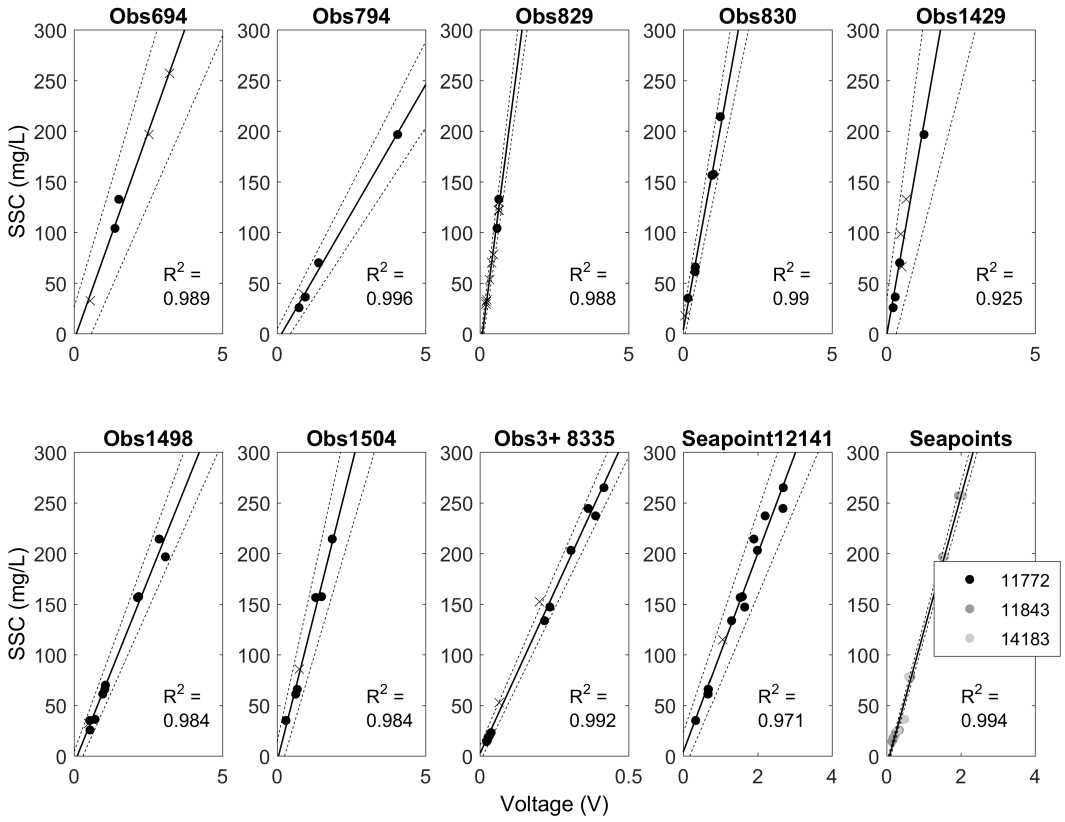

Figure 3.2: Calibration of OBS backscatter (V) to SSC (mg/L). Solid circles reflect "OOM" samples, when the OBS instruments were carried to random locations through San Pablo Bay and SSC grabs were taken at the same location and time. x's indicate when the OBS instruments were deployed at their site and SSC grabs were collected during that period at the same location. Each subfigure shows an independent calibration, and the R^2 for each fit is given in the lower right of each subfigure. For Seapoints 11772, 11843, and 14183, error analysis indicated that the calibration was more robust with all three instruments calibrated together than independently, suggesting that the response of these instruments was similar. No in-situ data were collected for Seapoints 11772, 11843, and 14183. For the remaining instruments, a better fit between backscatter and SSC was achieved when instrument-specific calibration was performed.

Williams, 2007 method worked well because it fit pressure to velocity on a burst-by-burst basis. Thus, even when pressure measurements underwent a shift, eg mid-day on Feb 8, 2014 at site N1T, (figure A.3a), the scaling of pressure meant that both the Bricker and Monismith, 2007 and Feddersen and Williams, 2007 methods identified similar stresses (figure A.3b), both methods removed the wave signal from the along-flow velocity (u) during the artifically-low pressure (figure A.3c) and normal pressure (figure A.3d) periods, and both methods resulted in no contribution to the measured stress from correlated motions in the wave frequency band during both periods (figures A.3e and f). Given that the pressure errors do not affect the computed Reynolds stress, we selected the Feddersen and Williams, 2007 method for computation of the Reynolds stress.

The shear stress due to currents, $\tau(z)$, is found from the measured Reynolds stresses, as

$$\tau(z) = \rho \left(\overline{u'w'}^2 + \overline{v'w'}^2 \right)^{1/2} = \rho u_*^2 \tag{3.8}$$

where the Reynolds stresses and friction velocity are found as described above.

We compute the bed shear stress due to waves as $\tau_{bw} = \frac{\rho}{2} f_w u_{br}^2$ (Wiberg & Sherwood, 2008, eqn 3). This relies on an estimate of the bottom orbital velocity, u_{br}, and the wave friction factor, f_w. The bottom orbital velocity is found from the spectra of horizontal measurements of velocity, following (Wiberg & Sherwood, 2008, eqn 11). In a laminar regime, the wave friction factor depends on the wave Reynolds number Re_w only, as $f_w = 2Re_w^{-0.5}$. The wave Reynolds number is $Re_w = A^2\omega/\nu$, where $A = u_{br}T/2\pi$ is the near-bed wave amplitude, T is the wave period, $\omega = 2\pi/T$ is the wave angular frequency, and ν is the kinematic viscosity. During CHC16 at site M2T, the maximum observed Re_w was 6000, which is less than the transition from smooth laminar flow to a rough-turbulent regime at $Re_w = 3 \times 10^5$, indicating that our data were well described by smooth laminar conditions (Nielsen, 1992).

The root-mean-square wave height, H_{rms}, was calculated from both velocity and pressure data, following Wiberg and Sherwood, 2008. When both were available, we used the velocity-generated value, as it more accurately reflects wave parameters. However, for site M2T at CHC16, the ADVs did not record data, therefore we only have pressure generated wave statistics. When wave statistics were large ($H_{rms} > 0.2$ m), pressure and velocity measurements matched quite well, with less than 20% difference between the two methods on more than 90% of the data (based on CHC14 data from M2T). When wave statistics were small, the two methods matched less well, with the pressure data yielding smaller estimates of H_{rms} than the velocity data. Because the velocity and pressure measurement techniques matched well when wave energy was high, we accepted the wave statistics H_{rms} and u_{br} from pressure measurements at M2T during CHC16.

With both the bed shear stress from waves and the shear stress from currents in hand, the combined bed shear stress is found as

$$\tau_{bcw} = \sqrt{\left(\tau_{bw} + \tau(z)\cos\phi\right)^2 + \left(\tau(z)\sin\phi\right)^2} \tag{3.9}$$

(Nielsen, 1992), where ϕ is the angle between currents and waves.

3.3.4 Bottom Roughness

The bottom roughness (z_0) was computed from the shear stress from currents ($\tau(z)$, equation 3.8). Shear stress at the measurement location, $\tau(z)$, was used to calculate the shear stress at the bed, τ_b, via $\tau(z) = \tau_b(1 - \frac{z}{h})$, where z was the ADV height above the bed measured each burst and h was the total water depth. We then computed the friction velocity at the bed, u_{*cb}, from $\tau_b = \rho u_{*cb}^2$. Finally, the bottom roughness, z_0, was found from the law of the wall (Jessica R. Lacy & MacVean, 2016), using the measured value for $u(z)$ and the precisely defined u_{*cb} for u_* (equation 3.3).

To ensure that the z_0 calculation was not contaminated by waves, we removed data when there were strong waves, $u_{br} > 0.05$ m/s. Estimating that equation 3.3 only holds in the bottom 1/5 of the water column, we removed data when $h < 5z$. Bed roughness values come out anomalously high when current was weak, because there was not a fully developed turbulent boundary layer. These values were filtered out by discarding data when u_* fell below a threshold set between $0.003 - 0.01$ m/s, and tuned by eye to maximize data for each deployment. We do not remove data due to periodic salinity stratification, as it did not change the bulk statistics. Finally, we removed flow in certain directions to avoid contaminating measurements of u_* when frame wakes could intersect the measurement volume.

To assess temporal variability in bottom roughness in San Pablo Bay, we computed the 4-day median bottom roughness (figure 3.8). This subsetting included 30 to 280 points per period, after filtering.

3.3.5 Bed Erodibility

To capture the change in bed erodibility, we evaluated m and τ_{crit} through the turbulent sediment flux, $\langle w'c' \rangle$, and the bed shear stress, τ_{bcw}, through a slightly modified version of equation 3.2:

$$\langle w'c' \rangle = m \left(\tau_{bcw} - \tau_{crit} \right) \tag{3.10}$$

Here, we assumed type II erosion and did not allow for variation with depth, that is, m and τ_{crit} were functions of time only. As Maa and Kim, 2002 and Mathew and Winterwerp, 2017 noted, measuring erodibility in the field is more robust on the accelerating portion of the flow, that is, during the beginning of the flood and beginning of the ebb. We therefore investigated equation 3.10 during the accelerating portion of the flood and decelerating portion of the ebb, with coordinates defined as positive in the on-shore direction. We also tested separating flood and ebb phases of the tide to determine if they eroded differently. Finding no significant differences between the flow directions, we included flood and ebb together in the subsequent analysis. Because we measured $\langle w'c' \rangle$ and τ_{bcw} at 0.3 mab, our measurement of $\langle w'c' \rangle$ does not reflect true erosion off the bed (E). Rather, it measures vertical turbulent transport of SSC at 0.3 mab, that is, mixing of eroded material higher in the water column. Thus, it is challenging to say when exactly the critical shear stress is surpassed, because we do not have measures of water column sediment concentration or flux close to the bed. Our

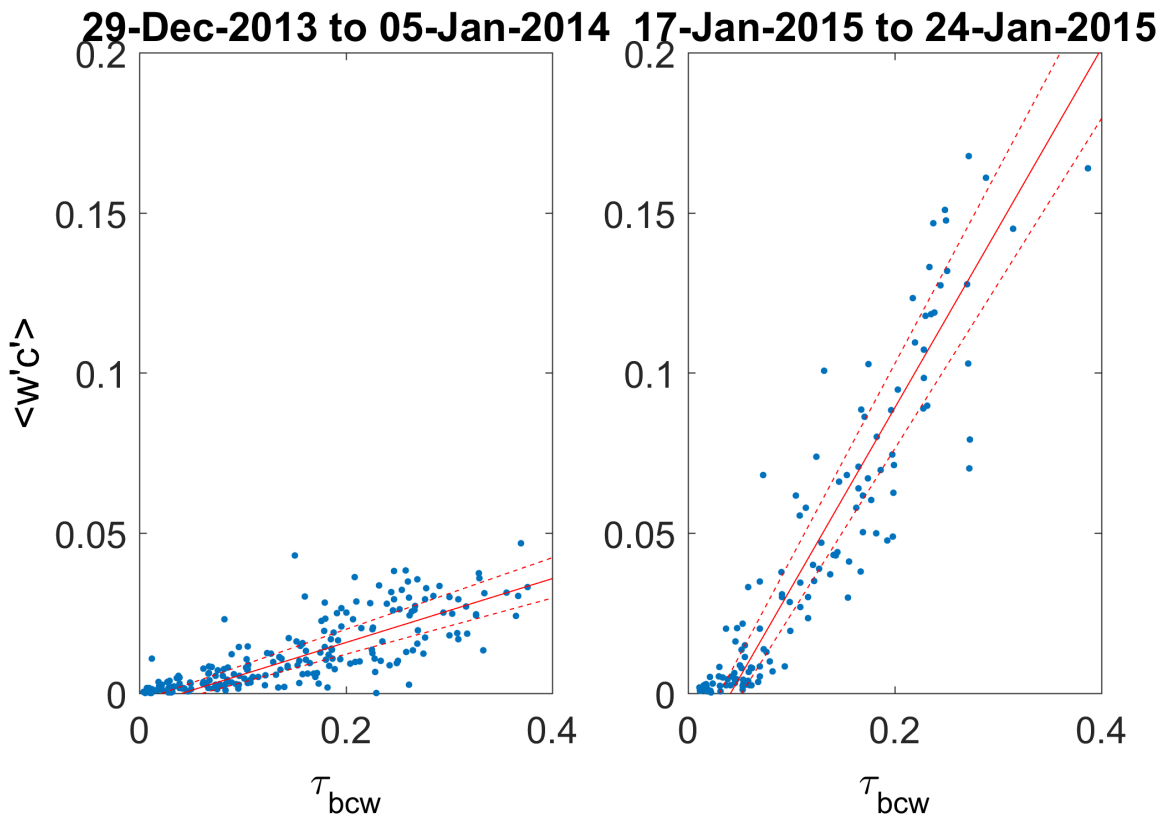

Figure 3.3: Computing erodibility at N1T during two 7-day periods, with data removed as described in section 3.3.5. The solid line shows the best fit assuming equation 3.10, and dashed lines show 95% confidence intervals. a) Dec 29, 2013 to Jan 5, 2014, $m = 0.100 \pm 0.012$, and $\tau_{crit} = 0.041 \pm 0.020$. b) Jan 17 to 24, 2015, $m = 0.561 \pm 0.046$, and $\tau_{crit} = 0.041 \pm 0.011$.

measurements of τ_{crit} and m are therefore water-column representations of the processes happening at the bed, rather than true measurements of bed processes.

We also removed τ_{bcw} during tidal periods when wave energy grew large, that is $u_{br} > 0.05$ m/s. This allowed us to investigate how much sediment is resuspended by tidal energy, and to remove the immediate effect of wave-enhanced resuspension. Figure 3.3 shows this computation for 7-day periods in winter $2013 - 2014$ and $2014 - 2015$ at site N1T. When erodibility was low (left), little sediment was resuspended given the applied bed shear stresses. During the next winter (right), more material was resuspended from the bed for an equivalent τ_{bcw}.

We computed m and τ_{crit} (with error estimates) for $7-$day periods overlapping at $2-$day intervals throughout the deployment, following equation 3.10. Each 7-day period contained up to 330 points from which we computed the fit, although fewer were available during windy periods.

3.3.6 Settling Velocity

For our preliminary analysis, we did not remove LISST data based on % transmission. Commonly, the optical transmission range is selected at 15% to 98% (e.g., Fettweis & Baeye, 2015; Schwarz et al., 2017). In our case, the LISST total concentration matched the SSC concentration quite well; we therefore accepted LISST data at % transmission below 15. All measured optical transmissions were below 80%, thus we required no upper limit.

We compute settling velocity, w_s, from the measured floc size analysis through the adapted Stokes' equation (Winterwerp, 1998), including the particle Reynolds number, Re_p:

$$\begin{aligned} w_s &= \frac{(\Delta\rho)g}{18\mu} D_p^{3-nf} \frac{D_{50}^{nf-1}}{1 + 0.15 Re_p^{0.687}} \\ Re_p &= \frac{w_s D_{50}}{\nu} \end{aligned} \tag{3.11}$$

using an interative technique to simultaneously solve for both w_s and Re_p. Here, $\Delta\rho$ (kg/m^3) is the effective density, computed as quotient between the optical backscatter measured SSC (kg/m^3) and the floc volume concentration from the LISST (m^3/m^3), for each 15 minute burst average, following Mikkelsen and Pejrup, 2001. The primary particle size, D_p, was computed from disaggregated sediment grabs from the bed. It remained constant at 8 μm across all deployments and all stations (figure 3.4, a). The fractal dimension of suspended particles, nf, was computed from the linear fit between $\Delta\rho$ and D_{50} as measured by the LISST (Mikkelsen & Pejrup, 2001). It was found to be 2.662 ± 0.028 (mean with 95% confidence bounds), consistent with fractal dimension of $2.2 - 3$ found in a San Francisco Bay transect (A. Manning & Schoellhamer, 2013). D_{50} is the median floc diameter measured by the LISST (m), μ is the molecular viscosity (kg/ms), and ν is the kinematic viscosity (m^2/s).

3.4 Results

3.4.1 Seasonal Climate

Maximum velocities reached 0.4 m/s at the 1 m MLLW sites, and 0.46 m/s at the 2 m MLLW site during spring tides. During neap periods, peak velocities were only 0.27 m/s at the 1 m MLLW sites, and 0.34 m/s at the 2 m MLLW site. During the spring periods, water levels ranged from 0.8 to 3.3 mab at the shallower sites and 1.9 to 4.4 mab at the 2 m MLLW site, while they were limited to 1.3 to 2.7 and 2.4 to 3.8 mab, respectively, during neap tides. Currents at all sites run in a generally NNW direction during flood tide, and opposite during ebb. At N1T, this parallels the direction of the narrow channel exiting the Petaluma River. Site M2T is nearly in line with N1T in the plane of tidal advection. At S1T, currents are directed more NW (flood)-SE (ebb) than the other sites, running parallel to the shore. During calm spring periods, suspended sediment ranged from 20 to 150 mg/L

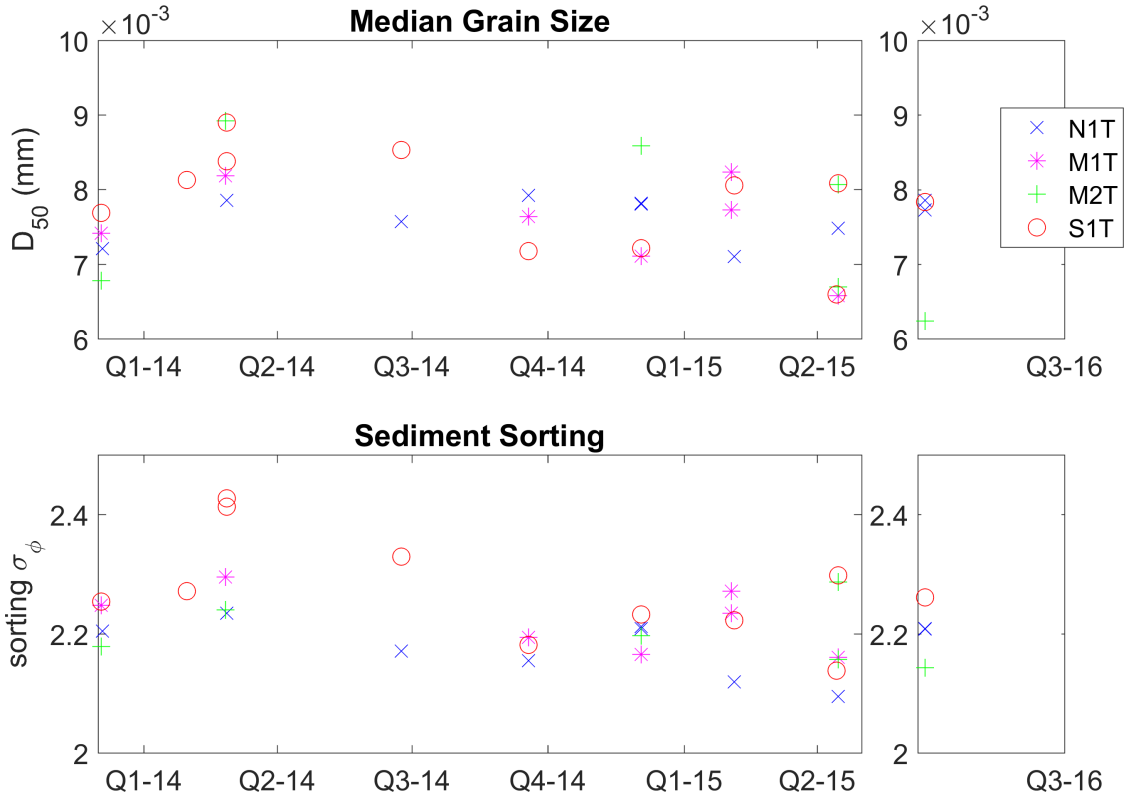

Figure 3.4: Primary sediment grain size from the bed at sites N1T, M1T, M2T, and S1T. (top) Median particle size (D_{50}(mm)) ranges between 6 and 10μm at all sites, during all periods. (bottom) Sediment sorting (σ_ϕ) ranges between 2 and 2.5.

at S1T and M1T, and up to 240 mg/L at the more exposed N1T. SSC was lower during calm neap periods, when it was limited to 10 to 100 mg/L at all sites. During windy periods, such as Dec 30, 2014 to Jan 1, 2015, SSC increased to 1100 mg/L at S1T, and 2000 mg/L at N1T.

Primary sediment grain size on the bed remained near 8 μm at all of the sites throughout the measurement periods (figure 3.4, top). Similarly, sediment sorting remained at $\sigma_\phi = 2 - 2.5$ (figure 3.4, bottom), where $\sigma_\phi = \frac{1}{2}(\phi_{84} - \phi_{16})$, and ϕ_{84} and ϕ_{16} give the grain size at 1 standard deviation above and below the mean (Inman, 1952).

During water years 2014, 2015, and 2016 when data were collected, California experienced below normal rainfall and river outflow conditions, based on the Dayflow model (California Department of Water Resources, http://www.water.ca.gov/dayflow/). 2014 and 2015 were critical water years in both the Sacramento and San Joaquin rivers, and 2016 was below normal in the Sacramento and dry in the San Joaquin. During water years 2014, 2015, and

2016, median daily flow between January 1 and April 30 was 43%, 22%, and 400% higher than summer flow, respectively. For comparison, median daily flow was 1010% higher during the winter of water year 2011, a wet year. Locally, the winter of $2013-2014$ had 12.54 in of rainfall in 42 days in San Francisco, $2014-2015$ had 18.19 in in 42 days, and $2015-2016$ had 23.26 in in 71 days (Null, 2018). These winters saw some of the longest periods of dry winter weather in San Francisco: the 43−day period of Dec 25, 2014 through Feb 2, 2015 was the longest recorded winter dry spell, based on data beginning in 1849, and the 32−day period from Dec 12, 2013 through Jan 8, 2014 was the 4^{th} longest period.

Figures 3.5, 3.6, and 3.7 show the measured tidal velocity, salinity, river outflow, and SSC during CHC13, CHC14, and CHC16. The $2013-2014$ winter was very dry, as demonstrated by the low river outflow in December 2013 and January 2014 (figure 3.5). During this dry period, salinity ranged from 24 to 29 PSU during a tidal cycle at S1T, and from 24 to 26 PSU at site N1T. The decrease in salinity in early February is a response to fresh water input. By summer 2014 salinity increased; at S1T it ranged between 26 and 30 PSU, and at N1T it increased to 26 to 28 PSU. The $2014-2015$ winter saw river outflow earlier in the season (in December 2014), and the lowest salinities measured during the deployment (figure 3.6). Then, salinity dropped to 10 to 20 PSU at S1T, and 6 to 13 PSU at N1T. Salinity was consistently lower at N1T than S1T, because it is farther from the main channel. At all sites, there were spring/neap fluctuations in the amount of suspended material.

3.4.2 Bottom Roughness

Bottom roughness (z_0) was between $4 \cdot 10^{-4}$ and $4 \cdot 10^{-6}$ m at all sites through all periods (figure 3.8), coarser than predicted by the sediment primary particle grain size.

3.4.2.1 Seasonal

The largest shift in bottom roughness was observed at site N1T during November 2014, in an order-of-magnitude smoothing of the bed (figure 3.9). During that winter, roughness remained high at sites S1T and M2T. Less dramatic changes were observed during winter $2013-2014$, where sites N1T, S1T, and M1T showed a small decrease in bed roughness over the season, and during summer 2014, where both N1T and S1T had slightly higher bed roughness than during the winter. While both $2013-2014$ and $2014-2015$ winters occurred during strong drought conditions (figures 3.5 and 3.6), this pattern suggests that winter allows for a smoothing of the bed, while a coarsening happens during spring and summer. The smoother bottom with a slow increase in roughness observed at S1T during CHC16 suggests that the wetter winter of $2015-2016$ yielded an even smoother bed, and summer conditions slowly allowed it to increase.

Bed-sediment grain size distributions show that primary particle grain size and the sediment sorting parameter did not change at either N1T or S1T over the data collection period (figure 3.4). In particular, the sediment grain size at N1T did not change during the de-

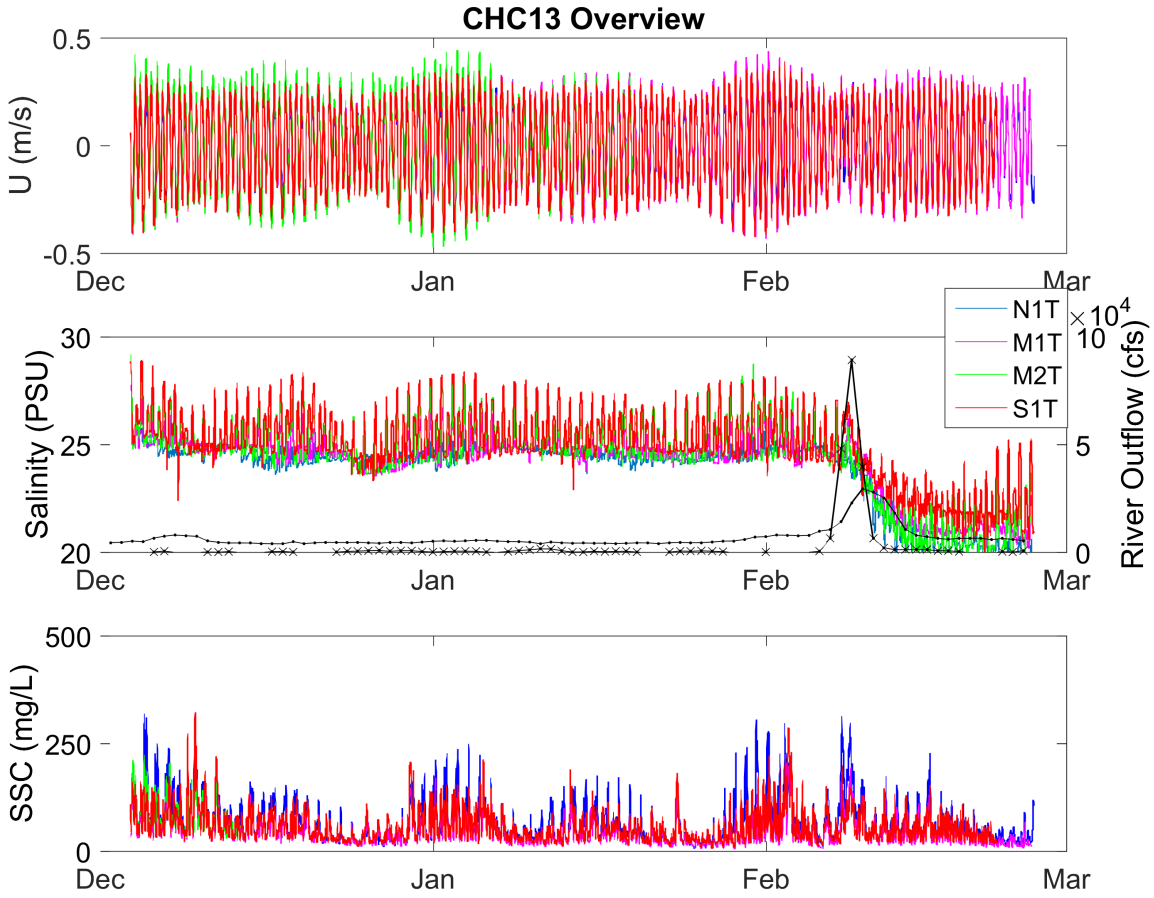

Figure 3.5: Conditions at sites N1T, M1T, M2T, and S1T during CHC13. Top: Velocity in flood (positive) and ebb (negative) directions. Middle: Salinity (left axis, colored lines) at each of the four sites, and river outflow from the Sacramento/San Joaquin Delta (right axis, solid black) and Petaluma River (right axis, x's). The Petaluma River is shown at 100-fold its measured outflow. Bottom: SSC at each site.

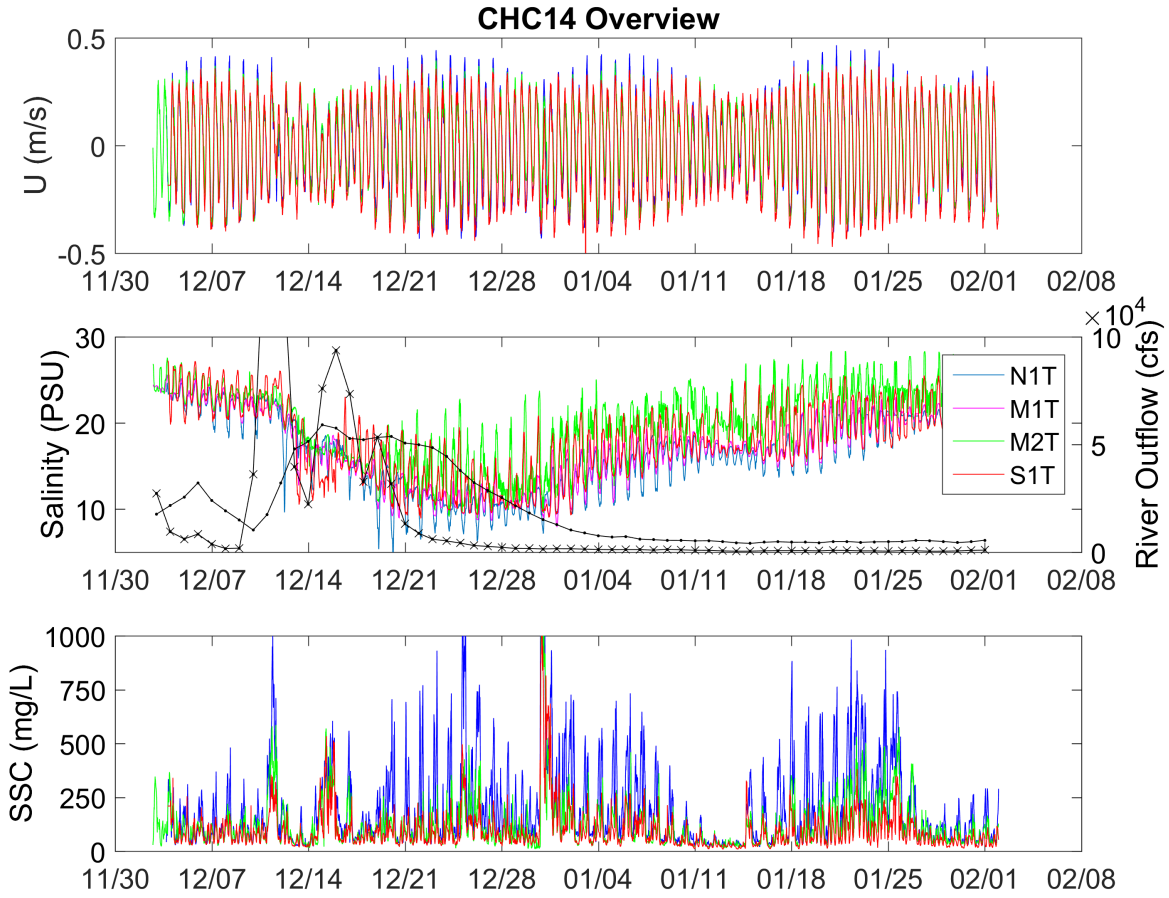

Figure 3.6: Conditions at sites N1T, M1T, M2T, and S1T during CHC14. Top: Velocity in flood (positive) and ebb (negative) directions. Middle: Salinity (left axis, colored lines) at each of the four sites, and river outflow from the Sacramento/San Joaquin Delta (right axis, solid black) and Petaluma River (right axis, x's). The Petaluma River is shown at 100-fold its measured outflow. Bottom: SSC at each site.

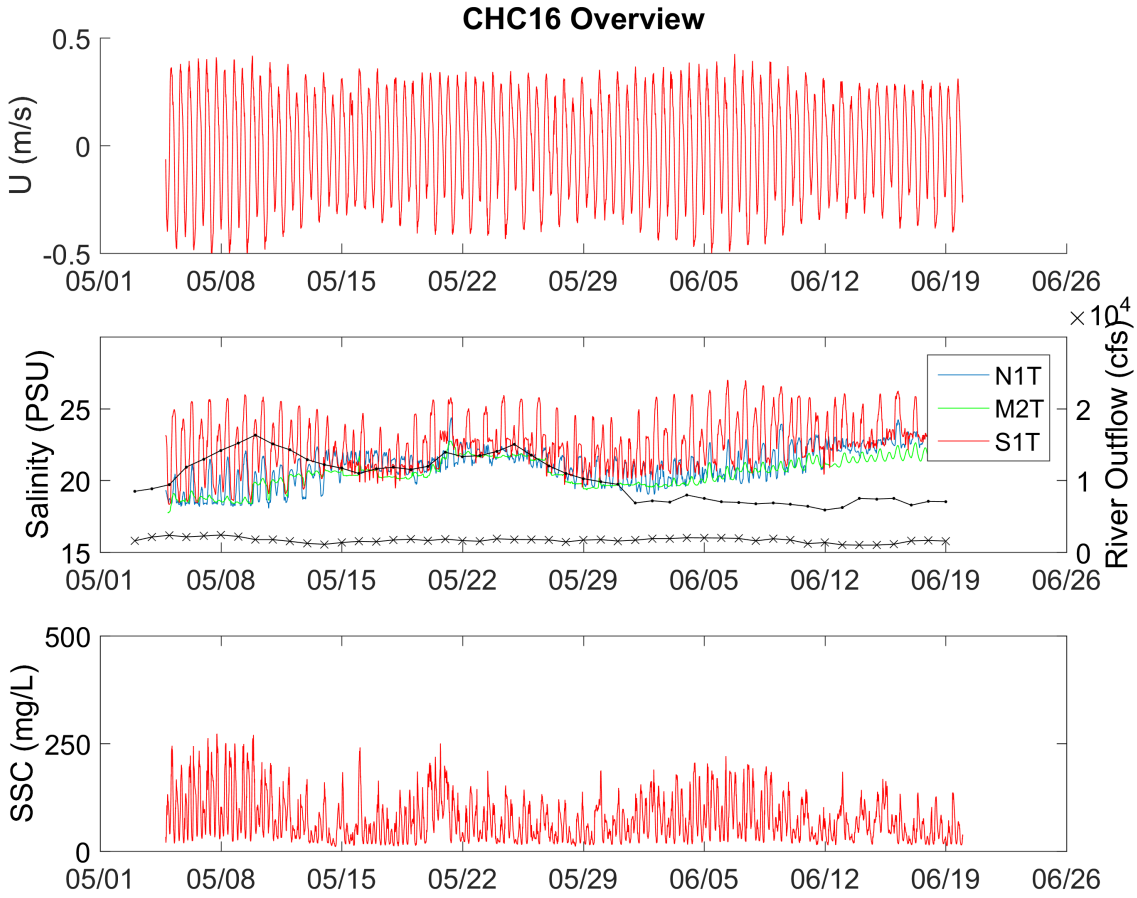

Figure 3.7: Conditions at sites N1T, M2T, and S1T during CHC16. Top: Velocity in flood (positive) and ebb (negative) directions. Middle: Salinity (left axis, colored lines) at each of the four sites, and river outflow from the Sacramento/San Joaquin Delta (right axis, solid black) and Petaluma River (right axis, x's). The Petaluma River is shown at 100-fold its measured outflow. Bottom: SSC at each site.

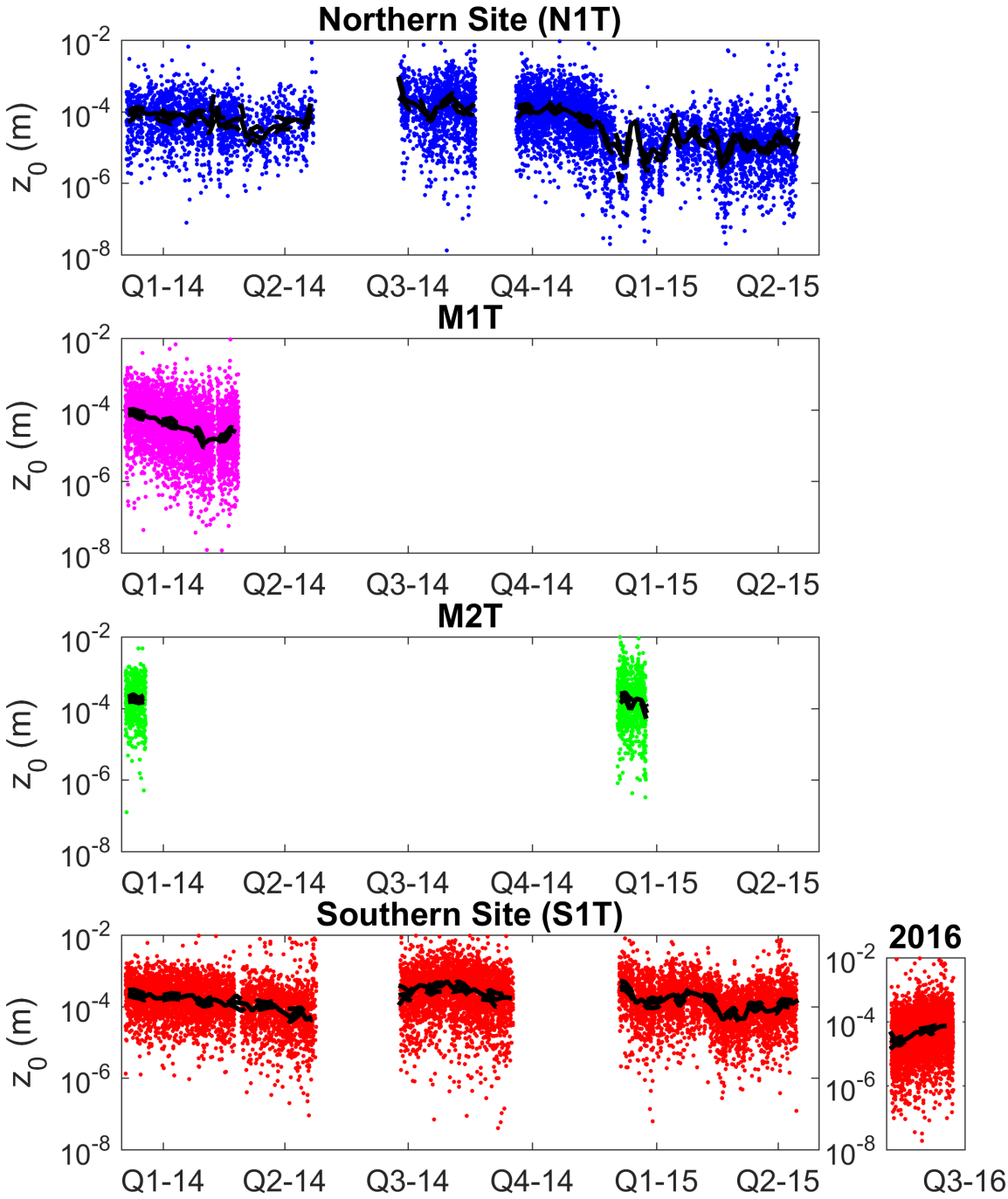

Figure 3.8: Filtered bottom roughness at sites N1T, M1T, M2T, and S1T. Data was filtered as stated in section 3.3.4. A 4-day median bottom roughness is shown for each site in black, with error bars computed as 90% confidence intervals via bootstrapping.

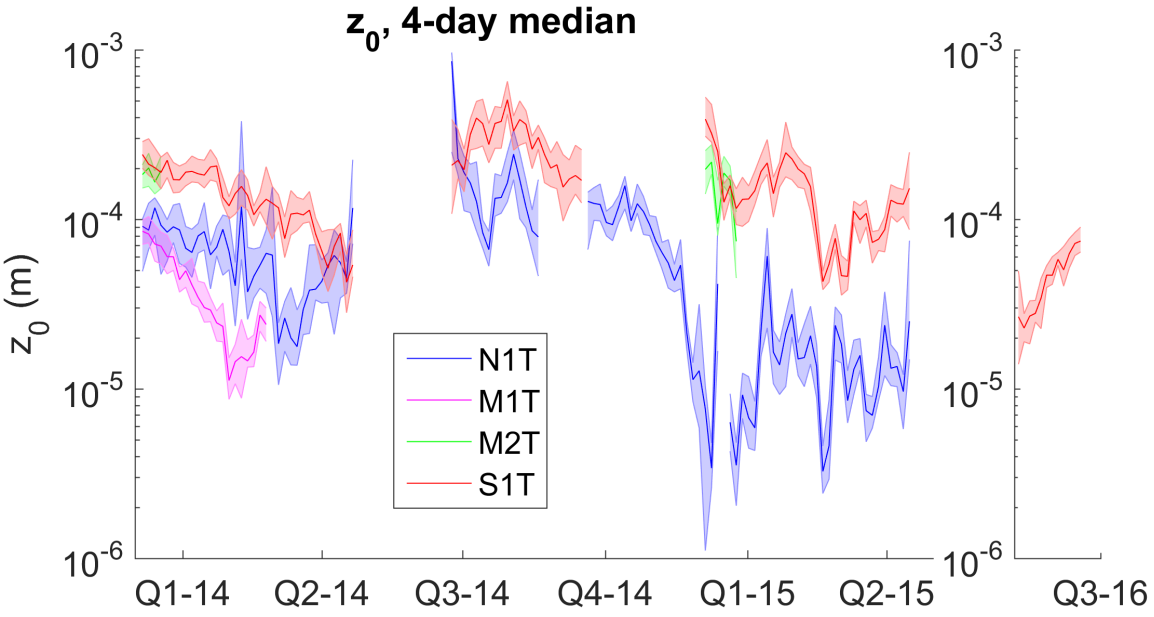

Figure 3.9: 4-day median bottom roughness shown for all sites, with shaded 90% confidence intervals. We note a smoothing of the bottom roughness at site N1T in late 2014.

crease in bed roughness of November 2014, suggesting that the smoothing is not due to new sediment with different grain characteristics.

The shift in bottom roughness at N1T during November 2014 occurred concurrently with a large wind-wave event (figure 3.10, top). A storm event such as this one may cause resuspension, and the flocs that settle on the bed following the event are reworked and the bed is smoother. While the event on November $17 - 19$ (figure 3.10, grey box) followed about a month-long period of low waves, it was by no means the largest such event to occur. However, it can be distinguished from other wind-wave events based on the direction of the storm. All prior large events during the deployments occurred with winds coming from 160 to 220°, that is, from the south, typical of spring, summer, and fall winds (Hayes et al., 1984). During this event, winds came from the northeast (figure 3.10), characteristic of northeasterly or southeasterly winds through the Bay and more typical during fall and winter (Hayes et al., 1984).

Previous work in San Francisco Bay supports the bottom roughness parameter values found in this work. In San Francisco Bay, Jessica R. Lacy and MacVean, 2016 find and Brand et al., 2015 apply in a numerical model a smoother bottom roughness in winter. With our work, we pinpoint the shift between a rough and smooth bed in November 2014, and note that it occurs concurrent with a winter storm.

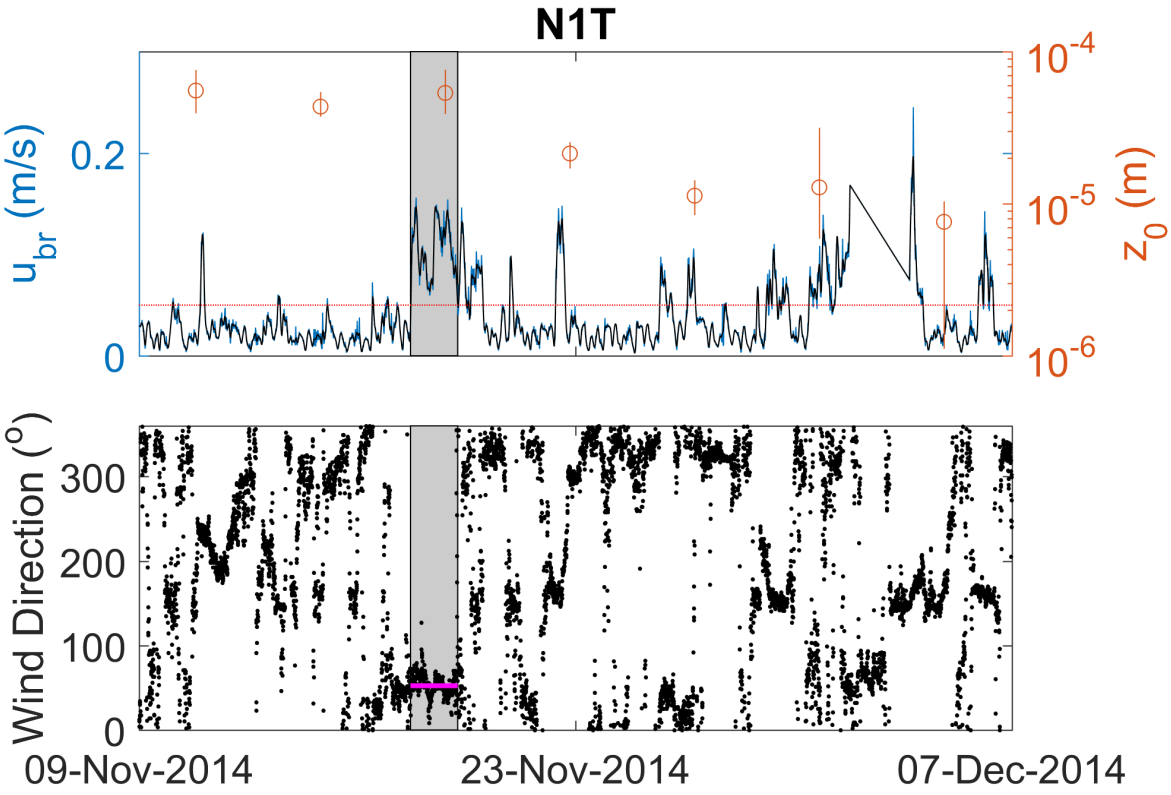

Figure 3.10: Top: Bottom orbital velocity (u_{br}, lines) and bottom roughness (z_0, circles) shown over about 30 days in November-December 2014. The black line shows the raw bottom orbital velocity smoothed to a 2-hour timescale. Error bars on bed roughness show the 90% confidence interval. A reference u_{br} is marked at 0.05 m/s. Bottom: Wind direction (°) over the same period collected at RCMC1, shown as the direction that wind is coming from. The grey box denotes the stormy period from November 17 to November 19. During that period, wind direction was consistent near 52°, shown in pink.

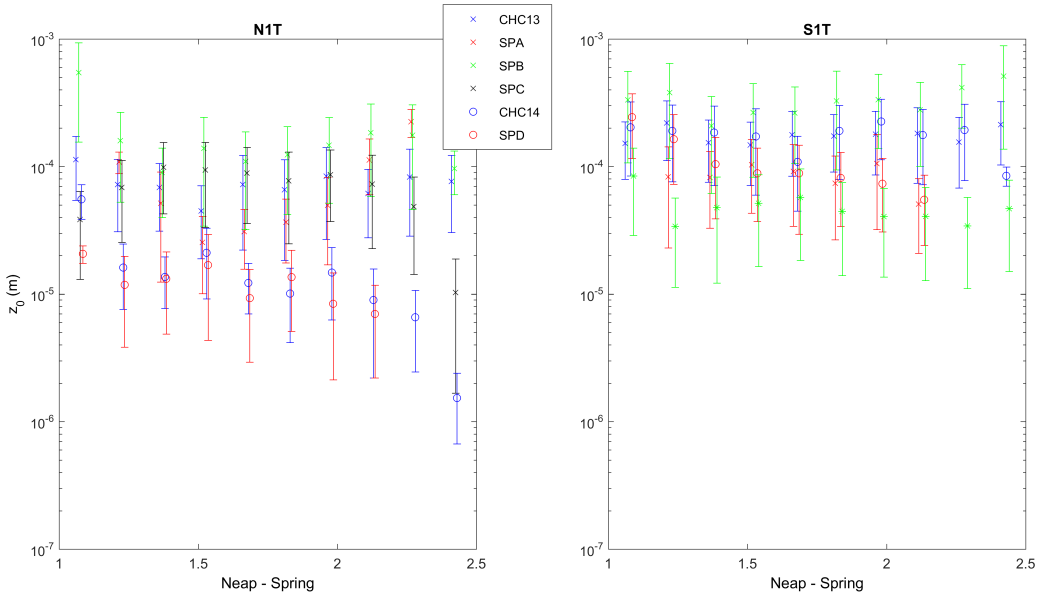

Figure 3.11: Bottom roughness during each season shown against spring-neap phase. Left: N1T. Right: S1T. Data were binned by spring-neap phase. The error bars show the 25 and 75 percentile data for each bin. We have offset slightly the spring-neap phase (computed as described in section 3.3.1) on the x-axis for visual clarity.

3.4.2.2 Spring-Neap

Bottom roughness varies with the spring-neap cycle at N1T after the seasonal shift occurs (figure 3.11, left). While bottom roughness remains constant over the spring-neap cycle through CHC13, SPA, SPB, and SPC, during spring tides of CHC14 and SPD roughness decreases, while during neap tides it increases. At S1T, bottom roughness does not change with the spring-neap cycle (figure 3.11, right).

3.4.2.3 Tidal

The tidal cycle yielded no effect on bottom roughness. This was expected since bottom roughness characterizes the bed; it should not fluctuate with the water-column property of tidal current velocity. While salinity varied through the tidal cycle, the lack of a tidal cycle signal on bottom roughness indicated that salinity also did not affect this parameter.

3.4.3 Bed Erodibility

Critical shear stress (τ_{crit}) varied little over the full data collection period, ranging between 0.02 and 0.15 Pa (figure 3.12, c,d). In particular, the relatively small fluctuations and high

error in critical shear stress indicate that discerning a change in critical shear stress over time or at different sites is not achievable through this approach.

Unlike τ_{crit}, the bed erosion constant (m) changes appreciably, and beyond its error estimates, throughout the deployments (figure 3.12, a,b). We therefore focus on fluctuations in this bed erosion constant, which we refer to as bed erodibility.

3.4.3.1 Seasonal

Bed erodibility is similar at all sites through most periods. It remains low during these times, although it increases at N1T and S1T during spring 2014. Bed erodibility diverges between N1T and S1T in December 2014-January 2015 and March 2015, suggesting that a site-specific forcing affects the bed's erodibility response. The increase in m at site N1T during this period mirrored the reduction in bed roughness there. However, while the bed roughness shift occurred in November of 2014 at N1T, the increase in erodibility did not begin until late December of 2014. These fluctuations suggest that both bay-wide and within-embayment processes affect bed erodibility.

The low erodibility seen during winter $2013-2014$, like the high bed roughness, may be a residual summer effect that we observed due to the extremity of the drought, while the increase in erodibility during the winter/spring seasons of $2013-2014$ and $2014-2015$, follow the periods of freshwater input from winter storms. On the site-specific scale, the more erodible bed seen at N1T (compared to S1T) during Dec 2014-Jan 2015 may be related to sediment input from the Petaluma River, however the shift in bed erodibility does not coincide with a large Petaluma River flow. Thus, it is more likely that wind-wave activity, a shift in biological activity such as benthic biota or extracellular polymeric substances (EPS), or another mechanism affecting erodibility may be at play.

3.4.3.2 Spring-Neap

During seasons without storm events, CHC13, SPB, SPD, and CHC16, the bed was between 1.36 and 3.84 times more erodible during spring periods than neap periods (table 3.2). This relationship accounts for at most 42% of the observed variation, and typically accounts for 5 to 30% of the variation. Given that bed erodibility varies by up to 4 fold within a single season, the spring-neap cycle is a minor factor in driving this parameter.

3.4.3.3 Tidal

The method of computing bed erodibility applied here (equation 3.10) does not allow for an analysis within tidal cycles.

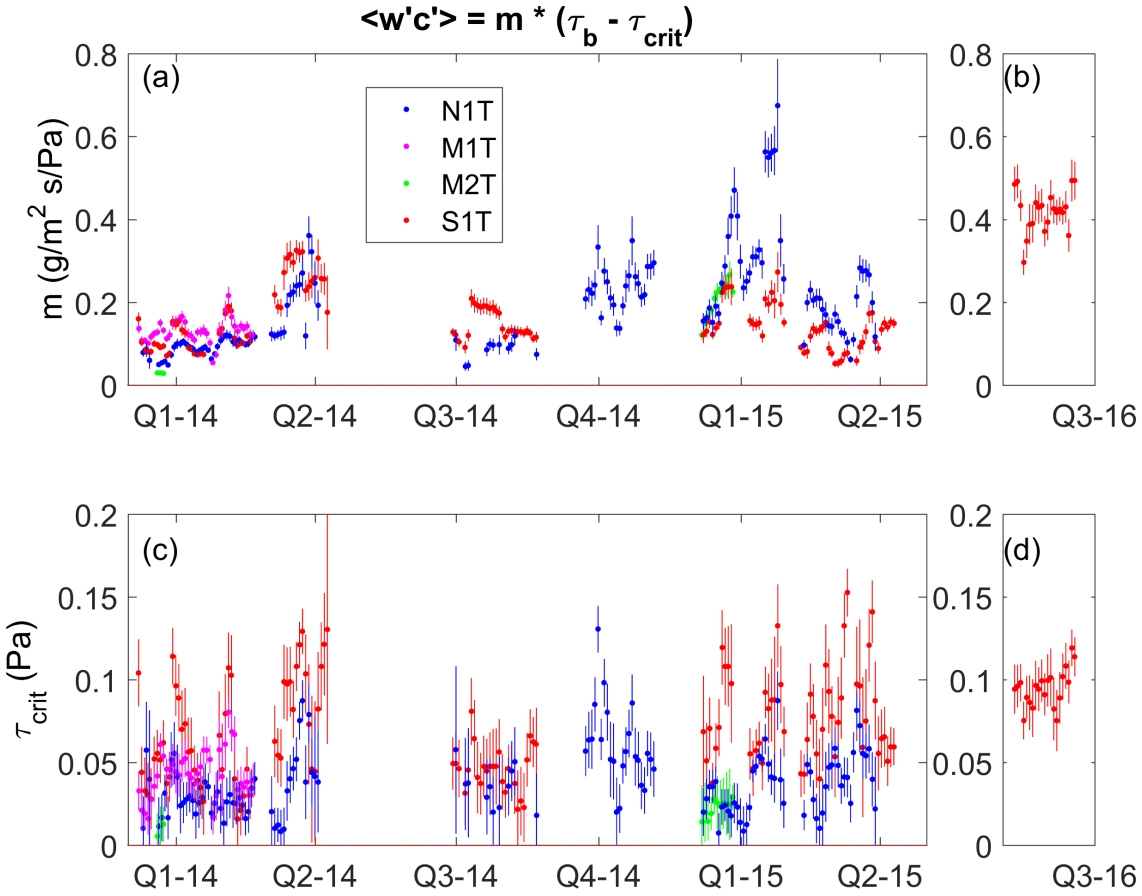

Figure 3.12: Bed erodibility model. Bed erodibility (m, top) and critical shear stress for erosion (τ_{crit}, bottom) at each of the 4 sites during Dec 2013 to May 2015 (a,c) and May-Jun 2016 (b,d).

	N1T		S1T	
deployment	R^2	m(spring)/m(neap)	R^2	m(spring)/m(neap)
CHC13	0.11	1.36	0.07	1.55
SPA		–		–
SPB	0.28	2.74	0.15	1.58
SPC		–		–
CHC14		–		–
SPD	0.12	3.84	0.04	1.60
CHC16		–	0.42	1.83

Table 3.2: The bed is between 1.36 and 3.84 times more erodible during spring periods than neap periods, defined as m(spring)/m(neap). We computed the fit for periods with low storm activity, to remove the effect of storm-altered erodibility on the spring-neap cycle. We also excluded SPC, since there was no relationship between m and the spring-neap cycle for this period.

3.4.4 Settling Velocity

3.4.4.1 Methods Comparison for computing Settling Velocity

While ADVs have been used extensively to compute particle settling velocity (Fugate & Friedrichs, 2002; George Voulgaris & Meyers, 2004; Cartwright et al., 2013), we found that the environment in San Pablo Bay is not appropriate to apply this tool (appendix A.2). The ADV method relies on the assumptions that unsteadiness and advective transport are negligible, which do not hold in San Pablo Bay. In fact, the settling velocity derived from the ADV method increases with τ_{bcw}, while the settling velocity from particle size measurements decreases with τ_{bcw}. Our conclusion that ADV estimates of settling velocity are not appropriate diverges from that found by George Voulgaris and Meyers, 2004, who inferred that ADV settling velocity estimates resembled reality better than LISST measurements at a lagoon in South Carolina, due to particle size range limitations of the LISST.

We applied only the LISST method for deriving particle size and settling velocity in our subsequent analysis. We have LISST data from summer 2016 only, so our investigation of particle size and settling velocity is limited to a roughly 4 week period, and does not include a seasonal analysis. We focus our exploration on the role of tidal and spring-neap cycles. In San Pablo Bay, floc size decreases with increasing shear stress (figure 3.13, left). This indicates that high stress is inducing floc breakup, while low shear stress or differential settling allows floc aggregation. This is consistent with the observations of Huang, 2017, who noticed that particle sizes increased as turbulent shear decreased in the San Francisco Bay Delta. For the observations here, as well as for Huang, 2017, shear stress provided the best predictor for floc size. Our observations of flocs show settling velocities (with standard deviation) of $w_s = 1.07(0.78 - 1.46) * 10^{-5}$ m/s.

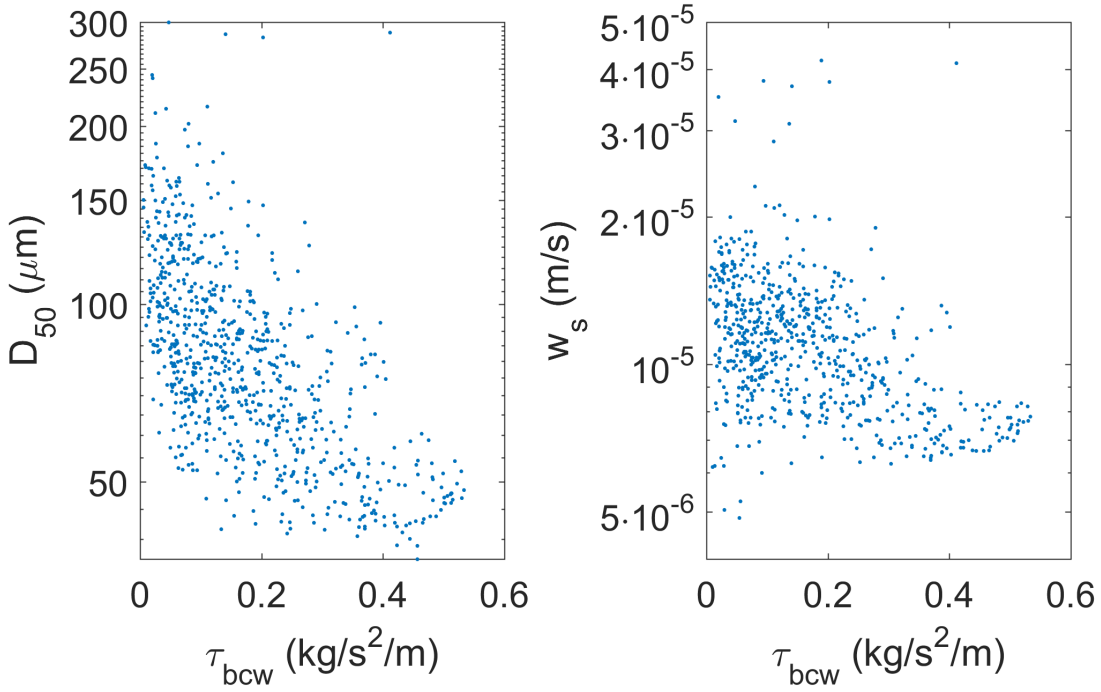

Figure 3.13: Bed shear stress (τ_{bcw}) from CHC16 site M2T, plotted against median floc size (left) and settling velocity (right). At smaller bed shear stresses, floc size and settling velocity increase.

During the CHC16 period, median floc size, as measured by the LISST, generally increased as current, indicated via bed shear stress, slowed (figure 3.13, left). To provide insight into the floc dynamics, we have winnowed down the 32 measured particle size classes to three: particles 23 μm, 88 μm, and 332 μm in diameter, representing small, medium, and large flocs, respectively (figures 3.14 and 3.15). Even the 23 μm particles are aggregates, because a grain size analysis of particles on the bed yielded 8 μm as the primary particle size. With settling velocity estimated through equation 3.11, it would take small flocs (23 μm) 3.7 hours to settle 0.5 m through quiescent water. Medium flocs would take 39 min to settle the same distance, and large flocs would take 7.4 min. This height, which corresponds to the height of the LISST above the bed, yields a particle clearing timescale. Total depth never exceeded 4 m at this site, suggesting that it would take under 1 hour for large flocs to be cleared from the full water column during non-turbulent conditions.

3.4.4.2 Tidal

The dominant floc dynamics on a tidal scale are illustrated in the ebb phase of a spring tide, shown on figure 3.14 between the marked periods of interest (1) and (7). The concentration of large particles (yellow) remains low through the ebb, before it increases near low water

(6) as shear stress decreases. This suggests that the high shear stress present in the middle of the ebb ($3-5$) breaks up any large flocs that form. Once shear stress declines late in the ebb, the smaller flocs form large flocs, which survive, and the concentration of large flocs increases (6). Then, the large particle concentration decreases as shear stress declines to zero (7), likely due to rapid settling. This combination of flocculation and settling also yields a decline in the concentration of small (blue) and medium (green) flocs (6-7). The rapid decline in the concentration of small and medium particles implies that flocculuation occurs effectively instantaneously.

During the same ebb period, small particles increase in concentration from (2) to (6), as water level declines. We conclude that both resuspension due to high bed shear stress and offshore advection of shallow waters play a role in increasing SSC. In particular, as bed shear stress increases early in the ebb (2-4), the total particle concentration increases, suggesting that local resuspension is the cause. Subsequently bed shear stress declines (4-6), yet the total concentration, and the concentration of small flocs, continues to increase. This suggests that offshore advection of shallow, high sediment concentration waters plays a role during late ebb.

As the small particles increase in concentration with resuspension and advection, the concentration of medium particles stays constant during the periods of high shear stress (3-5). This is similar to the limited concentration of large particles observed during a longer period, but similarly centered on the period of high shear stress (2-just past 5). This suggests that like with large particles, the concentration of medium particles is limited by high turbulent shear. When shear stress declines (5-6), medium particles increase in concentration, indicating that they are no longer being broken up.

The concentration limit on medium particles combined with the steady increase in small particles yields the counter-rotating circles observed in the bottom-left (23 μm) and bottom-center (88 μm) panels of figure 3.14. Here, a steady increase in the proportion of small particles while the proportion of medium particles decreases from (3) through (5) yields a clockwise rotation of the fraction of 23 μm particles and a counter-clockwise rotation of the fraction of 88 μm particles.

During ebb phase of neap tide (figure 3.15), flocs again behave similarly, although with less complex dynamics. Here, the peak concentration during ebb is nearly an order of magnitude smaller than during spring tide. However, as with spring tide, the concentration of large particles increases only when the shear stress declines during late ebb (5-6), suggesting that there is too much turbulent shear during peak ebb to allow large flocs to remain. As with the spring ebb tide, the total particle population declines near slack water (following 6 and 1-2), suggesting that larger flocs are forming from smaller flocs and subsequently settling. Unlike the spring ebb tide, the proportion of medium flocs continues to increase during the peak ebb period. This suggests that the maximum bed shear stress was not great enough during this tide (0.15 kg/m^2/s, compared with 0.6 kg/m^2/s during the analyzed spring) to limit the concentration of medium flocs formed.

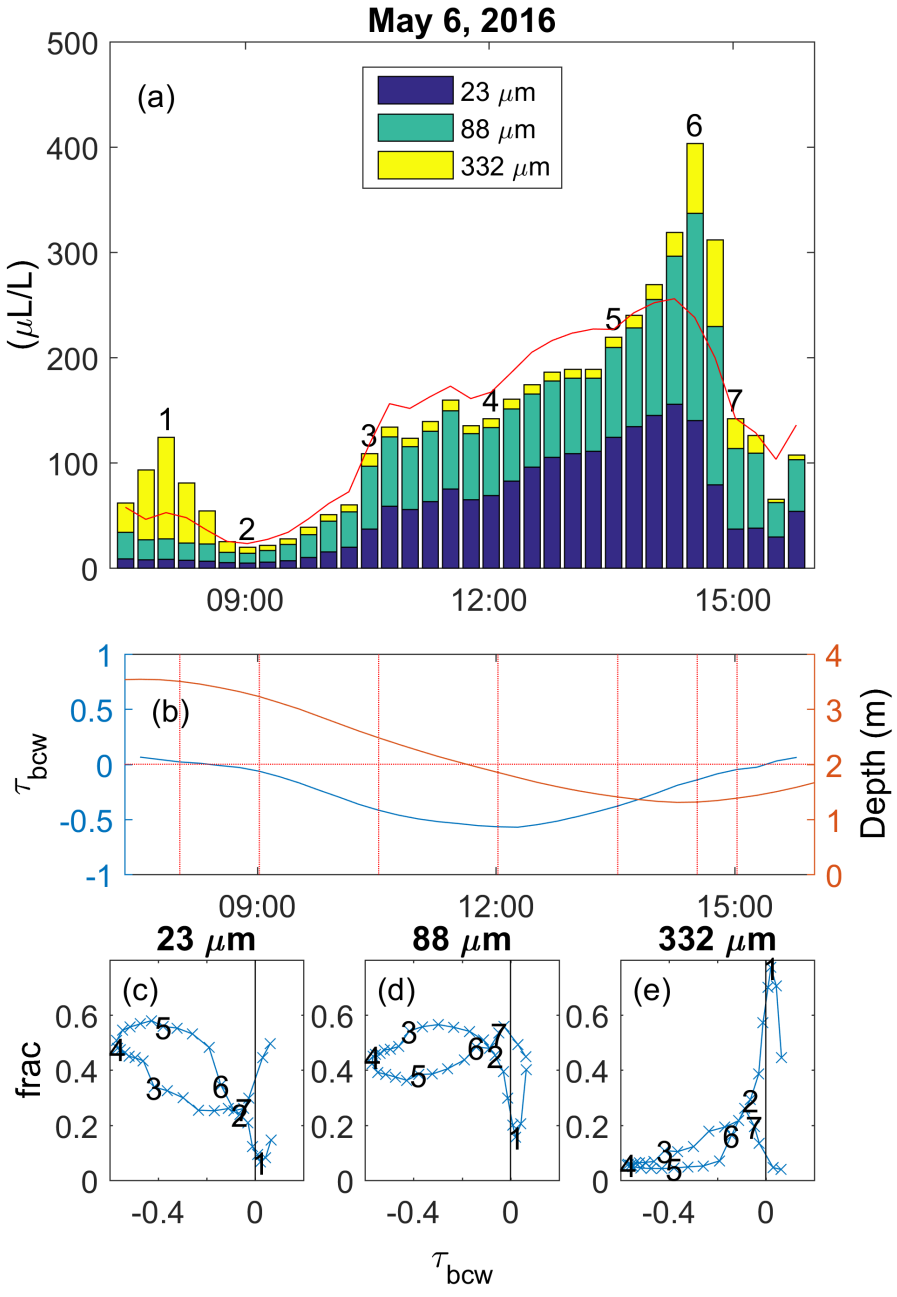

Figure 3.14: A spring ebb period, on May 6, 2016, during low wave activity. (a) shows the concentration (in μL/L) of flocs of size 23 μm, 88 μm, and 332 μm at 0.5 mab. The red line gives the SSC at 0.5 mab measured through a Seapoint CTD. Numbers 1 through 7 denote periods of interest. (b) shows the bed shear stress from currents and waves (τ_{bcw}) and depth (m). The bed shear stress is plotted as negative during ebbing flow. Vertical red lines refer to the periods marked 1 through 7. The bottom panels show the fractional proportion of 23 μm (c), 88 μm (d), and 332 μm (e), where we show class concentration/ total concentration ($23 + 88 + 332\mu m$) against bed shear stress.

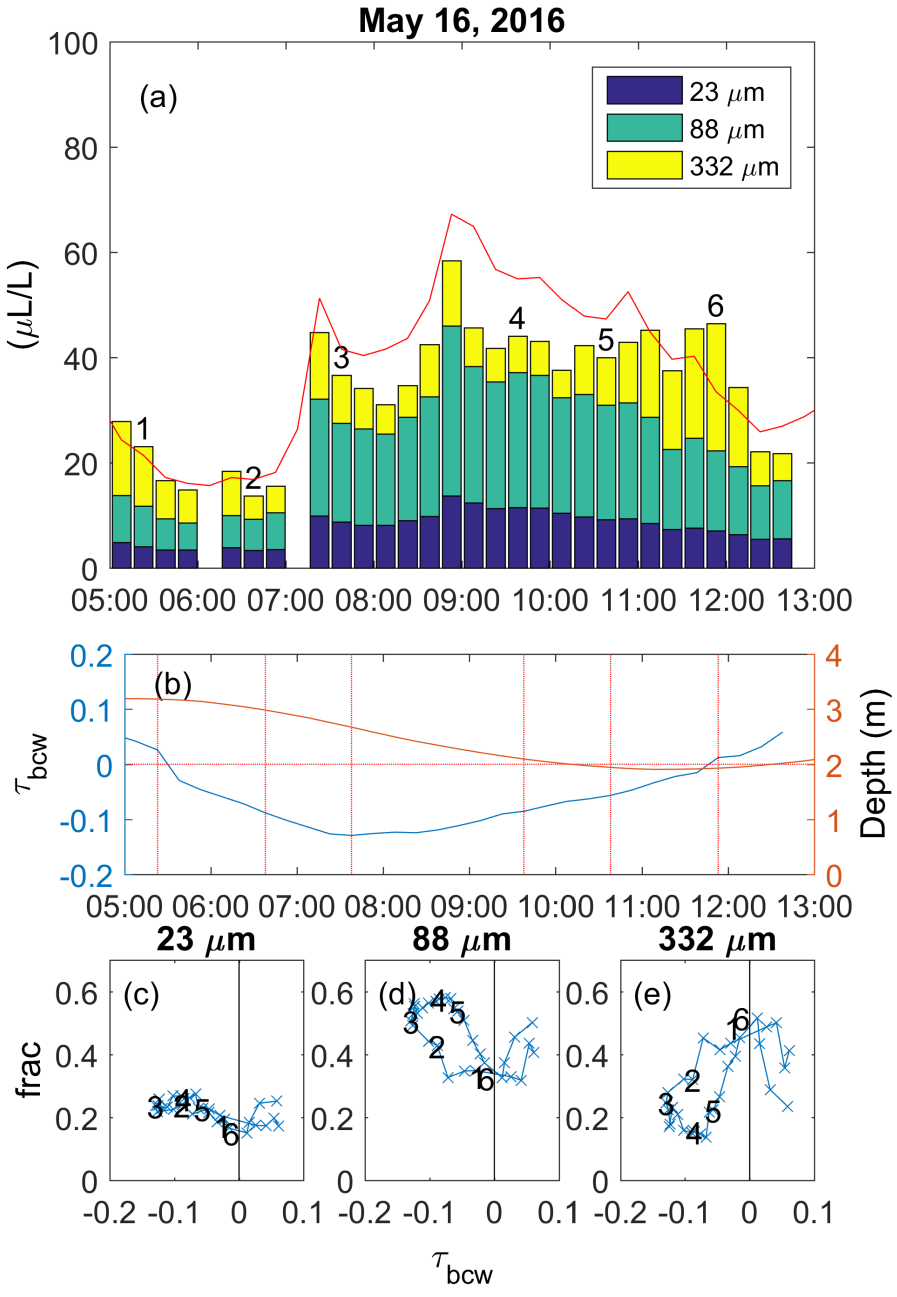

Figure 3.15: A neap, ebb period, on May 16, 2016, during low wave activity. As with figure 3.14, (a) shows the concentration (in μL/L) of flocs of size 23 μm, 88 μm, and 332 μm at 0.5 mab. The red line gives the SSC at 0.5 mab measured through a Seapoint CTD. Numbers 1 through 6 denote periods of interest. (b) shows the depth (m) and bed shear stress from currents and waves (τ_{bcw}). The bed shear stress is plotted as negative during ebbing flow. Vertical lines refer to the periods marked 1 through 6. The bottom panels show the fractional proportion of 23 μm (c), 88 μm (d), and 332 μm (e), where we show class concentration/ total concentration ($23 + 88 + 332$ μm) against bed shear stress.

3.4.4.3 Spring-Neap

These dynamics were consistent through multiple tidal periods on spring (figure 3.16) and neap (figure 3.17) tides. In particular, spring tides show consistently the clockwise and counter-clockwise rotating periods during ebb in the fraction of small (figure 3.16, $4th$ row left) and medium (figure 3.16, $4th$ row center) classes. This balance between the size classes supports the idea that medium particle classes reach some peak concentration while the small particles increase, thanks to breakup of medium particles at high shear stress. The opposing behavior of small and medium particle concentrations is not observed during neap tides, however, as the total concentration (figure 3.17, $3rd$ row) and proportional concentration (figure 3.17, $4th$ row) of small and medium particles behave similarly during ebb, supporting the notion that bed shear may be large enough during spring tides to affect medium particles, but it does not reach these magnitudes during neap tides. The relative concentration of large particles (figures 3.16 and 3.17, $4th$ row right) peaks as shear stress nears zero, allowing such particles to form. The total concentration of small particles generally increases during low water (figures 3.16 and 3.17, $1st$ row left). This supports the idea that the amount of sediment resuspended is similar across the Bay, and at lower water there is less volume to mix this resuspended mass into, yielding higher concentrations. Then, these higher concentrations advect past our site during ebb. Both spring and neap periods show some decrease in concentrations of small particles at very low water, indicating that the flocculation and settling dynamics we noted earlier likely play a role, but they are not easy to distinguish here.

Finally, we compare SSC measured by the OBS and the LISST (figures 3.16 and 3.17, $2nd$ row). During spring tide, the concentration of small particles perfectly follows the OBS measurments, while the concentration of large particles is nearly uncorrelated. For medium particles however, OBS and LISST measured concentrations diverge at higher SSC during spring tides, but not during neap tides, when the maximum SSC is lower. This further supports the idea that medium particles are broken up by high shear stress, which generally occurs when there is high SSC.

3.4.4.4 Seasonal

We do not have LISST data from other periods of the deployment, and do not reach conclusions regarding the role of seasonal cycles on particle size or settling velocities.

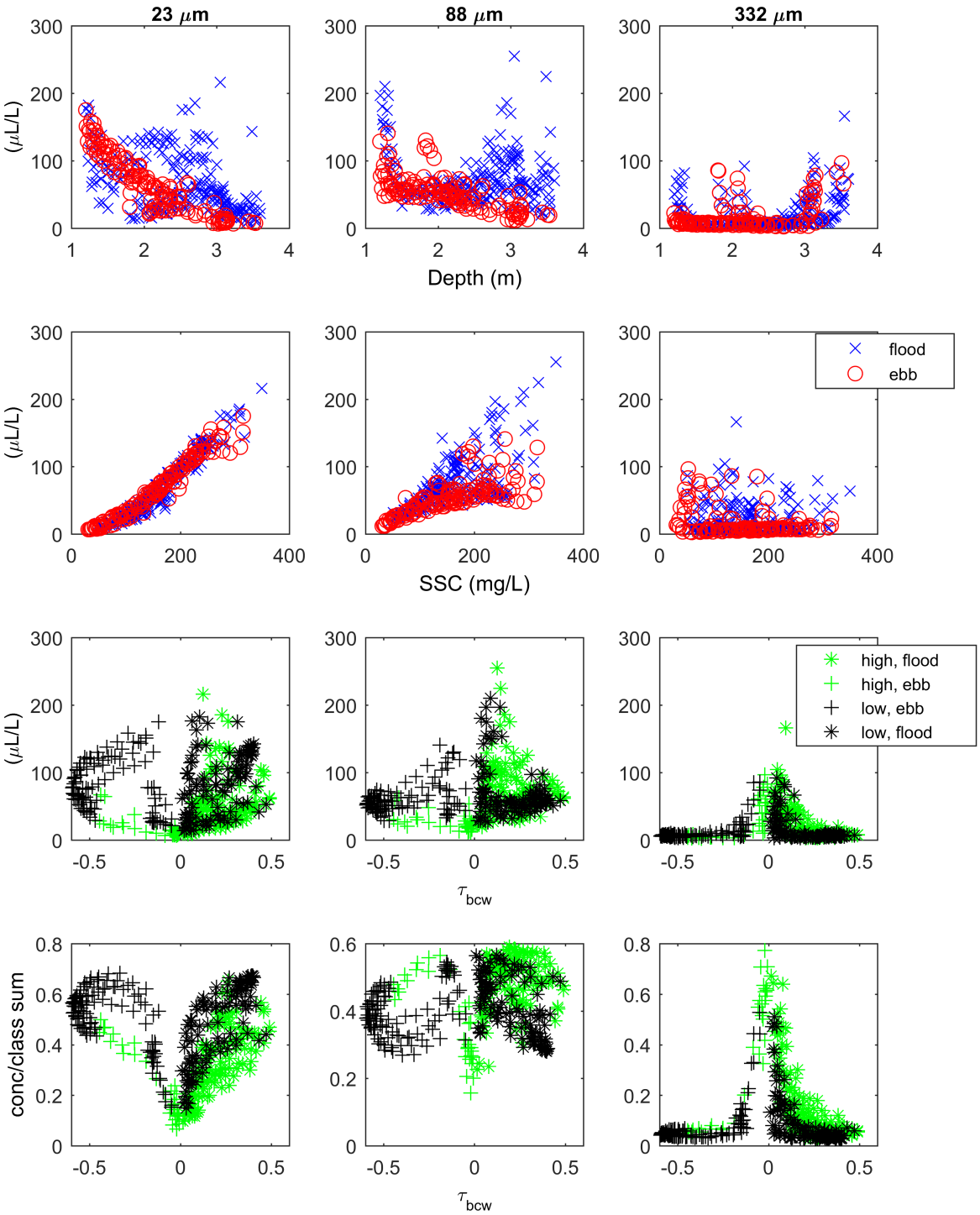

Figure 3.16: Spring periods (May 6, 2016, 00:00 through May 11, 2016, 00:00).

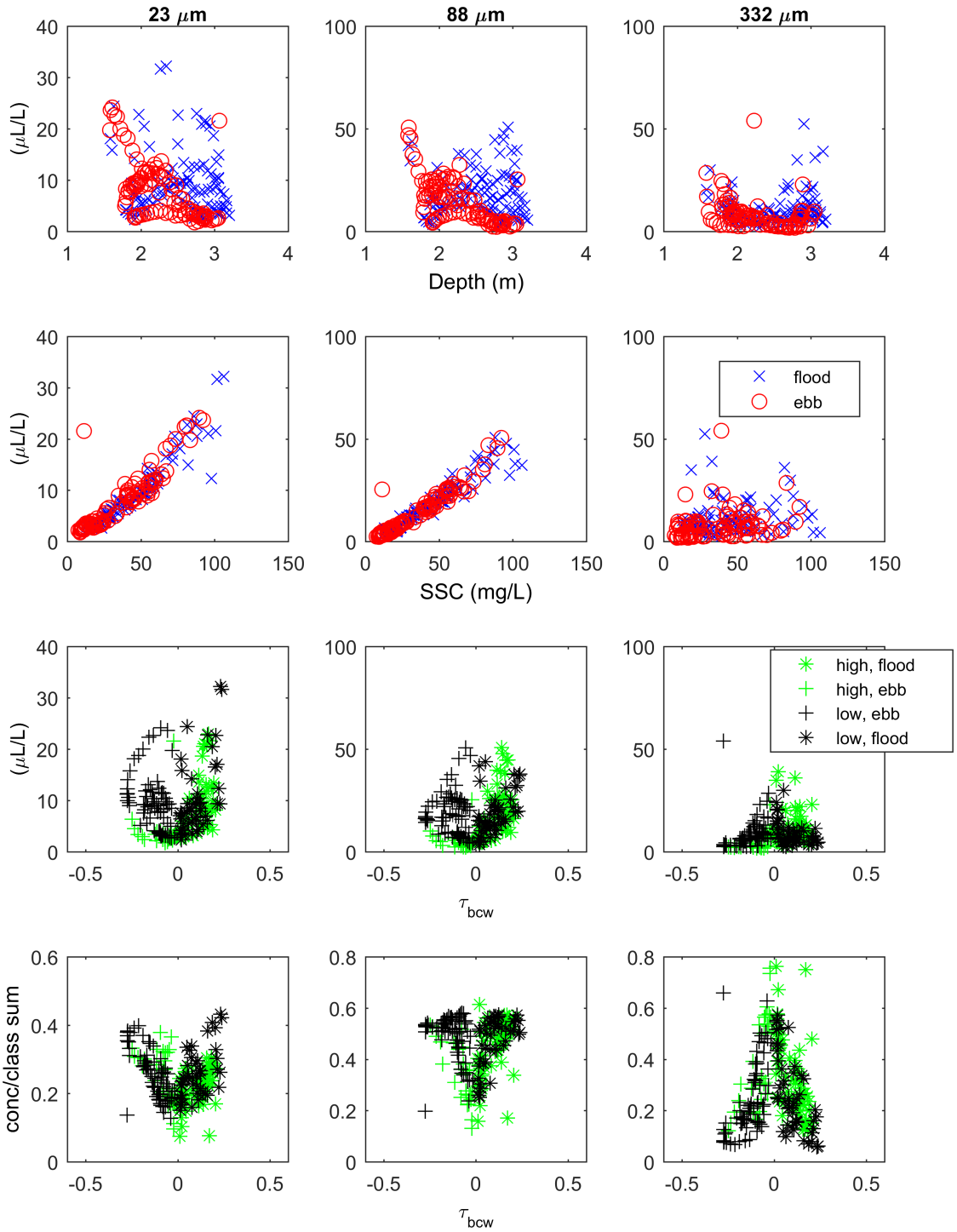

Figure 3.17: Neap periods (May 13, 2016, 00:00 through May 18, 2016, 00:00).

3.5 Discussion

3.5.1 Variability in bottom roughness, bed erodibility, and settling velocity

3.5.1.1 Seasonal

The decrease in bottom roughness at site N1T in November 2014 is aligned in time with a large storm coming from the northeast, as discussed in section 3.4.2.1. These winds may promote enough turbulent energy in San Pablo Bay to resuspend more bed material, which then flocculates less in suspension or deflocculates to some extent and re-settles on the bed. If smaller flocs dominate the surface layer of the bed, a smoother bed would be apparent. Applying $k_b = 30z_0$ (Nielsen, 1992), this yields a physical bottom roughness of 300 μm when $z_0 = 10^{-4}$ m, and 30 μm when $z_0 = 10^{-5}$ m. Thus, it is possible that smaller flocs become dominant in the water column, either in the bulk of the water column or close to the bed in the wave-boundary layer, producing the shift in bottom roughness observed at N1T. Alternatively, the 'down-estuary' winds of this storm help advect a new sediment supply to this site, which is deposited on top of coarse material that was reworked during the summer. Even though the primary particle size did not change at N1T, if new material flocculates less it could yield a smoother bottom. The shift in bottom roughness could also be connected to strong erosion on the bed. As the surface layer erodes, the erosion rate decreases, corresponding to increasing strength of the bed and smaller, more cohesive, particles (R. B. Krone, 1999). Site S1T did not see the same shift in bottom roughness as site N1T during November 2014. If the bottom roughness shift was brought about by a storm, this may be indicative of the more protected conditions at S1T, or the greater overall bed shear stress seen at site N1T.

The observed seasonal signal in bottom roughness and bed erodibility may be tied to daily winds in the summer. While summer winds were stronger at N1T (u_{br} reached 0.2 m/s) than at the more protected S1T (u_{br} rarely exceeded 0.1 m/s), both sites saw regular wind activity and wave-driven resuspension. Such regular, short period summer wind events may help to erode small flocs off the bottom and leave or re-work large particles, yielding a less erodible, coarser bed. Despite the difference in the role of winds and the impact on bottom orbital velocities at these two sites, the bed roughness remains consistent at both (figure 3.9), generally near and above 10^{-4} m. The low erosion rate constant at both sites in summer 2014 supports the idea that repetitive daily winds have winnowed the bed.

In addition, biological processes may play a role in driving sediment dynamics. The observed large shift in bottom roughness at N1T may not be due to wind forcing alone, but rather to an unmeasured shift in biology. For example, a seasonal die-off of bed biota could allow the bed to become smoother in the winter. Then, the appearance of a relatively large storm in mid-November causes a reworking of the bed, which would not be possible during the summer season. While the dramatic shift in bed roughness is observed at site N1T only, this spatial difference could result from variations in biology at the sites.

While the bottom roughness response may be partially tied to winter storms, bed erodibility may be more connected to a seasonal biological signal. In particular, the delay between rainy season freshwater input and the increase in bed erodibility supports the idea that a shift in clam or phytoplankton communities, responding to seasonal freshwater inputs, is responsible for such an increase. Poulton, Lovvorn, and Takekawa, 2004 found significantly fewer *Potamocorbula amurensis* and *Macoma balthica* clams at China Camp during spring than fall, and they noticed a lack of species that prefer higher salinities, including *Gemma gemma* clams and *Ampelisca abdita* amphipods, during their study in $1999-2000$, likely due to the very wet years prior ($1996-2000$). Such species may have been present during the dry years of this study. Since denser communities of clams stabilize bed sediments (Crimaldi, Thompson, Rosman, Lowe, & Koseff, 2002), a seasonal and an annual shift in the types and abundance of clams could play a role in the winter increase in bed erodibility. Amos et al., 2004 noted that the estuarine seabed of Venice Lagoon was less erodible during the summer, due to the stabilizing presence of cyanobacteria, microphytobenthos, and seagrass. Like the seasonal shift in clam presence, phytoplankton growth on sediments varies on a seasonal scale, appearing annually at the highest levels during June and July (Lesen, 2006). A seasonal response of clams and phytoplankton in San Pablo Bay could yield a smoother, more erodible bed in the winter season.

However, biologic activity on the bed can increase and decrease both τ_{crit} and m (Grabowski et al., 2011). The presence of infaunal clams can 'loosen' the sediment surface through their vertical movements, increasing erodibility. Benthic organisms that feed in suspension can repack materials from particles into pellets, often converting easily suspended particles into bedload. Other water-column feeders and deposit feeders can break down large organic matter and destabilize the sediment surface. Biogenic structures can also have a complex relationship with bed erodibility. Burrows and tunnels can lead to increased or decreased τ_{crit}, yet studies agree that burrows increase m once the erosion threshold has been surpassed. Roots and rhizomes have a stabilizing effect on bed erodibility. And there is general consensus that EPS increases τ_{crit} and decreases m, however field studies have occasionally yielded equivocal results. With the role of benthic community so varied, it is challenging to anticipate the expected response of bed erodibility with a possible seasonal shift in the biologic makeup of the bed.

Bottom roughness and bed erodibility may respond to similar processes (figure 3.18). The more erodible bed seen when there is a smoother bottom suggests that the smaller flocs that yield the smoother bed are more readily picked up. A similar effect would be expected from the presence of benthic biota, which would produce a rougher and more consolidated bed. We might have expected that a rougher bottom would yield more turbulence and a more erodible bed. The observed opposite result suggests that hydrodynamic processes are not the dominant driver of sediment characteristics. This seasonal-annual scale connection between roughness and erodibility demonstrates the role of long-term processes in controlling sediment dynamics.

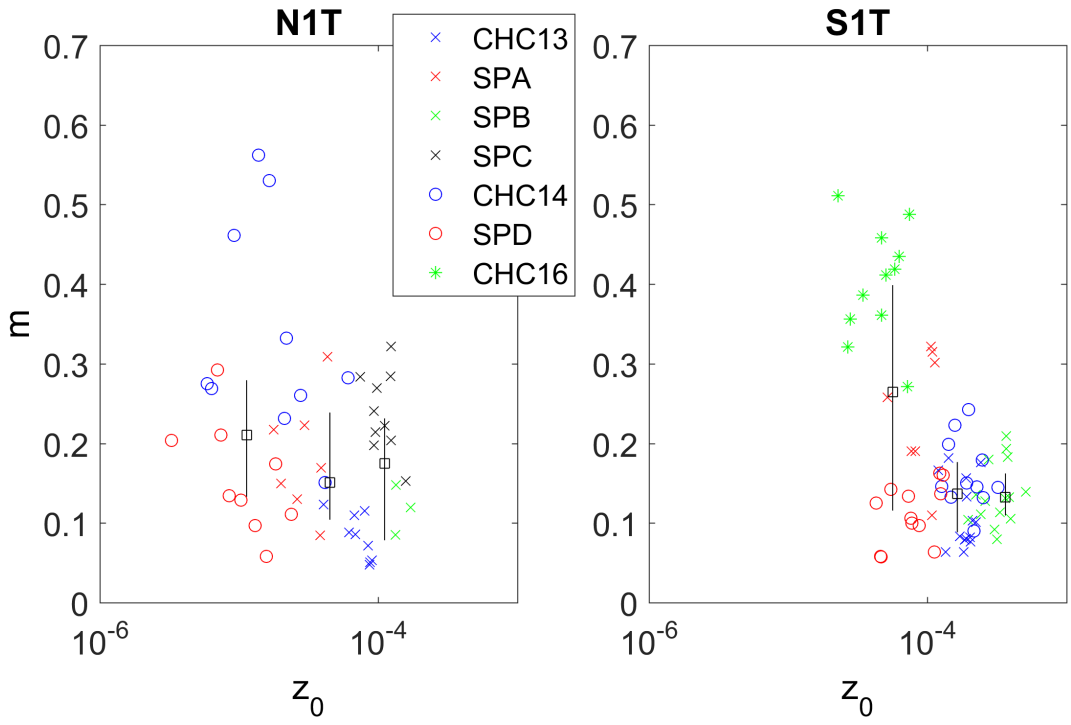

Figure 3.18: Bottom roughness (z_0) compared with bed erodibility parameter (m) for 4−day averages from all deployments at sites N1T (left) and S1T (right). The median erodibility (and 25 to 75% confidence intervals) are shown for binned z_0 in black squares. At S1T in particular, higher bottom roughness corresponds with smaller bed erodibility.

3.5.1.2 Spring-Neap

Flocs in the water column become smaller during spring tides; the particle settling velocity is thus lower during spring than neap. Total suspended sediment concentration is greater during spring periods than neap due to both the increased velocities, which resuspend more material, as well as the smaller settling velocities, which allow suspended material to remain in the water column longer.

When the bottom gets smoother at site N1T, following the shift in November 2014, it also becomes responsive to the spring-neap cycle (figure 3.11). Given that spring periods see smaller flocs formed in the water column, such flocs settling to the bed may also be driving the spring-neap variation in bottom roughness, suggesting that the bed is generally accumulating material.

During earlier periods at N1T and at all deployments of S1T, the spring-neap cycle is not correlated with bottom roughness, and the physical bottom roughness is coarser than the anticipated floc size (section 3.5.1.1). A net eroding bed during these phases might yield the observed coarseness, and the lack of response to the spring-neap cycle.

3.5.2 Implications of Variability on Sediment Transport Dynamics

Do these variations in bottom roughness, bed erodibility, and settling velocity affect suspended sediment concentration or direction and magnitude of suspended sediment flux?

Bottom roughness plays a role in generating turbulence in the water column; a smoother bed creates less turbulence. For example, at a mean current speed of $U = 0.4$ m/s at 0.3 mab, a rough bed ($z_0 = 10^{-4}$ m) has $u_* = 0.021$ m/s, while a smoother bed ($z_0 = 10^{-5}$ m) has $u_* = 0.016$ m/s. This variation in turn implies that mean velocity at 1 mab is lower for the smooth bed (0.45 m/s), and higher for the rough bed (0.46 m/s). A bed that is smoother by an order of magnitude will yield a wave friction factor (f_w) that is smaller by about 3-fold, leading in turn to a smaller bed stress from waves (τ_{bw}) (Jessica R. Lacy & MacVean, 2016). As noted by Brand et al., 2010 and MacVean and Lacy, 2014, it is generally near bed stress generated by wind-wave activity that erodes sediment from the bed. Thus, less turbulence is generated in the wave-current boundary layer over a smooth bed, and less sediment is resuspended into the water column.

Less turbulence also means less water column mixing and more settling and deposition of suspended particles. Applying a Rouse profile (e.g., Mehta, 2014) with the assumption that SSC is 300 mg/L at 0.1 mab, if the suspended mass is entirely small (23 μm) particles, concentration at 1 mab decreases from 296 mg/L to 295 mg/L under the u_* given by the transition from a rough to a smooth bed . However, if this mass is large (332 μm) particles, concentration shifts from 206 mg/L to 183 mg/L with the u_* shift from rough to smooth.

Finally, with less turbulence larger flocs can form, leading to faster settling and more deposition. A smoother bed therefore suppresses sediment resuspension and allows for faster deposition, providing a subtle push towards less sediment in the water column.

However, a more erodible bed implies more sediment is resuspended in the water column, and a more erodible bed is generally correlated with a smoother bed in San Pablo Bay (figure 3.18). The 10-fold increase in bed erodibility suggests that the overall effect of bed erosion may dominate the shift in bottom roughness regarding the implications for suspended sediment concentration.

As concentration in the water column is modulated by bottom roughness, bed erodibility, and settling velocity, so is sediment flux. Sediment flux is impacted by concentration, velocity, and water level, as $SSF = \langle uhc \rangle$; if concentration decreases, flux also declines. Low sediment erodibility in the summer can thus yield lower sediment transport. In addition, the tidal variation in settling velocity allows for net transport. Particle flocculation at slack water allows for rapid suspended material deposition, and the decline in concentration provides evidence that this occurs. Faster net particle settling would limit the distance of particle transport to less than the full tidal range, while slower particle settling suggests that transport lasts beyond a tidal cycle, and is more broadly influenced by net flux.

Droughts may become more prevalent in California, as weather shifts around the world. Fewer storms and lower freshwater flows in San Pablo Bay could yield longer periods of high bottom roughness and low erodiblity as observed during winter $2013 - 2014$, in general

suppressing sediment concentration and flux. Low bed erosion during a drought winter could maintain summer time bottom roughness (even if it is biogenically induced), and the smaller daily winds could yield overall low concentration conditions.

Lower suspended sediment concentrations and fluxes could yield less sediment supply to marshes and restoration projects, resulting in slower marsh growth and the possibility for restoration projects to fall behind sea level rise. However, it could also mean more sediment retention in the estuary, counter-acting or slowing the long-term erosion of San Pablo Bay. Such a transition could also allow for more or longer periods of water column phytoplankton growth, and a gradual or dramatic shift in the ecosystem.

3.6 Conclusions

With this work, we found that bottom roughness varied between $4 \cdot 10^{-4}$ and $4 \cdot 10^{-6}$ m, bed erodibility varied between 0.02 and 0.15 Pa, and settling velocity varied at 0.78 to $1.46 \cdot 10^{-5}$ m/s in San Pablo Bay from data collection over approximately 2 years. Both bottom roughness and bed erodibility varied on a seasonal scale, suggesting that numerical models for sediment transport may need to account for seasonal variation in setting external parameters. Particle size varied with tidal and spring-neap cycles. Smaller particles present during spring tides settled slower; combined with increased resuspension due to faster velocities this yielded higher concentrations during spring periods.

Chapter 4

Stratification Mechanisms in Estuarine Shallows

4.1 Introduction

Estuarine stratification is fundamental to the physics and ecology of coastal embayments. It influences residual estuarine circulation, primary productivity, and mixing of low oxygen near-bottom waters. Vertical salinity stratification suppresses turbulent mixing, allowing surface waters and bottom waters to become decoupled. Spatial and temporal variability of stratification is a leading contributor to circulation and transport, including the creation of estuary turbidity maxima (ETM) in many systems, which has inspired studies of the mechanisms driving vertical salinity stratification (J. H. Simpson et al., 1990; Scully & Geyer, 2012; Aristizabal & Chant, 2014).

Interpretation of observations and dynamics of estuarine stratification is made difficult by the role that the advection of horizontal gradients play in the evolution of local stratification. Deconvolving the effects of advection, straining, and local mixing, which are sometimes additive and sometimes competitive, remains a key challenge in estuarine physics.

To be clear about the mechanisms involved in the temporal variation of vertical salinity gradients, we start with a simplified salt advection-diffusion equation:

$$\frac{\partial S}{\partial t} = -u\frac{\partial S}{\partial x} + \frac{\partial}{\partial z}\left(K_z\frac{\partial S}{\partial z}\right) \tag{4.1}$$

where S describes the salinity field (PSU), u gives velocity in the dominant flow direction (m/s), and K_z describes salt diffusion (m^2/s). To capture the evolution of salinity stratification, we take the vertical derivative of equation 4.1, which when expanded becomes:

$$\frac{\partial}{\partial t}\left(\frac{\partial S}{\partial z}\right) = -\frac{\partial u}{\partial z}\frac{\partial S}{\partial x} - u\frac{\partial}{\partial x}\left(\frac{\partial S}{\partial z}\right) + \frac{\partial^2}{\partial^2 z}\left(K_z\frac{\partial S}{\partial z}\right) \tag{4.2}$$

The left hand side represents the evolution of stratification, which may be increasing in strength (i.e., $\frac{\partial S}{\partial z}$ becoming more negative) or decreasing (positive time derivative). The key

processes that we wish to differentiate between are the terms on the right hand side. The first term here describes the transformation of lateral salinity gradients by shear. This creates $\partial S/\partial z$ gradients when faster moving surface waters transport low salinity waters (which originate up-estuary) on top of high salinity waters on ebb tides. This mechanism creates $\partial S/\partial z$ gradients during ebb tides, and erases them on flood tides, commonly referred to as strain-induced periodic stratification (SIPS) (J. H. Simpson et al., 1990). The second term on the right-hand side describes the advection of salinity fronts. When there is lateral variation in the vertical salinity gradient, often most pronounced around frontal transitions between stratified and unstratified water masses, tidal flows (either flood or ebb tides) can translate the frontal transition, leading to local increases or decreases in vertical salinity gradients. The third term describes the removal of vertical salinity gradients through turbulent mixing: when K_z (m^2/s) is large, mixing occurs faster.

Prior to developing a framework to describe salinity stratification in estuaries, J. H. Simpson, 1971 described temperature-induced stratification and mixing in coastal seas. The potential energy anomaly, ϕ, is defined as the total amount of work per unit volume necessary to completely mix the water column. They found that the western irish sea stratifies in spring and summer, thanks to both a buoyancy input at the surface through solar heating and the lack of tidal energy to mix it out given the deep bathymetry (J. H. Simpson, 1971). This potential energy anomaly framework developed for surface-heating-induced stratification was then expanded to estuarine systems where stratification resulted from freshwater input in J. H. Simpson et al., 1990. Here, ϕ is defined as:

$$\phi = \frac{g\beta}{H}\int_0^H (\overline{s} - s)\, z dz \tag{4.3}$$

with gravity (g), the haline expansion coefficient (β), salinity (s), depth averaged salinity ($\overline{s}$), and total depth (H).

This potential energy anomaly framework gives rise to the Simpson number (or horizontal gradient Richardson number), which provides some insight into the role of mixing in allowing stratification (Stacey, Burau, & Monismith, 2001; Geyer & MacCready, 2014).

$$Si = \frac{\frac{-g}{\rho}\frac{\partial \rho}{\partial x}H^2}{u_*^2} \tag{4.4}$$

Water density (ρ) is described primarily by salinity, and the level of turbulence is captured by the friction velocity, u_*. Equation 4.4 describes the ratio of potential energy change due to straining with the rate of production of turbulent kinetic energy. When Si is small, enough turbulent kinetic energy is available to overturn stable stratification, leading to well-mixed conditions. Somewhat larger values of Si yield the SIPS regime with periodic stratification, and high values of Si lead to stratification throughout the tidal cycle (Geyer & MacCready, 2014).

In recent years, the tidally-variable longitudinal (along the axis of the estuary) descriptions that emerged from the work of Simpson and Jay have been further modified to incorporate the effects of lateral circulation on the variability of estuarine stratification. Starting

with Lerczak and Geyer, 2004, lateral circulation began to be recognized as a critical factor in establishing the vertical structure of salinity and velocity and, by extension, the residual circulation. Other findings include J. R. Lacy, Stacey, Burau, and Monismith, 2003; Stacey, Fram, and Chow, 2008; Collignon and Stacey, 2012; Scully and Geyer, 2012; Collignon and Stacey, 2013 and McSweeney, Chant, and Sommerfield, 2016. Taken together, these studies demonstrate the three-dimensionality of estuarine stratification dynamics and the importance of straining in both the longitudinal and lateral directions. In the context of these studies, however, the role of advection of existing vertical variability in establishing local conditions is less well established, due to either the conditions at the study sites, the instrumentation deployed, or the structure of the modeling framework employed.

We note that most of the studies presented above have focused on the mechanisms creating vertical salinity stratification in estuarine channels, while fewer have investigated the dynamics along broad shallows characterized by a sloping bed. It is often assumed and observed that salinity in shallow estuarine regions is fully mixed through the water column (MacVean & Lacy, 2014; Brand et al., 2015). If stratification does develop, however, these regions provide an additional opportunity to examine the balance between advection, straining, and mixing. In fact, due to the slow variations in depth and bathymetry, broad shoals may provide a superior location to understand how local conditions respond to and influence regional variations in vertical stratification.

4.2 Methods

4.2.1 Field Site

Our field site is San Pablo Bay, in the northern arm of San Francisco Bay (figure 4.1). It receives freshwater flows from the east, where the Sacramento and San Joaquin Rivers converge and then pass through Suisun Bay. In the Mediterranean Climate of northern California, nearly all rainfall occurs from November through April, with a dry summer season. San Pablo Bay is a prototypical channel-shoal estuary, with a roughly $10 - 12$ m deep channel running east-west along the Bay axis and shoals gradually sloping to the margins to the north. These mudflats extend laterally about 10 km from a depth of about -3 m MLLW to the shore. The bed slope at our study sites ranged from 1/1600 to 1/3000. Bed sediments are predominantly mud and vary little across sites (section 3.4.1). Tides in San Pablo Bay are mixed semi-diurnal. The highest spring tidal range is 2.5 m, while the smallest neap tidal range is 1 m. The motivation for the field experiment was to understand stratification and sediment transport dynamics in the shoals on tidal and seasonal timescales; the stratification data is the focus of the work presented here.

Figure 4.1: Deployment sites in San Pablo Bay, California. Map created via Caltopo.com.

4.2.2 Instrumentation

Instruments were deployed nearly continuously from December 2013 through April 2015, and again May-June 2016, and were cleaned and re-deployed approximately every 3 months (figure 4.1). Salinity, temperature, and depth were measured at a single depth at 3-4 stations and at 2 to 3 depths at a single station, throughout the deployment, sampling every 5 to 10 minutes (table 4.1). Co-located acoustic doppler velocimeters (ADVs) at 1 to 4 of the sites were used to measure mean flood and ebb velocities. ADV data were collected at 10 Hz for 3.5 minutes at a sample interval of 15 to 20 minutes.

The stations were located at the 1 and 2 m MLLW contours, following the number in the station name. The southern station S1T was closest to China Camp marsh, the focal period for other aspects of this study (Foster-Martinez, Lacy, Ferner, & Variano, 2018), and had

a distance of about 4 km to the navigation channel. Stations M1T and M2T in the middle were centrally located, while stations N1T and N2T towards the north were farthest from the navigation channel and salinity inputs. The north stations were adjacent to the dredged outflow from the Petaluma River; station N1T was about 0.75 km from this channel.

Note that only the 2-m sites N2T and M2T had CTDs located at multiple depths, and that no ADVs were deployed at site N2T. Thus, all analyses relying on salinity data at multiple depths co-located with velocity use M2T data. Because the ADV at M2T failed during the summer 2016 deployment, we substitute the rotated velocity data from site S1T. Even though the velocity direction is different between the sites, the timing of the water direction change during slack periods differs by less than 30 minutes. Thus, for our purposes, the substitution is appropriate.

4.3 Overview of Conditions

For both winters of the deployment (2013−2014 and 2014−2015), California experienced critical drought conditions (California Department of Water Resources, http://www.water.ca.gov/dayflow/). During the $2013-2014$ winter, what storm events did occur took place in February, March, and April, after our winter deployment in December and January. Meanwhile, the 2014−2015 winter had a series of intense storms in December. Therefore, we consider the $2013-2014$ winter to be more characteristic of fall conditions, and the $2014-2015$ winter to be a more typical California winter.

Vertical salinity stratification occurs in San Pablo Bay shallows at 2 m MLLW on nearly every tidal cycle. For example, figure 4.2 shows 6 days of data from summer 2016, where $\frac{\partial S}{\partial z} < 0$ is induced near high water on most tides.

Horizontal and vertical stratification in San Pablo Bay shallows vary with tidal phase (figures 4.3 and 4.4). We apply two methods to compute horizontal stratification, one 'local' method, relying on measurements at a single site, and one 'non-local' method, relying on measurements at multiple sites. The non-local method computes $\frac{\partial S}{\partial x} = \frac{S_2 - S_1}{x_2 - x_1}$ in east/west (E/W) and north/south (N/S) components, by creating imaginary stations directly aligned with actual stations. For example, an imaginary station directly east of M1T is created by interpolating between M2T and N1T. Because of the grid configuration of stations (figure 4.1), this yields 1 E/W gradient estimate and $1-2$ N/S gradient estimates per deployment (figure 4.3, a and b). The local method (figure 4.4) is described in further detail in section 4.4.1.

The non-local method reveals that horizontal salinity gradients are stronger near high water, where they reach $18 * 10^{-4}$ (PSU/m) in E/W direction and $-8 * 10^{-4}$ (PSU/m) in N/S direction (figure 4.3, a and b). This implies that horizontal salinity gradients are stronger closer to the channel, and flood currents advect these stronger gradients into the shallows where they are measured by our network.

Vertical salinity gradients were near 0 during late ebb through mid-flood, and the strongest vertical stratification was observed near high water or early ebb, reaching -1 (PSU/m) (fig-

Site	Instrument	CHC13 Nov 13 - Feb 14	SPA Feb 14-Jun 14	SPB Jun 14 - Sep 14	SPC Sep 14 - Dec 14	CHC14 Dec 14- Feb 15	SPD Feb 15-Apr 15	CHC16 May 16 - Jun 16
N1T	RBR CTD	0.88	0.89	0.87	0.925	0.79	0.59	0.60
38.076°, −121.447°	Sontek ADV	0.305	0.30	0.30	0.33	0.295	0.335	–
N2T	RBR CTD	–	0.30	0.35	0.40	–	0.35	–
38.055°, −121.432°	RBR CTD	–	0.60 (bs)	0.60 (bs)	0.60 (bs)	–	1.80	–
M1T	RBR CTD	0.86	–	–	–	1.11	–	–
38.046°, −122.463°	Sontek ADV	0.315	–	–	–	–	–	–
	RBR CTD	–	–	–	–	0.56	–	0.30
M2T	RBR CTD	0.95	–	–	–	–	–	1.40
38.046°, −122.447°	Seabird CTD	0.66(bs)	–	–	–	–	–	0.84(bs)
	Sontek ADV	0.31	–	–	–	0.30	–	–
S1T	RBR CTD	0.91	0.87	0.90	0.97	0.91	0.90	0.50
38.013°, −122.465°	Sontek ADV	0.29	0.30	0.30	–	0.315	0.285	0.32

Table 4.1: Instruments deployed during the field campaign. Heights listed are as m above bed, except when noted as below surface (bs). All data is released under (Jessica R. Lacy, Allen, Foster-Martinez, Ferreira, & O'Neill, 2017)

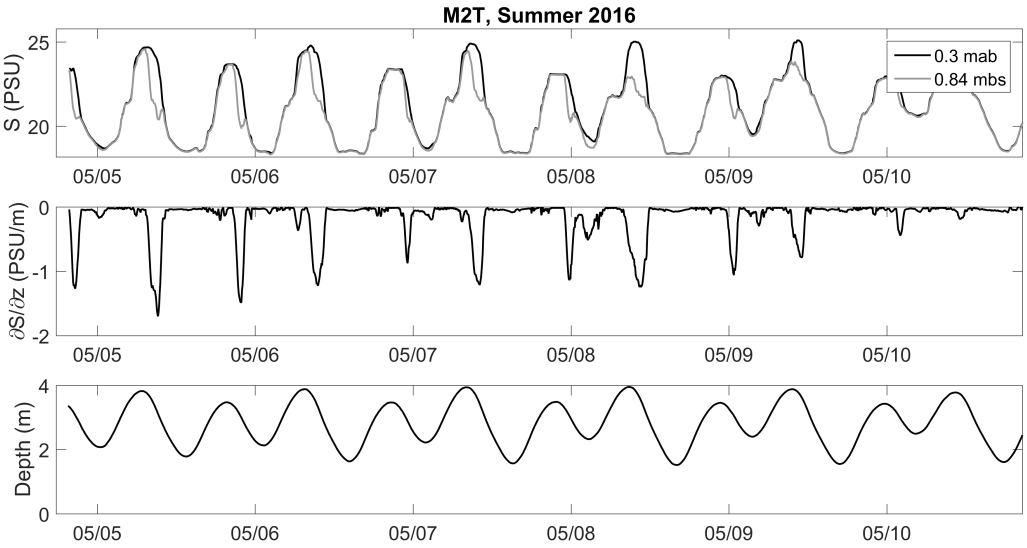

Figure 4.2: Stratification due to salinity occurs near high water on nearly every tidal cycle at 2 m MLLW (site M2T) in San Pablo Bay, during the summer 2016 deployment. Top: salinity measured at 0.3 m ab (black) and 0.84 m bs (grey). Middle: vertical salinity gradients ($\partial S/\partial z$) between the two sensors showing periodic stratification. Bottom: total water depth at the station. On some tides, e.g. mid-day on May 8, the bottom waters get saltier than the surface waters, causing stratification. On other tides, e.g. mid-day on May 5, the surface waters freshen before the bottom waters, yielding stratification.

ure 4.3d). The strongest vertical salinity gradients were seen during spring 2014 and 2015. It is likely that winter $2014-2015$ would also have shown strong vertical salinity gradients thanks to the December 2014 freshwater input, but the CTD in the upper water column at M2T failed during that deployment, and we were unable to observe vertical gradients.

4.3.1 Spatial Variability of Stratification

We capture spatial changes in salinity stratification through the local method. It assumes that temporal salinity variation at a site is due to advection only. Simplifying equation 4.1 by ignoring diffusion (the last term), we computed $\frac{\partial S}{\partial x}$ using co-located velocity measurements which were rotated to the dominant flood-ebb direction:

$$\frac{\partial S}{\partial x} = -\frac{1}{u}\frac{\partial S}{\partial t} \tag{4.5}$$

We removed values when $|u| < 0.02$ (m/s) so as to not overly magnify salinity gradients during slack water. However, horizontal salinity estimates from equation 4.5 are less accurate as velocities slow during high and low water.

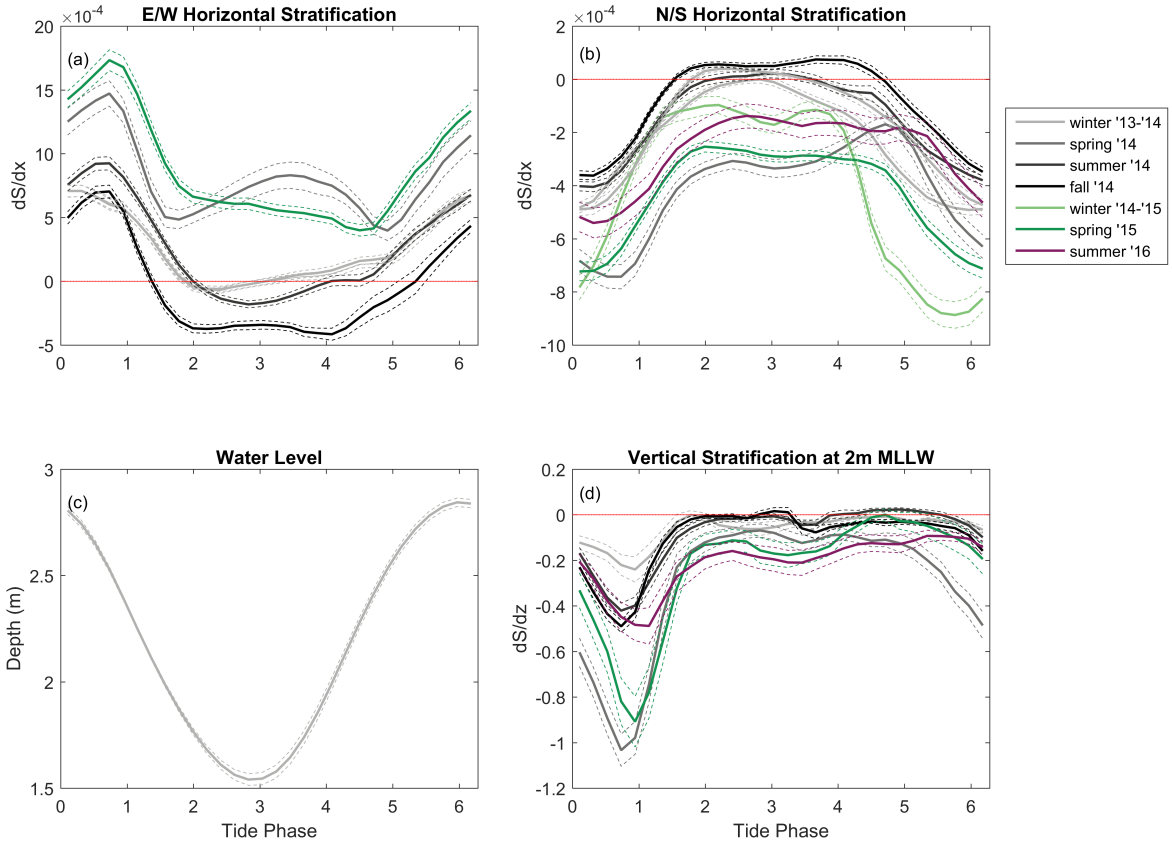

Figure 4.3: Horizontal and vertical stratification observed in San Pablo Bay shallows, phase averaged by tidal phase. Horizontal salinity gradients were computed between stations (the described 'non-local' method). Vertical salinity gradients were computed at stations M2T or N2T, depending on data availability (table 4.1). Dashed lines show standard error on the phase-averaged means. (a) Horizontal salinity gradients in the E/W direction, positive towards the east. (b) Horizontal salinity gradients in the N/S direction, positive towards the north. (c) Phase-averaged water level at site M1T during winter 2013 deployment, which is representative of phase-averaged water level at other sites and seasons. Note that high water occurs near 0 and 2π and low water occurs near π. (d) Vertical salinity gradients, positive upwards.

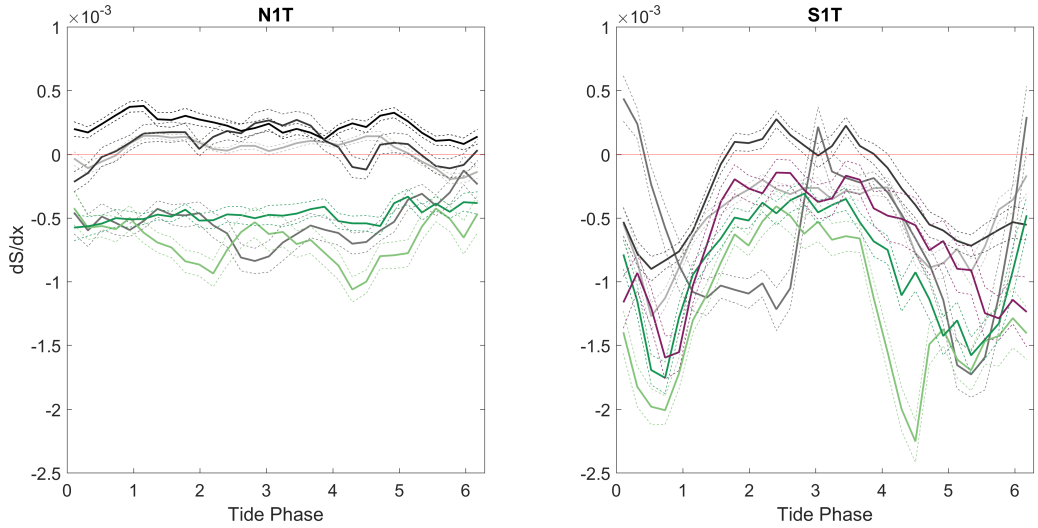

Figure 4.4: Phase-averaged horizontal salinity gradients computed locally on a seasonal basis at sites N1T and S1T. Dashed lines show standard error on the phase-averaged means. Seasons are represented by the same colors as figure 4.3.

At both sites N1T and S1T, flood tides were directed towards the northwest, closer to north at N1T. Thus, figure 4.4, which shows horizontal salinity gradients in the flood-ebb direction (x increases on-shore), is comparable to the non-local salinity gradients shown in figure 4.3b. This indicates that horizontal salinity gradients were stronger at S1T, and that S1T has more variation within the tidal cycle. This is consistent with the observation that horizontal gradients are stronger closer to the channel. The decrease in horizontal salinity gradients at S1T at high water indicates that the local estimate fails to capture the broader scale gradients at all tidal phases. The consistent salinity gradient at N1T across the tidal cycle shows that there is little spatial variation in the salinity gradient further in to San Pablo Bay (figure 4.4).

4.3.2 Seasonal Variability of Stratification

During periods of low freshwater input, we observe smaller lateral salinity gradients. On a non-local scale, winter $2013-2014$, summer 2014, and fall 2014 all show smaller salinity gradients in the E/W and N/S directions (figure 4.3, a and b).

The local salinity gradient at N1T is positive during winter $2013-2014$ and summer and fall 2014, and negative during the remaining deployments (figure 4.4). The positive gradient indicates that it is saltier on-shore and fresher towards the bay, that is, a reverse estuary. This reverse estuary appears during the dry periods of the deployment, in particular during the dry winter of $2013-2014$. This may be created by a long residence time in the bay, low freshwater input from local creeks during the dry season, and evapotranspiration in the

shallows, yielding higher salinity water near shore.

4.4 Separating Straining, Advection, and Mixing

The observed onset of stratification during flood contradicts the traditional model for salinity stratification in estuaries, which assumes that periodic salinity is due to along-channel straining during ebb tide only. Similar to Scully and Geyer, 2012 and Aristizabal and Chant, 2014, our data indicate that along-channel straining only is not adequate to describe the stratification.

We use a 'proof by contradiction' method to identify which of these mechanisms is responsible for the onset of stratification events at our site. We do this by assuming that only one of the mechanisms, for example SIPS, is responsible for a stratification event, and then showing that computed quantities are either consistent or inconsistent with this assumption.

4.4.1 Attributing Stratifying events

The onset of stratification must be due to some combination of straining and advection, since mixing can only act to reduce the gradients associated with stratification. First, we assume that stratification develops due to straining only, not frontal advection. Then equation 4.2 simplifies to

$$\frac{\partial}{\partial t}\left(\frac{\partial S}{\partial z}\right) = -\frac{\partial u}{\partial z}\frac{\partial S}{\partial x} \tag{4.6}$$

With our data, we can compute $\frac{\partial}{\partial t}\left(\frac{\partial S}{\partial z}\right)$, and we assume a constant $\frac{\partial S}{\partial x}$ of $-4*10^{-4}$ (PSU/m), consistent with winter/ spring conditions in the N/S direction (figure 4.3b). This allows us to solve for $\frac{\partial u}{\partial z}$ from equation 4.6. While we do not have measurements of $\frac{\partial u}{\partial z}$ because we have only a single velocity measurement at site M2T, we can check the computed $\frac{\partial u}{\partial z}$ by comparing its direction to the direction of the measured near-bottom velocity, at 0.3 mab. During most parts of the tidal cycle (with possible exceptions for short periods near slack water), we assume that the vertical shear should be oriented in the same direction as the near-bottom velocity. Thus, we check to see if $\frac{\partial u}{\partial z}/U > 0$. If this test holds, then our original assumption that straining is causing the observed stratification, is supported. If this test does not hold, then our assumption is not supported, and it is more likely that frontal advection is producing the observed stratification.

Similarly, if we assume that stratification occurs due to frontal advection (and again neglect mixing), then equation 4.2 simplifies to

$$\frac{\partial}{\partial t}\left(\frac{\partial S}{\partial z}\right) = -u\frac{\partial}{\partial x}\left(\frac{\partial S}{\partial z}\right) \tag{4.7}$$

Again, we can compute $\frac{\partial}{\partial t}\left(\frac{\partial S}{\partial z}\right)$, and we have measured near-bottom u. Thus, we solve for $\frac{\partial}{\partial x}\left(\frac{\partial S}{\partial z}\right)$. We expect stronger vertical stratification off-shore, with mixed conditions on-shore,

and the x-coordinate is defined to increase further on-shore, i.e. flood is positive. That is, $\frac{\partial S}{\partial z} < 0$ off-shore (smaller x), and $\frac{\partial S}{\partial z} \approx 0$ on-shore (larger x). Thus, $\frac{\partial}{\partial x}\left(\frac{\partial S}{\partial z}\right) > 0$. So, if we find this, then the assumption that frontal advection produced the observed stratification is supported. While, if $\frac{\partial}{\partial x}\left(\frac{\partial S}{\partial z}\right) < 0$, then it is more likely that straining produced the observed stratification.

Figures 4.5 and 4.6 show examples of stratification events where this strategy provides insight into the mechanism causing the stratification. In figure 4.5, the observed stratification onset is likely due to frontal advection, while in figure 4.6, the stratification is caused by SIPS.

During both winter $2013-2014$ and summer 2016 deployments, stratification occurred due to both SIPS and front mechanisms. As described above, we can identify periods when each mechanism is likely to be the dominant cause of stratification based on whether we find inconsistencies in equations 4.6 and 4.7. Initially, we identify stratification events as periods when $\frac{\partial S}{\partial z} < -0.2$. Events where the total top-bottom stratification difference does not drop below -0.5 PSU are removed, to avoid low water levels from amplifying small variations between the two sensors. The start (end) points of the stratification events are identified by locating the first (last) moment when a smoothed $\frac{\partial}{\partial t}\left(\frac{\partial S}{\partial z}\right)$ drops below $-2*10^{-6}$. Each event is then separated into 'stratification' and 'de-stratification' phases, divided by the point of maximum smoothed $\frac{\partial S}{\partial z}$.

We then categorize a stratification event as consistent with SIPS when $\frac{\partial u}{\partial z}/U$ computed through equation 4.6 is greater than 0. We also require that $\frac{\partial u}{\partial z} > 0.1$, which prevents small variations in $\frac{\partial}{\partial t}\left(\frac{\partial S}{\partial z}\right)$ from overly influencing the classification. Points thus classified are termed 'not-fronts'. Likewise, we identify periods consistent with frontal advection when $\frac{\partial}{\partial x}\left(\frac{\partial S}{\partial z}\right)$ from equation 4.7 is greater than $5*10^{-4}$. We also require that $|u| > 0.025$, which reduces the impact of small temporal fluctuations and small velocities. These points are called 'not-SIPS'.

When more than 25% of points within a stratification or de-stratification event are classified as 'not-fronts' or 'not-SIPS', we categorize the whole event as such. If both, or neither, are true, the event is considered 'unknown'. This yields classifications for individual points (denoted with red circles and blue x's) and entire stratifying or destratifying events (denoted with red, blue, or purple lines), as shown in figure 4.7.

Based on this analysis, of the 26 stratification events classified in winter $2013-2014$, stratification onset for 15 is not due to fronts, stratification onset for 9 is not due to SIPS, and 2 are unknown. The same analysis is applied to summer 2016 data. However, some classifications remain questionable due to uncertainty related to the tidal velocities (as noted in section 4.2.1) and likely due to the role of lateral velocities (figure 4.8). Thus, the assumption of a single horizontal salinity gradient and tidal currents from equation 4.2 may not hold, and we conclude that cross-flow salinity gradients and local fronts may drive the measured vertical salinity gradients. Because winter $2013-2014$ yielded a more complete data set with less indication of cross-flow dynamics, we focus the remaining analysis on those data.

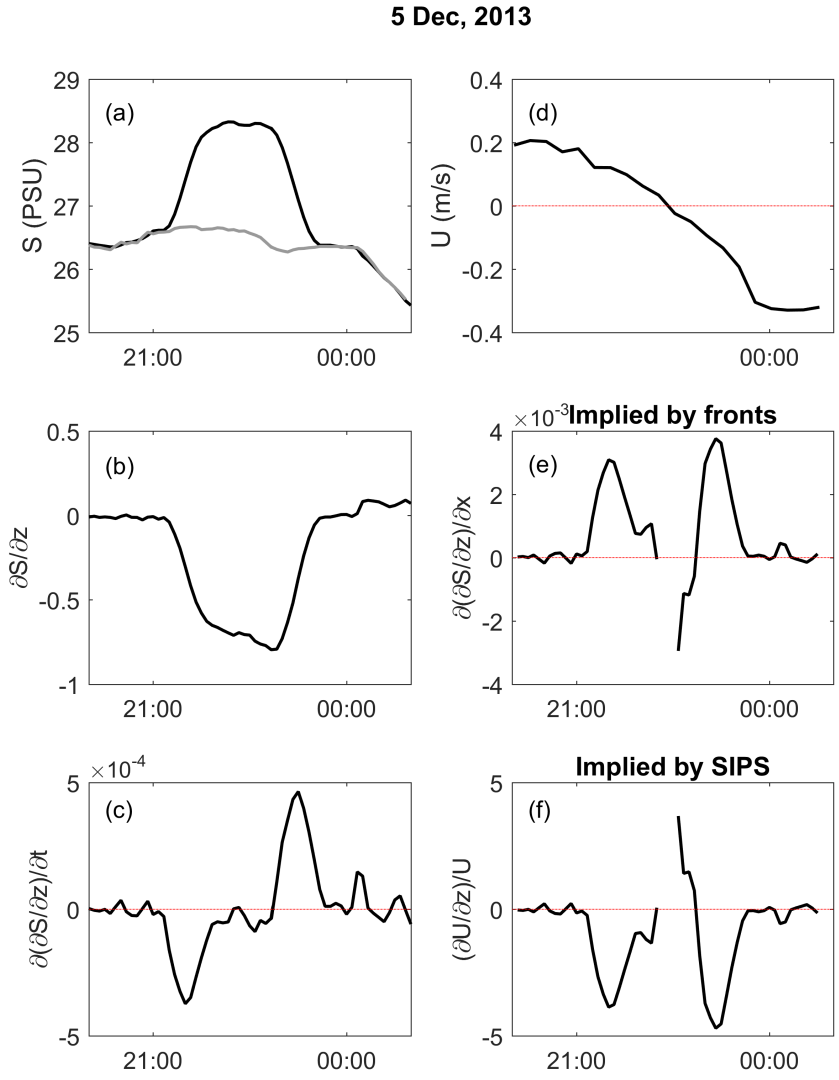

Figure 4.5: Stratification event observed on 5 December 2013, at site M2T. (a) Measured near-bottom (black) and near-surface (grey) salinities (PSU). (b) Computed vertical salinity stratification. (c) Computed time variation of vertical salinity stratification, which is negative during the stratification period, and positive during the de-stratification period. (d) Measured near-bottom velocity, flood positive. (e) Computed horizontal variation in vertical salinity gradients, assuming equation 4.7 holds. Positive $\frac{\partial}{\partial x}\left(\frac{\partial S}{\partial z}\right)$ indicates that this assumption is consistent with the observed event. (f) Computed $\frac{\partial U}{\partial z}$ assuming equation 4.6, divided by measured U. Negative $\frac{\partial U}{\partial z}/U$ indicates that $\frac{\partial U}{\partial z}$ and U have opposite signs, and the observed stratification event is likely not due to straining.

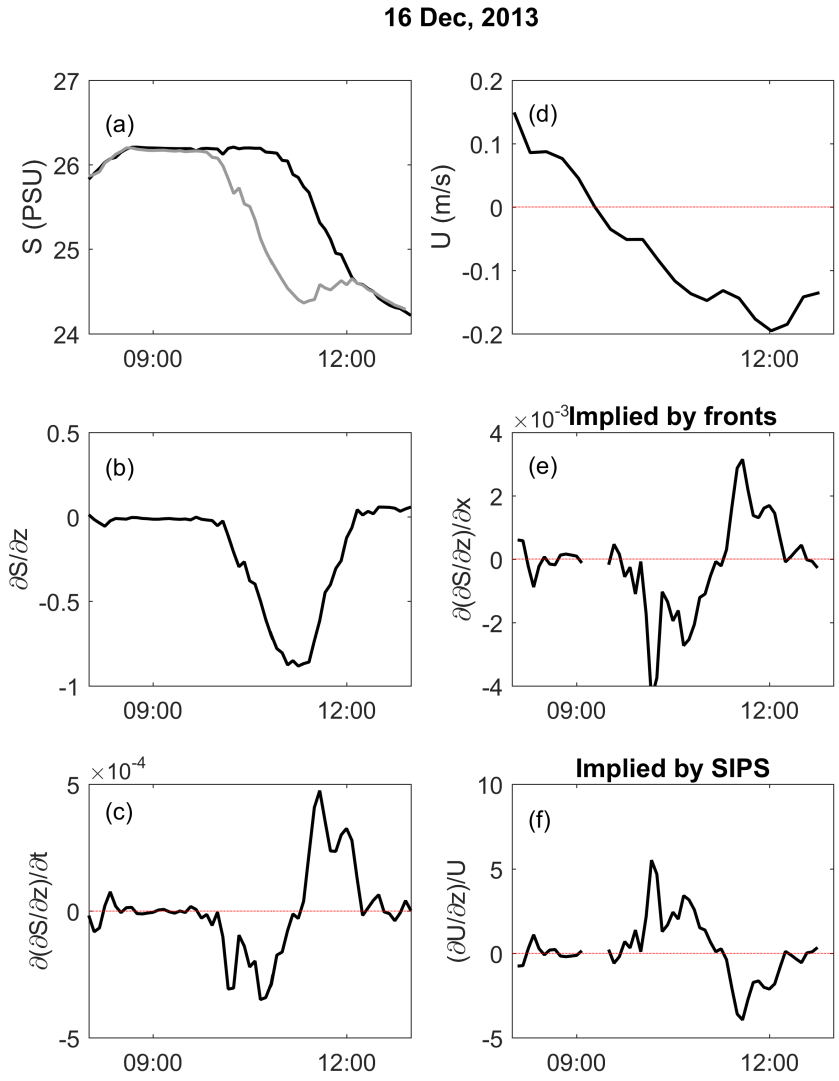

Figure 4.6: Stratification event observed on 16 December 2013, at site M2T. (a) Measured near-bottom (black) and near-surface (grey) salinities (PSU). (b) Computed vertical salinity stratification. (c) Computed time variation of vertical salinity stratification, which is negative during the stratification period, and positive during the de-stratification period. (d) Measured near-bottom velocity, flood positive. (e) Computed horizontal variation in vertical salinity gradients, assuming equation 4.7 holds. Negative $\frac{\partial}{\partial x}\left(\frac{\partial S}{\partial z}\right)$ during the stratification period indicates that the onset of stratification is likely not due to frontal advection. Positive $\frac{\partial}{\partial x}\left(\frac{\partial S}{\partial z}\right)$ during the de-stratification period indicates that the removal of stratification may be due to frontal advection. (f) Computed $\frac{\partial U}{\partial z}$ assuming equation 4.6, divided by measured U. Positive $\frac{\partial U}{\partial z}/U$ during the onset of stratification indicates that the observed stratification may be created due to straining. Negative $\frac{\partial U}{\partial z}/U$ during the removal of stratification indicates that de-stratification is likely not due to straining.

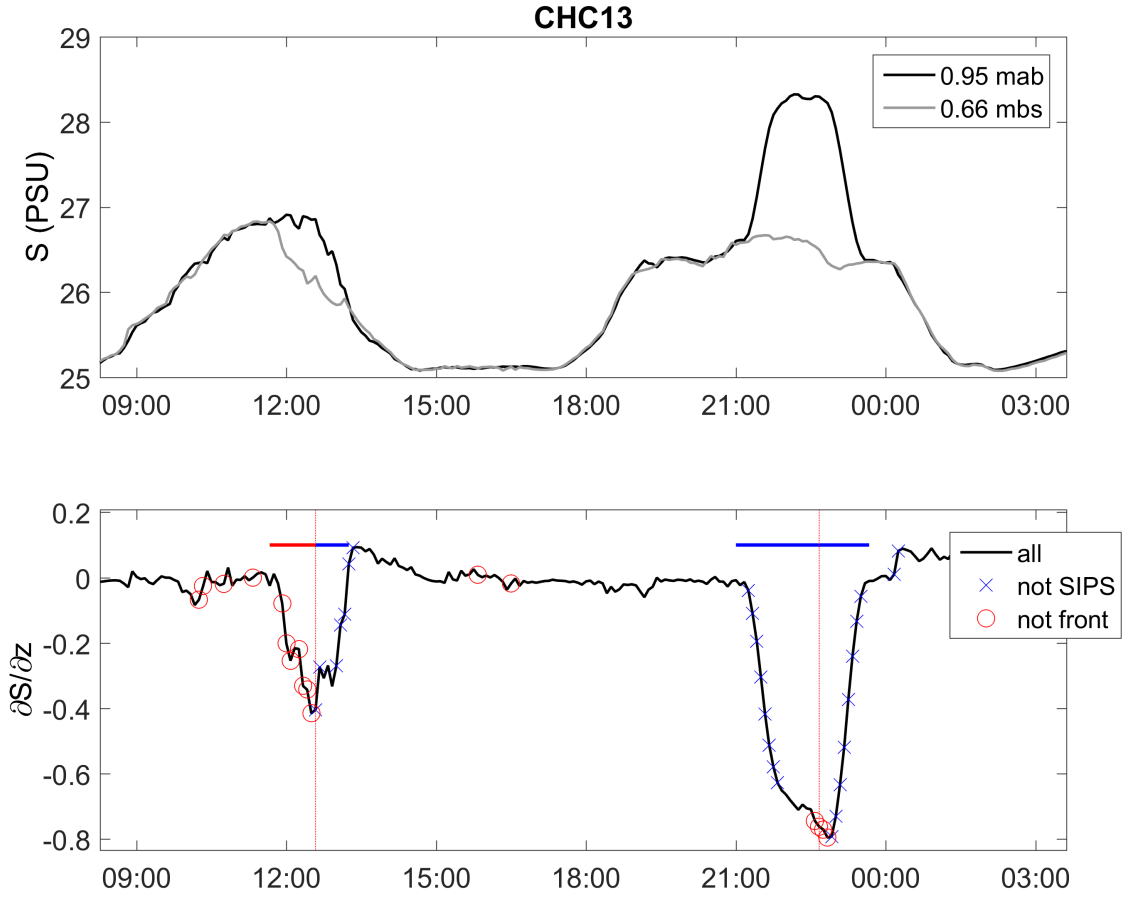

Figure 4.7: Top: Near-bottom (black) and near-surface (grey) salinities, from winter 2013 deployment at site M2T. Bottom: Measured $\frac{\partial S}{\partial z}$. Red circles and blue x's show times when equations 4.6 and 4.7 yield contradictions, respectively. Horizontal lines denote periods of stratifying and de-stratifying events, and are red or blue if the period has been identified as 'not fronts' or 'not SIPS', respectively.

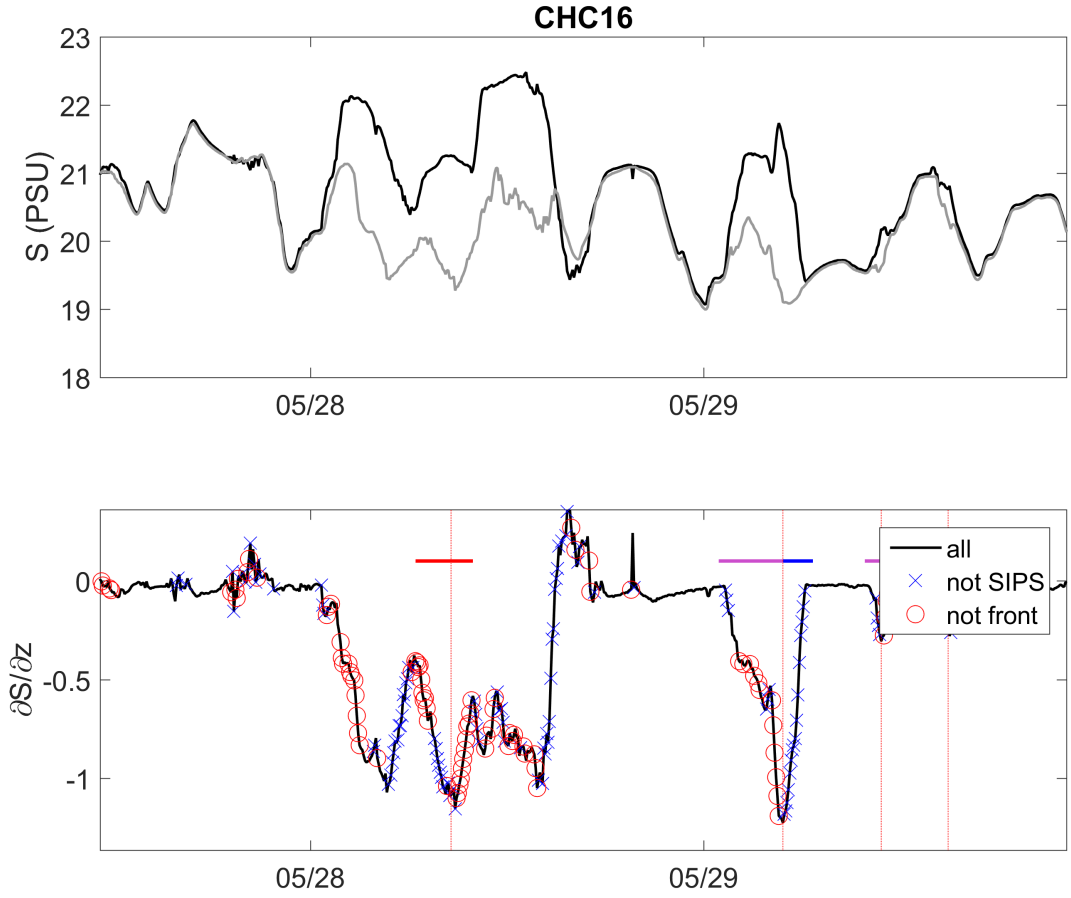

Figure 4.8: Top: Near-bottom (black) and near-surface (grey) salinities, from summer 2016 deployment at site M2T. Bottom: Measured $\frac{\partial S}{\partial z}$. Red circles and blue x's show times when equations 4.6 and 4.7 yield contradictions, respectively. Horizontal lines denote periods of stratifying and de-stratifying events, and are red, blue, or purple if the period has been identified as 'not fronts', 'not SIPS', or 'unknown', respectively. The stratification event on May 28, 2016 does not lend itself to simple classification.

4.4.2 Attributing Destratification Mechanisms

While we can apply equations 4.6 and 4.7 to both stratifying and de-stratifying events, the assumption that diffusion can be ignored may not be valid for de-stratification. Because diffusion acts counter to gradients, it is safe to ignore diffusion when considering the creation of gradients. However, for gradient destruction, diffusion and mixing as well as frontal advection and straining may play a role. Despite this, we attribute de-stratification events as described in section 4.4.1, regardless of the potential contribution of turbulent mixing.

To discern the role of mixing in de-stratifying the flow, we compute Si (equation 4.4), applying an assumed salinity gradient of $\frac{\partial S}{\partial x} = -4 * 10^{-4}$ (PSU/m) for each point in time. We use a constant salinity gradient to reduce the variability in Si. The friction velocity, u_* is computed via $u_*^2 = \sqrt{\overline{u'w'}^2 + \overline{v'w'}^2}$, where the contaminating influence of waves was removed from the Reynolds stress estimates, $\overline{u'w'}$ and $\overline{v'w'}$, by wave-turbulence decomposition (Shaw & Trowbridge, 2001; Feddersen & Williams, 2007). Geyer and MacCready, 2014 report that $Si \approx 0.2$ represents the transition between full water column mixing and permanently stratified conditions. Because we apply an assumed lateral salinity gradient, the precise magnitude of Si is not meaningful, but relative changes are.

For all stratification events, we compute the median Si during the stratification phase and during the destratification phase (figure 4.9). As expected, we observe relatively high Si during the stratification phase, since turbulent mixing is not strong enough to suppress the stratifying dynamics. Figure 4.9 denotes each event by whether the onset phase is classified as 'not SIPS', 'not fronts', or 'unknown'. For most 'not front' events, Si is larger during the stratification phase than the destratification phase, and is below 1 for all events during the destratification phase. This suggests that while these events are created due to tidal straining, their destruction is due to mixing. Of the 7 identified 'not SIPS' events, 4 fall near the $1:1$ line, and have relatively high Si on both the stratifying and destratifying phases. This suggests that both their onset and removal are due to frontal advection. For the other 3 'not SIPS' events, Si is larger during the stratifying phase than during the destratifying phase, suggesting that while stratification onset is likely due to frontal advection, its removal is due to mixing. In bulk, these results suggest that stratification events caused by SIPS are often destroyed through mixing, but stratification due to frontal advection can be removed through advective or mixing processes.

4.4.3 Analytical Framework

The observations discussed in section 4.4 show that two mechanisms are responsible for creating vertical salinity stratification in San Pablo Bay shallows. These observations only lightly touch on the role of mixing in permitting stratification to form and destroying it. In the following section, we present an analytical framework that considers the role of vertical mixing and the balance between vertical mixing and advection of well-mixed waters in removing salinity gradients. This idealized framework assumes a 2D salinity gradient exists over a sloping bed (figure 4.10), representing broad estuarine systems like the San Pablo Bay

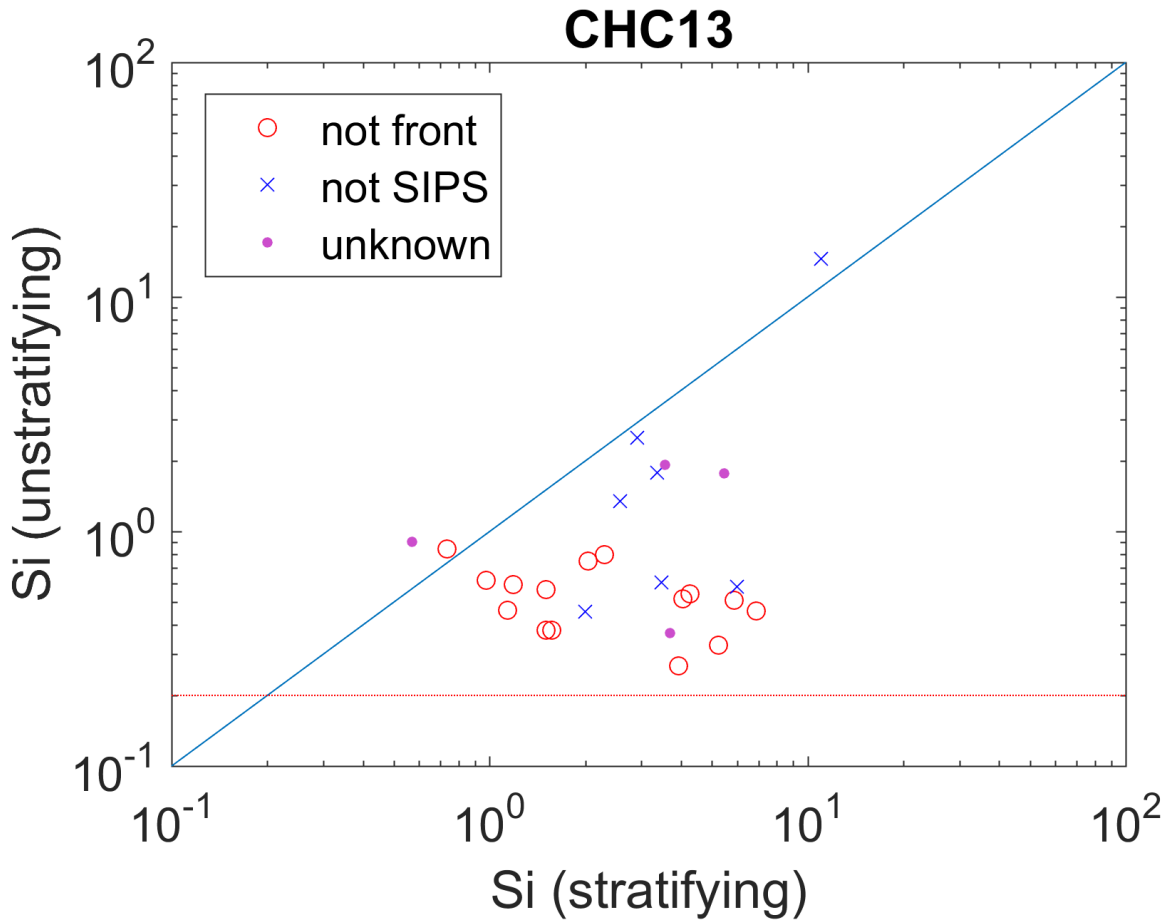

Figure 4.9: Median Si from periods of stratification events. The x-axis shows the median Si during the stratifying phase of the event, and the y-axis plots the median Si during the de-stratifying phase of the event. Red circles, blue x's and purple dots denote events identified as 'not fronts','not SIPS', or 'unknown' based on the stratifying phase, respectively. A 1:1 line is shown in blue, and a horizontal line at $Si = 0.2$ shows the critical Simpson number. Red circles tend to have higher Si during the stratifying phase than during the un-stratifying phase, indicating that mixing is stronger during the de-stratifying phase. For some blue x's, Si is similar during the stratifying and un-stratifying phases, suggesting that both the stratification and de-stratification occur due to similar mechanisms, likely frontal advection. Other blue x's have large Si on the stratifying phase with lower Si on the de-stratifying phase, suggesting that the onset of stratification is due to frontal advection, but the disappearance of stratification is due to mixing.

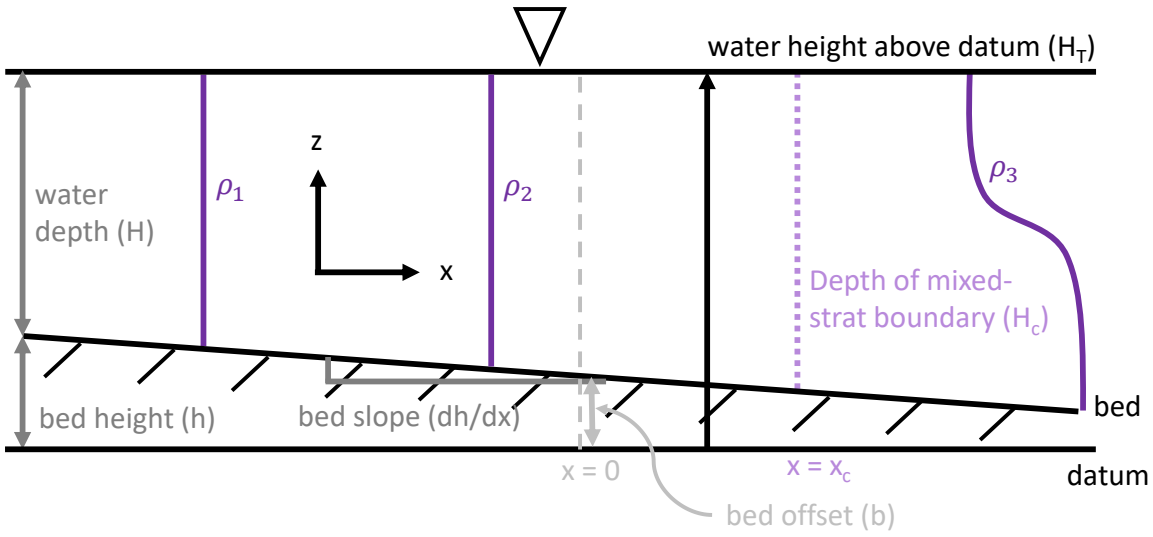

Figure 4.10: Two-dimensional idealized estuarine system. The delineation between vertically well-mixed and possibly stratified, associated with $Si = Si_c$, occurs at critical depth H_c and x-location x_c. Density profiles are shown in purple, with less dense waters found on-shore.

shallows. We assume that lateral (along-shore) variation in depth, bed slope, currents, and salinity gradients are negligible.

The Simpson number, equation 4.4, has small values when mixing is strong enough to overcome strain-induced stratification. At some critical value, Si_c, mixing is weak enough such that stratification is possible. Rearranging equation 4.4 with Si_c yields a critical water depth:

$$H_c = \sqrt{\frac{Si_c u_*^2}{\frac{-g}{\rho}\frac{\partial \rho}{\partial x}}} \tag{4.8}$$

At depths greater than H_c, stratification is possible. At smaller depths, turbulence is strong enough to mix the full water column.

Along a sloping bed, the location of this regime shift between well-mixed and potentially stratified moves horizontally as the critical depth changes. The bed height is given by $h(x) = -\frac{dh}{dx}x + b$, where b is the bed height at $x = 0$, and the total water depth changes tidally, as $H(x) = H_T - h(x)$. Thus, solving for the x-location of the critical depth H_c, yields

$$x_c = \frac{(H_c + b - H_T)}{dh/dx} \tag{4.9}$$

x_c moves landward or seaward as H_c and H_T change in time, the former due to changes in u_* associated with mean current speed and the latter with water level from the tides. We

define the rate of this movement:

$$u_c \equiv \frac{\partial x_c}{\partial t}. \tag{4.10}$$

Because this velocity describes the translation of where vertical stratification is *possible* rather than where vertical stratification actually *exists*, we call it the 'mixed-stratified delineation' velocity. When u_c is directed bay-ward and assuming that this process controls the balance between mixed and stratified, the frontal boundary will move bay-ward at u_c. When u_c is directed land-ward, it describes the possibility of vertical stratification (induced by straining or advective processes) existing, not necessarily the rate of vertical stratification or fronts moving on-shore.

Using parameters appropriate for San Pablo Bay, namely tidal range $H = 1$ m, bed slope $\frac{\partial h}{\partial x} = 1/2000$, tidal velocity magnitude $U = 0.4$ (m/s), water level above the datum $H_{base} = 3$ m, horizontal density gradient $\frac{\partial \rho}{\partial x} = -4 * 10^{-4}$ kg/m^3/m, drag coefficient $C_D = 0.003$, and critical Simpson number $Si_c = 0.2$, the delineation between mixed and stratified moves across 10 km of mudflats every tidal cycle (figure 4.11c). The velocity of this delineation, u_c, is much larger than the tidal advective velocity, U_{tides}, (figure 4.11d), which indicates that it is unlikely that advection of well-mixed waters off-shore during ebb erases the observed stratification. Rather, it is more likely that mixing erases the observed stratification, thanks to the translation of this delineation off-shore as turbulence increases with ebb velocities.

To distinguish between the role of mixing (due to current induced turbulence) and water level in contributing to the mixed/stratified delineation velocity, we compute the components of u_c. The full form of equation 4.10, once combined with equation 4.9, gives

$$u_c = \frac{1}{dh/dx}\left(\frac{\partial H_c}{\partial t} + \frac{\partial b}{\partial t} - \frac{\partial H_T}{\partial t}\right) \tag{4.11}$$

Note that

$$\frac{\partial H_c}{\partial t} = \frac{U}{N}\omega\sqrt{Si_c C_D}\frac{\sin(\omega t)}{\sqrt{\sin^2(\omega t)}}\cos(\omega t) \tag{4.12}$$

, $\frac{\partial b}{\partial t} = 0$, and

$$\frac{\partial H_T}{\partial t} = -H\omega\sin(\omega t) \tag{4.13}$$

Here, $N^2 = \frac{-g}{\rho}\frac{d\rho}{dx}$ is the horizontal buoyancy frequency. The roles of the variation in mixing depth ($\partial H_c/\partial t$) and water level ($\partial H_T/\partial t$) in u_c are thus comparable (figure 4.12).

For the parameters representing San Pablo Bay, we find that u_c is larger than U_{tides}, indicating that it is more likely that mixing controls destratification than frontal advection (figure 4.11d). However, other systems, characterized by other values of tidal range, H, bed slope, $\frac{dh}{dx}$, horizontal density gradient, $\frac{\partial \rho}{\partial x}$, or critical Simpson number, Si_c, may not behave similarly. To test the role of parameters in controlling these processes, we investigated the parameter space (figure 4.13).

In exploring the parameter space, we allowed 2 parameters to vary while keeping the other 2 fixed at the values for San Pablo Bay. Figure 4.13 shows contour plots of $\log_{10}(|U_{tides}|/|u_c|)$

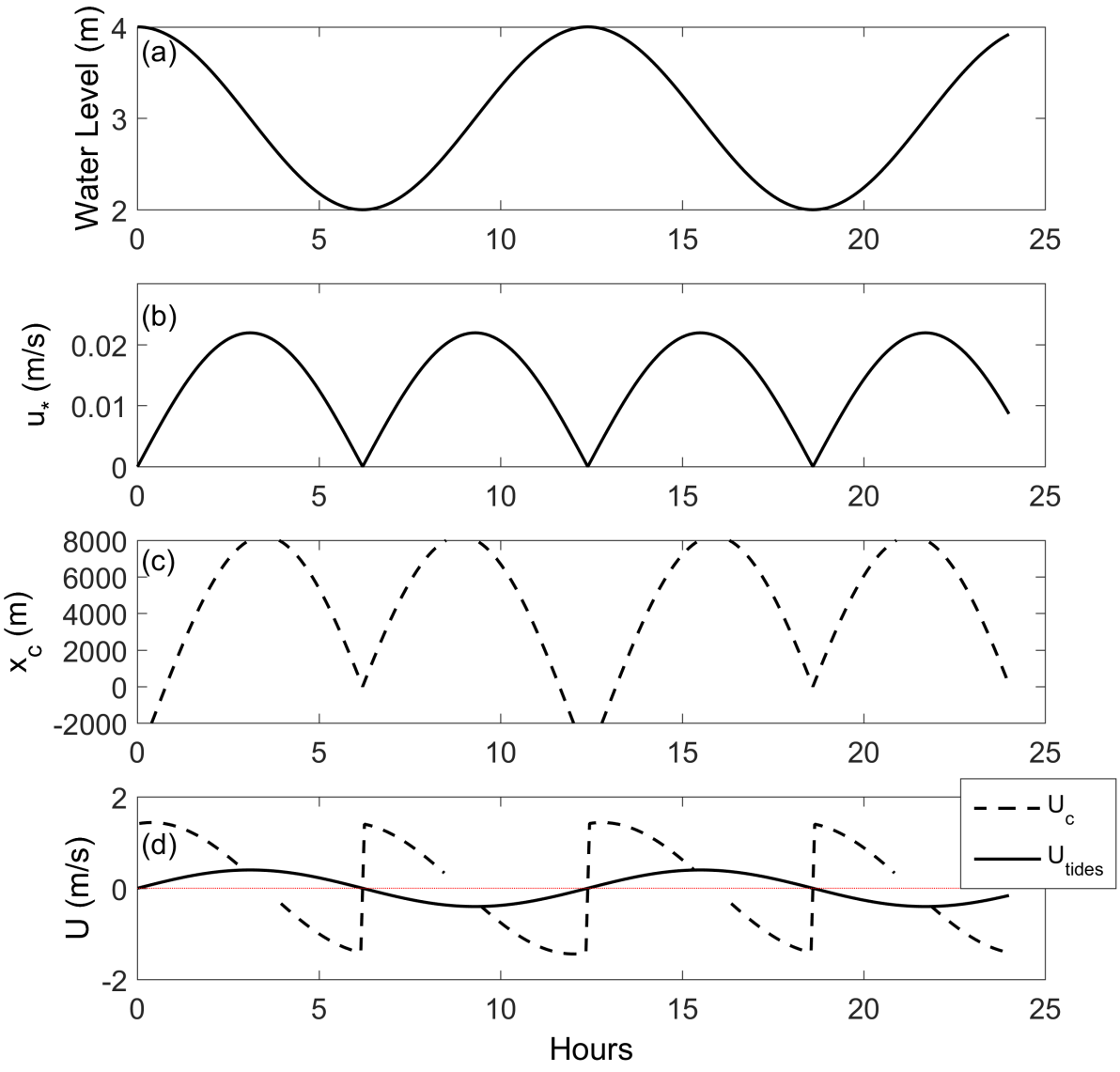

Figure 4.11: (a) Water level (H_T) defined by an artificial M2 tide: $H_T = r\cos(\omega t) + H_{base}$, plotted for a 24-hour day. (b) Friction velocity (u_*) created by tidal currents, where $U_{tides} = -U\sin(\omega t)$ and $u_*^2 = C_D U_{tides}^2$. (c) Horizontal position of the delineation between mixed and potentially stratified, x_c, equation 4.9. Note that positive x-position is more bay-ward, as sketched in figure 4.10. (d) Comparison between advective velocity due to tides, U_{tides} and translation speed of the mixed/stratified delineation, U_c, equation 4.10. Note that ebb velocities are positive. U_c is larger in magnitude than U_{tides}, suggesting that for the parameters shown here, de-stratification will occur due to mixing, rather than advection of well-mixed waters.

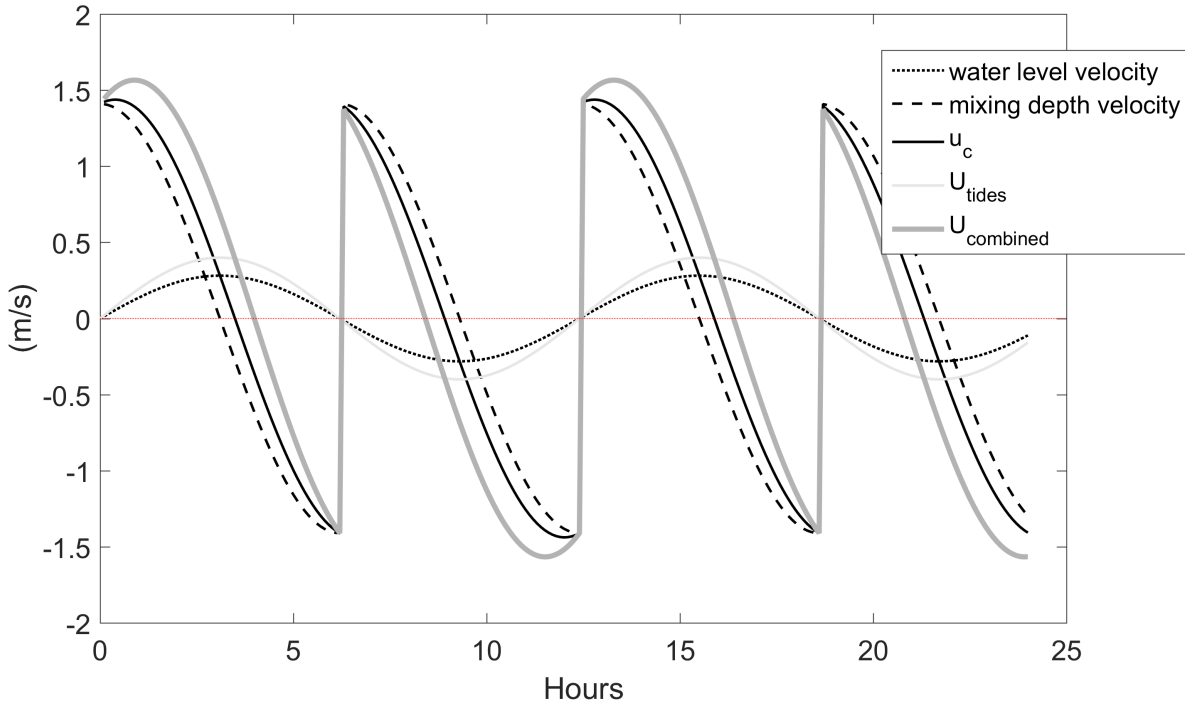

Figure 4.12: Constituents of the velocities affecting de-stratification; ebb is positive. Water level velocity and mixing depth velocity represent equation 4.13 and equation 4.12, respectively. u_c is computed as the sum of water level velocity and mixing depth velocity, equation 4.11. Advective tidal velocity, $U_{tides} = -U\sin(\omega t)$. $U_{combined} = u_c + U_{tides}$ represents the combined effect of x_c translation and tidal advection on the location of de-stratification. The strongest role is played by the mixing depth velocity, with water level velocity and tidal advection acting together. During early ebb, all components are directed off-shore, while during late ebb the mixing depth velocity is oriented on-shore, even though the water depth velocity and tidal advection are still directed off-shore. This is reversed during early flood, when strong mixing pushes x_c off-shore, while rising water level and flood velocities push it on-shore. During late flood mixing intensity declines, and the possibility of stratified waters is pushed on-shore by all three components.

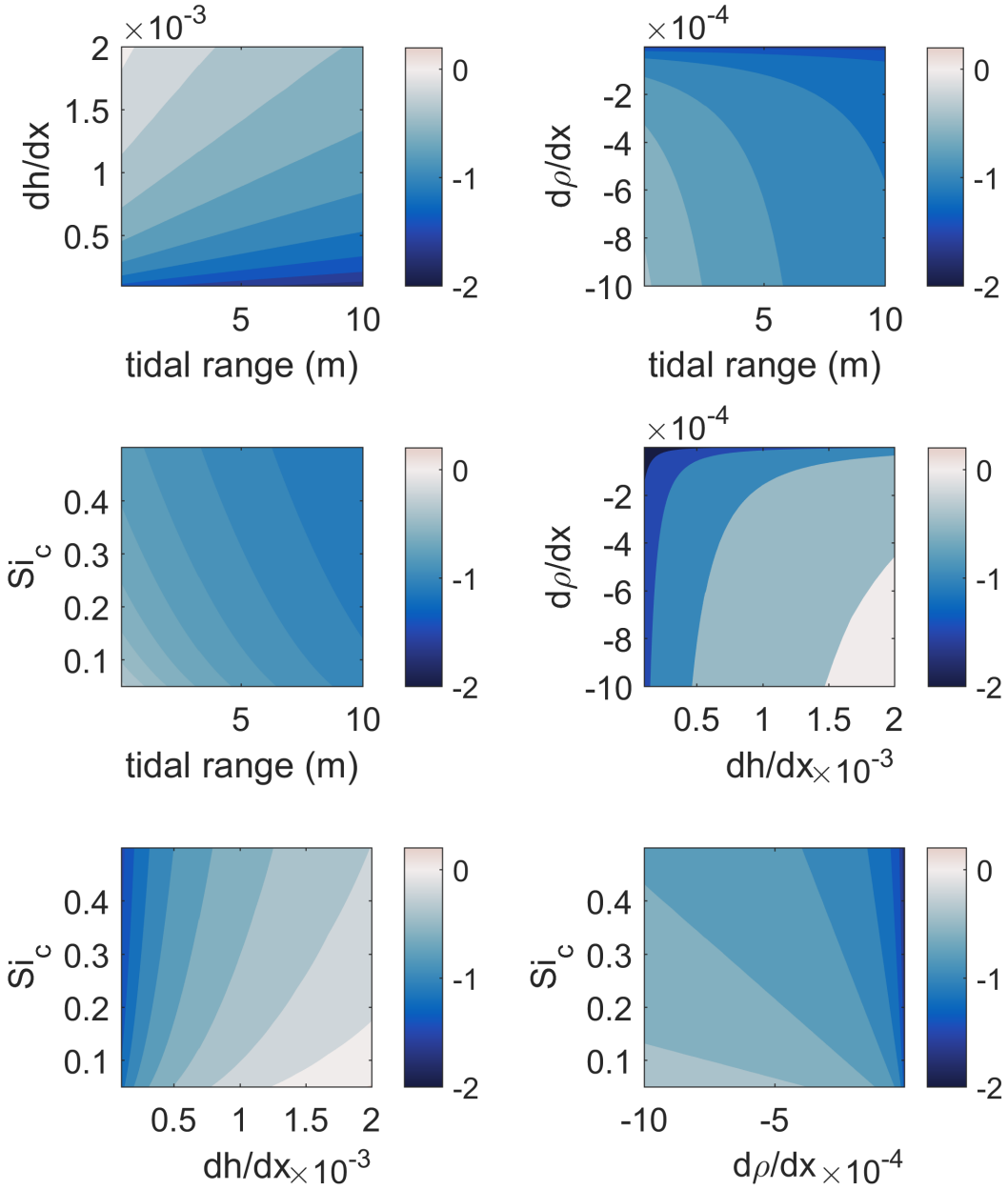

Figure 4.13: Variation in parameter values affects the relative magnitude of tides and mixing velocities. Each figure shows $\log_{10}(|U_{tides}|/|u_c|)$. Thus, negative values indicate that u_c is larger, and positive values indicate that U_{tides} is larger. For each figure, two parameters are allowed to vary, while the other two remain fixed. Tidal range (H) varies between 0.1 and 10 m, bed slope (dh/dx) varies between 1/500 and 1/10000, horizontal density gradient ($\partial\rho/\partial x$) varies between -10^{-6} and -10^{-3} kg/m^4, and critical Simpson number (Si_c) varies between 0.05 and 0.5. When parameters were held constant, $H = 1$, $dh/dx = 1/2000$, $d\rho/dx = -4 * 10^{-4}$, and $Si_c = 0.2$.

given the 2 varying parameters. Negative values indicate that u_c is larger (and the dominant process), while positive values indicate that U_{tides} is larger. Except for a few extreme cases, we saw negative values of $\log_{10}(|U_{tides}|/|u_c|)$. This is consistent with our finding above that mixing is the primary control on destratification in shallow estuarine systems with sloping beds, not only in the idealized San Pablo Bay case.

The parameter space exploration shows that $|u_c|$ increases relative to $|U_{tides}|$ when tidal range increases, when bed slope decreases, when salinity gradients get weaker, and for larger values of Si_c (figure 4.13). Of the parameter ranges tested, bed slope has a particularly large impact on the controlling processes, while tidal range has less of an effect. Tidal range affects the 'water level velocity' only, with a larger tidal range causing faster $\frac{\partial H_T}{\partial t}$ (equation 4.13). When bed slope is small, $\log_{10}(|U_{tides}|/|u_c|) \approx -2$, indicating that mixing dynamics translate much faster than tidal advection. At such bed slopes, the role of the second parameter (H, $\frac{\partial \rho}{\partial x}$, and Si_c) is reduced: the small bed slope results in such large horizontal shifts needed to accommodate small shifts in H_c and H_T that the effect of variation in the second parameter is overridden. Strong horizontal salinity gradients (large N) can produce stronger vertical salinity gradients, which require more turbulent energy to overturn. Thus, stronger $\frac{d\rho}{dx}$ implies a smaller critical depth, H_c, and slower $\frac{\partial H_c}{\partial t}$ (equation 4.12). Finally, we varied Si_c not to represent a change in the physical system, but to reflect the uncertainty in this critical value. As Si_c increases, the critical depth at which full water column mixing is no longer possible increases, and $\frac{\partial H_c}{\partial t}$ increases (equation 4.12).

4.5 Discussion

4.5.1 Variation of Stratification Dynamics

While the role of SIPS in producing estuarine stratification is well-established, fewer studies have focused on the role of frontal advection in yielding local stratification. In particular, the balance between these two mechanisms in producing stratification in broad estuarine shallows is not well characterized. We show that vertical salinity stratification appears regularly in the estuarine shallows of San Pablo Bay, due in nearly equal measure to frontal advection and strain-induced periodic stratification (SIPS). Because frontal advection relies on an existing vertical gradient, the appearance of such stratification in estuarine shallows suggests that there exists a long-term decoupling between surface and bottom waters. This allows a reduction in mixing, a reduction of exchange between the surface and bottom, and potentially oxygen depleted bottom waters.

While the broad extent of the shallows in San Pablo Bay suggests that the front that induces stratification may endure from one tidal cycle to the next, our analysis of the mixed-stratified boundary indicates that mixing erases stratification in shallow systems such as San Pablo Bay. Thus, there is a connection between the shallows and the tidal channel that regularly influences stratification in the mudflat.

4.5.2 Implications for Stratification Dynamics

On a spring-neap timescale, the compressed tidal range during neap periods may result in a smaller role of frontal advection in producing stratification in the shallows.

On a seasonal timescale, we noticed how the direction of lateral stratification changed between high and low water during dry seasons. During high water, the higher salinities were bay-ward, as seen throughout the tidal period during wetter seasons. During low water, however, higher salinities were found landward. This may result from a reduction in total freshwater supply to the system and evapotranspiration. Such a seasonal shift in the direction of lateral stratification can indicate the extent of mixing in the bay, and signal a divide between water that encounters the channel and water that is perpetually in the shoals.

4.6 Conclusions

In this work, we characterize the mechanisms controlling periodic vertical salinity stratification in estuarine shallows. We observed the onset of vertical salinity gradients due to two mechanisms: tidal straining and frontal advection.

Similar to methods applied by J. H. Simpson et al., 1990, Scully and Geyer, 2012, and Aristizabal and Chant, 2014, we are attempting to attribute physical mechanisms to observed salinity gradients. In contrast to these previous works, our analysis investigates not only the temporal variation of salinity gradients, but also adds a focus on the frontal boundary movement in space. This characterization elucidates the competition between destratification mechanisms.

Chapter 5

Hydrodynamics and Sediment Dynamics in San Francisco Estuary Margins

5.1 Introduction

As sea levels rise in the coming decades, tidal marshes will need to increase their elevation by up to 2.6 cm/year by 2100 to combat the increase in water level, and bay-sourced sediment is an important part of this marsh growth (Knowles, 2010). Understanding how sediment particles are transported and deposit in the shallowest part of the estuary will be key to making accurate predictions for sea level rise. However, we currently have trouble predicting suspended sediment transport in part because numerical models require parameterization and lack adequate field measurements of the parameters. The rate of particle settling, known as settling velocity, w_s, is one of these parameters, and appropriate values in San Francisco Bay are not fully explored in space and applicability.

Settling velocities are hard to predict: we have not yet found the universal relationship between particle properties and settling velocity, even in still water (Burd & Jackson, 2009). For spherical particles of diameter D, in the creeping flow regime ($Re_p < 5$), the Stokes settling velocity is given by

$$w_s = \frac{(\rho_s - \rho_w)\, g D^2}{18\mu} \tag{5.1}$$

where $Re_p = \frac{w_s D}{\nu}$ and ρ_s and ρ_w give the densities of the particle and the water, respectively. For dense ($\rho_s = 2600$ kg/m^3) particles, equation 5.1 describes the settling velocities up to diameter $D = 180$ μm. Another empirical model allows us to predict settling velocities of larger non-flocculated particles in quiescent flow based on particle size, density, shape, and smoothness (Dietrich, 1982). While this applies in limited circumstances only, the relationship between size and settling velocity remains: at constant density, larger particles fall

faster. Therefore, understanding the size of particles is an important step towards predicting their settling velocity.

Many particles in estuarine systems are aggregates, which requires understanding particle porosity through, for example, fractal dimension, as well as particle size. One study of suspended particles in San Francisco Bay found that average floc diameters varied between 81 to 163 μm, with the full size distribution ranging between 50 and 1000 μm (Mehta, 2014). Flocs are formed from smaller particles colliding with each other and sticking, so we describe the particle dynamics on a size-class by size-class basis. For a given particle size class of mass m, the rate of change of number concentration, n, is given by

$$\begin{aligned}\frac{dn(m,t)}{dt} =& \frac{\alpha}{2}\int_0^m \beta\left(m_j, m-m_j\right) n\left(m-m_j,t\right) n\left(m_j,t\right) dm_j \\ &- \alpha n\left(m,t\right)\int_0^\infty \beta\left(m,m_j\right) n\left(m_j,t\right) dm_j \\ &- n\left(m,t\right)\frac{w_s\left(m\right)}{Z} + I\left(m,t\right)\end{aligned} \tag{5.2}$$

where m, m_j, and $m-m_j$ are the masses of the particles that are interacting. The first term on the right describes aggregation from particles of size m_j and $m-m_j$, to form particles of size m. The coagulation kernel, $\beta\left(m_j, m-m_j\right)$, determines the rate of collisions between particles of the two sizes. The probability that two particles will stick once they have collided is given by α, that is, their collision efficiency. The second term on the right is the removal of particles of size m due to coagulation with another particle. The third term is loss due to settling, at rate $w_s\left(m\right)$, through a water layer of depth Z, and the fourth term is input of particles of size m (Burd & Jackson, 2009).

The coagulation kernel contains three mechanisms for particle collision: Brownian motion, fluid shear, and differential settling. The relative importance of each of these depends on the particle size and the flow conditions, including turbulence. In particular, turbulence increases shear, yielding an increase in collisions. At small particle sizes, Brownian motion can dominate the occurrence of collisions, while at large particle sizes, differential sedimentation dominates (Lambert & Variano, 2016).

One simple model for settling velocities and flocculation assumes that differential settling and Brownian motion are not important for collisions (Stolzenbach & Elimelech, 1994). It also assumes that the non-linear correction to the drag law can be ignored, flocs all have a fractal dimension of 2, and flocs are subject to consistent turbulence conditions for long enough to reach their equilibrium size (Winterwerp, 1998). Given these simplifications, it combines a flocculation model with a settling velocity model to predict the floc settling velocity at equilibrium, $w_{s,e}$.

$$w_{s,e} = w_{s,p} + \alpha' \frac{k_A}{k_B} D_p \frac{\Delta g}{\nu}\frac{C}{\sqrt{G}} \tag{5.3}$$

Here, $w_{s,p}$ is the settling velocity of the primary particles, α' represents particle shape, k_A and k_B are empirical parameters, $\Delta = \left(\rho_s - \rho_w\right)/\rho_w$, C is the suspended matter concen-

tration, G quantifies the turbulent shear, and D_p is the diameter of the primary particles (Winterwerp, 1998). Once parameterized to a specific location, this model enables prediction of floc settling velocities based on ambient conditions, including turbulent shear, suspended sediment concentration, and primary particle diameter.

Turbulence can affect floc form, and thus affect settling velocities in a few important ways. It can alter the flow characteristics to shift the particle size distributions of flocs. At low energy levels, increasing the turbulence will primarily increase collisions, leading to larger flocs. However at higher energy levels, turbulence increases breakup of flocs through shear, driving the population distribution towards smaller flocs. If the timescale for floc coagulation or breakup is much larger than the timescale on which the turbulence changes, the primary effect of increased turbulence can be to resuspend material into the water column, shifting the suspended population towards a coarser distribution. Finally, simplified models suggest that turbulence may increase particle settling rates by preferentially sweeping falling particles into downward-moving flow, or alternately, it may decrease settling rates by trapping particles in vortical flow regions (Monchaux, Bourgoin, & Cartellier, 2012). Which of these mechanisms occurs in real-world flows, and how strongly it matters, remain open questions. Some measurements of these effects suggest that settling velocities are altered enough in turbulence to strongly change the vertical distribution of sediment, however none of these studies apply to the case of fine sediments in estuarine turbulence (Nielsen, 2007; Kawanisi & Shiozaki, 2008; Good et al., 2014). Thus, without a firm understanding of the relationship between turbulence and particle settling rate, predictive models of estuarine physics suffer from reduced precision and accuracy. We therefore rely on empirical models that are generally very site specific.

5.1.1 Floc Settling in San Francisco Bay

In San Francisco Bay, there is conflicting evidence about the relationship between turbulence and floc size. First, it was seen that settling increased with increased turbulence in San Francisco Bay: in one study, the fastest settling particles appeared 39 min after peak velocity (A. Manning & Schoellhamer, 2013). On the South San Francisco Bay mudflats, aggregates were larger during flood and ebb periods (with high currents) than during slack water (Brand et al., 2010). Both studies thus suggest that as mean flow increases, particle settling gets faster. Alternatively, a second set of evidence showed that aggregates were larger during slack water in the San Francisco Bay Delta (Huang, 2017). Similarly, chapter 3 shows that particles increase in size as current slows in San Pablo Bay.

5.1.2 Motivation

Suspended sediment transport can affect estuarine ecosystems by limiting light availability, transporting nutrients and pollutants, and depositing or eroding material. Models that predict sediment transport require accurate settling velocities (w_s), and an understanding of

how they change. Numerical models can be quite sensitive to settling velocities: halving the settling velocity caused high suspended sediment events to last longer (Jordi et al., 2008).

With this work, we aim to first characterize turbulence and sediment dynamics in tidal creeks at the edges of San Francisco Bay, and second to capture the range and fluctuations in settling velocity there. In particular, our work reveals a basin-scale seiche in some of these estuarine environments; we investigate its influence on local turbulence and sediment dynamics. Previous work has primarily been focused along the main channel of the Bay (A. Manning & Schoellhamer, 2013) with some studies investigating the shoals (Brand et al., 2010); measurements of settling velocities in San Francisco Estuary margins are lacking.

5.2 Methods

5.2.1 Field Data Collection

We conducted two sets of deployments in tidal creeks, focusing on suspended sediment concentration along-side velocity, salinity, temperature, and turbulence data.

For the first deployment set, we visited Stege Marsh, at A (June 30, 2016 and July 19, 2016) and B (July 28, 2016), and Martin Luther King Jr. (MLK) Regional shoreline at C (July 14, 2016) for about 6 hours during flood-high slack-ebb on each of the visits (figure 5.1). For each deployment, a profiling ADV (Nortek Vectrino Profiler, VCN 8123) was deployed with the sample volume at $10 - 20$ cmab, collecting 3-dimensional velocity data (figure 5.2, table 5.2.1). We collected 35 vertical bins of data, spaced at 1 mm intervals between 4 and 7.4 cm below the probe head. During the same period, an RBR CTD+Tu (SN 17015) was deployed at $10 - 15$ cmab collecting salinity, temperature, depth, and turbidity data at 1 Hz, and a second CTD+Tu (SN 18517) was used to collect periodic profiles at 6 Hz. When not profiling, this CTD was placed within the top 0.5 m of the water column. Grab samples were collected periodically and analyzed for suspended sediment concentration.

For the second set, we deployed instrumentation in Alviso Slough, site D, during January $13 - 14$, 2015 for 24 hours (figure 5.1). A single-cell ADV (Nortek Vector) collected velocity and backscatter data at 8 Hz, and the RBR CTD collected salinity, temperature, depth, and turbidity data at 1 Hz (figure 5.3). Both were deployed at 15 cmab; we also deployed identical instrumentation at 60 cmab but do not discuss it here. Again, periodic grab samples were collected and analyzed for suspended sediment concentration.

5.2.2 Data Analysis

5.2.2.1 Instrument orientation

The ADV used at the Stege Marsh and MLK Regional Shoreline sites (the Nortek Vectrino Profiler) did not have an accelerometer for measuring tilt-roll-yaw. Therefore, we manually corrected the measured velocities for instrument tilt, based on the magnitude of measured vertical velocity, $\overline{w}$. We computed $\overline{w}$ assuming a range of instrument tilt from $-30°$ to $30°$,

Date	Site	Instrument	Sensor Elevation (mab)
June 30, 2016	A	ADV	0.138
		CTD	did not function
July 14, 2016	C	ADV	0.195
		CTD	0.1
July 19, 2016	A	ADV	0.121
		CTD	0.09
July 28, 2016	B	ADV	0.114
		CTD	0.1

Table 5.1: Instrumentation deployed at sites A, B, and C on figure 5.1. ADV Vectrino Profiler sensor elevation is the distance from the central transducer to the bed. The height of the CTD was not measured on July 14, 2016 or July 28, 2016, but photos indicate an approximate distance of 0.1 m.

Figure 5.1: Instrument deployments at Stege Marsh (sites A and B), MLK Regional Shoreline (site C), and Alviso Slough (site D).

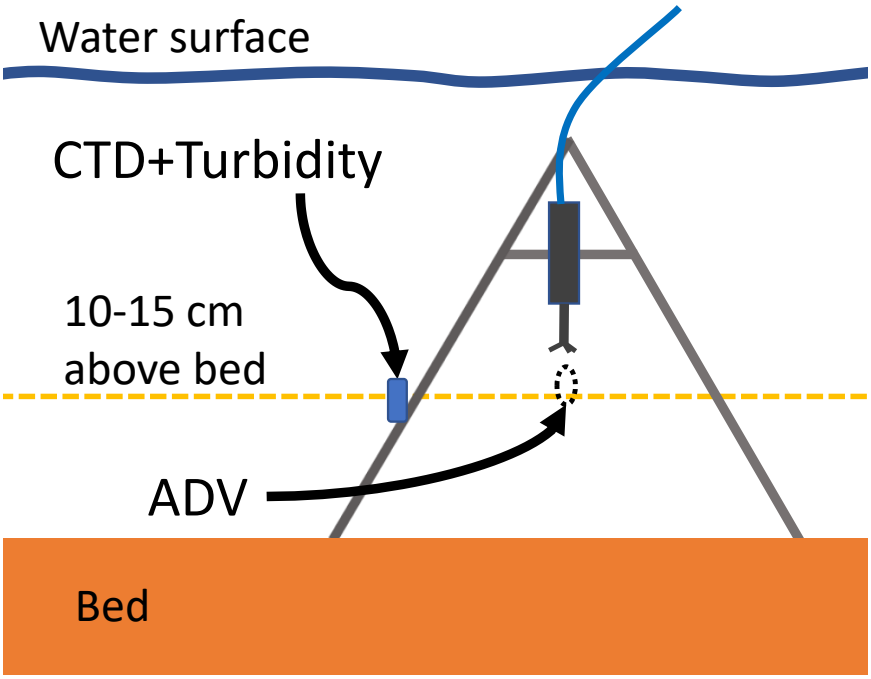

Figure 5.2: Instrument setup at Stege Marsh and MLK Regional Shoreline during summer 2016.

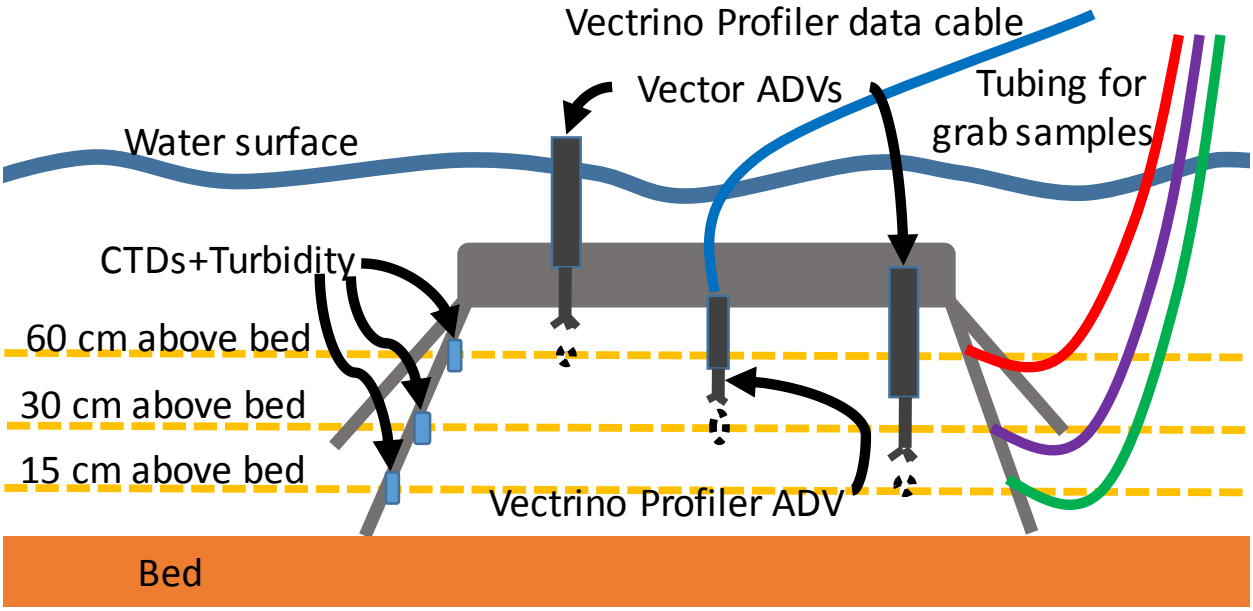

Figure 5.3: Instrument setup at Alviso Slough during January 2015.

and identified the tilt that yielded the minimum $\overline{|w|}$ across the entire deployment. This relies on the assumption that $\overline{|w|}$ was smallest when z is perfectly vertical, which should be reasonable in a system with no sharp steps or other reasons for vertical flows. Based on this analysis, we removed a tilt of $-2.95°$ from the June 30, 2016 deployment, a tilt of $3.05°$ from July 19, and $-4.95°$ from July 28 at Stege Marsh, and $-4.50°$ from July 14 at MLK Regional Shoreline.

5.2.2.2 Calibration of suspended sediment concentration to backscatter

For each site, we calibrated the acoustic backscatter (ABS) measured by the ADV to grab samples of suspended sediment concentration (SSC) via the optical backscatter (OBS). For each grab sample, we analyzed SSC following the Hoover/Lacy sediment sample processing protocol (Hoover & Lacy, 2011). In this method, a set volume of well-mixed sample is vacuum filtered through a pre-weighed nuclepore 0.4 μm polycarbonate filter. The filter is then dried and weighed, and the total SSC is computed based on the filtered weight of sediment (mg) divided by the measured water volume (L).

At the Stege Marsh sites, about 10 grab samples were collected during each deployment and analyzed for SSC. Due to failure of the CTD during the June 30 deployment, we calibrated the OBS to SSC using the July 19 and July 28 data only, and then calibrated ABS to the OBS-derived SSC. Likewise, the ADV and OBS were calibrated to SSC at Alviso Slough using the 10 samples collected there. This two-step method is consistent with the strategy employed in section 3.3.1.

5.2.2.3 Turbulence Quantities

We computed the ADV-derived turbulent Reynolds stresses $\rho\overline{u'w'}$ as averages over 2 minute periods at Stege Marsh and MLK Regional Shoreline, and 10 minute periods at Alviso Slough, following section 3.3.3 and appendix A. Likewise, we found the ADV-derived turbulent sediment flux $\overline{w'C'}$, which we refer to interchangeably as $\langle w'C' \rangle$. Velocity data was despiked following Goring and Nikora, 2002. We did not remove waves from either quantity as the power spectra indicate that waves do not contribute to the computed Reynolds stress or sediment flux.

We also computed u_* from fits to the law of the wall at Stege Marsh and MLK Regional Shoreline by using vertical profiles of mean velocity (equation 3.3, figures 5.4 and 5.5). As shown in figure 5.4, the upper bins measured at MLK Regional Shoreline were contaminated, and therefore not included in the log-law estimates. At the Stege Marsh sites, bin contamination did not appear to be an issue (figure 5.5).

5.2.2.4 Settling Velocity: ADV method

Suspended sediment transport is described with the advection-diffusion equation (1.1). Cartwright et al., 2013 and Fugate and Friedrichs, 2002 use this to find particle settling velocity by simplifying it to equation 3.6, where we assume no sediment exchange across the water surface

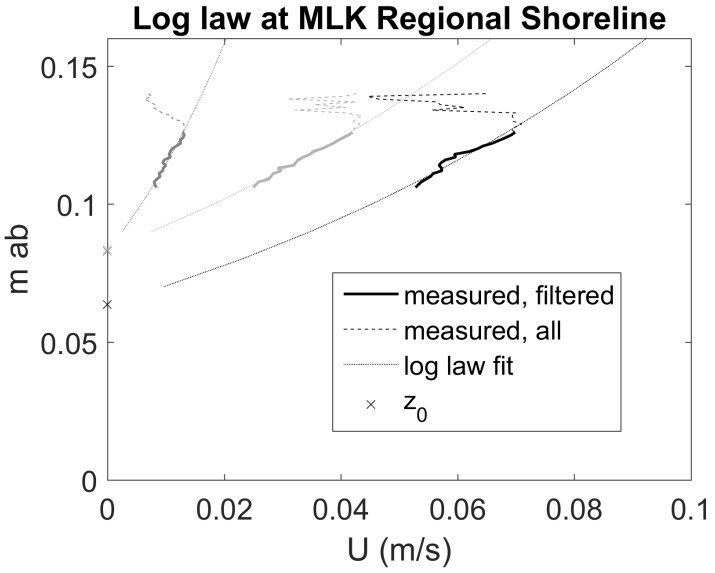

Figure 5.4: Log-law fits at MLK Regional Shoreline for bursts on July 14, 2016 during 2 minute periods starting at 14:41, 14:47, and 15:25 GMT in light-gray, black, and mid-gray, respectively. The filtered bins (solid line) show the velocities used for computing the log-law, while the dashed line shows all measured bins. The log-law fit (dotted line) yields a z_0 (x), which may be high thanks to the rough, algae filled and rocky bottom and which is not measured precisely because the presence of algae made it challenging to capture the exact distance to bed.

(reasonable) or with the bed (potentially problematic if sediment is depositing or eroding). However, once an ADV is calibrated from backscatter to particle concentration, it captures both $\overline{C}$ and $\overline{w'C'}$. This method also assumes that downward settling is balanced by upward turbulent diffusion, and advection and unsteadiness are negligible. Unlike the Rouse profile, this method does not rely on the assumption of a particular form for the eddy diffusivity profile, so it provides an advantage in stratified or other environments where the vertical structure of eddy diffusivity may be altered. This method relies on vertical accuracy of measured ADV velocity, which can yield about 30 times less noise than in the horizontal directions when the instrument is oriented vertically (G. Voulgaris & Trowbridge, 1998). Equation 3.6 also assumes that a non-settling 'wash'-load of particles is present in the water column, contributing to the measured backscatter. Because these fine particles do not settle, $\frac{\partial C_{wash}}{\partial z} = 0$, and they do not contribute to the measured vertical flux, $\overline{w'C'}$. Therefore, settling velocity measurements are improved by removing this concentration from the left-hand side of equation 3.6. It is also important to note that even though an ADV tracks movement of scatterers in the water (suspended sediment and other particles) rather than water movement, this does not affect the estimate of w' in equation 3.6 (Cartwright et al., 2013). We note that $w' \approx 10 \cdot w_s$ in these data, further supporting the conclusion that

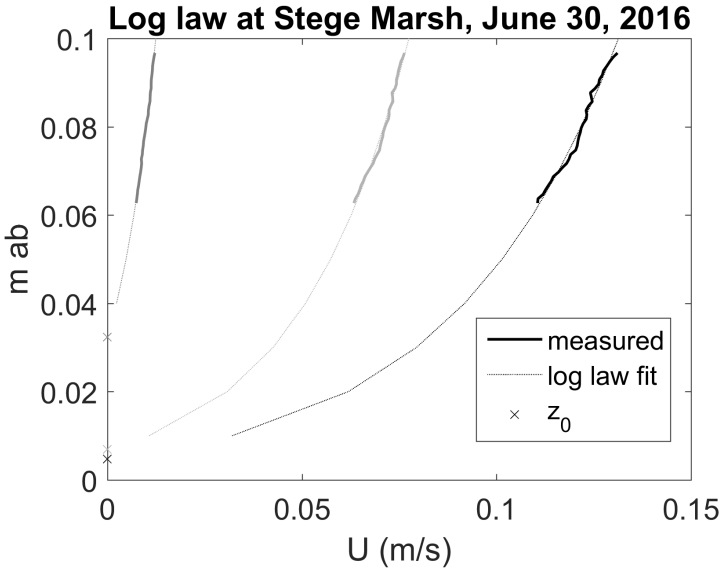

Figure 5.5: Log-law fits at Stege Marsh for bursts on June 30, 2016 during 2 minute periods starting at 16:14, 16:20, and 16:22 GMT in light-gray, black, and mid-gray, respectively. The solid line shows the velocities used for computing the log-law. The log-law fit (dotted line) yields a z_0 (x).

$(w - w_s)' \approx w'$. Finally, tilt in the instrument can be corrected by rotating the measured 3-D velocities, however the additional error induced by a slight tilt (up to about 10° off from vertical) is negligible (Cartwright et al., 2013).

5.2.2.5 Settling Velocity: Rouse Profile

Rouse profiles can indicate the role of gravitational settling to eddy diffusion,

$$\frac{C}{C_0} = \left[\frac{z_0\,(h-z)}{z\,(h-z_0)}\right]^{w_s/u_*} \tag{5.4}$$

where the dimensionless ratio $w_s/\kappa u_*$ is the Rouse number, R_n (Mehta, 2014). This assumes steady state concentration profiles with no lateral advection, that is, particle settling is balanced by vertical turbulent diffusion. It also assumes that vertical diffusivity takes a parabolic form, $D_T(z) = \kappa u_* z\left(1 - \frac{z}{h}\right)$, given primarily by distance from the bed or surface, and that mass and momentum diffusivity are equivalent. Using the measured vertical profiles of suspended sediment (eg. figures 5.11 and 5.12, middle) and the measured u_* (section 5.2.2.3), this yielded an implied particle settling velocity.

5.3 Results: Hydrodynamics and sediment fluxes in low energy perimeter environments

5.3.1 Mean Quantities

We measured near bed velocity, salinity, temperature, and turbidity. The CTDs were not perfectly calibrated to one another, noticable particularly in the measured salinity at Stege Marsh and MLK Regional Shoreline, however the trends shown by the instruments indicate the relative behavior of salinity near the bed and near the surface.

At Alviso Slough, SSC was higher on ebb than flood, suggesting a net erosional regime within the slough. Towards the end of the sample period, we observed higher salinity during a strong flood, indicative of bay-sourced water advecting up to the instrument location (figure 5.6).

At Stege Marsh, SSC was higher on flood than ebb during all three periods, consistent with net deposition in the marsh (figures 5.7, 5.8, and 5.9). For the July 19 and July 28 deployments, we had CTD data, which showed vertical salinity stratification appearing near the end of the measurement periods. Temperature increased over the data collection period at both sites, which is consistent with the idea of colder water entering a shallow slough during the morning, and exiting later in the day after it was exposed to sunlight.

At MLK Regional Shoreline, SSC remained low through the measurement period (figure 5.10). It was unclear if the peaks in SSC were due to flow induced resuspension or advection, or if they came from more biological sources such as passage of a bat ray (*Mylobatis californica*) or perturbation resulting from our sampling efforts. Observations in the field showed that waves could resuspend bed material, vegetation growing on the bed captured sediment in the water column, and particles settled rapidly, falling approximately 10 cm in as many seconds. Contrary to expectations, salinity increased during ebb. Freshwater input in the fringing marsh would be expected to be non-existant during this period, so the salinity increase could be due to freshwater evaporation or to trapping within the marsh. Without additional data, we cannot evaluate this further, however we note that the tidal creek where we measured was the only inlet to this marsh, so asymmetrical routing through the marsh was not the cause. As with the Stege Marsh sites, temperature increased over the deployment at this location.

During the deployments, periodic CTD profiles revealed that temperature gradually increased at all sites as the water warmed during the course of the day, but the water column did not stratify due to temperature (figures 5.11, 5.12, 5.13, and 5.14, top). Similarly, salinity was well-mixed in the water column through most periods, although towards the end of the measurement periods, during ebb, on June 30 and July 19 at Stege Marsh, salinity stratification appeared (figures 5.11 and 5.12, bottom). The lack of stratification during flood may suggest that this site demonstrates strain-induced periodic stratification (e.g. J. H. Simpson et al., 1990), although it is impossible to completely determine as we did not sample a full tidal period. These periods of stratification during ebb show stronger gradients of suspended

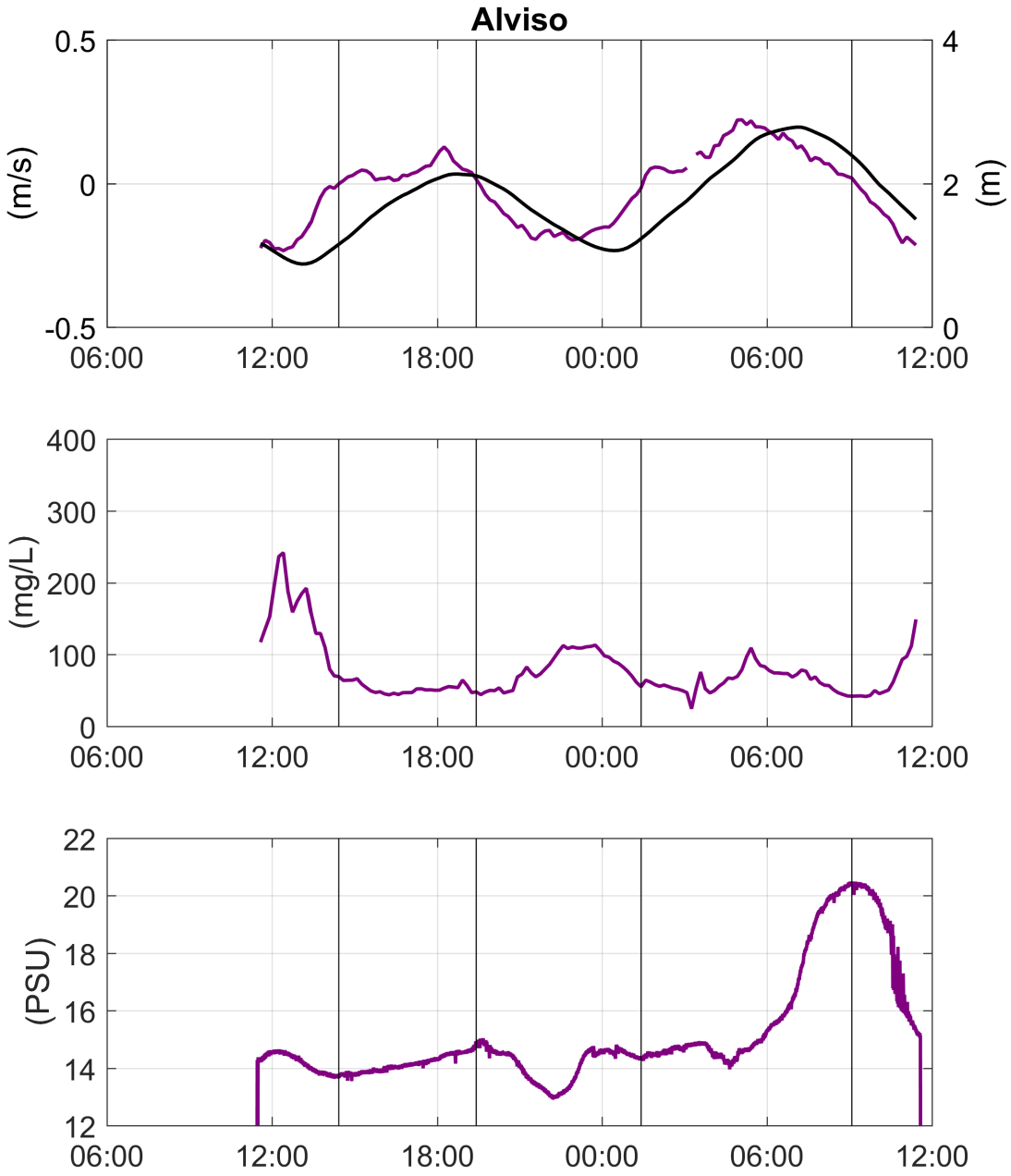

Figure 5.6: Site dynamics at Alviso Slough on Jan 13 – 14, 2015. Top: mean velocity at 15 cm ab (left, purple) and water level (right, black), with positive velocity oriented in the flood direction. Middle: SSC at 15 cm ab from calibrated ADV backscatter. Bottom: Salinity at 15 cm ab. The time points of slack water are denoted with vertical grey lines. SSC is higher on ebb than flood, suggesting net erosional regime in the slough. Strong flood towards the end of the sample period shows higher salinity from bay-sourced water.

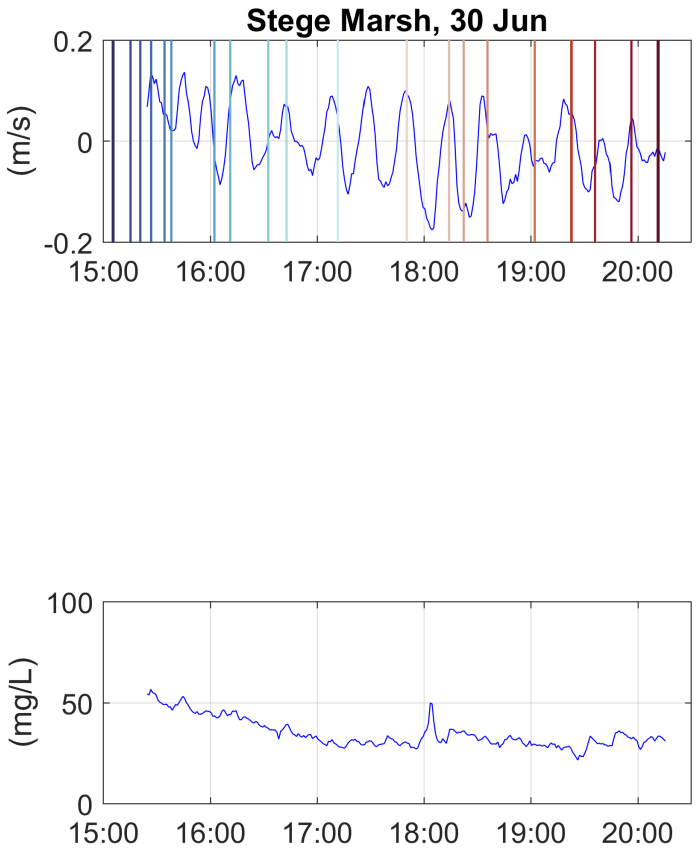

Figure 5.7: Site Dynamics at Stege Marsh, on June 30, 2016. Top: mean velocity (blue), with times at which profiles were collected shown as vertical lines. These profiles of temperature, SSC, and, salinity are shown with the same colors in figure 5.11. 3^{rd}: SSC near the bed from the calibrated ADV backscatter (blue). The fixed near-bed CTD did not function for this deployment, therefore no data is shown.

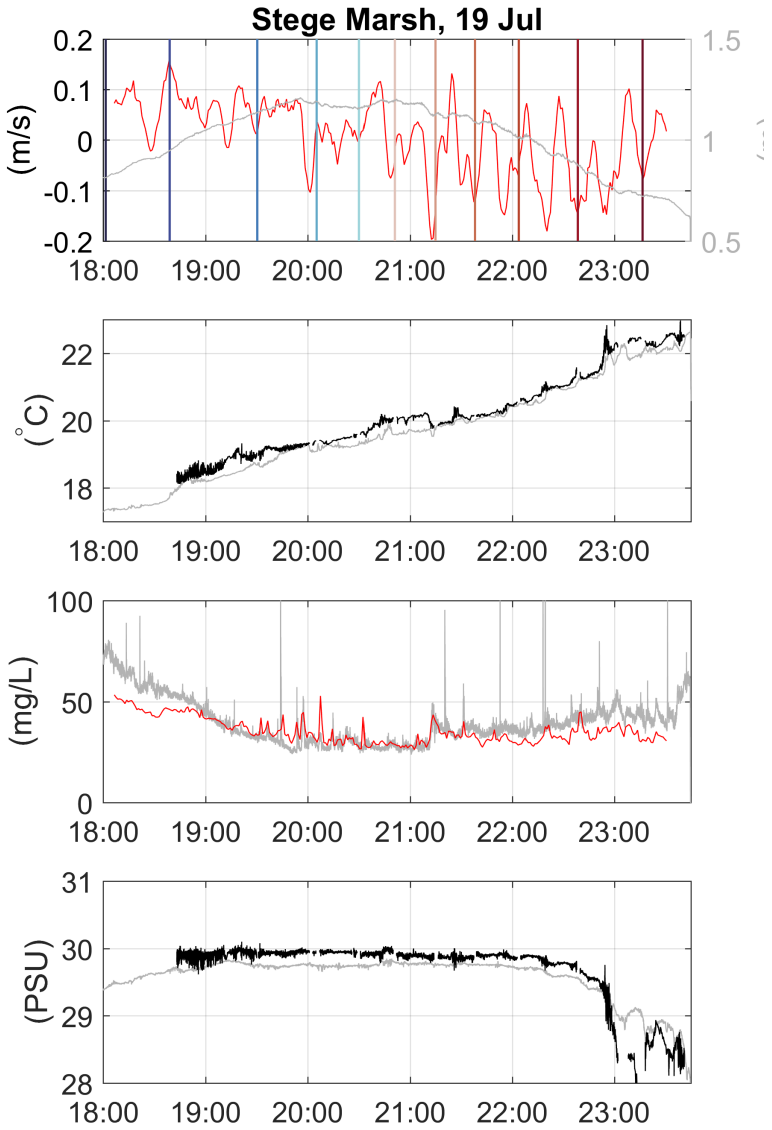

Figure 5.8: Site Dynamics at Stege Marsh, on July 19, 2016. Top: mean velocity (left, red) and water level (right, gray), with times at which profiles were collected shown as vertical lines. These profiles of temperature, SSC, and, salinity are shown with the same colors in figure 5.12. 2^{nd}: Temperature (°) near the bed (gray) and near surface (black). 3^{rd}: SSC near the bed from the calibrated ADV backscatter (red) and Tu sensor (gray). Bottom: Salinity near the bed (gray) and near surface (black).

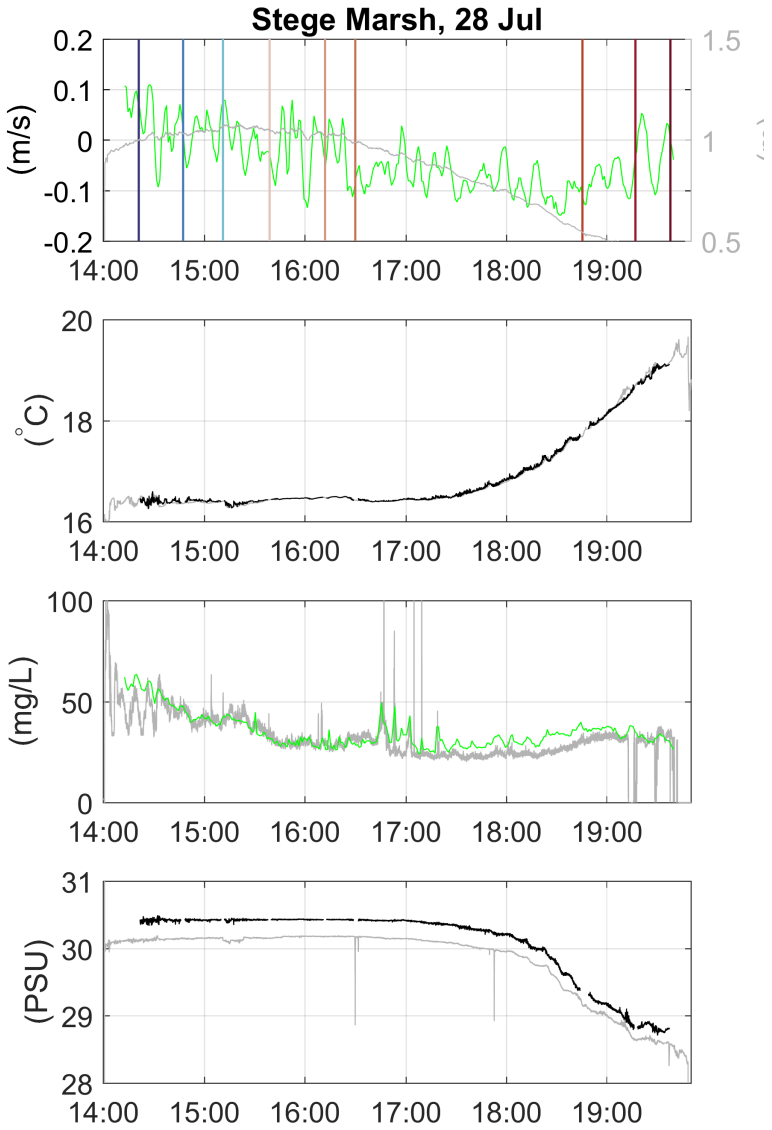

Figure 5.9: Site Dynamics at Stege Marsh, on July 28, 2016. Top: mean velocity (left, green) and water level (right, gray), with times at which profiles were collected shown as vertical lines. These profiles of temperature, SSC, and, salinity are shown with the same colors in figure 5.13. 2^{nd}: Temperature (°) near the bed (gray) and near surface (black). 3^{rd}: SSC near the bed from the calibrated ADV backscatter (green) and Tu sensor (gray). Bottom: Salinity near the bed (gray) and near surface (black).

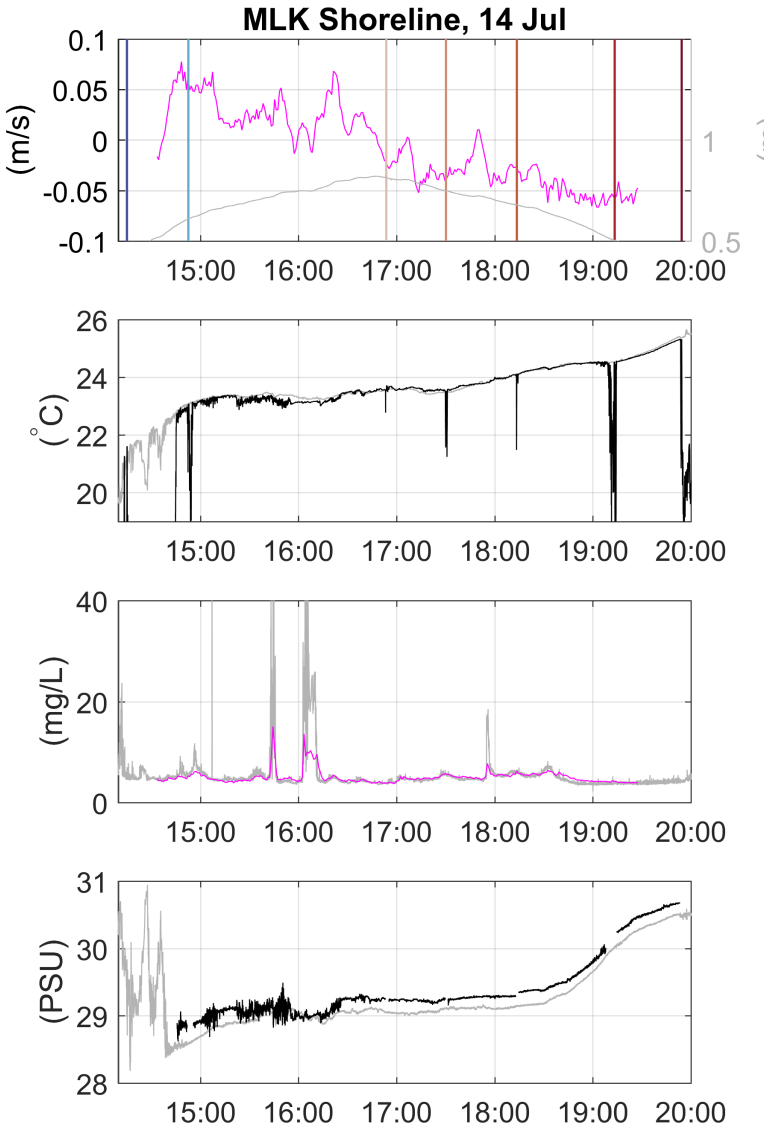

Figure 5.10: Site Dynamics at MLK Regional Shoreline, on July 14, 2016. Top: mean velocity (left, pink) and water level (right, gray), with times at which profiles were collected shown as vertical lines. These profiles of temperature, SSC, and, salinity are shown with the same colors in figure 5.14. 2^{nd}: Temperature (°) near the bed (gray) and near surface (black). 3^{rd}: SSC near the bed from the calibrated ADV backscatter (pink) and Tu sensor (gray). Bottom: Salinity near the bed (gray) and near surface (black).

sediment, particularly on June 30.

At both Stege Marsh locations and the MLK Regional Shoreline, velocities oscillated at a super-tidal frequency, suggesting a basin-scale seiche (figures 5.7, 5.8, 5.9, and 5.10, top, and figure 5.15). At the Stege Marsh sites, a strong seiche at 9 and 24 minute periods appeared, while an oscillation around 22 minutes and its harmonics appeared at the MLK Regional Shoreline site. The orbital velocity for the seiches was 0.086 and 0.77 m/s at site A, 0.058 m/s at site B, and 0.020 m/s at site C, computed as $u_{br} = \sqrt{2\sum_i (S_{xx} + S_{yy})_i \Delta f_i}$ following Wiberg and Sherwood, 2008. Here, the frequency, f, was limited to $1/(3*60)$ to $1/(40*60)$ Hz to capture the seiche oscillations, and S_{xx} and S_{yy} capture the spectra of the horizontal velocity measurements. This corresponded with characteristic wave periods, $T = \frac{\sqrt{2}\sum_i S_{xx,i}\Delta f_i}{\sum_i f_i S_{xx,i}\Delta f_i}$, of 16 and 14.5 min, 10.5 min, and 13.4 min, and wave excursion amplitudes, $A = u_{br}T/2\pi$, of 13 and 11 m, 6 m, and 2.5 m, respectively. We note that the characteristic wave period does not capture the multiple dominant oscillation frequencies. However, the corresponding wave excursion amplitude suggests the physical extent of near bottom oscillation due to the seiche.

To evaluate the role of seiches in suspended sediment transport, we compute a decomposed seiche-averaged suspended sediment flux (SSF), similar to that performed by Jessica R. Lacy, Gladding, Brand, Collignon, and Stacey, 2014 on a tidal scale. The mean SSF is $\langle uhc \rangle$ (kg/ms), where $\langle$ and $\rangle$ represent the averaging period. With u and c collected at 10 cmab this represents a single point estimate of the full water column, however as shown in figures 5.11 and 5.12, the vertical gradient of suspended sediment concentration is small.

The SSF was decomposed so as to evaluate the contributions of seiche-scale motions to the total flux. For each of the velocity, water depth, and SSC, we separated the quantities into a mean and fluctuation component, as $x = \langle x_s \rangle + x'$, where $\langle x_s \rangle$ represented the seiche-averaged quantity, and x' reflected the seiche and fluctuating scale motions. For these sites, we found the seiche-scale motions by decomposing the velocity to $u = \overline{u} + u_{seiche} + u'$, where $\overline{u}$ was found through a 5^{th} order butterworth filter at a cutoff frequency of 1/1.15 hours, and u_{seiche} was computed through a 10 or 8 min filter (for July 19 and July 28, respectively) on the quantity $u - \overline{u}$. The corresponding 0-crossings in the computed u_{seiche} were used to designate 'seiche-periods' for the analysis of SSF, with a full seiche period denoting the time period used to compute $\langle x_s \rangle$. This decomposition thus allowed us to separate motions above the seiche scale, $\langle x_s \rangle$, from within-seiche scale motions, x'.

This decomposition resulted in 5 non-zero terms: $\langle u_s \rangle \langle h_s \rangle \langle c_s \rangle$ represents the tidally induced transport; $\langle u' \langle h_s \rangle c' \rangle$ reflects a seiche-phase correlation; and $\langle u' h' \langle c_s \rangle \rangle$ gives a seiche induced Stokes drift or the correlation between seiche-varying velocity and depth. The remaining two non-zero terms, $\langle \langle u_s \rangle h' c' \rangle$ and $\langle u' h' c' \rangle$, were very small and are not discussed.

As shown in figures 5.16 and 5.17, the primary component of the total flux was the tidal constituent, and it responded primarily to the direction of mean flow. During flood, SSF was up-estuary, while during ebb it was seaward. At both sites, the seiche-phase correlation contributed to the total flux in a small fashion, only rarely opposing the direction of the tidal constituent. The seiche-scale Stokes drift was also small, but more frequently opposed

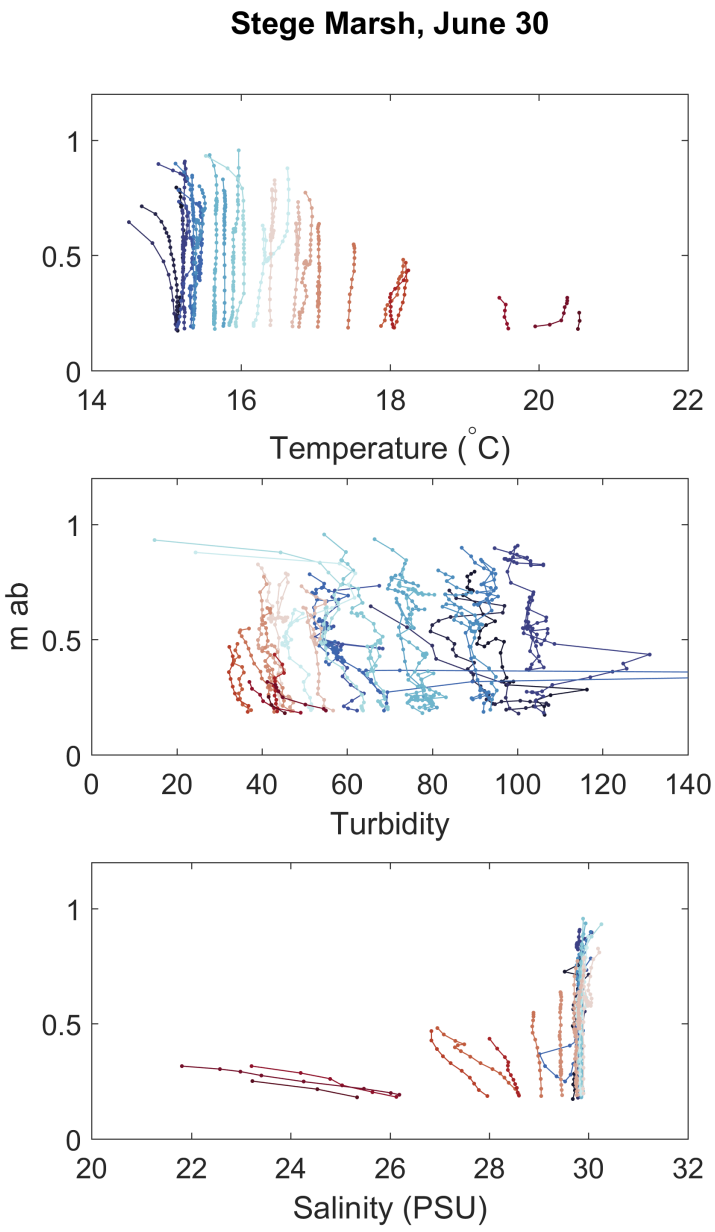

Figure 5.11: Profiles of temperature (top), turbidity (middle), and salinity (bottom) throughout the measurement period on June 30 at Stege Marsh. Periods during the flood are shown in blue, and ebb are shown in red, with light colors indicating high water and the transition from flood to ebb, as illustrated in figure 5.7, top. Salinity stratification developed during the ebb.

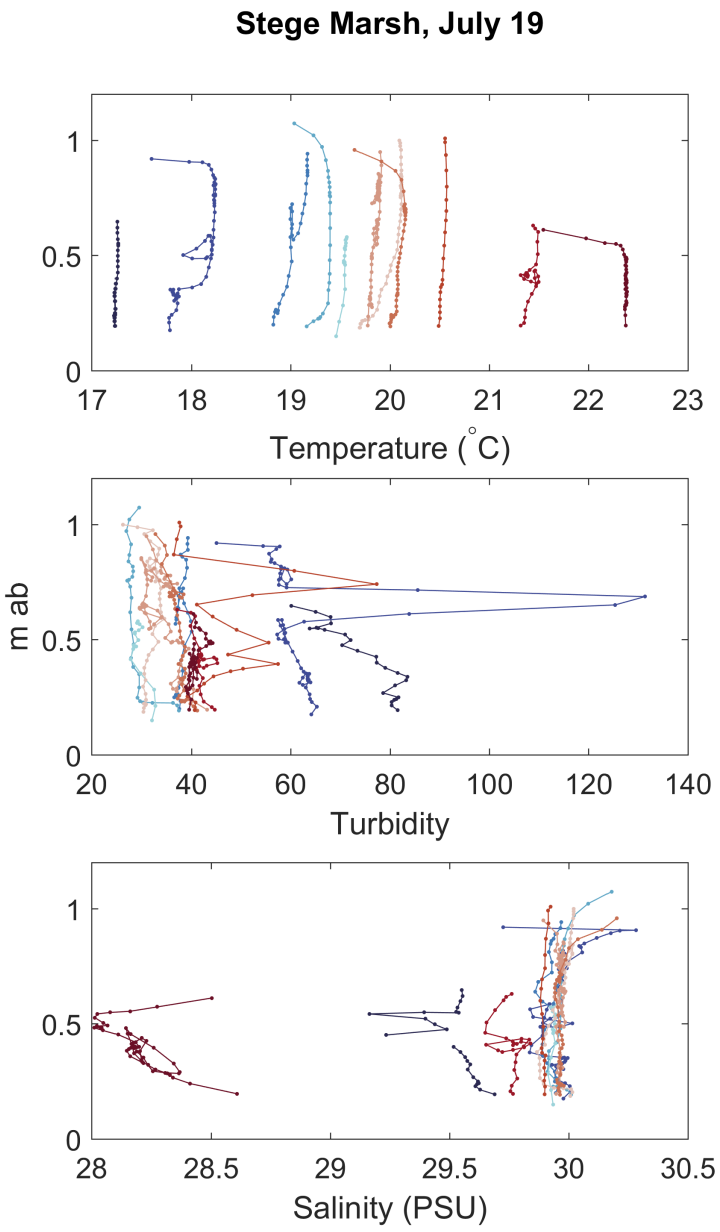

Figure 5.12: Profiles of temperature (top), turbidity (middle), and salinity (bottom) throughout the measurement period on July 19 at Stege Marsh. Periods during the flood are shown in blue, and ebb are shown in red, with light colors indicating high water and the transition from flood to ebb, as illustrated in figure 5.8, top. Salinity stratification developed during the ebb.

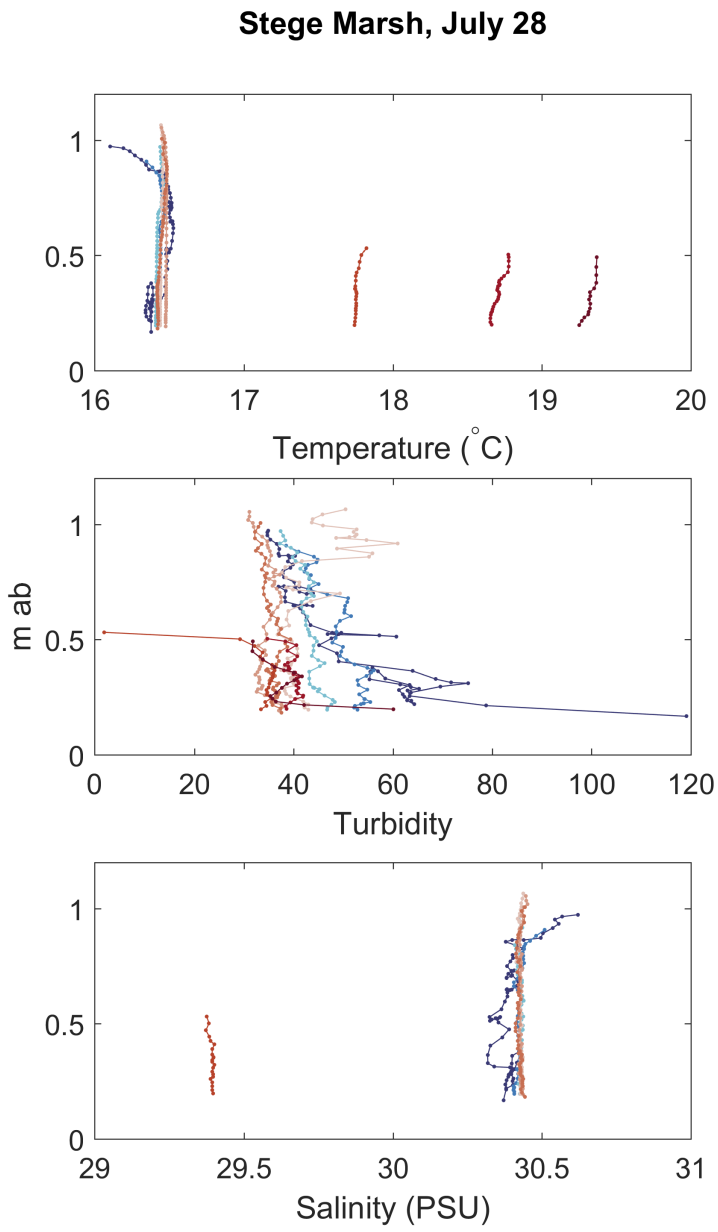

Figure 5.13: Profiles of temperature (top), turbidity (middle), and salinity (bottom) throughout the measurement period on July 28 at Stege Marsh. Periods during the flood are shown in blue, and ebb are shown in red, with light colors indicating high water and the transition from flood to ebb, as illustrated in figure 5.9, top. Salinities for the last two profiles were not collected.

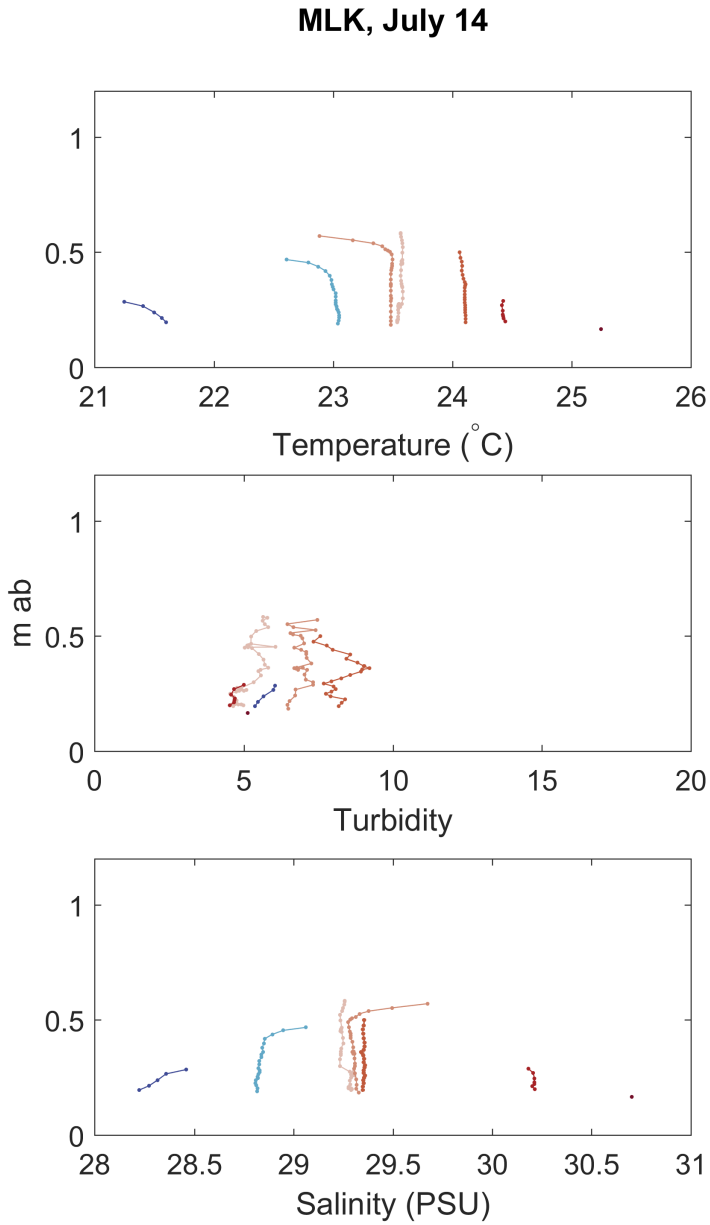

Figure 5.14: Profiles of temperature (top), turbidity (middle), and salinity (bottom) throughout the measurement period on July 14 at MLK Regional Shoreline. Periods during the flood are shown in blue, and ebb are shown in red, with light colors indicating high water and the transition from flood to ebb, as illustrated in figure 5.10, top. Salinities for the last two profiles were not collected.

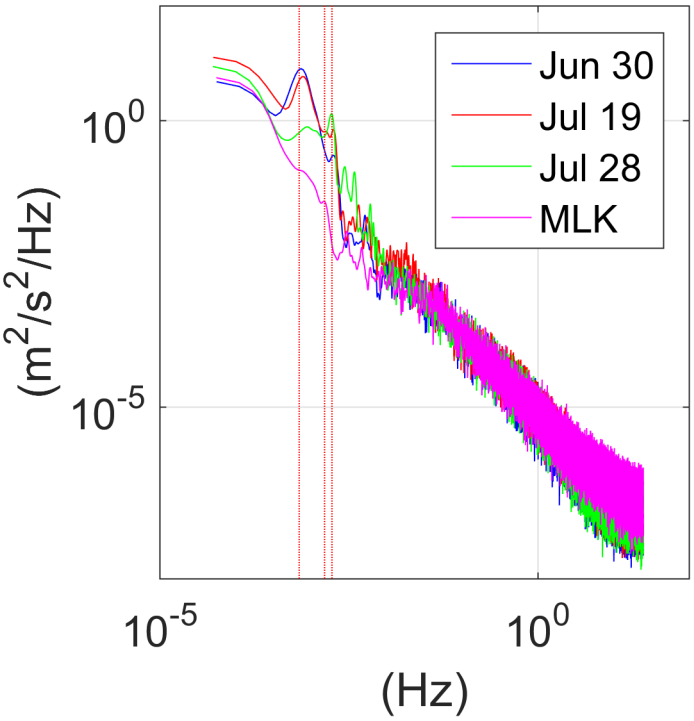

Figure 5.15: Power spectral density for Stege Marsh and MLK Regional Shoreline, showing the dominant oscillations at 24 and 9 minutes (vertical red lines) at the Stege Marsh sites. The oscillation at the MLK site had a less clear period.

the direction of tidal-induced transport. Jessica R. Lacy et al., 2014 also observed that the Stokes drift frequently opposed the advective flux on a tidal scale. The dominance of tidal scale motions in driving sediment flux indicates that the seiche-induced oscillation has a largely negligible effect on sediment transport.

5.3.2 Turbulent Quantities

At these sites, u_* computed through the velocity profile oscillated with the mean current velocity, U, while turbulence from a Reynolds stress $\overline{u'w'}$ yielded a lower u_* (figures 5.18, 5.19, 5.20, and 5.21). The observed seiching affected near bed turbulent stresses in that it drove near bed velocities. However it is unclear if seiching caused any further impact in turbulent stresses.

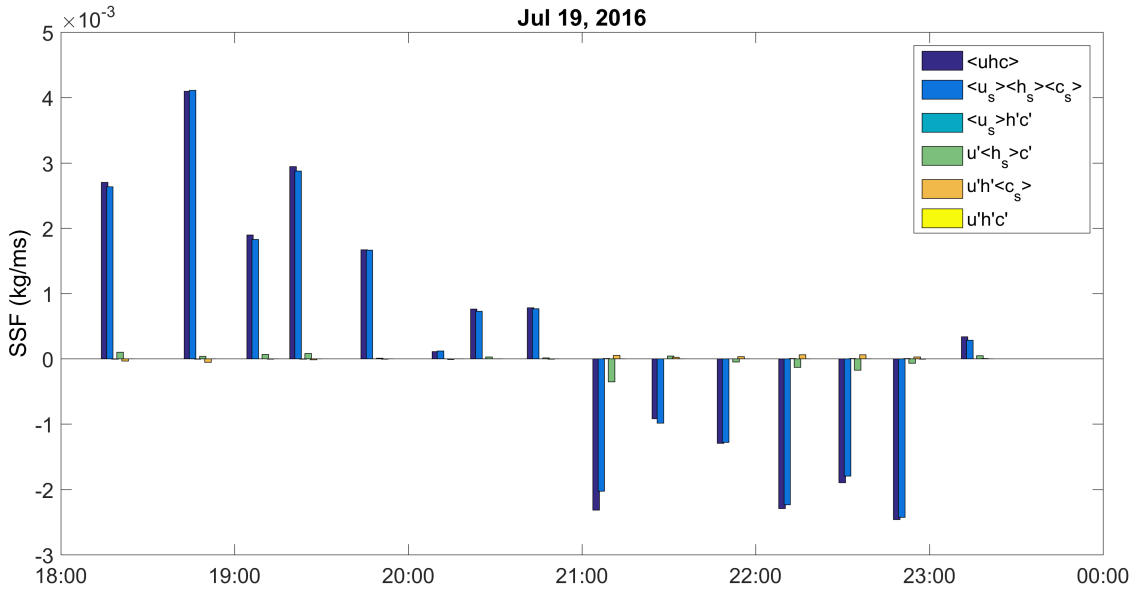

Figure 5.16: Suspended sediment flux computed at Stege Marsh on July 19, decomposed as described in section 5.3.1.

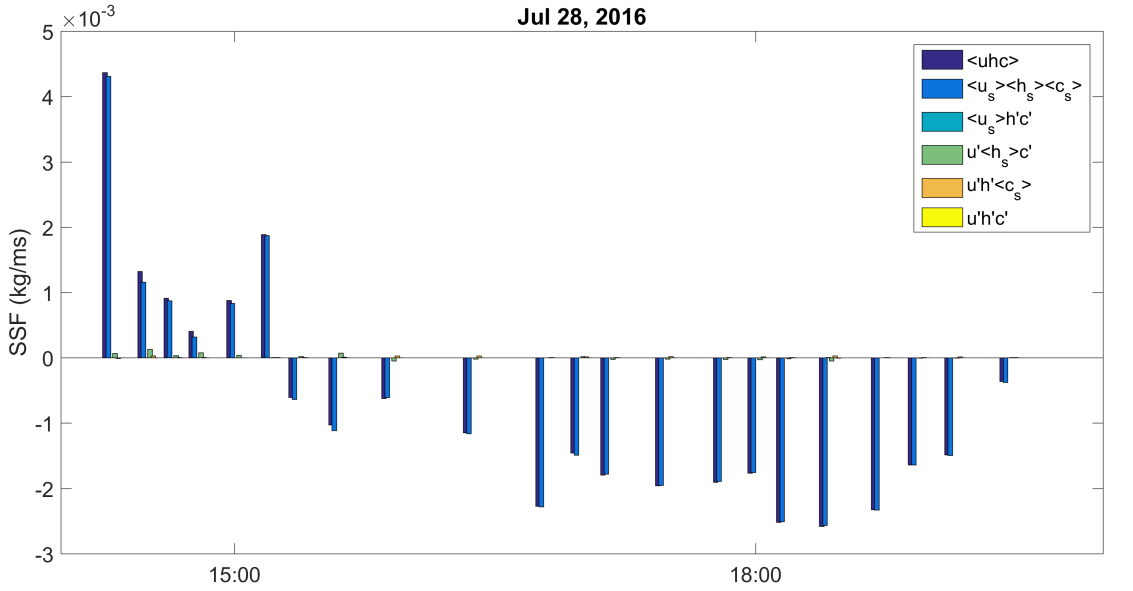

Figure 5.17: Suspended sediment flux computed at Stege Marsh on July 28, decomposed as described in section 5.3.1.

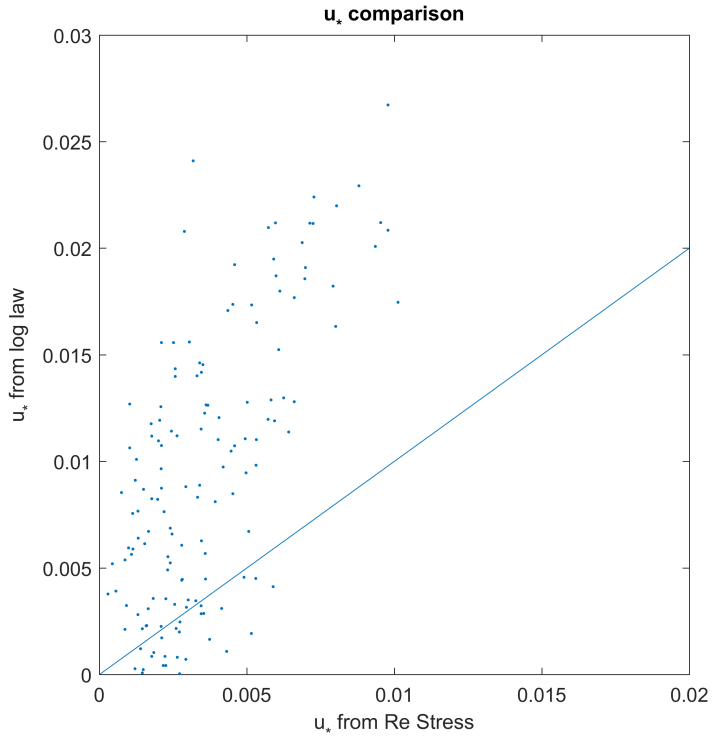

Figure 5.18: Friction velocity from the log law compared with friction velocity from the turbulent Reynolds stress at Stege Marsh on June 30. A 1:1 line is shown in blue.

5.4 Results: sediment settling velocity

As mentioned in section 5.3.1, at Alviso Slough, suspended sediment was higher on ebb than flood (figure 5.6). At Stege Marsh on the other hand, suspended sediment was higher on flood than ebb (figures 5.7, 5.8, and 5.9).

5.4.1 ADV method

As described in appendix A.2 and section 5.1, the ADV method for computing settling velocity relies on an assumed balance between particle settling and vertical turbulent mixing, with no input from resuspension, settling, or advection. While these assumptions may not hold for the locations measured, we present the initial evaluation of settling velocity through a point-by-point method and a bulk method.

In the point-by-point method, settling velocity was computed from equation 3.6, where $\overline{w'C'}$ at each point in time was divided by the respective $\overline{C} - C_{wash}$. We did not include the data from MLK Regional Shoreline in this analysis, as the concentrations were so low that computing settling was not reasonable.

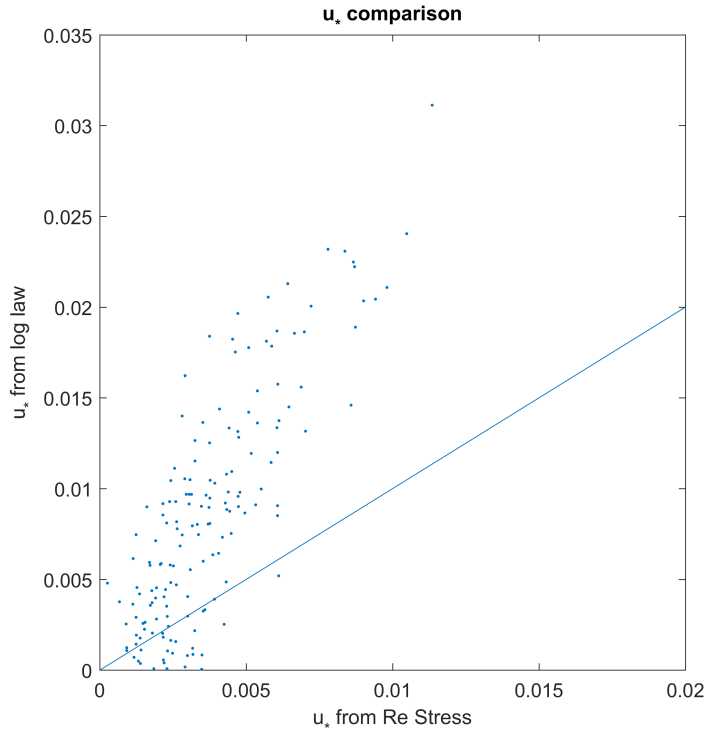

Figure 5.19: Friction velocity from the log law compared with friction velocity from the turbulent Reynolds stress at Stege Marsh on July 19. A 1:1 line is shown in blue.

At the Stege Marsh sites and Alviso Slough, settling velocity increased with increased turbulence (figures 5.22 and 5.23), but there was no clear distinction between ebb and flood at any of the sites. Seiche phase at Stege Marsh also did not indicate a difference in settling velocity.

In the bulk method, we compute a single settling velocity for the locations by plotting $\overline{w'C'}$ against $\overline{C} - C_{wash}$ and fitting a line (figures 5.24 and 5.25). This method again applies the assumptions required for equation 3.6. While there is no difference between ebb and flood at Alviso Slough, this analysis suggests that particles settle faster during ebb than flood at Stege Marsh (table 5.4.1). However, the fits at Stege Marsh yielded very low coefficients of determination, indicative of the data spread, and casting doubt on the fit. Suspended sediment concentrations were higher at Alviso Slough, and periods where concentrations were high (generally above 30 mg/L) had larger $\overline{w'C'}$, driving the overall relationship and yielding the high settling velocity.

These figures (5.24 and 5.25) also suggest the relationship shown in figure 5.22 and 5.23. Most easily observed in figure 5.25, we see that at low SSC (below about 30 mg/L), there is a lower slope to the $\overline{w'C'}$ vs. SSC relationship than at high SSC. Since u_* generally follows $\overline{w'C'}$, this relationship produces the trend noticed in figures 5.22 and 5.23.

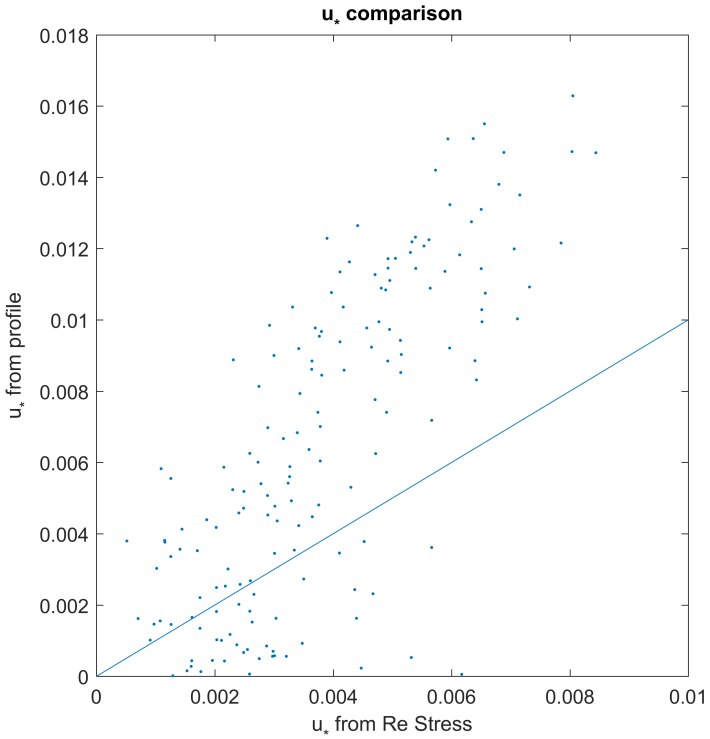

Figure 5.20: Friction velocity from the log law compared with friction velocity from the turbulent Reynolds stress at Stege Marsh on July 28. A 1:1 line is shown in blue.

	Alviso Slough		Stege Marsh	
	w_s (mm/s)	R^2	w_s (mm/s)	R^2
All data	0.34 ± 0.04	0.48	0.077 ± 0.02	0.01
Flood	0.33 ± 0.06	0.46	0.034 ± 0.02	0.03
Ebb	0.34 ± 0.06	0.39	0.19 ± 0.04	0.12

Table 5.2: Settling velocities computed through the bulk method at Alviso Slough and Stege Marsh.

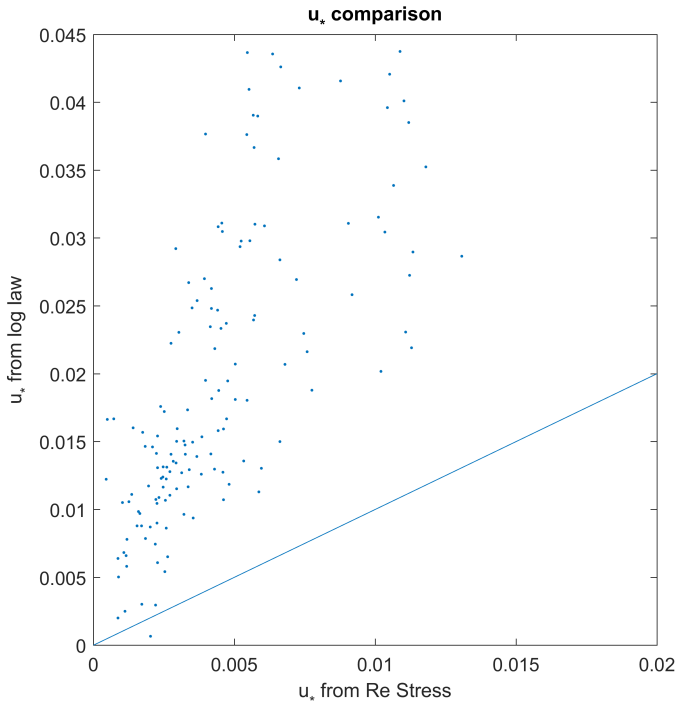

Figure 5.21: Friction velocity from the log law compared with friction velocity from the turbulent Reynolds stress at MLK Regional Shoreline. A 1:1 line is shown in blue.

5.4.2 Rouse Profiles

While the suspended sediment profiles collected here yielded only a few valid estimates of settling velocity through Rouse profiles, they are on the same order of magnitude as the estimates found through the ADV method. This suggests that the ADV method captures the characteristic speed of particle settling, even while it may not be refined enough to indicate trends.

5.4.3 Scaling Analysis

As shown in appendix A.2, use of the ADV to compute particle settling requires that advection, unsteadiness, resuspsension, and deposition all become negligible relative to settling, however this is often not true in San Pablo Bay. We similarly compared the magnitudes of terms for the settling velocity equation at Alviso Slough and Stege Marsh, where we estimated the magnitude of $u\frac{\partial\langle C\rangle}{\partial x}$ as $u = \pm 0.3$ and 0.1 m/s at Alviso and Stege, respectively and $\frac{\partial\langle C\rangle}{\partial x} = 0.05$ mg/L/m at both sites. At both Alviso Slough and Stege Marsh, the unsteady and advective terms were on similar orders of magnitude as vertical turbulent diffusion (figures 5.26 and 5.27).

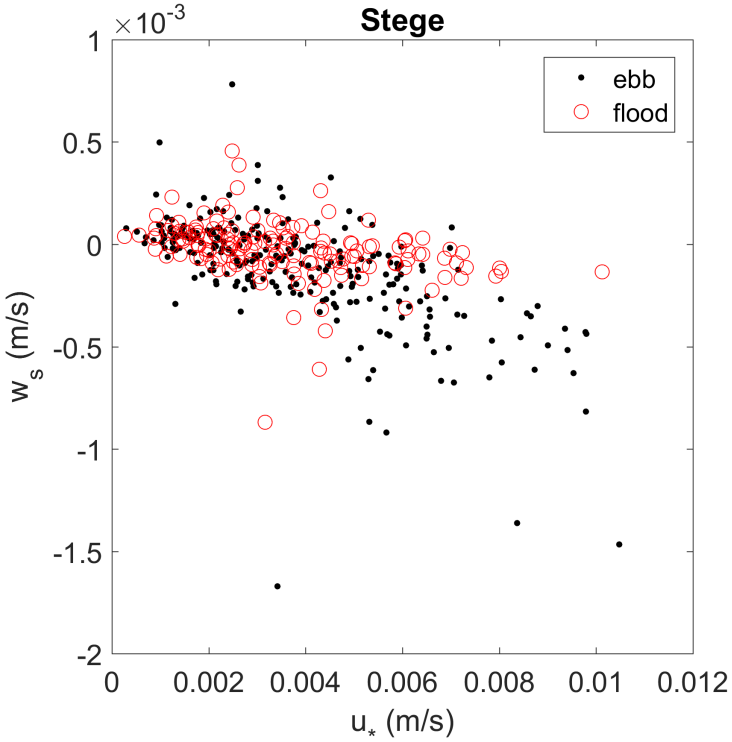

Figure 5.22: Settling velocity computed on a point-by-point basis during all 3 Stege Marsh deployments, compared with turbulent u_* from Reynolds stress.

5.5 Discussion

While we observe faster settling velocities with increasing turbulence (figures 5.22 and 5.23), this may result from contributions from advection, resuspension, or local unsteadiness that negate the assumptions required for applying equation 3.6, as described in section 5.4.3. If this relationship is, in fact, true, it may indicate that larger flocs form during the high velocity periods of ebb and flood, consistent with the results of Brand et al., 2010. However, given that we observed the same relationship from an ADV (higher velocity indicates faster settling) in San Pablo Bay, where we noted that larger flocs were present at slack water through LISST measurements, we conclude that it is highly possible that the observed relationship between w_s and u_* does not convey the full story.

The observed difference in particle settling velocity between flood and ebb at Stege Marsh (figure 5.24) may come from real contributions from particle aggregation or breakup within the tidal marsh, or sediment capture by emergent vegetation, such as selective trapping of small particles, or artificial contributions from advection and straining. As shown in the scaling analysis, unsteadiness and advection can artificially lead to increased or decreased measured velocities. Alternatively, lateral SSC gradients can be strained in to vertical SSC

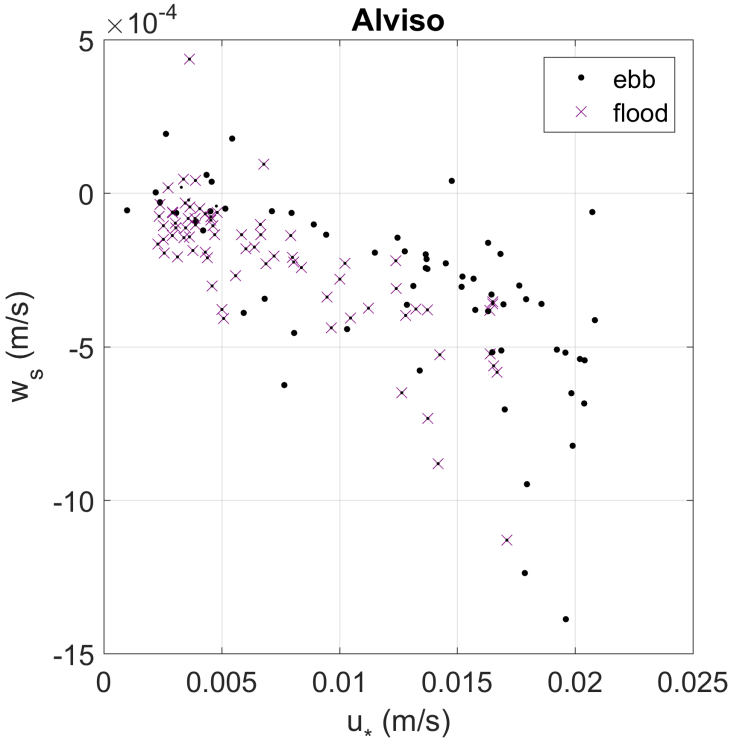

Figure 5.23: Settling velocity computed on a point-by-point basis at the Alviso Slough deployment, compared with turbulent u_* from Reynolds stress.

gradients, where waters that are well-mixed on flood can be strained during ebb, producing strong vertical SSC gradients, $\frac{\partial \langle C \rangle}{\partial z} < 0$. Since the computed $\overline{w'C'}$ can be modeled as $-K\frac{\partial \langle C \rangle}{\partial z}$, a stronger vertical SSC gradient during ebb would yield a stronger $\overline{w'C'}$ and thus a larger settling velocity. This mechanism would artificially inflate the measured settling velocity.

We observe high suspended sediment concentrations during short periods (such as minutes) at Stege Marsh (figures 5.7, 5.8, and 5.9, 3^{rd} row), but do not see such fluctuations at Alviso Slough (figure 5.6, 2^{nd} row). This suggests that seiching at Stege Marsh plays a role in suspended sediment dynamics, either through seiche-augmented resuspension or seiche-impacted advection, even though seiching does not play a strong role in driving suspended sediment flux (figures 5.16 and 5.17). As shown in the top panel of figures 5.7, 5.8, and 5.9, seiching affects near-bed velocities strongly. If resuspension is responsible for the short-term high concentrations, we conclude that particle settling is responsible for the decline, suggesting a high fall velocity of the resuspended material. If advection is responsible, we expect strong gradients present at this site, either along-channel or cross-channel. However, the small change in suspended particle concentration over the full deployment period (about 50 mg/L) suggests that strong particle gradients are unlikely.

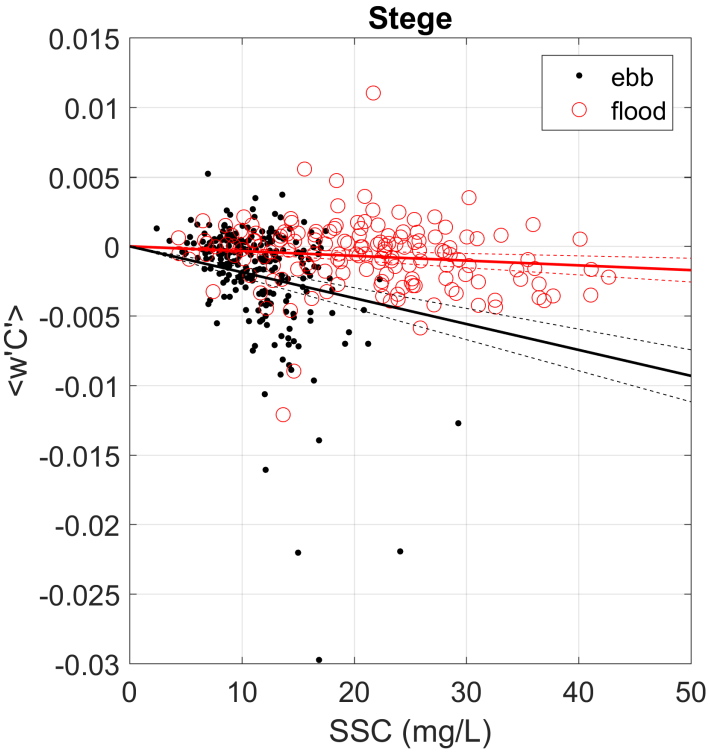

Figure 5.24: Settling velocity on a bulk basis during all 3 Stege Marsh deployments, computed following equation 3.6 for the flood (circles) and ebb (dots) periods.

5.5.1 Future Analyses

While we have probed aspects of the hydrodynamics, sediment dynamics, and particle settling at these sites, additional lines of investigation remain open and interesting.

Stratification may play a role in these creek systems, thanks to either salinity, sediment, or a combination of the two. As shown in figures 5.11 and 5.12, salinity stratification was induced towards the end of the sampling period on both June 30 and July 19 at Stege Marsh site A. This salinity profile corresponded with a stronger turbidity profile on June 30 (dark red in middle and bottom panels of figure 5.11). This may indicate that salinity stratification suppresses turbulence, allowing less of the turbid waters near the bed to mix higher in the water column. Or, the along-channel horizontal salinity gradient that yields the vertical salinity gradient when sheared may also correspond with an along-channel sediment gradient. For such a mechanism to yield the observed vertical sediment profile, it requires lower SSC upstream in the along-channel salinity gradient. However, this is not consistent with our observation of low SSC at high water. This suggests that turbulence suppression due to salinity stratification is perhaps more likely to produce the observed sediment profiles. The onset of salinity stratification on July 19 does not yield a similar shift in sediment

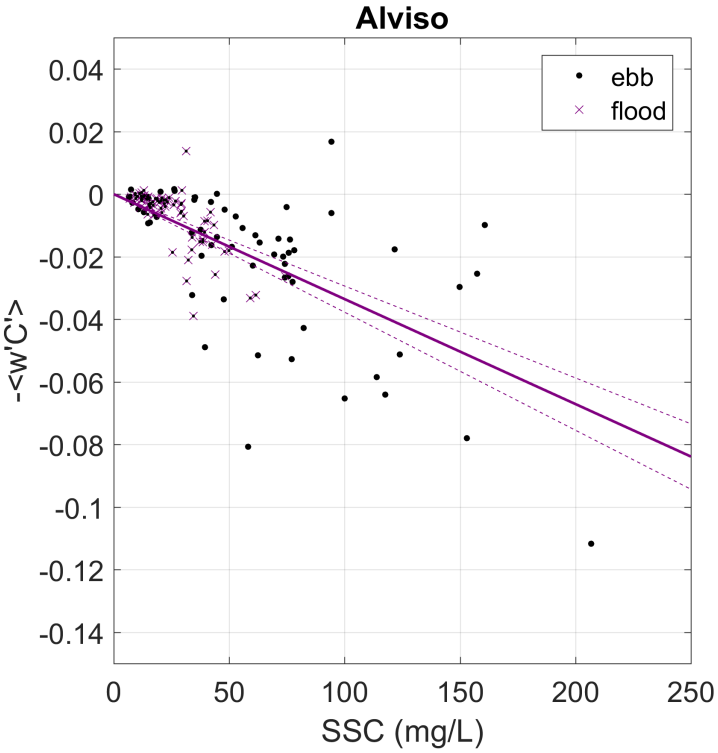

Figure 5.25: Settling velocity on a bulk basis during the Alviso deployment, computed following equation 3.6 for all periods.

stratification (figure 5.12, middle and bottom). Questions therefore remain regarding the extent of sediment stratification, how it correlates with salinity stratification, and what mechanisms produce it.

As mentioned above, salinity induced stratification can suppress vertical mixing. Our data present an opportunity to investigate the extent of turbulence alterations due to stratification, and the role of seiches in altering the salinity profile (does vertical salinity stratification strengthen during strong bay-ward seiches, and weaken during land-ward seiches?), producing turbulence, and impacting the connection between salinity stratification and turbulent mixing.

Similarly, there is a disconnect between the u_* measured through the law of the wall, and the quantity measured directly from Reynolds stresses, with $(\overline{u'w'} + \overline{v'w'})^{1/4}$ yielding lower values (figures 5.18, 5.19, 5.20, and 5.21). Given the tight connection between mean velocity and law-of-the-wall u_*, this discrepancy remains open and interesting. To what extent is it explained through typical scatter in these quantities? Is it at all connected with seiche oscillations? Given the clarity of the log fits at these sites (figures 5.4 and 5.5), we suspect that the discrepancy between the two quantities during high velocities may lead in interesting directions.

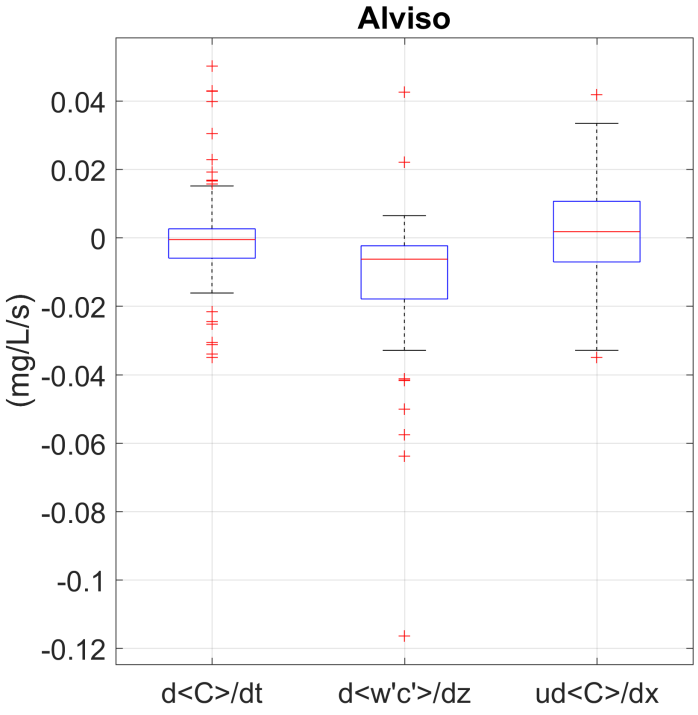

Figure 5.26: Scaling of the unsteady, vertical turbulent diffusion, and advective terms in equation 1.1 at Alviso Slough.

Finally, as described in section 5.5, we consider the balance between resuspension and advection in driving short-term increases in particle concentration. Our preliminary findings suggest that it is unlikely that advection yields the observed fluctuations, and seiche-scale flux is generally negligible. However, we do not consider the role of cross-channel advection or exchange between the channel and creek edges. A closer look at the short peaks in SSC at $21:20$ on July 19, at $16:45$ to $17:10$ on July 28, and others, may suggest a role played by cross-channel exchange, local resuspension, or other processes.

These questions may help in probing the hydrodynamics and sediment transport in estuarine tidal creeks. While it may not be possible to find a relationship between settling velocity and physical forcing, these data suggest additional possibilities for investigation within the realm of turbulence, stratification, and particle transport.

5.6 Conclusions

We characterized some of the dynamics seen in tidal creeks at the edges of San Francisco Bay. In particular, we noted the appearance of a basin-scale seiche. While this seiche strongly impacts near bed velocities, its role on suspended sediment concentration and transport

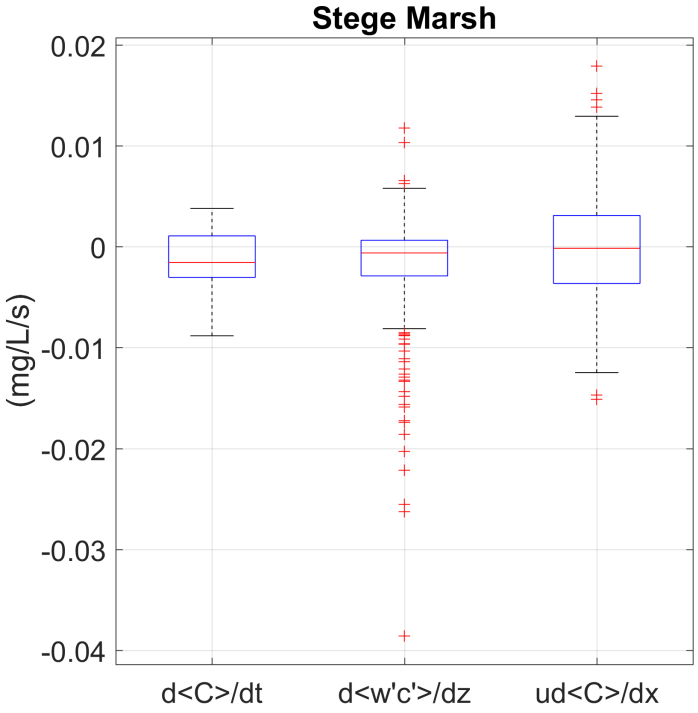

Figure 5.27: Scaling of the unsteady, vertical turbulent diffusion, and advective terms in equation 1.1 at Stege Marsh.

is minimal. We also computed sediment settling velocities, and while we cannot infer the temporal change of particle size or settling velocity in these tidal margin sites, our inferences of the bulk rate of particle settling (table 5.4.1) suggest that estuary margins may be home to a smaller particle size and slower settling velocity than the Bay center.

Chapter 6

Conclusions

With this work, we investigated the roles of turbulence, sediment, and salinity in driving dynamics in coastal and estuarine systems. In systems ranging from the California inner shelf to estuarine tidal creeks of San Francisco Bay, these processes interact.

6.1 Turbulence on the bottom boundary in a region influenced by internal waves

Understanding the turbulence budget at the bottom boundary will enable better predictions of mixing and transport in coastal shelves and contribute to our models of energy transformation by internal waves. We used acoustic measurements of mean and turbulent velocities to characterize the near-bed turbulence at a 30m deep site on the California shelf near Point Sal.

In agreement with previous studies, our results indicated that the near-bed shear production and turbulent dissipation had an approximate balance over a period of eight weeks. The observation site has many drivers of flow dynamics, including vertical stratification, lateral density gradients, tides, surface waves, and internal waves. Our results indicated that the relationship between shear production and dissipation was largely unaffected by the weak stratification produced buoyancy near the bed, and was likewise un-remedied by turbulent diffusive transport. While turbulent diffusive transport was similar in magnitude to dissipation, it generally acted to export TKE from the bottom boundary. However, including turbulent diffusive transport in the local TKE budget did not improve the balance between production and dissipation. Consequently, it was not an important import or export mechanism in the bottom boundary.

We also examined the role of internal waves on energy dissipation, and did not observe any effect. Dissipation, scaled by energy produced by mean currents in the bottom boundary region, did not vary with the phase of internal waves. This may indicate that internal waves affect the mean velocity at the same timescale as they drive dissipation, suggesting that the role of internal waves on turbulence cannot be viewed through this lens. We did not observe

an increase in (scaled) dissipation in the bottom boundary layer near the onset of internal waves, as we anticipated. We conclude that the impact of internal waves on the near-bottom turbulence was not discernable at this site.

We investigated turbulence in the bottom boundary through the approximate balance between production and dissipation. We did not find any influence of internal bores on the turbulence equilibrium. Our study constitutes a high temporal resolution view into turbulence in the bottom boundary layer in the presence of mid-water column internal bores. While the importance of internal waves in ocean mixing and creating turbulence have been well studied, questions remain regarding the role of the bottom boundary on internal wave energy budgets and the role of internal waves on turbulence in the bottom boundary. Understanding turbulence generation, transport, and dissipation near the bed can help predict and characterize sediment resuspension and motion.

6.2 Seasonal variation in sediment parameters for numerical modeling

Understanding the temporal and spatial variation of sediment transport parameters will help make numerical models more accurate and mechanistic. We used field observations of suspended sediment in San Pablo Bay to extract the parameters used in numerical models, and investigated their spatial and temporal variation.

We found that bottom roughness varied between $4 \cdot 10^{-4}$ and $4 \cdot 10^{-6}$ m, bed erodibility varied between 0.02 and 0.15 Pa, and settling velocity varied at 0.78 to $1.46 \cdot 10^{-5}$ m/s from data collection over approximately 2 years. Both bottom roughness and bed erodibility varied on a seasonal scale, suggesting that numerical models for sediment transport may need to account for seasonal variation in setting external parameters. Such variation is likely to stem from the seasonal onset of rainy periods and wind-wave storm events; it was more pronounced during the second, less drought-stricken winter. Particle size varied with tidal and spring-neap cycles. Sediment particles became smaller when tidal velocities increased, breaking up with increased shear. On the spring-neap scale smaller particles present during spring tides settled slower; combined with increased resuspension due to faster velocities this yielded higher concentrations during spring periods.

This work highlights the temporal and spatial scale of variation in parameters typically used for numerical modeling, and offers ideas for predicting such parameters based on observed conditions.

6.3 Stratification dynamics in estuarine shoals

In this work, we characterized the mechanisms controlling periodic vertical salinity stratification in estuarine shallows. While it is commonly assumed that such regions are well-mixed, we observed the onset of vertical salinity gradients due to two mechanisms: tidal straining

and frontal advection. Similar to methods applied by J. H. Simpson et al., 1990, Scully and Geyer, 2012, and Aristizabal and Chant, 2014, we attempted to attribute physical mechanisms to the onset of observed salinity gradients. While previous works in estuaries have highlighted the role of strain in inducing stratification, this work demonstrates the importance of frontal advection.

In contrast to these previous works, our analysis investigated not only the temporal variation of salinity gradients, but also added a focus on the frontal boundary movement in space. This characterization elucidates the competition between destratification mechanisms in the shoals of an estuary, and shows that mixing is more likely to control destratification than advection in broad shallows such as these. Our results show that bed slope is particularly important in controlling the role of mixing relative to advection: with small slopes, mixing becomes the dominant control of destratification, and water level, horizontal salinity gradient, and the critical Simpson number are less important.

6.4 Hydrodynamics and sediment dynamics at estuary margins

We characterized some of the dynamics seen in tidal creeks at the edges of San Francisco Bay. In particular, we noted the appearance of a basin-scale seiche. While this seiche strongly impacts near bed velocities, its role on suspended sediment concentration and transport is minimal. We also computed sediment settling velocities, and while we cannot infer the temporal change of particle size or settling velocity in these tidal margin sites, our inferences of the bulk rate of particle settling suggest that estuary margins may be home to a smaller particle size and slower settling velocity than the Bay center.

Bibliography

Achete, F. M., van der Wegen, M., Roelvink, D., & Jaffe, B. (2015). A 2-D process-based model for suspended sediment dynamics: A first step towards ecological modeling. *Hydrology and Earth System Sciences*, *19*(6), 2837–2857. doi:10.5194/hess-19-2837-2015

Agrawal, Y. & Pottsmith, C. (2000). Instruments for particle size and settling velocity observations in sediment transport. *Marine Geology*, *168*, 89–114. doi:10.1016/S0025-3227(00)00044-X

Allen, R. M., Simeonov, J. A., Calantoni, J., Stacey, M. T., & Variano, E. A. (2018). Turbulence in the presence of internal waves in the bottom boundary layer of the California inner shelf. *Ocean Dynamics*, *68*(4-5), 627–644. doi:10.1007/s10236-018-1147-7

Amos, C., Bergamasco, A., Umgiesser, G., Cappucci, S., Cloutier, D., DeNat, L., ... Cristante, S. (2004). The stability of tidal flats in Venice Lagoon- the results of in-situ measurements using two benthic, annular flumes. *Journal of Marine Systems*, *51*(1-4), 211–241. doi:10.1016/j.jmarsys.2004.05.013

Aristizabal, M. & Chant, R. (2014). Mechanisms driving stratification in Delaware Bay estuary. *Ocean Dynamics*, *64*(11), 1615–1629. doi:10.1007/s10236-014-0770-1

Arthur, R. S. & Fringer, O. B. (2014). The dynamics of breaking internal solitary waves on slopes. *Journal of Fluid Mechanics*, *761*, 360–398. doi:10.1017/jfm.2014.641

Bever, A. J. & MacWilliams, M. L. (2013). Simulating sediment transport processes in San Pablo Bay using coupled hydrodynamic, wave, and sediment transport models. *A multi-discipline approach for understanding sediment transport and geomorphic evolution in an estuarine-coastal system: San Francisco Bay*, *345*(0), 235–253. doi:10.1016/j.margeo.2013.06.012

Bluteau, C. E., Jones, N. L., & Ivey, G. N. (2011). Estimating turbulent kinetic energy dissipation using the inertial subrange method in environmental flows. *Limnology and Oceanography: Methods*, *9*, 302–321. doi:10.4319/lom.2011.9.302

Bourgault, D., Morsilli, M., Richards, C., Neumeier, U., & Kelley, D. (2014). Sediment resuspension and nepheloid layers induced by long internal solitary waves shoaling orthogonally on uniform slopes. *Continental Shelf Research*, *72*, 21–33. doi:10.1016/j.csr.2013.10.019

Brand, A., Lacy, J. R., Gladding, S., Holleman, R., & Stacey, M. (2015). Model-based interpretation of sediment concentration and vertical flux measurements in a shallow estu-

arine environment. *Limnology and Oceanography*, *60*(2), 463–481. Retrieved November 13, 2015, from http://onlinelibrary.wiley.com/doi/10.1002/lno.10047/pdf

Brand, A., Lacy, J. R., Hsu, K., Hoover, D., Gladding, S., & Stacey, M. T. (2010). Wind-enhanced resuspension in the shallow waters of South San Francisco Bay: Mechanisms and potential implications for cohesive sediment transport. *Journal of Geophysical Research*, *115*(C11). doi:10.1029/2010JC006172

Brennan, M. L., Schoellhamer, D. H., Burau, J. R., & Monismith, S. G. (2002). *Tidal asymmetry and variability of bed shear stress and sediment bed flux at a site in San Francisco Bay, USA* (J. C. Winterwerp & C. Kranenburg, Eds.). WOS:000177780800007. Amsterdam: Elsevier Science Bv.

Bricker, J. D. & Monismith, S. G. (2007). Spectral Wave-Turbulence Decomposition. *Journal of Atmospheric and Oceanic Technology*, *24*(8), 1479–1487. doi:10.1175/JTECH2066.1

Burd, A. B. & Jackson, G. A. (2009). Particle Aggregation. *Annual Review of Marine Science*, *1*, 65–90. WOS:000267421700004. doi:10.1146/annurev.marine.010908.163904

Callaway, J. C., Borgnis, E. L., Turner, R. E., & Milan, C. S. (2012). Carbon Sequestration and Sediment Accretion in San Francisco Bay Tidal Wetlands. *Estuaries and Coasts*, *35*(5), 1163–1181. doi:10.1007/s12237-012-9508-9

Cartwright, G. M., Friedrichs, C. T., & Smith, S. J. (2013). A test of the ADV-based Reynolds flux method for in situ estimation of sediment settling velocity in a muddy estuary. *Geo-Marine Letters*, *33*(6), 477–484. doi:10.1007/s00367-013-0340-4

Cheng, R. T., Ling, C. H., Gartner, J. W., & Wang, P. F. (1999). Estimates of bottom roughness length and bottom shear stress in South San Francisco Bay, California. *Journal of Geophysical Research-Oceans*, *104*(C4), 7715–7728. WOS:000079784700008. doi:10.1029/1998JC900126

Cheng, R. & Gartner, J. (1984). *Tides, tidal and residual currents in San Francisco Bay California - results of measurements, 1979-1980* (Report No. 84-4339). Retrieved from http://pubs.er.usgs.gov/publication/wri844339

Cloern, J. E. & Jassby, A. D. (2012). Drivers of change in estuarine-coastal ecosystems: Discoveries from four decades of study in San Francisco Bay. *Reviews of Geophysics*, *50*(4). doi:10.1029/2012RG000397

Collignon, A. G. & Stacey, M. T. (2012). Intratidal Dynamics of Fronts and Lateral Circulation at the Shoal-Channel Interface in a Partially Stratified Estuary. *Journal of Physical Oceanography*, *42*(5), 869–883. doi:10.1175/JPO-D-11-065.1

Collignon, A. G. & Stacey, M. T. (2013). Turbulence Dynamics at the Shoal-Channel Interface in a Partially Stratified Estuary. *Journal of Physical Oceanography*, *43*(5), 970–989. doi:10.1175/JPO-D-12-0115.1

Colosi, J. A., Kumar, N., Suanda, S. H., Freismuth, T. M., & MacMahan, J. H. (2017). Statistics of Internal Tide Bores and Internal Solitary Waves Observed on the Inner Continental Shelf off Point Sal, California. *Journal of Physical Oceanography*, *48*(1), 123–143. doi:10.1175/JPO-D-17-0045.1

Conomos, T. J., for the Advancement of Science, A. A., & of Limnology and Oceanography, A. S. (Eds.). (1979). *San Francisco Bay: The urbanized estuary: Investigations into*

the Natural History of San Francisco Bay and Delta with reference to the influence of man: Fifty-eighth annual meeting of the Pacific Division/American Association for the Advancement of Science held at San Francisco State University, San Francisco, California, June 12-16, 1977. San Francisco, Calif: The Division.

Crimaldi, J. P., Thompson, J. K., Rosman, J. H., Lowe, R. J., & Koseff, J. R. (2002). Hydrodynamics of larval settlement: The influence of turbulent stress events at potential recruitment sites. *Limnology and Oceanography*, *47*(4), 1137–1151. doi:10.4319/lo.2002.47.4.1137

Davis, K. A. & Monismith, S. G. (2011). The Modification of Bottom Boundary Layer Turbulence and Mixing by Internal Waves Shoaling on a Barrier Reef. *Journal of Physical Oceanography*, *41*(11), 2223–2241. doi:10.1175/2011JPO4344.1

Deltares. (2018). *D-Flow Flexible Mesh Technical Reference Manual*. Deltares. Delft, The Netherlands.

Dever, E. & Winant, C. (2002). The evolution and depth structure of shelf and slope temperatures and velocities during the 1997-1998 El Nino near Point Conception, California. *Progress in Oceanography*, *54*, 77–103. Retrieved September 6, 2017, from http://ac.els-cdn.com/S0079661102000447/1-s2.0-S0079661102000447-main.pdf?_tid=14e0c954-932a-11e7-b016-00000aab0f26&acdnat=1504719640_ca8531b95e39a039f141bcb7930aaa3d

Dietrich, W. E. (1982). Settling Velocity of Natural Particles. *Water Resources Research*, *18*(6), 1615–1626. WOS:A1982PW10100003. doi:10.1029/WR018i006p01615

Dyer, K. R. (1989). Sediment processes in estuaries: Future research requirements. *Journal of Geophysical Research: Oceans*, *94*(C10), 14327–14339. doi:10.1029/JC094iC10p14327

Dyer, K. & Manning, A. (1999). Observation of the size, settling velocity and effective density of flocs, and their fractal dimensions. *Journal of Sea Research*, *41*(1-2), 87–95. doi:10.1016/S1385-1101(98)00036-7

Ettema, R. & Mutel, C. F. (2014). *Hans Albert Einstein: His Life as a Pioneering Engineer*. ASCE.

Feddersen, F., Trowbridge, J. H., & Williams, A. J. (2007). Vertical Structure of Dissipation in the Nearshore. *Journal of Physical Oceanography*, *37*(7), 1764–1777. doi:10.1175/JPO3098.1

Feddersen, F. & Williams, A. J. (2007). Direct Estimation of the Reynolds Stress Vertical Structure in the Nearshore. *Journal of Atmospheric and Oceanic Technology*, *24*(1), 102–116. doi:10.1175/JTECH1953.1

Ferre, B., Sherwood, C. R., & Wiberg, P. L. (2010). Sediment transport on the Palos Verdes shelf, California. *Continental Shelf Research*, *30*(7), 761–780. doi:10.1016/j.csr.2010.01.011

Fettweis, M. & Baeye, M. (2015). Seasonal variation in concentration, size, and settling velocity of muddy marine flocs in the benthic boundary layer. *Journal of Geophysical Research: Oceans*, *120*(8), 5648–5667. doi:10.1002/2014JC010644

Feyrer, F., Nobriga, M. L., & Sommer, T. R. (2007). Multidecadal trends for three declining fish species: Habitat patterns and mechanisms in the San Francisco Estuary,

California, USA. *Canadian Journal of Fisheries and Aquatic Sciences*, *64*(4), 723–734. WOS:000247602200013. doi:10.1139/F07-048

Fong, D. A., Monismith, S. G., Stacey, M. T., & Burau, J. R. (2009). Turbulent Stresses and Secondary Currents in a Tidal-Forced Channel with Significant Curvature and Asymmetric Bed Forms. *Journal of Hydraulic Engineering*, *135*(3), 198–208. doi:10.1061/(ASCE)0733-9429(2009)135:3(198)

Foster-Martinez, M., Lacy, J., Ferner, M., & Variano, E. (2018). Wave attenuation across a tidal marsh in San Francisco Bay. *Coastal Engineering*, *136*, 26–40. doi:10.1016/j.coastaleng.2018.02.001

Fugate, D. C. & Friedrichs, C. T. (2002). Determining concentration and fall velocity of estuarine particle populations using ADV, OBS and LISST. *Continental Shelf Research*, *22*(11), 1867–1886. Retrieved May 15, 2014, from http://www.sciencedirect.com/science/article/pii/S0278434302000432

Ganju, N. K., Schoellhamer, D. H., Murrell, M. C., Gartner, J. W., & Wright, S. A. (2007). Constancy of the relation between floc size and density in San Francisco Bay. In J. P. .-.-Y. Maa, L. P. Sanford, & D. H. Schoellhamer (Eds.), *Proceedings in Marine Science* (Vol. 8, pp. 75–91). Estuarine and Coastal Fine Sediments Dynamics. Elsevier. doi:10.1016/S1568-2692(07)80007-6

Geyer, W. R. & MacCready, P. (2014). The Estuarine Circulation. *Annual Review of Fluid Mechanics*, *46*(1), 175–197. doi:10.1146/annurev-fluid-010313-141302

Good, G., Ireland, P., Bewley, G., Bodenschatz, E., Collins, L., & Warhaft, Z. (2014). Settling regimes of inertial particles in isotropic turbulence. *Journal of Fluid Mechanics*, *759*. doi:10.1017/jfm.2014.602

Goring, D. G. & Nikora, V. I. (2002). Despiking Acoustic Doppler Velocimeter Data. *Journal of Hydraulic Engineering*, *128*, 117–126. Retrieved March 31, 2014, from https://mail-attachment.googleusercontent.com/attachment/u/1/?ui=2&ik=f4df28b4f9&view=att&th=144e5bb7879d474d&attid=0.1&disp=safe&realattid=f_ht1r7j3x0&zw&saduie=AG9B_P9M7XmJmZ377vYiyc3MUy_s&sadet=1396301929057&sads=N2SiBEKHFvsml5Fl5pnkKHnPLHk

Grabowski, R. C., Droppo, I. G., & Wharton, G. (2011). Erodibility of cohesive sediment: The importance of sediment properties. *Earth-Science Reviews*, *105*(3-4), 101–120. doi:10.1016/j.earscirev.2011.01.008

Grant, W. D. & Madsen, O. S. [O S]. (1986). The Continental-Shelf Bottom Boundary Layer. *Annual Review of Fluid Mechanics*, *18*(1), 265–305. doi:10.1146/annurev.fl.18.010186.001405

Gross, T. F. & Nowell, A. R. (1983). Mean flow and turbulence scaling in a tidal boundary layer. *Continental Shelf Research*, *2*(2-3), 109–126. Retrieved February 2, 2017, from http://www.sciencedirect.com/science/article/pii/0278434383900110

Hayes, T. P., Kinney, J. J., & Wheeler, N. J. (1984). *California Surface Wind Climatology*. State of California Air Resources Board, Aerometric Projects and Laboratory Branch Meteorology Section. Retrieved September 19, 2017, from https://www.arb.ca.gov/research/apr/reports/l013.pdf

He, C., Scott, E., Graham, M., & Binns, A. (2014). Measurement and numerical modeling studies of the highest bottom shear stress in the Randle Reef area. *Canadian Journal of Civil Engineering*, *41*(9), 828–838. doi:10.1139/cjce-2014-0070

Helfrich, K. R. & Melville, W. K. (2006). Long nonlinear internal waves. *Annu. Rev. Fluid Mech. 38*, 395–425. Retrieved March 6, 2017, from http://annualreviews.org/doi/abs/10.1146/annurev.fluid.38.050304.092129

Hill, P., Newgard, J., Law, B., & Milligan, T. (2013). Flocculation on a muddy intertidal flat in Willapa Bay, Washington, Part II: Observations of suspended particle size in a secondary channel and adjacent flat. *Continental Shelf Research*, *60*, S145–S156. doi:10.1016/j.csr.2012.06.006

Hoover, D. & Lacy, J. R. [Jessica R]. (2011). Hoover/Lacy Suspended Sediment Sample Processing Protocol.

Howard, R. J. & Serre, E. (2015). Large-eddy simulation in a mixing tee junction: High-order turbulent statistics analysis. *International Journal of Heat and Fluid Flow*, *51*, 65–77. doi:10.1016/j.ijheatfluidflow.2014.11.009

Huang, I. B. (2017). *Cohesive sediment flocculation in a partially-stratified estuary* (Doctoral dissertation, Stanford). Retrieved February 4, 2018, from https://purl.stanford.edu/dw007zh9379

Inman, D. L. (1952). Measures for Describing the Size Distribution of Sediments. *Journal of Sedimentary Petrology*, *22*(3), 125–145. Retrieved February 8, 2018, from https://gsw.silverchair-cdn.com/gsw/Content_public/Journal/jsedres/22/3/10.1306_D42694DB-2B26-11D7-8648000102C1865D/3/125.pdf?Expires=1518149767&Signature=OGBffEWU9jdoqQOqZbRKk8lcZZlFRRXvf-Ruwl2YdeARxzh5Gh4kPAS5s~CYKc~bDXnx1mS5YkR1iSrnNxUcEhKRcXU~QF-1jVSPfBjs7fg7j32zNW6o3Ajf4PqNdZFewbSrQuVL~6N1vNpS0EVJJ3mN9PssRPp98sCMwh5vJC0tEckajSHTxY1PscfyxMyLPxdWqjK9Aw__&Key-Pair-Id=APKAIUCZBIA4LVPAVW3Q

Joensuu, M., Pilditch, C. A., Harris, R., Hietanen, S., Pettersson, H., & Norkko, A. (2018). Sediment properties, biota, and local habitat structure explain variation in the erodibility of coastal sediments: Variation in the erodibility of coastal sediments. *Limnology and Oceanography*, *63*(1), 173–186. doi:10.1002/lno.10622

Jones, C. A. & Jaffe, B. E. [Bruce E.]. (2013). Influence of history and environment on the sediment dynamics of intertidal flats. *A multi-discipline approach for understanding sediment transport and geomorphic evolution in an estuarine-coastal system: San Francisco Bay*, *345*(0), 294–303. doi:10.1016/j.margeo.2013.05.011

Jordi, A., Basterretxea, G., Casas, B., Angles, S., & Garces, E. (2008). Seiche-forced resuspension events in a Mediterranean harbour. *Continental Shelf Research*, *28*(4-5), 505–515. doi:10.1016/j.csr.2007.10.009

Kaimal, J. C., Wyngaard, J., Izumi, Y., & Coté, O. R. (1972). Spectral characteristics of surface-layer turbulence. *Quarterly Journal of the Royal Meteorological Society*, *98*(417), 563–589. Retrieved February 5, 2016, from http://onlinelibrary.wiley.com/doi/10.1002/qj.49709841707/full

Kawanisi, K. & Shiozaki, R. (2008). Turbulent Effects on the Settling Velocity of Suspended Sediment. *Journal of Hydraulic Engineering*, *134*(2), 261–266. doi:10.1061/(ASCE)0733-9429(2008)134:2(261)

Knowles, N. (2010). Potential Inundation Due to Rising Sea Levels in the San Francisco Bay Region. *San Francisco Estuary and Watershed Science*, *8*(1). Retrieved April 30, 2018, from https://escholarship.org/uc/item/8ck5h3qn

Krone, R. B. (1962). *Flume studies of the transport of sediment in estuarial shoaling processes: Final report*. University of California, Berkeley. Hydraulic Engineering Laboratory.

Krone, R. B. (1999). Effects of bed structure on erosion of cohesive sediments. *Journal of Hydraulic Engineering-Asce*, *125*(12), 1297–1301. WOS:000083682900009. doi:10.1061/(ASCE)0733-9429(1999)125:12(1297)

Krone, R. (1979). Sedimentation in the San Francisco Bay System. In T. Conomos (Ed.), *San Francisco Bay: The Urbanized Estuary* (pp. 85–96). Pacific Division of the American Association for the Advancement of Science, San Francisco, California 94118.

Lacy, J. R. [J. R.], Sherwood, C. R., Wilson, D. J., Chisholm, T. A., & Gelfenbaum, G. R. (2005). Estimating hydrodynamic roughness in a wave-dominated environment with a high-resolution acoustic Doppler profiler. *Journal of Geophysical Research-Oceans*, *110*(C6), C06014. WOS:000230482200001. doi:10.1029/2003JC001814

Lacy, J. R. [J. R.], Stacey, M. T., Burau, J. R., & Monismith, S. G. (2003). Interaction of lateral baroclinic forcing and turbulence in an estuary. *Journal of Geophysical Research-Oceans*, *108*(C3), 3089. WOS:000182224300005. doi:10.1029/2002JC001392

Lacy, J. R. [Jessica R.], Allen, R. M., Foster-Martinez, M. R., Ferreira, J. C., & O'Neill, A. C. (2017). Hydrodynamic and sediment transport data from San Pablo Bay and China Camp marsh (northern San Francisco Bay), 2013-2016. Retrieved from https://doi.org/10.5066/F7HM56MX

Lacy, J. R. [Jessica R.], Gladding, S., Brand, A., Collignon, A., & Stacey, M. (2014). Lateral Baroclinic Forcing Enhances Sediment Transport from Shallows to Channel in an Estuary. *Estuaries and Coasts*. doi:10.1007/s12237-013-9748-3

Lacy, J. R. [Jessica R.] & MacVean, L. J. (2016). Wave attenuation in the shallows of San Francisco Bay. *Coastal Engineering*, *114*, 159–168. doi:10.1016/j.coastaleng.2016.03.008

Lamb, K. G. (2014). Internal Wave Breaking and Dissipation Mechanisms on the Continental Slope/Shelf. *Annual Review of Fluid Mechanics*, *46*(1), 231–254. doi:10.1146/annurev-fluid-011212-140701

Lambert, R. A. & Variano, E. A. (2016). Collision of oil droplets with marine aggregates: Effect of droplet size. *Journal of Geophysical Research: Oceans*, *121*(5), 3250–3260. doi:10.1002/2015JC011562

Leichter, J. J., Wing, S. R., Miller, S. L., & Denny, M. W. (1996). Pulsed delivery of subthermocline water to Conch Reef (Florida Keys) by internal tidal bores. *Limnology and Oceanography*, *41*(7), 1490–1501. Retrieved September 13, 2017, from http://onlinelibrary.wiley.com/doi/10.4319/lo.1996.41.7.1490/full

Lerczak, J. A. & Geyer, W. R. (2004). Modeling the Lateral Circulation in Straight, Stratified Estuaries*. *Journal of Physical Oceanography*, *34*(6), 1410–1428. doi:10.1175/1520-0485(2004)034⟨1410:MTLCIS⟩2.0.CO;2

Lesen, A. E. (2006). Sediment organic matter composition and dynamics in San Francisco Bay, California, USA: Seasonal variation and interactions between water column chlorophyll and the benthos. *Estuarine, Coastal and Shelf Science*, *66*(3-4), 501–512. doi:10.1016/j.ecss.2005.10.003

Lesser, G., Roelvink, J., van Kester, J., & Stelling, G. (2004). Development and validation of a three-dimensional morphological model. *Coastal Engineering*, *51*(8-9), 883–915. doi:10.1016/j.coastaleng.2004.07.014

Maa, J. P.-y. & Kim, S.-c. (2002). A Constant Erosion Rate Model for Fine Sediment in the York River, Virginia. *Environmental Fluid Mechanics; Dordrecht*, *1*(4), 345–360. doi:http://dx.doi.org/10.1023/A:1015799926777

MacVean, L. J. & Lacy, J. R. [Jessica R.]. (2014). Interactions between waves, sediment, and turbulence on a shallow estuarine mudflat. *Journal of Geophysical Research: Oceans*, *119*(3), 1534–1553. doi:10.1002/2013JC009477

Madsen, O. S. [Ole Secher]. (1994). Spectral wave-current bottom boundary layer flows. *Coastal engineering*, *94*, 384–397. Retrieved February 5, 2016, from http://ascelibrary.org/doi/abs/10.1061/9780784400890.030

Manning, A. & Schoellhamer, D. [D.H.]. (2013). Factors controlling floc settling velocity along a longitudinal estuarine transect. *Marine Geology*, *345*, 266–280. doi:10.1016/j.margeo.2013.06.018

Manning, A. J. (2001). *A study of the effect of turbulence on the properties of flocculated mud* (Doctoral dissertation, University of Plymouth).

Mariotti, G., Valentine, K., & Fagherazzi, S. (2015). Time-dependent behavior of a placed bed of cohesive sediment subjected to erosion and deposition cycles. *Ocean Dynamics*, *65*(2), 287–294. doi:10.1007/s10236-014-0798-2

Markussen, T. N. & Andersen, T. J. (2014). Flocculation and floc break-up related to tidally induced turbulent shear in a low-turbidity, microtidal estuary. *Journal of Sea Research*, *89*, 1–11. doi:10.1016/j.seares.2014.02.001

Mathew, R. & Winterwerp, J. C. (2017). Surficial sediment erodibility from time-series measurements of suspended sediment concentrations: Development and validation. *Ocean Dynamics*, *67*(6), 691–712. doi:10.1007/s10236-017-1055-2

McDougall, T., J. & Barker, P. M. (2011). *Getting started with TEOS-10 and the Gibbs Seawater (GSW) Oceanographic Toolbox*. SCOR/IAPSO WG127.

McMillan, J. M. & Hay, A. E. (2017). Spectral and Structure Function Estimates of Turbulence Dissipation Rates in a High-Flow Tidal Channel Using Broadband ADCPs. *Journal of Atmospheric and Oceanic Technology*, *34*(1), 5–20. Retrieved September 15, 2017, from http://journals.ametsoc.org/doi/abs/10.1175/JTECH-D-16-0131.1

McSweeney, J. M., Chant, R. J., & Sommerfield, C. K. (2016). Lateral variability of sediment transport in the Delaware Estuary. *Journal of Geophysical Research: Oceans*, *121*(1), 725–744. doi:10.1002/2015JC010974

Mehta, A. J. (2014). *An Introduction to Hydraulics of Fine Sediment Transport*. Google-Books-ID: ANw7DQAAQBAJ. World Scientific Publishing Company.

Mietta, F., Chassagne, C., & Winterwerp, J. (2009). Shear-induced flocculation of a suspension of kaolinite as function of pH and salt concentration. *Journal of Colloid and Interface Science*, *336*(1), 134–141. doi:10.1016/j.jcis.2009.03.044

Mikkelsen, O. & Pejrup, M. (2001). The use of a LISST-100 laser particle sizer for in-situ estimates of floc size, density and settling velocity. *Geo-Marine Letters*, *20*(4), 187–195. doi:10.1007/s003670100064

Monchaux, R., Bourgoin, M., & Cartellier, A. (2012). Analyzing preferential concentration and clustering of inertial particles in turbulence. *International Journal of Multiphase Flow*, *40*, 1–18. doi:10.1016/j.ijmultiphaseflow.2011.12.001

Monismith, S. G., Kimmerer, W., Burau, J. R., & Stacey, M. T. (2002). Structure and flow-induced variability of the subtidal salinity field in northern San Francisco Bay. *Journal of Physical Oceanography*, *32*(11), 3003–3019.

Moum, J. N., Farmer, D. M., Shroyer, E. L., Smyth, W. D., & Armi, L. (2007). Dissipative Losses in Nonlinear Internal Waves Propagating across the Continental Shelf. *Journal of Physical Oceanography*, *37*(7), 1989–1995. doi:10.1175/JPO3091.1

Moum, J. N., Klymak, J. M., Nash, J. D., Perlin, A., & Smyth, W. D. (2007). Energy Transport by Nonlinear Internal Waves. *Journal of Physical Oceanography*, *37*(7), 1968–1988. doi:10.1175/JPO3094.1

Munk, W. & Wunsch, C. (1998). Abyssal recipes II: Energetics of tidal and wind mixing. *Deep Sea Research Part I: Oceanographic Research Papers*, *45*(12), 1977–2010. Retrieved March 6, 2017, from http://www.sciencedirect.com/science/article/pii/S0967063798000703

Nielsen, P. (1992). *Coastal bottom boundary layers and sediment transport*. World scientific.

Nielsen, P. (2007). Mean and variance of the velocity of solid particles in turbulence. In *Particle-Laden Flow* (pp. 385–391). Springer. Retrieved February 5, 2016, from http://link.springer.com/chapter/10.1007/978-1-4020-6218-6_30

Null, J. (2018). Golden gate weather services. Retrieved from http://ggweather.com/sf/season.html

Ölçmen, S. M. & Simpson, R. L. (2008). Experimental transport-rate budgets in complex 3-D turbulent flow near a wing/body junction. *International Journal of Heat and Fluid Flow*, *29*(4), 874–890. doi:10.1016/j.ijheatfluidflow.2007.12.004

Omand, M. M., Leichter, J. J., Franks, P. J. S., Guza, R. T., Lucas, A. J., & Feddersen, F. (2011). Physical and biological processes underlying the sudden surface appearance of a red tide in the nearshore. *Limnology and Oceanography*, *56*(3), 787–801. doi:10.4319/lo.2011.56.3.0787

Pawlowicz, R., Beardsley, B., & Lentz, S. (2002). Classical tidal harmonic analysis including error estimates in MATLAB using T_tide. *Computers & Geosciences*, *28*(8), 929–937. doi:10.1016/S0098-3004(02)00013-4

Pineda, J. (1994). Internal tidal bores in the nearshore: Warm-water fronts, seaward gravity currents and the onshore transport of neustonic larvae. *Journal of Marine Research*, *52*(3), 427–458. doi:https://doi.org/10.1357/0022240943077046

Pope, S. B. (2000). *Turbulent flows*. Cambridge university press.

Poulton, V. K., Lovvorn, J. R., & Takekawa, J. Y. (2004). Spatial and overwinter changes in clam populations of San Pablo Bay, a semiarid estuary with highly variable freshwater inflow. *Estuarine, Coastal and Shelf Science*, *59*(3), 459–473. doi:10.1016/j.ecss.2003.10.005

Ralston, D. K., Cowles, G. W., Geyer, W. R., & Holleman, R. C. (2017). Turbulent and numerical mixing in a salt wedge estuary: Dependence on grid resolution, bottom roughness, and turbulence closure. *Journal of Geophysical Research: Oceans*, *122*(1), 692–712. doi:10.1002/2016JC011738

Reidenbach, M. A., Monismith, S. G., Koseff, J. R., Yahel, G., & Genin, A. (2006). Boundary layer turbulence and flow structure over a fringing coral reef. *Limnology and Oceanography*, *51*(5), 1956–1968. Retrieved February 2, 2017, from http://onlinelibrary.wiley.com/doi/10.4319/lo.2006.51.5.1956/full

Reynolds, W. C. & Hussain, A. K. M. F. (1972). The mechanics of an organized wave in turbulent shear flow. Part 3. Theoretical models and comparisons with experiments. *Journal of Fluid Mechanics*, *54*(2), 263–288. doi:10.1017/S0022112072000679

Safak, I., Allison, M., & Sheremet, A. (2013). Floc variability under changing turbulent stresses and sediment availability on a wave energetic muddy shelf. *Continental Shelf Research*, *53*, 1–10. doi:10.1016/j.csr.2012.11.015

Sahin, C., Ari Guner, H. A., Ozturk, M., & Sheremet, A. (2017). Floc size variability under strong turbulence: Observations and artificial neural network modeling. *Applied Ocean Research*, *68*(Supplement C), 130–141. doi:10.1016/j.apor.2017.08.012

Sanford, L. P. & Maa, J. P. Y. (2001). A unified erosion formulation for fine sediments. *Marine Geology*, *179*(1-2), 9–23. WOS:000171111800002. doi:10.1016/S0025-3227(01)00201-8

Sanford, T. B. & Lien, R. C. (1999). Turbulent properties in a homogeneous tidal bottom boundary layer. *Journal of Geophysical Research-Oceans*, *104*(C1), 1245–1257. WOS:000078116300004. doi:10.1029/1998JC900068

Schoellhamer, D. H., Ganju, N., & Shellenbarger, G. G. (2008). Chapter 2 Sediment Transport in San Pablo Bay. *Technical Studies for the Aquatic Transfer Facility: Hamilton Wetlands Restoration Project, Technical Report*.

Schoellhamer, D. [DavidH.]. (2011). Sudden Clearing of Estuarine Waters upon Crossing the Threshold from Transport to Supply Regulation of Sediment Transport as an Erodible Sediment Pool is Depleted: San Francisco Bay, 1999. *Estuaries and Coasts*, *34*(5), 885–899. doi:10.1007/s12237-011-9382-x

Schwarz, C., Cox, T., van Engeland, T., van Oevelen, D., van Belzen, J., van de Koppel, J., ... Temmerman, S. (2017). Field estimates of floc dynamics and settling velocities in a tidal creek with significant along-channel gradients in velocity and SPM. *Estuarine, Coastal and Shelf Science*, *197*(Supplement C), 221–235. doi:10.1016/j.ecss.2017.08.041

Scully, M. E. & Geyer, W. R. (2012). The Role of Advection, Straining, and Mixing on the Tidal Variability of Estuarine Stratification. *Journal of Physical Oceanography*, *42*(5), 855–868. doi:10.1175/JPO-D-10-05010.1

Shaw, W. J. & Trowbridge, J. H. (2001). The direct estimation of near-bottom turbulent fluxes in the presence of energetic wave motions. *Journal of Atmospheric and Oceanic Technology*, *18*(9), 1540–1557. WOS:000171134100009. doi:10.1175/1520-0426(2001)018⟨1540:TDEONB⟩2.0.CO;2

Shaw, W. J., Trowbridge, J. H., & Williams, A. J. (2001). Budgets of turbulent kinetic energy and scalar variance in the continental shelf bottom boundary layer. *Journal of Geophysical Research-Oceans*, *106*(C5), 9551–9564. WOS:000168653300039. doi:10.1029/2000JC000240

Sherwood, C. R., Lacy, J. R., & Voulgaris, G. (2006). Shear velocity estimates on the inner shelf off Grays Harbor, Washington, USA. *Continental Shelf Research*, *26*(17-18), 1995–2018. doi:10.1016/j.csr.2006.07.025

Simpson, J. H. (1971). Density stratification and microstructure in the western Irish Sea. In *Deep Sea Research and Oceanographic Abstracts* (Vol. 18, pp. 309–319). Elsevier. Retrieved June 1, 2017, from http://www.sciencedirect.com/science/article/pii/0011747171900362

Simpson, J. H., Brown, J., Matthews, J., & Allen, G. (1990). Tidal Straining, Density Currents, and Stirring in the Control of Estuarine Stratification. *Estuaries*, *13*(2), 125–132. doi:10.2307/1351581

Stacey, M. T., Burau, J. R., & Monismith, S. G. (2001). Creation of residual flows in a partially stratified estuary. *Journal of Geophysical Research: Oceans*, *106*(C8), 17013–17037. doi:10.1029/2000JC000576

Stacey, M. T., Fram, J. P., & Chow, F. K. (2008). Role of tidally periodic density stratification in the creation of estuarine subtidal circulation. *Journal of Geophysical Research: Oceans*, *113*(C8). doi:10.1029/2007JC004581

Stolzenbach, K. D. & Elimelech, M. (1994). The effect of particle density on collisions between sinking particles: Implications for particle aggregation in the ocean. *Deep Sea Research Part I: Oceanographic Research Papers*, *41*(3), 469–483. Retrieved February 4, 2016, from http://www.sciencedirect.com/science/article/pii/0967063794900914

Toorman, E. A. (2000). *Cohesive sediment transport modeling: European perspective* (W. H. McAnally & A. J. Mehta, Eds.). WOS:000173565800001. Amsterdam: Elsevier Science Bv.

Trembanis, A., Wright, L., Friedrichs, C., Green, M., & Hume, T. (2004). The effects of spatially complex inner shelf roughness on boundary layer turbulence and current and wave friction: Tairua embayment, New Zealand. *Continental Shelf Research*, *24*(13-14), 1549–1571. doi:10.1016/j.csr.2004.04.006

Trowbridge, J. H., Geyer, W. R., Bowen, M. M., & Williams III, A. J. (1999). Near-Bottom Turbulence Measurements in a Partially Mixed Estuary: Turbulent Energy Balance, Velocity Structure, and Along-Channel Momentum Balance*. *Journal of Physical Oceanography*, *29*(12), 3056–3072. Retrieved February 5, 2016, from http://journals.

ametsoc.org/doi/abs/10.1175/1520-0485(1999)029%3C3056:NBTMIA%3E2.0.CO%3B2

van der Wegen, M. & Jaffe, B. E. [B. E.]. (2014). Processes governing decadal-scale depositional narrowing of the major tidal channel in San Pablo Bay, California, USA. *Journal of Geophysical Research: Earth Surface*, *119*(5), 1136–1154. doi:10.1002/2013JF002824

Verney, R., Lafite, R., Claude Brun-Cottan, J., & Le Hir, P. (2011). Behaviour of a floc population during a tidal cycle: Laboratory experiments and numerical modelling. *Continental Shelf Research*, *31*(10), S64–S83. doi:10.1016/j.csr.2010.02.005

Voulgaris, G. [G.] & Trowbridge, J. H. (1998). Evaluation of the Acoustic Doppler Velocimeter (ADV) for Turbulence Measurements*. *Journal of Atmospheric and Oceanic Technology*, *15*(1), 272–289. doi:10.1175/1520-0426(1998)015⟨0272:EOTADV⟩2.0.CO;2

Voulgaris, G. [George] & Meyers, S. T. (2004). Temporal variability of hydrodynamics, sediment concentration and sediment settling velocity in a tidal creek. *Continental Shelf Research*, *24*(15), 1659–1683. doi:10.1016/j.csr.2004.05.006

Walter, R. K., Squibb, M. E., Woodson, C. B., Koseff, J. R., & Monismith, S. G. (2014). Stratified turbulence in the nearshore coastal ocean: Dynamics and evolution in the presence of internal bores. *Journal of Geophysical Research: Oceans*, *119*(12), 8709–8730. doi:10.1002/2014JC010396

Walter, R. K., Woodson, C. B., Arthur, R. S., Fringer, O. B., & Monismith, S. G. (2012). Nearshore internal bores and turbulent mixing in southern Monterey Bay: Internal Bores and Turbulent Mixing. *Journal of Geophysical Research: Oceans*, *117*(C7), n/a–n/a. doi:10.1029/2012JC008115

Wiberg, P. L., Law, B. A., Wheatcroft, R. A., Milligan, T. G., & Hill, P. S. (2013). Seasonal variations in erodibility and sediment transport potential in a mesotidal channel-flat complex, Willapa Bay, WA. *Continental Shelf Research*, *60*, S185–S197. doi:10.1016/j.csr.2012.07.021

Wiberg, P. L. & Sherwood, C. R. (2008). Calculating wave-generated bottom orbital velocities from surface-wave parameters. *Computers & Geosciences*, *34*(10), 1243–1262. doi:10.1016/j.cageo.2008.02.010

Wiles, P. J., Rippeth, T. P., Simpson, J. H., & Hendricks, P. J. (2006). A novel technique for measuring the rate of turbulent dissipation in the marine environment. *Geophysical Research Letters*, *33*(21), L21608. WOS:000241983100002. doi:10.1029/2006GL027050

Winterwerp, J. C. (1998). A simple model for turbulence induced flocculation of cohesive sediment. *Journal of Hydraulic Research*, *36*(3), 309–326. doi:10.1080/00221689809498621

Wright, L., Kim, S.-C., & Friedrichs, C. (1999). Across-shelf variations in bed roughness, bed stress and sediment suspension on the northern California shelf. *Marine Geology*, *154*(1-4), 99–115. doi:10.1016/S0025-3227(98)00106-6

Wright, S. A. & Schoellhamer, D. H. (2004). Trends in the Sediment Yield of the Sacramento River, California, 1957 fffdfffdfffd 2001. *San Francisco Estuary and Watershed Science*, *2*(2). Retrieved January 30, 2018, from https://ca.water.usgs.gov/user_projects/sfbay/publications_group/wright_schoellhamer_trends.pdf

Yakovenko, S. N. (2011). Second- and third-order moment budgets in a turbulent patch resulting from internal gravity wave breaking. *Journal of Physics: Conference Series*, *318*(7), 072022. doi:10.1088/1742-6596/318/7/072022

Yang, Y., Wang, Y. P., Li, C., Gao, S., Shi, B., Zhou, L., ... Dai, C. (2016). On the variability of near-bed floc size due to complex interactions between turbulence, SSC, settling velocity, effective density and the fractal dimension of flocs. *Geo-Marine Letters*, *36*(2), 135–149. WOS:000372910200005. doi:10.1007/s00367-016-0434-x

Appendix A

Appendix for Chapter 3, Seasonal Variation in Sediment Parameters

A.1 Supplementary Figures

A.1.1 Using T-Tide to reconstruct tidal velocities and pressure

We deployed instruments in San Pablo Bay from December 2013 through April 2015, and again in May and June of 2016. However, some of the instruments did not function during some deployment periods, and there were short periods in-between deployments when instruments were not present. We used T-Tide to construct continuous streams of velocity and pressure data at the measurement sites (Pawlowicz et al., 2002). Comparing the predicted (black) and measured (red) pressure signals at CHC16M2T showed that there was no consistent bias in the reconstructed signal, and the correlation coefficient between the two quantities was 0.974 (figure A.1). Although the match between predicted and measured pressure varied through the spring-neap cycle, the prediction performed equally well at all depths.

A.1.2 Computing Reynolds stress through wave-turbulence decomposition

We compare high-frequency pressure sensors with ADVs through the root-mean-square wave height, H_{rms}, as both instruments enable a computation of this quantity. From pressure measurements, root-mean-square wave height is computed from a spectral density of surface elevation, following Wiberg and Sherwood, 2008, , eq 4. From velocity measurements, this metric is computed in frequency space using horizontal velocity, filtered to exclude motions outside the frequency range for waves, following Wiberg and Sherwood, 2008, , eq 12. The pressure sensors revealed an artificially low H_{rms} from a number of deployments (figure A.2). However, the trend in $H_{rms,P}$ generally followed the trend in $H_{rms,u}$, suggesting that the

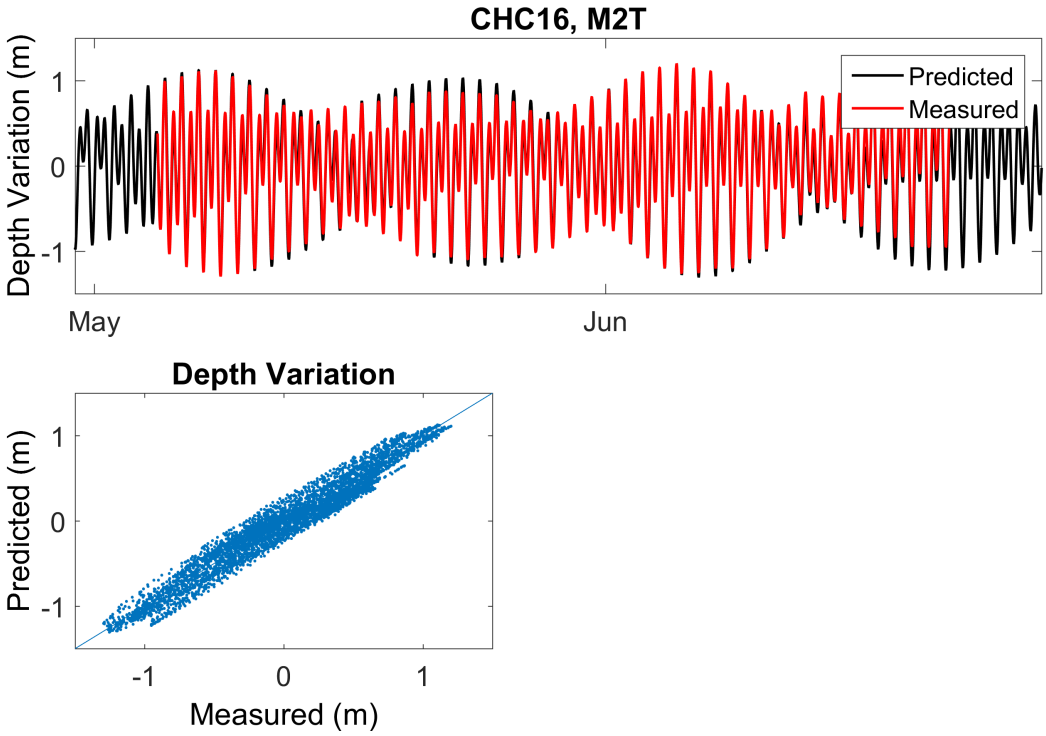

Figure A.1: (top) T-Tide predicts depth at site M2T during CHC16 (black) reasonably well, using data from CHC13 and CHC14 to generate the tidal components. (bottom) A comparision between predicted and measured depth during this period aligns well on the 1:1 line (blue), with a correlation coefficient of 0.974.

pressure instrument recorded the wave motions, even while the magnitude was suppressed at times. It is very clearly noticeable that the pressure is recording in an artificially low regime in figure A.3a, where $H_{rms,P}$ jumps from a suppressed state to a 'clean' state near the end of Feb 8, 2014.

Despite the off-set in the pressure measurement, our analysis indicates that it can still be used to compute the Reynolds stress. A comparison of the techniques by Bricker and Monismith, 2007 and Feddersen and Williams, 2007 shows that both yield similar estimates of the Reynolds stress, and both remove the impact of waves (figure A.3), even though Bricker and Monismith, 2007 relies only on the frequency range of wave motions, while Feddersen and Williams, 2007 requires measurements of pressure and velocity. The success of the Feddersen and Williams, 2007 method is due to pressure scaling when it was artificially suppressed, as described in section 3.3.3.

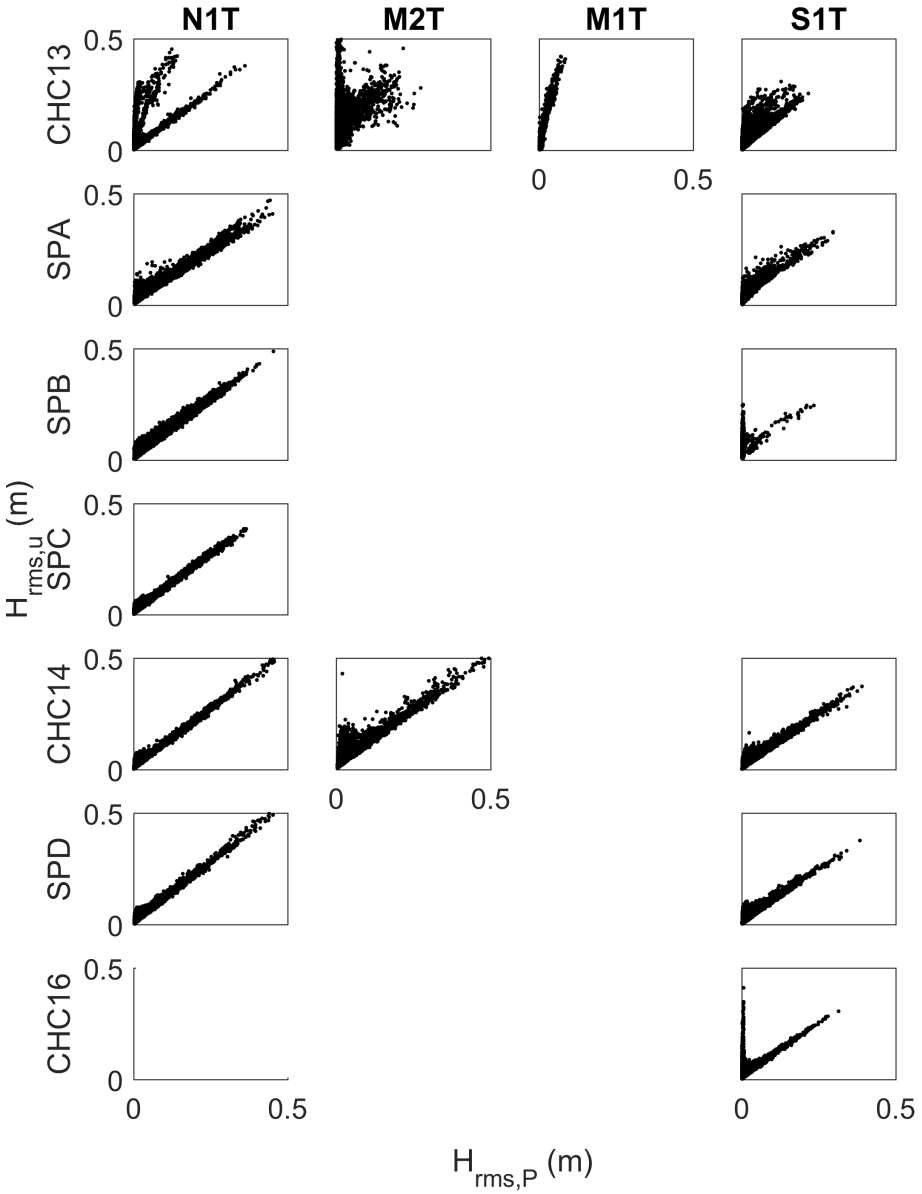

Figure A.2: Root-mean-square wave height (H_{rms}) computed from velocity (u) vs pressure (P), during all deployments. When no figure is shown, either the instrument malfunctioned or no instrument was deployed during that period. The pressure derived data performed poorly for a number of deployments.

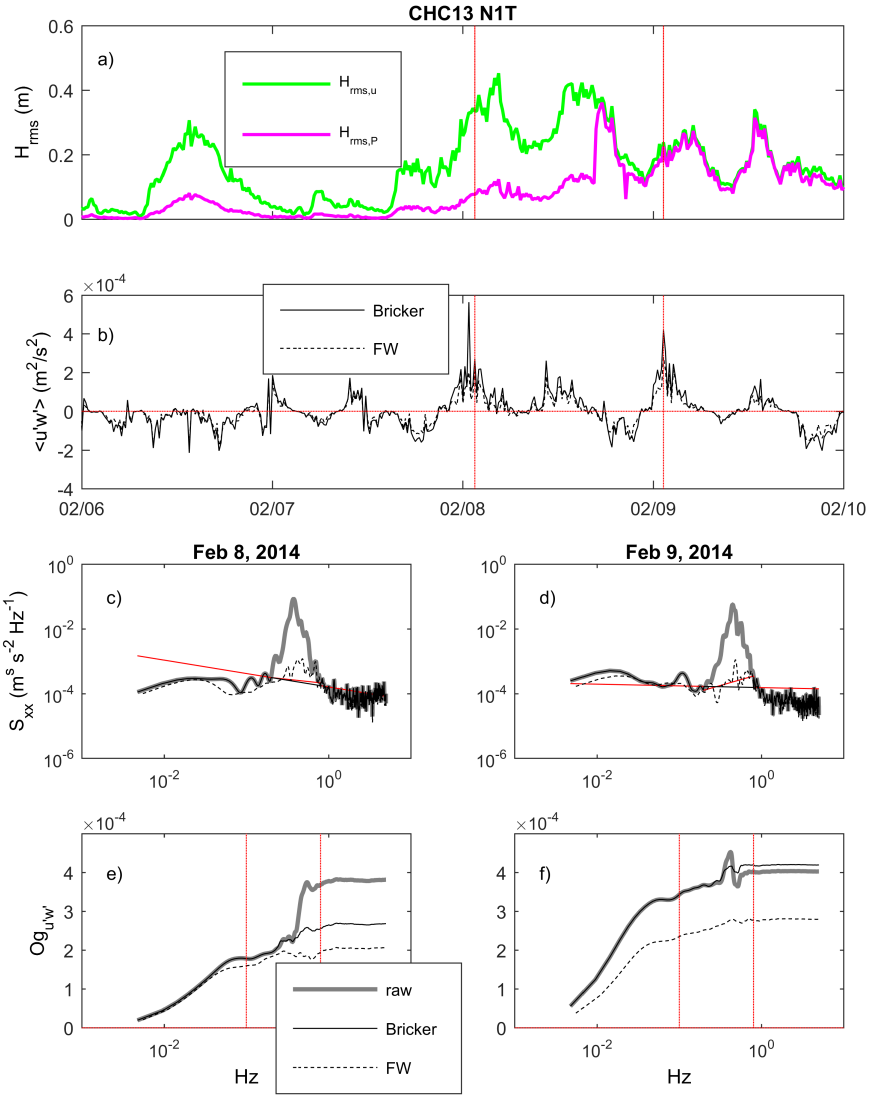

Figure A.3: Wave-turbulence decomposition, from CHC13N1T. a) Root-mean-square wave height (H_{rms}) based on velocity (u) and pressure (P). Mid-day on Feb 8, 2014, the pressure-based value jumps to the scale of the velocity-based calculation. b) Reynolds stresses ($\overline{u'w'}$) from Bricker and Monismith, 2007 and Feddersen and Williams, 2007 methods. Both methods yield similar estimates of Reynolds stess. Red vertical lines indicate the times of burst analysis shown in sub-figures (c,e) and (d,f). c) Power spectral density and e) Ogive curves based on a burst collected early on Feb 8, 2014. Before wave-removal (grey line), the computed stress was much higher than after wave removal by the Bricker (solid black) or FW (dashed black) method. d) Power spectral density and f) Ogive curves based on a burst collected early on Feb 9, 2014. The lack of difference between the Bricker and FW methods during both bursts indicates that the jumps in pressure do not affect the measured Reynolds stress.

A.2 Settling Velocity from ADV

While ADVs have been used extensively to compute particle settling velocity (Fugate & Friedrichs, 2002; Cartwright et al., 2013), we found that the environment in San Pablo Bay is not appropriate to apply this tool. The ADV method relies on the assumption that local unsteadiness and advective transport are negligible compared with settling and turbulent resuspension, that is, the terms on the left can be ignored in the transport equation (A.1), leading to equation 3.6:

$$\frac{\partial \langle C \rangle}{\partial t} + \frac{\partial \left(\langle u \rangle \langle C \rangle \right)}{\partial x} = w_s \frac{\partial \langle C \rangle}{\partial z} - \frac{\partial}{\partial z} w'C' \tag{A.1}$$

That assumption has been applied and justified in a number of studies that use ADVs to measure settling velocities (Fugate & Friedrichs, 2002; George Voulgaris & Meyers, 2004; Cartwright et al., 2013). However, it relies on a site-specific justification, and may not always be valid. For example, Schwarz et al., 2017 concluded that transient vertical fluxes during accelerating periods and horizontal flux divergence can impair the effectiveness of equation 3.6. We apply 1) a scaling analysis and 2) a term-wise estimation to equation A.1 to evaluate the appropriateness of the ADV method for measuring settling velocity with these data.

A simple scaling of equation A.1 yields a normalized equivalent in units of c as

$$\frac{H}{TW_s}\frac{\partial c}{\partial t'} + \frac{HU}{W_s L} u' \left(\frac{\partial c}{\partial x'} \right) = \frac{\partial c}{\partial z'} + \frac{K}{HW_s}\frac{\partial}{\partial z'} \left(k \frac{\partial c}{\partial z'} \right) \tag{A.2}$$

Here, H, T, W_s, U, L, and K are typical scales for water depth, time, settling velocity, horizontal velocity, length, and vertical eddy diffusivity, and quantities marked with ($'$) have been made dimensionless using the corresponding scale. In the estuarine setting we studied, time scales with the dominant tidal period, $T \sim 10^4$s. From our observations, water depth scales at $H \sim 2$m, max tidal velocity reaches $U \sim 0.4$m/s, and eddy viscosity scale is set at $K \sim 3 * 10^{-3}\text{m}^2/\text{s}$. The distance between two sensors in San Pablo Bay is about $L \sim 4000$m, and the settling velocity is roughly $W_s \sim 10^{-4}$m/s. Applying these scales to equation A.2, we find that relative to the settling term, the scaled unsteady (equation A.2, term 1) and advective (equation A.2, term 2) terms are both 2, and the scaled diffusive term (equation A.2, term 4) is 15. This order $1 - 10$ scaling of each term suggests that none of them can be ignored for the conditions here, and in particular unsteadiness and advection are relevant.

George Voulgaris and Meyers, 2004 found that the unsteady and advective terms were orders of magnitude smaller than the settling term, suggesting that advection had little impact in affecting ADV derived estimates of settling velocity at their site. Likewise, Cartwright et al., 2013 indicated that as long as the unsteady and advective terms were more than 4 times smaller than the settling term, then the ADV method is appropriate for finding settling velocity.

We performed a second estimate of terms in the advection-diffusion equation (A.1) to provide an independent analysis of the applicability of this method for settling velocity during CHC13. Here, we estimated the unsteady term (term 1) at site M1T. We computed

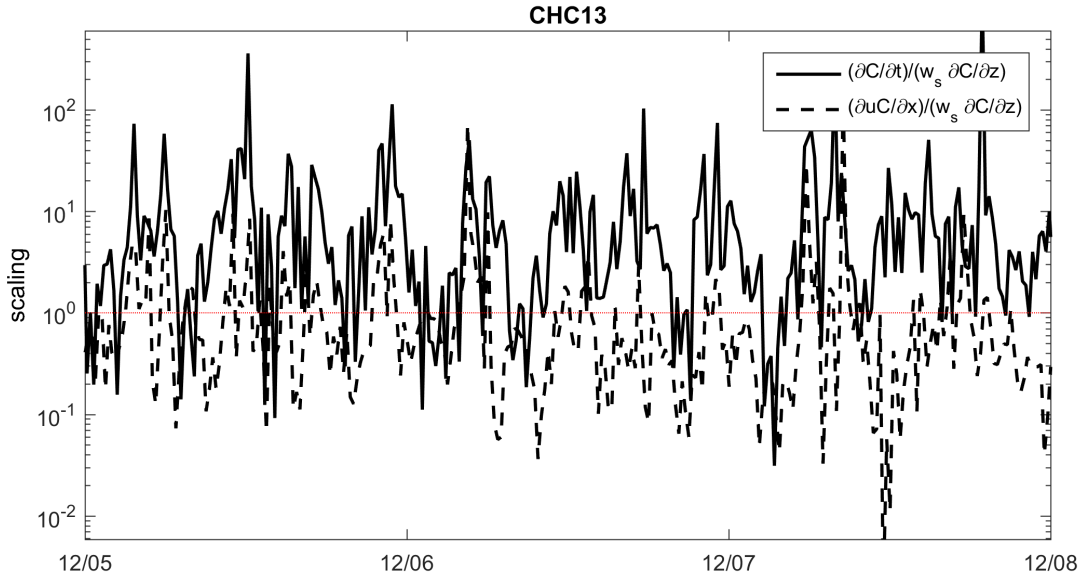

Figure A.4: Comparison of the relative importance of the unsteady term (solid) and advective term (dashed) with the settling term, during 3 days of CHC13. We have applied a constant w_s of 10^{-4} m/s. The unsteady term and settling term are computed at site M1T, while the advective term is computed between sites M2T and N1T.

the advective term (term 2) between sites M2T and N1T, as these locations were tidally aligned. For the settling term (term 3), we used the OBS sensors deployed at 0.31 and 0.7 mab at site M1T to compute $\partial C/\partial z$, and we assumed a constant settling velocity of $w_s = 10^{-4}$m/s. The estimates shown in figure A.4 indicate that it is rare that both the unsteady term and advective term are smaller than the assumed settling term, and thus can be only rarely neglected. If we assume a smaller settling velocity of $w_s = 2 * 10^{-5}$m/s, consistent with the LISST measurements, this scaling reveals even fewer periods when both the unsteady and advective terms are small relative to the settling term. While figure A.4 shows only 3 days of measured data, this scaling appears consistent over longer periods.

We conclude that the ADV method does not provide reliable estimates of settling velocity thanks to slow settling particles and gentle concentration gradients. Our subsequent analysis of particle settling relies on LISST measurements of suspended particle size.